CHEMIA

STUDIA UNIVERSITATIS BABEȘ-BOLYAI CHEMIA

S T U D I A
UNIVERSITATIS BABEŞ–BOLYAI
CHEMIA

2

CUPRINS – CONTENT – SOMMAIRE – INHALT

Studia Universitatis Babes-Bolyai Chemia has been selected for coverage in Thomson Reuters products and custom information services. Beginning with V. 53 (1) 2008, this publication is indexed and abstracted in the following:

- Science Citation Index Expanded (also known as SciSearch®)
- Chemistry Citation Index®
- Journal Citation Reports/Science Edition

MEASUREMENTS AND CORRELATIONS
OF THE VISCOSITY OF ISOPROPANOL MIXTURES
WITH DIESEL FUEL AND BIODIESEL

IRINA NIȚĂ[a,*], OLGA IULIAN[b], SIBEL OSMAN[a], TIMUR CHIȘ[a]

ABSTRACT. Isopropanol could be an additive or substitute for diesel fuel due to some of its key properties. Viscosity influences the atomization and spray formation, affecting the combustion process and the emission of diesel engine. Experimental data of viscosity of diesel fuel + isopropanol and biodiesel + isopropanol mixtures over the entire composition range at five temperatures (288.15, 293.15, 303.15, 313.15 and 323.15 K) are presented. Based on experimental data, the ability of predictive and correlative models to estimate the viscosity of the studied systems was tested. The best accuracy in viscosity estimation at a desired temperature is given by a polynomial equation, followed by Grunberg-Nissan equation. The value of Grunberg-Nissan interaction parameter G_{12} increases with temperature increasing, following a trend described by a polynomial equation. Negative values for deviation in viscosity were obtained for diesel fuel + isopropanol mixtures and positive values for biodiesel + isopropanol mixtures. The best fit with viscosity experimental data for viscosity dependence on temperature was provided by Vogel model.

Keywords: viscosity, biodiesel, isopropanol, diesel, viscosity models

INTRODUCTION

The search for sustainable and alternative fuels is a major topic of today research, taking into account that the use of fossil fuels is an important source for environmental pollution. It was proved that oxygenated fuels improve the combustion process, reducing harmful emissions like greenhouse gas and particulate matter [1]. The effect of biodiesel and alcohols such as

---

[a] *Ovidius University, of Constanta, Faculty of Applied Sciences and Engineering, 124 Mamaia Blvd, RO-900521 Constanta, Romania.*
[b] *Polytechnica University of Bucharest, Faculty of Applied Chemistry and Materials Science, 132 Calea Grivitei, RO-010737, Bucharest, Romania.*
[*] *Corresponding author: irinan9090@yahoo.com.*

methanol, ethanol and butanol addition to diesel fuel, on blends properties and diesel engine behaviour, respectively, have been widely investigated [2-5] due to their renewable nature and improved combustion. The need to diversify the biofuels used as additives or substitutes for fossil fuels is a stringent necessity taking into account the continuously increasing demand for energy in transport sector. Isopropanol could be a promising fuel alternative for emission control of combustion of fuel blends in compression engines. It was proved that isopropanol together with ethanol and n-butanol can be produced by fermentation of sugars from lignocellulosic biomass in the presence of appropriate bacteria [6].

The interest for isopropanol as additive or substitute for diesel fuel is due to some of its key properties that overcome methanol and ethanol like higher cetane number and energy content, reduced corrosivity due to its less water-absorbing nature, greater miscibility with diesel fuel, more like diesel fuel viscosity and density [7]. The addition of isopropanol to diesel fuel was proved to reduce the harmfully emissions of diesel engine [8]. Some properties of diesel fuel and biodiesel, as density and viscosity, important for diesel engine operation, can be improved by isopropanol addition. Experimental and correlated data of these properties for diesel + isopropanol and biodiesel + isopropanol mixtures are rarely reported in the literature. Density experimental data together with calculated excess molar volume values of pseudo-binary diesel fuel and biodiesel with isopropanol mixtures and corresponding ternary mixture, have been reported [9, 10]. As far as we know, in the literature have been presented data on viscosity only for the ternary diesel + biodiesel + isopropanol mixture [5].

Viscosity which expresses the internal resistance or friction to flow of a fluid, influences the atomization process and spray formation in accordance with the characteristics of the injection system of diesel engine [11], affecting the combustion process, and the exhaust emission composition, respectively. As viscosity is an important parameter to characterize fuels used for diesel engine, the main aim of the current study which is a continuation of our experimental work on properties of blends of fossil fuels with biofuels [10,12], is to report experimental viscosity data of pseudo-binary mixtures of diesel fuel and biodiesel with isopropanol over the entire composition range at 288,15 K to 323.15 K. The effects of alcohol fraction and temperature on the viscosity of diesel fuel + isopropanol and biodiesel + isopropanol systems have been investigated. The accuracy of different equations to estimate the viscosity of these systems with isopropanol have been assessed. An equation for the dependency on temperature of G_{12} interaction parameter from Grunberg – Nissan model is proposed. Deviation in viscosity ($\Delta\eta$) was obtained based on viscosity data. The results are useful for modelling diesel

engine behaviour fuelled by such blends in order to identify the best blend composition and to optimise engine design, resulting in reduced environment pollution.

MODELS FOR VISCOSITY ESTIMATION

Viscosity of a liquid mixture at atmospheric pressure depends on mixture composition and temperature. Various models proposed in the literature to correlate the experimental viscosity of liquid mixtures were tested for diesel fuel with biofuel blends. Mixing rules like simplified Grunberg-Nissan [13], Kendall-Monroe [14] and Frenkel [15] predict the viscosity of liquid mixtures from the viscosity of mixture components at a desired temperature, without the need of adjustable parameters (Table 1). Other correlative-predictive or correlative models with parameter were used to calculate the viscosity of diesel fuel blends with biofuels: Grunberg-Nissan [13] and polynomial type [16], respectively (Table 1). Exponential type temperature dependent equations: Andrade [17], Vogel [18] and Tat and Van Gerpen [19] were used to estimate the viscosity of different diesel fuel with biofuel blends (Table 1). The significance of symbols used in Eqs. (1-8) is as follows: η represents the dynamic viscosity of the mixture, η_1, η_2 and x_1, x_2 represent the dynamic viscosity and mole fraction, respectively for the components of the mixture, T represents the absolute temperature, G_{12}, *a, b, c, A, B, C* are adjustable parameters.

Table 1. Models for viscosity calculation

Model	Ref.	Equation	
		Viscosity dependence on composition	
Grunberg-Nissan simplified	[12]	$\eta = \exp(x_1 ln\eta_1 + x_2 ln\eta_2)$	(1)
Kendall-Monroe	[13]	$\eta = \left(x_1\eta_1^{1/3} + x_2\eta_2^{1/3}\right)^3$	(2)
Frenkel	[14]	$\eta = exp(x_1^2 ln\eta_1 + x_2^2 ln\eta_2 + 2x_1x_2 ln\eta_{12})$ where $\eta_{12} = 0.5\eta_1 + 0.5\eta_2$	(3)
Grunberg-Nissan	[12]	$\eta = exp(x_1 ln\eta_1 + x_2 ln\eta_2 + x_1x_2 G_{12})$	(4)
Polynomial	[15]	$\eta = ax^2 + bx + c$	(5)
		Viscosity dependence on temperature	
Andrade	[16]	$\eta = Aexp(B/T)$	(6)
Vogel	[17]	$\eta = exp(A + B/(C + T))$	(7)
Tat and Van Gerpen	[18]	$\eta = exp(A + B/T + C/T^2)$	(8)

The ability of different models to accurately predict the viscosity of fuels mixtures can be assessed by the means of statistical indicators like average relative deviation (ARD %) and standard deviation (SD). The following equations were used:

$$ARD(\%) = \frac{100}{N} \sum_{i=1}^{N} \left(\frac{|\eta_{xp,i} - \eta_{cal,i}|}{\eta_{exp,i}} \right) \tag{9}$$

$$SD = \left(\frac{\sum_{i=1}^{N} (\eta_{exp,i} - \eta_{cal,i})^2}{N-m} \right)^{1/2} \tag{10}$$

where η_{exp} and η_{cal} represent the experimental and calculated viscosity, respectively, N represents the number of experimental points, and m is the number of model parameters.

RESULTS AND DISCUSSION

Experimental data of dynamic viscosity of diesel fuel + isopropanol and biodiesel + isopropanol mixtures in the temperature range of 288.15 K to 323.15 K are presented in Table 2.

Table 2. Experimental data of viscosity of diesel fuel + isopropanol and biodiesel + isopropanol mixtures

Mole fraction	Dynamic viscosity (mPa·s)				
(x₂)	288.15 K	293.15 K	303.15 K	313.15 K	323.15 K
Diesel fuel (1) + isopropanol (2)					
0.0000	4.0629	3.5437	2.7978	2.2529	1.8505
0.1002	3.8959	3.4019	2.6495	2.1461	1.7952
0.1997	3.6824	3.2163	2.5431	2.0526	1.7010
0.3972	3.3610	2.8982	2.3201	1.8659	1.5322
0.5982	3.1501	2.7482	2.1358	1.6932	1.3865
0.7970	2.9045	2.5375	1.9451	1.5184	1.2218
0.9086	2.8412	2.4288	1.8470	1.4216	1.1254
1.0000	2.8999	2.4633	1.8358	1.3825	1.0514
Biodiesel (1) + isopropanol (2)					
0.0000	7.5205	6.4987	5.0198	4.0301	3.2988
0.1021	7.1280	6.1997	4.8583	3.8611	3.1252
0.2019	6.4882	5.6214	4.4765	3.4920	2.8690
0.3984	5.7949	5.0505	3.9295	3.1726	2.5511
0.6027	4.9749	4.3562	3.3849	2.6926	2.1919
0.7987	3.9183	3.3453	2.5928	2.0017	1.6374
0.9301	3.1481	2.7238	2.0874	1.6164	1.2820
1.0000	2.8999	2.4633	1.8358	1.3825	1.0514

The viscosity of isopropanol is lower than that of diesel fuel and biodiesel, respectively. The decrease of dynamic viscosity of diesel fuel + isopropanol and biodiesel + isopropanol pseudo-binary systems with alcohol concentration increasing and temperature increasing can be observed as expected. The decreasing trend of viscosity with alcohol content increasing is higher for biodiesel + isopropanol system. The addition of isopropanol to biodiesel brings the viscosity of the resulting mixture closer to that of diesel fuel. It can be observed that the decrease of the viscosity of diesel fuel + isopropanol mixtures with the increasing alcohol content shows a minimum point in the concentration zone of $x = 0.9$ for temperature ranging from 288.15 K to 303.15 K. The minimum reduces with temperature increasing, to disappear for temperatures greater than 303.15 K.

Viscosity – composition correlation

Equations (1-5) (Table 1) were used to calculate the dynamic viscosity of diesel fuel + isopropanol and biodiesel + isopropanol mixtures for temperature ranging from 288.15 K to 323.15 K. Based on experimental data of dynamic viscosity, the fitting parameters of Eq. (4) and Eq. (5) were calculated (Table 3). The obtained values for interaction parameter G_{12} are greater for biodiesel + isopropanol mixture, compared to diesel fuel + isopropanol mixture. The same observation was reported in the literature on biodiesel and diesel fuel blends with ethanol and n-butanol [4].

Table 3. Fitting parameters of Grunberg-Nissan (Eq.4) and polynomial type (Eq.5) models and corresponding accuracies (SD)

Parameter	Temperature (K)				
	288.15	293.15	303.15	313.15	323.15
Diesel fuel + isopropanol					
Eq. (4)					
G_{12}	-0.2593	-0.2090	-0.1061	0.0071	0.1895
SD (mPa·s)	0.0521	0.0399	0.0209	0.0112	0.0090
Eq. (5)					
a	0.9675	0.7460	0.3604	0.1579	-0.0225
b	-2.1997	-1.8706	-1.3390	-1.0409	-0.7849
c	4.0839	3.5580	2.7926	2.2525	1.8591
SD (mPa·s)	0.0402	0.0367	0.0184	0.0100	0.0097
Biodiesel + isopropanol					
Eq. (4)					
G_{12}	0.5352	0.6033	0.7512	0.8303	0.9642
SD (mPa·s)	0.1295	0.1232	0.0823	0.0983	0.1018
Eq. (5)					
a	-0.6842	-0.8085	-0.8950	-0.8168	-0.7515
b	-3.9247	-3.2208	-2.3170	-1.8105	-1.4421
c	7.4763	6.4673	5.0356	4.0081	3.2658
SD (mPa·s)	0.1052	0.1017	0.0559	0.0684	0.0501

It can be observed (Table 3) that the values of G_{12} parameters increase with temperature increasing, following a trend described by polynomial equations:

$$G_{12,d} = 0.0002T^2 - 0.1086T + 14.5130 \qquad (R^2 = 0.9908) \qquad (11)$$
$$G_{12,bd} = 0.00002T^2 + 0.0033T - 1.6791 \qquad (R^2 = 0.9680) \qquad (12)$$

where $G_{12,d}$ refers to diesel fuel + isopropanol system and $G_{12,bd}$ refers to biodiesel + isopropanol system.

The value of parameter G_{12} was also determined for the temperature of 313.15 K (the reference temperature in accordance with fuels quality standards) following the equations proposed by Lapuerta et al. [4]:

$$G_{12,d} = 0.11n^2 - 1.242n + 2.897 \qquad (13)$$
$$G_{12,bd} = 0.141n^2 - 1.486n + 3.851 \qquad (14)$$

where n represents the number of carbon atoms from the alcohol molecule. The resulting values were $G_{12,d} = 0.161$ and $G_{12,b} = 0.662$, respectively. It can be observed that these values are not very close to the values obtained based on experimental data but, it should be noticed that Eqs. (13) and (14) have been proposed for linear chain alcohols.

The accuracy of Eqs. (1-5) to estimate the viscosity of diesel fuel + isopropanol and biodiesel + isopropanol mixtures over the temperature range of 288.15 K to 323.15 K, expressed by ARD (%) is presented in Figure 1. The best results (smaller ARD values) have been obtained for diesel fuel + isopropanol system.

Between the mixing rules, Eq. (1) shows the best results in predicting the viscosity of diesel fuel + isopropanol mixtures (ARD < 3.4%), and Eq. (3) for biodiesel + isopropanol mixtures (ARD < 7.69 %). Mixing rules (Eqs. 1 - 3) have lower accuracy compared to equations with parameters (Eqs. 4 and 5). As presented in Fig.1, the best accuracy in viscosity estimation at a desired temperature is given by Eq. (5) (ARD < 0.89 % for diesel fuel + isopropanol system and ARD < 1.41 % for biodiesel + isopropanol system), followed by Eq. (4) (ARD < 1.21 % for isopropanol mixtures with diesel fuel and ARD < 3.48 % for isopropanol mixtures with biodiesel). Comparing the results obtained with Grunberg-Nissan simplified model (Eq. 1) with Grunberg-Nissan model (Eq. 4), it can be observed that the application of interaction parameter G_{12} improves the result for both studied systems with isopropanol. Similar results were reported in the literature for blends of diesel fuel with ethanol and n-butanol, and biodiesel with ethanol, n-propanol, and n-butanol [4]. This result is expected for complex systems like diesel fuel and biodiesel mixtures with

isopropanol, taking into account the structural differences between the alcohol molecule (highly polar) and the hydrocarbons molecules from diesel fuel (non-polar n-alkanes and reduced polarity aromatics) and fatty acid esters molecules from biodiesel (low polarity).
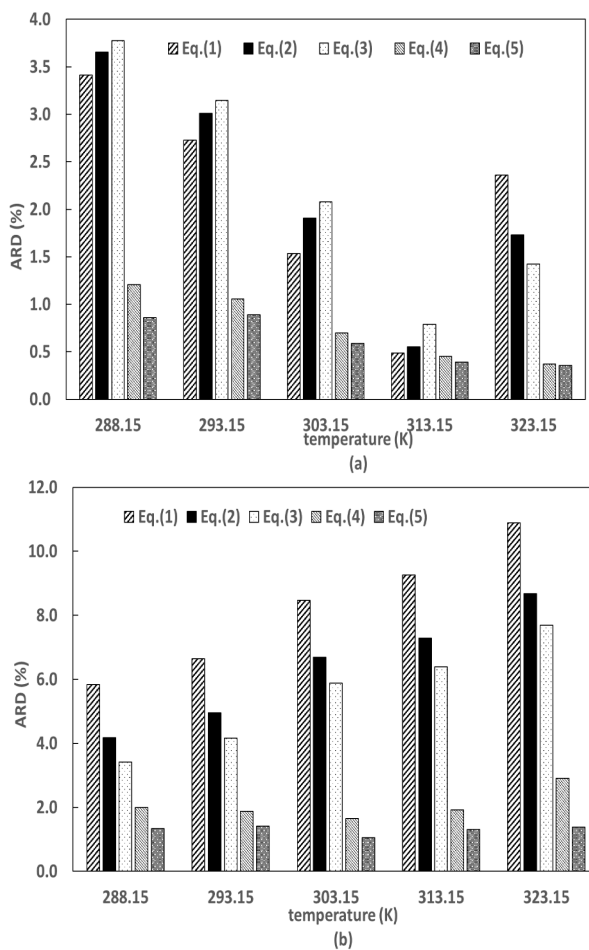
Figure 1. Accuracies (ARD %) of viscosity calculated with models described by Eqs.(1 - 5) for (a) diesel fuel + isopropanol and (b) biodiesel + isopropanol systems

Figure 2 presents dynamic viscosity calculated with Eqs. (1- 5), versus experimental viscosity for the reference temperature of 313.15 K. Eq. (4) was applied using G_{12} parameter value determined based on experimental data, and in accordance with Eqs. (13) and (14), respectively.
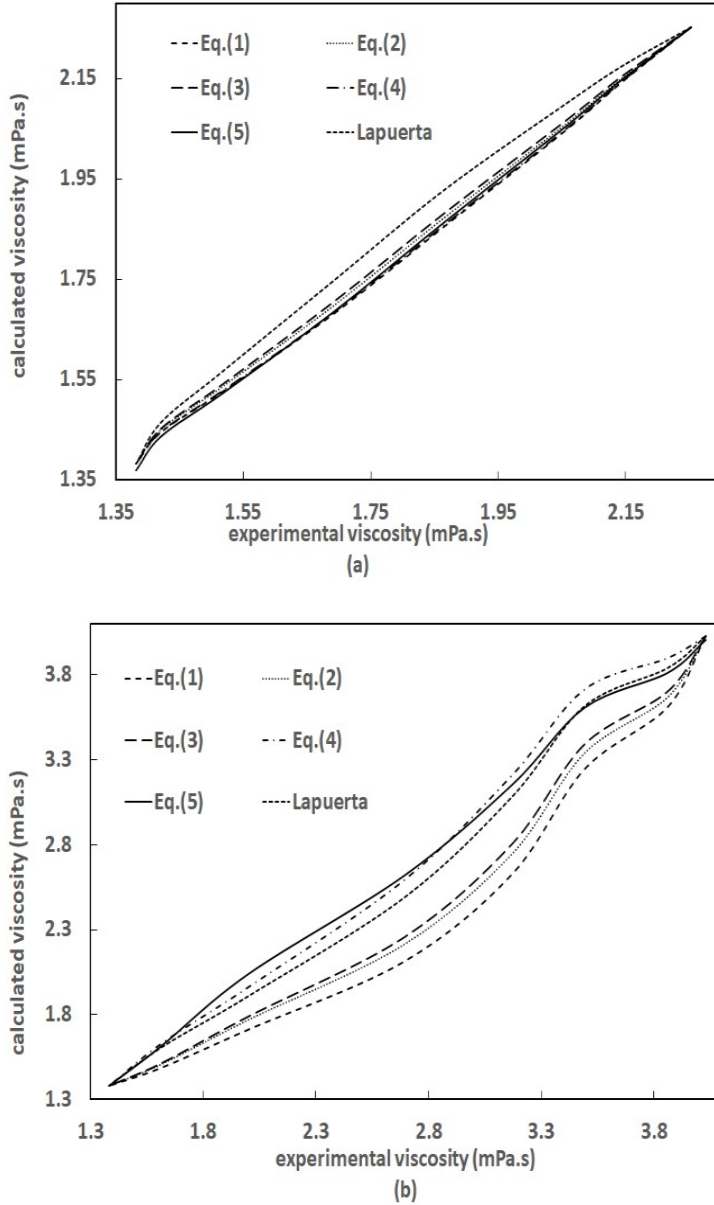
Figure 2. Calculated viscosity versus experimental viscosity for (a) diesel fuel + isopropanol and (b) biodiesel + isopropanol system at 313.15 K (G_{12} parameter value is calculated based on experimental data (Eq.4) and applying equations proposed by Lapuerta et al. [4])

Viscosity estimation with Grunberg-Nissan model with the value of G_{12} parameter determined based on experimental data is more accurate than using the value determined based on Lapuerta equation [4] but, it must be noted that the accuracy of Grunberg-Nissan model using Lapuerta value for G_{12} parameter is greater than that corresponding to mixing rules (Eqs.1-3).

In order to evaluate the viscosity deviation at mixing ($\Delta\eta$) which is important in practice (production and equipment design), the following relation was used:

$$\Delta\eta = \eta - (x_1\eta_1 + x_2\eta_2) \tag{15}$$

Figure 3 presents deviation in viscosity variation with alcohol content of diesel fuel + isopropanol and biodiesel + isopropanol mixtures. The difference in the variation of $\Delta\eta$ with composition for diesel fuel + isopropanol and biodiesel + isopropanol mixtures can be influenced by molecular interactions, but also by the size and shape of mixtures components. Diesel components include linear and cyclic n-alkanes, olefins and aromatics, but non-polar n-alkane are predominant. Biodiesel is a mixture of monoalkyl esters of fatty acids with reduced polarity.

The $\Delta\eta$ as well as interaction parameter G_{12} are majority negative for diesel fuel + isopropanol mixtures indicating that specific interaction between unlike molecules is absent. Similar behaviour with diesel fuel + isopropanol system was reported in the literature for binary mixture of cyclopentane with isopropanol [19]. The $\Delta\eta$ as well as interaction parameter G_{12} are positive for biodiesel + isopropanol mixtures. Moderately positive values should indicate that specific interaction would be present between the functional groups of the components.
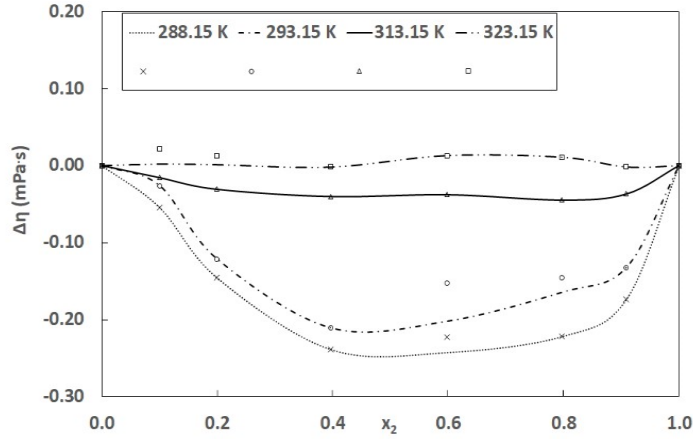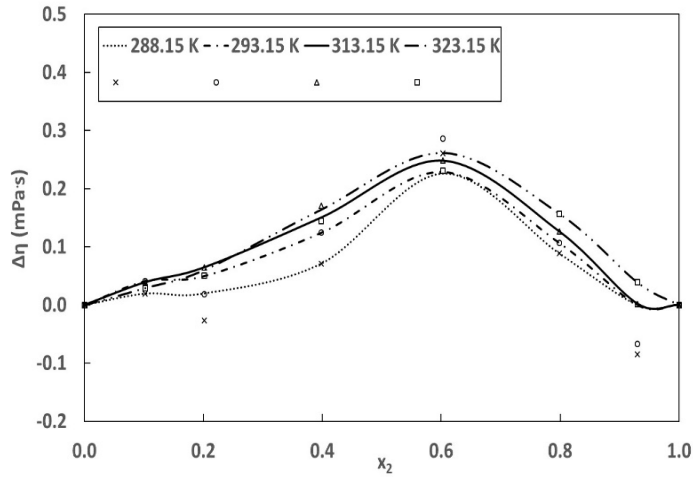
Figure 3. Deviation in viscosity ($\Delta\eta$) versus alcohol mole fraction for
(a) diesel fuel + isopropanol and (b) biodiesel + isopropanol systems at 313.15 K
(lines - smoothed data; points- calculated data)

Viscosity – temperature correlation

Equations (6-8) were applied to calculate the dynamic viscosity of diesel fuel + isopropanol and biodiesel + isopropanol mixtures for temperature range of 288.15 K to 323.15 K.

Table 4. Fitting parameters of Eqs. (6), (7) and (8) and
standard deviations (SD) for diesel fuel + isopropanol mixtures

Parameter	x_2							
	0.0000	0.1002	0.1997	0.3972	0.5982	0.7970	0.9086	1.0000
	Eq. (6)							
A	0.0029	0.0029	0.0029	0.0026	0.0016	0.0009	0.0006	0.0003
B	2086.86	2073.58	2060.29	2061.29	2191.12	2320.42	2453.40	2659.42
SD	0.0255	0.1879	0.2593	0.3655	0.4469	0.5155	0.5505	0.5775
	Eq. (7)							
A	-3.1768	-5.7556	-5.7955	-5.9645	-6.4316	-6.9646	-7.4941	-8.3081
B	775.24	2019.16	2030.69	2058.80	2171.65	2310.79	2456.12	2715.16
C	-118.79	-3.8879	-1.7195	-0.7634	-1.3932	-0.3894	-0.2797	1.5381
SD	0.0109	0.0532	0.0330	0.0409	0.0206	0.0101	0.0164	0.0103
	Eq. (8)							
A	-5.8459	-5.8361	-5.8304	-5.9785	-6.4611	-6.9723	-7.4997	-8.2633
B	2085.95	2069.82	2052.84	2068.20	2190.57	2316.05	2460.05	2687.79
C	13.6359	13.5377	13.4225	13.5176	14.3164	15.1317	16.0650	17.5347
SD	0.0945	0.0361	0.0603	0.0402	0.0236	0.0430	0.0062	0.0103

Table 5. Fitting parameters of Eqs. (6), (7) and (8) and
standard deviations (SD) for biodiesel + isopropanol mixtures

Parameter	x_2							
	0.0000	0.1021	0.2019	0.3984	0.6027	0.7987	0.9301	1.0000
	Eq. (6)							
A	0.0037	0.0036	0.0034	0.0030	0.0025	0.0011	0.0008	0.0003
B	2188.08	2188.48	2176.17	2176.76	2190.30	2346.59	2389.98	2659.41
SD	0.0772	0.0290	0.0488	0.0317	0.0183	0.0340	0.0051	0.0116
	Eq. (7)							
A	-1.8004	-5.6588	-5.6805	-5.8003	-5.9924	-6.7652	-7.1499	-8.3081
B	486.81	2203.62	2175.79	2182.69	2189.00	2340.26	2389.72	2715.16
C	-160.61	1.1434	0.2523	0.9095	0.1349	0.0601	-0.0659	1.5381
SD	0.0122	0.0362	0.0603	0.0402	0.0233	0.0428	0.0061	0.0103
	Eq. (8)							
A	-5.5886	-5.6304	-5.6729	-5.7773	-5.9865	-6.7597	-7.1511	-8.2633
B	2187.93	2186.70	2171.64	2169.13	2186.16	2336.06	2390.55	2687.79
C	14.3033	14.2867	14.1915	14.1726	14.2860	15.2748	15.6113	17.5347
SD	0.0945	0.0361	0.0603	0.0402	0.0236	0.0430	0.0062	0.0103

The values of the fitting parameters determined based on experimental viscosity data, and the corresponding standard deviations are listed in Table 4 and 5.

Comparison of the performance of Eqs. (6-8) used to calculate the dynamic viscosity of mixtures of diesel fuel and biodiesel with isopropanol at different temperatures can be made based on accuracy data (ARD %) presented in Figure 4. Similar good accuracies were obtained with Eqs. (6), (7), and (8), ARD (%) was no greater than 1.13 % for mixtures of isopropanol with diesel fuel, and no greater than 0.96 % for mixtures with biodiesel, but it

should be noted that Vogel model provides the best fit (ARD < 1.12 % for isopropanol mixtures with diesel fuel and ARD < 0.88 % for isopropanol mixtures with biodiesel). Vogel model can be recommended for dynamic viscosity calculation for diesel fuel + isopropanol and biodiesel + isopropanol mixtures.
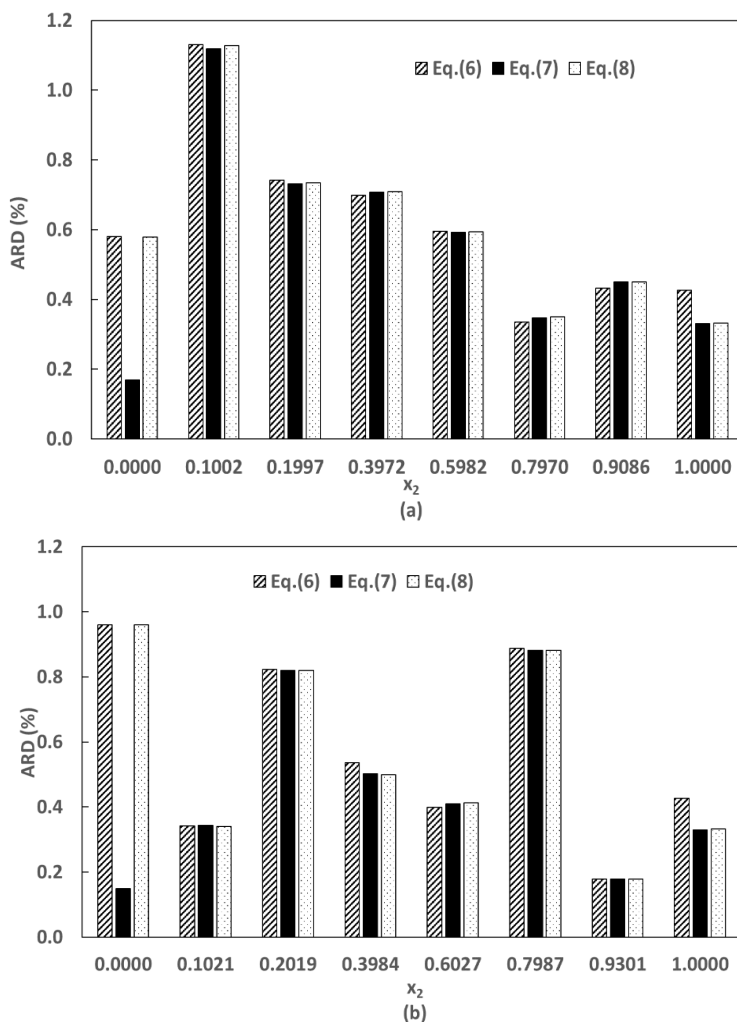

Figure 4. Deviation between calculated (Eqs. 6 - 8) and experimental dynamic viscosity for (a) diesel fuel + isopropanol and (b) biodiesel + isopropanol mixtures

CONCLUSIONS

Experimental measurements of dynamic viscosity of diesel fuel+ isopropanol and biodiesel + isopropanol systems over the entire composition range at 288,15 K, 293.15 K, 303.15 K, 313.15 K, and 323.15 K under atmospheric pressure have been reported. The addition of isopropanol to biodiesel helps to reduce the viscosity of biodiesel and to bring it closer to that of diesel fuel.

The ability of different models to estimate the viscosity of diesel fuel and biodiesel mixtures with isopropanol as a function of composition or temperature was assessed. A three parameters polynomial equation has the best accuracy of viscosity estimation at a given temperature for diesel fuel or biodiesel mixtures with isopropanol.

An equation is proposed to describe the dependency on temperature for the interaction parameter from Grunberg-Nissan model.

Positive values of $\Delta\eta$ have been obtained for diesel fuel + isopropanol mixtures and negative values for biodiesel + isopropanol mixtures. Among exponential equations used to estimate the viscosity of diesel fuel and biodiesel mixtures with isopropanol at different temperatures, Vogel model can be recommended.

EXPERIMENTAL SECTION

Diesel fuel used in this study was supplied by a local company and fulfils the requirements of the European Standard EN 590. Biodiesel obtained from a biodiesel producer follows the European Standard EN 14214 requirements. Table 6 shows properties of these two fuels. Isopropanol of at least 99.0% purity, contained 0.1 ppm of water and has an acidity value of 0.001 %. Pseudo-binary mixtures of diesel fuel with isopropanol, and biodiesel with isopropanol were prepared by mass using an analytical balance with a precision of $1 \cdot 10^{-4}$ g. In order to prevent evaporation, samples were kept in glass bottles tightly closed and filled at least of 90 % of the volume.

Viscosity of the investigated pseudo-binary systems was measured according to ASTM D 7042 method on an Anton Paar SVM 3000 viscometer at atmospheric pressure and at temperatures ranging from 288.15 K, to 323.15 K. The temperature of the samples was maintained by the integrated thermostated bath with an accuracy of +/- 0.02 K. The viscometer was calibrated using ambient air and double distilled water before each series of measurements. The uncertainty in viscosity data was estimated to be ± 0.35 %.

Table 6. Properties of diesel fuel and biodiesel

Property	Method	Diesel fuel		Biodiesel	
		EN 590	exp*	EN 14214	exp*
Kinematic viscosity at 40°C (mm²/s)	EN 3104	2.0 – 4.5	2.7393	3.50 – 5.00	4.6699
Density at 15°C (kg/m³)	EN 12185	820 - 845	840.1	860 - 900	881.2
Water content (mg/kg)	EN 12937	max 200	97	max 500	259
Sulphur content (mg/kg)	ASTM D5453	max 10	8.2	max 10	5.0
Methylic esters of fatty acid (% wt)	EN 14103		0	min 96.5	98.2
Monglycerides (% wt)	EN 14105			max 0.80	
Diglycerides (% wt)	EN 14105			max 0.20	
Triglycerides (% wt)	EN 14105			max 0.20	
Mean molar mass (g/mol)			211		296
Cetane number	EN 4264	min 49	50	>51	52.8
Free glycerol (% wt)	EN 14105			max 0.02	0.015
Total glycerol (% wt)	EN 14105			max 0.25	0.23

*experimentally determined

REFERENCES

1. R. F. B. Junior; C. A. Martins; *Fuel*, **2015**, *148*, 191–201.
2. G. R. Moradi; B. Karami; M. Mohadesi; *Journal of Chemical Engineering Data*, **2013**, *58(1)*, 99-105.
3. A. Todorut; A. Molea; I. Barabas; *Periodica Polytechnica Chemical Engineeering*, **2020**, *64(2)*, 213-220.
4. M. Lapuerta; J. Rodriguez-Fernandez; D. Fernandez-Rodriguez; R. Patino-Camino; *Fuel*, **2017**, *199*, 332-338.
5. M. Gulum; A. Bilgin; *Energy*, **2018**, *148(1)*, 341-361.
6. S. B. Bankar; G. Jurgens; S. A. Survase; H. Ojamo; T. Granström; *Renewable Energy*, **2015**, *83*, 1076-1083.
7. P. Geng; E. Cao; Q. Tan; L. Wei; *Renewable and Sustainable Energy Reviews*, **2017**, *71*, 523–534.
8. A. Frassoldati; A. Cuoci; T. Faravelli; U. Niemann; E. Ranzi; R. Seiser; K. Seshadri; *Combust. Flame*, **2010**, *157(1)*, 2–16.
9. M. Feyzi; Z. Shahbazi; L. Norouzi; *Journal of Molecular Liquids*, **2018**, *249*, 1271-1278.
10. G. R. Sandu; I. Nita; S. Osman; O. Iulian; *UPB Sci. Bull. series B*, **2018**, *80(1)*, 87-100.
11. M. Das; M. Sarkar; A. Datta; A. K. Santra; *Fuel*, **2018**, *220*, 769-779.

12. L. Grunberg; A. H. Nissan; *Nature*, **1949**, *164*, 799-800.
13. J. Kendal; K. P. Monroe; *J. Am. Chem. Soc.*, **1917**, *39(9)*, 1787-1802.
14. J. Frenkel; *J. Phys. Chem.,* **1947**, *51(4)*, 1032-1033.
15. E. Alptekin; M. Canakci; *Renewable Energy*, **2008**, *33*, 2623-2630.
16. E. N. C. Andrade; *Nature*, **1930**, *125*, 309-310.
17. H. Vogel; *Physikalische Zeitschrift*, **1921**, *22*, 645-646.
18. M. Tat; J. Van Gerpen; *J. Am. Oil Chem. Soc.*, **1999**, *76*, 1511-1513.
19. H. Kumar; M. Singla; A. Khosla; R. Gaba; *J. Mol. Liq.*, **2011**, *158*, 182-186.

NOVEL COMPOSITE BASED ON ZIRCONIA AND GRAPHITE. FIRST RESULTS OF APPLICATION FOR SYNTHETIC DYES REMOVAL

**KATARINA STEPIĆ[a], RADOMIR LJUPKOVIĆ[a,*],
ALEKSANDRA ZARUBICA[a], STEFAN ĐORĐIJEVSKI [b],
BRANKO MATOVIĆ[c], JUGOSLAV KRSTIĆ[d],
ALEKSANDAR BOJIĆ[a]**

ABSTRACT. In this research composite based on zirconia and graphite was synthesized using the sol-gel method. Aim of this research is to activate and increase the photocatalytic activity of ZrO_2 by combining with graphite-based material. Our results show that we obtained material that can remove both cationic and anionic dyes by sorption and photocatalytic processes. Obtained composite is very effective in sorption of RB19 with up to 100% removal. Photocatalytic activity of composite is higher than pristine GO and goes up to 100% for RB19 degradation and about 50% degradation of MB. These results are promising and present an excellent base for further research.

Keywords: *Composite, Zirconia, Graphite, Methylene blue, Reactive blue 19, Sorption, Photocatalysis, UV degradation*

INTRODUCTION

The dyes and their intermediates are the second most dangerous water pollutant, immediately after agriculture, and dye contamination of water is a major global problem that caused severe issues for nature and human society [1]. They are easy to recognize in the water, even at very low concentrations (aesthetically undesirable and easily soluble), and some dyes and their degradation products may be toxic and carcinogens, which is why

[a] *Department of Chemistry, Faculty of Science and Mathematics, University of Niš, Višegradska 33, Niš 18000, Serbia.*
[b] *Mining and Metallurgy Institute, Bor, Zeleni bulvar, Serbia.*
[c] *Institute for Nuclear Sciences Vinča, University of Belgrade, Belgrade 11351, Serbia.*
[d] *Institute of Chemistry, Technology and Metallurgy, University of Belgrade, Njegoševa 11, 11000 Belgrade, Serbia.*
[*] *Corresponding author: radomir.ljupkovic@pmf.edu.rs, ljupkovic@gmail.com.*

they are very harmful to the aquatic world [2]. Some of the dyes mentioned in this paper are Methylene blue (MB) and Reactive blue 19 (RB 19). Methylene blue is an organic salt (methylthioninium chloride) that has wide application in the cotton, silk, paper and wood industry. This dye can have various harmful effects, although it is not strongly dangerous, it can induce eye burns which may be responsible for permanent injury to the eyes of humans and animals [3]. Also, it can cause short periods of rapid or difficult breathing if inhaled [4]. Reactive blue 19 is an anthraquinone dye and is most commonly used in the textile industry because of its high color stability and low degradability [5]. RB 19 is very toxic for aquatic organisms and unsuitable for human health [6]. The main difference between these two dyes is that RB 19 contains two anionic sulfonate groups on its structure which renders a negative charge to it, while MB has a positive charge because of cationic groups on its structure.

Methods such as adsorption [7], biodegradation [8], oxidation [9], photocatalytic degradation [10] and ultrafiltration [11] have been used for the removal of dye pollutants from wastewater. Among all these processes, sorption is considered a conventional, but efficient, easy and economic process. Adsorption is an effective method for water decolorization that does not result in the formation of hazardous substances [12]. Many materials (commercial active carbon, bioadsorbents, natural materials and wastes from agriculture) have been used for adsorption processes and the choice depends on the properties of the required adsorbent [13].

Photocatalytic reactions are known as a sustainable method of the removal of many environmental pollutants in which we use photocatalysts to initiate reactions decomposition of contaminants under ultraviolet (UV) or sunlight irradiation without using chemical substances or producing chemical wastes. Today, UV water purification is one of the most effective method for water treatment with an efficiency greater than 99%. Photocatalytic treatments are also cheap and eco-friendly methods for water purification, where the main limiting factors are wide band gap and fast electron/hole recombination of used photocatalyst [14]. The surface properties of photocatalytic material have been modified to improve photocatalytic activity. Various heterogeneous semiconductors (TiO_2, ZnO, SnO_2, ZrO_2) are most commonly used for this purpose [15].

Nowadays, graphene and its derivates are used in environmental applications for the removal of different pollutants from wastewater. Graphene oxide (GO) is a layered solid compound with a large number of oxygen-containing functional groups that are known to stabilize the colloidal form of GO material [16]. A useful discovery is that graphene oxide can be directly used as an effective absorbent for the decoloration of methylene blue. The main advantages of GO usage for the removal of MB are high absorption capacity for MB and a fast adsorption process [7]. There are methods of

synthesis of GO which can be divided into bottom-up methods where carbon molecules build pristine graphene, and "top-down" methods where layers of graphene derivatives are obtained from a carbon source, such as graphite [17,18]. Bottom-up synthesis covers chemical vapor deposition, epitaxial growth, etc. are time consuming [19]. Graphene oxide can be prepared by the conventional and modified Hummers-Offeman method [20], whose principle is the oxidation of graphite with strong oxidizing agents to exfoliate graphite. GO coatings can also been made on various supports. L.C. Pop et al. deposited GO on a polypropylene membrane by the patented process. GO suspension was obtained by the oxidative-exfoliation method by using a mixture of sulphuric and phosphorous acid in combination with $KMnO_4$, followed with H_2O_2 adding and washing with water, hydrochloric acid and ethanol [21].

It has been reported that doping of graphene oxide based materials with a variety of heterogeneous semiconductors results in surface modification and significant improvement in its adsorptive and photocatalytic properties. As example, Wang et al. synthesized $g\text{-}C_3N_4/CeO_2/N\text{-}rGO$ heterocomposite which exhibits enhanced photocatalytic activity in compare to pristine $g\text{-}C_3N_4$, CeO_2 nanorods [22]. Chauhan et al. found that GO/ZnO photocatalyst constantly developed over silicon substrate have 33% higher photodegradation of MB dye compared to pristine ZnO [23]. ZrO_2 is a widely used catalyst in photocatalyst reaction, mainly because of its favorable textural, structural, morphological and surface properties. Zirconium oxide is chemically inert, non-toxic, and insoluble in water, and because of these features, it is great dopant material [24].

The application of zirconia-graphene oxide based composites is explained in this paper, as one of the effective doped photocatalysts for the removal of organic dyes from water. It is presented an economical and eco-friendly method for obtaining ZrO_2-graphene oxide based composite by using a modified sol-gel method, and also the influence of zirconium-doping on physical and chemical properties and activity of graphene oxide. Decolorization of cationic dye MB and anionic dye RB 19 was used as a test reaction for examination of the activity of sorbents, while degradation of the above mentioned dyes under UV light irradiation was used as a test reaction for examination of the activity of catalysts.

RESULTS AND DISCUSSION

Characterization of synthesized materials

FT-IR spectrum of pure GO contains broad band with a maximum at 3442.47 cm^{-1} which can be assigned to vibrations of water molecules and O-H bonds. Most of the other present peaks can be assigned to C=C, and C-O

vibrations, with exception of the band at 645.10 cm^{-1} which represent O-H bending vibrations. At 1100.72 cm^{-1} is a peak that represents C-O-C vibrations [25]. The peak at 1212.85 cm^{-1} can be assigned either to C-O vibrations or vibrations that originate from covalent sulfates. Different C=C vibrations are represented by peaks at 1563.10, 1583.34, and 1630.11 cm^{-1}, while C=O can be described by peak at 1718.83 cm^{-1} [26]. All these peaks are represented in the following Figure 1.
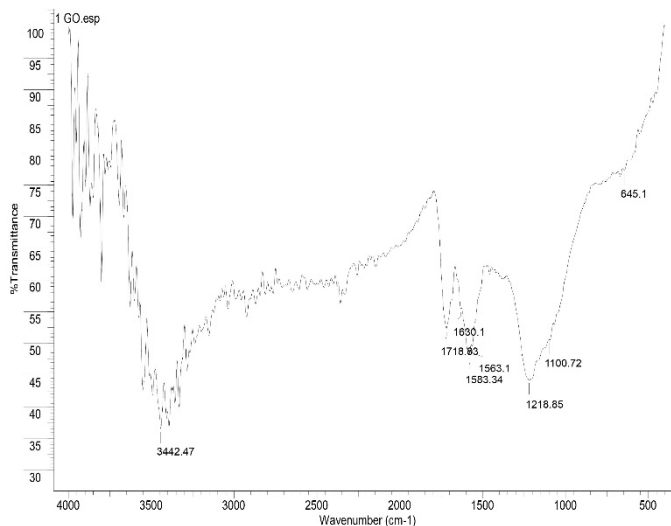
Figure 1. FT-IR spectrum of GO sample.
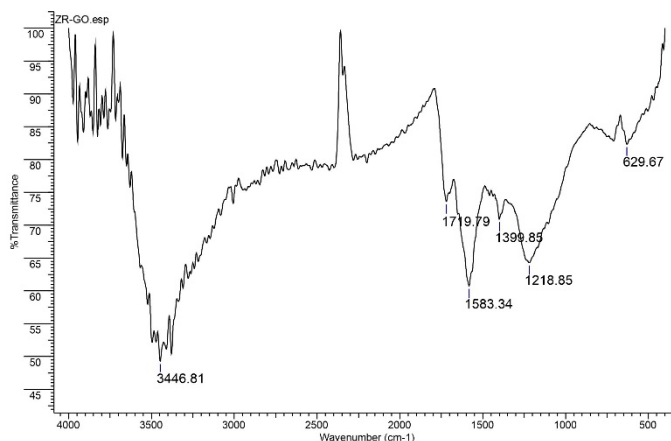
Figure 2. FT-IR spectrum of composite ZrO$_2$/GO.

In FT-IR spectra of ZrO_2/GO loss of bands for C-O-C (1100.72 cm^{-1}) and C=C (1563.10 and 1630.11 cm^{-1}) is observed. The band at 629.67 cm^{-1} can be assigned to Zr-O vibrations. The peak at 1399.65 cm^{-1} can be originated from Zr-OH vibrations. Other present vibrations are assigned to common graphite/graphene oxide vibrations: 1218.85 cm^{-1} for C-O, 1583.34 cm^{-1} for C=C stretching, 1718.83 cm^{-1} for C=O, and 3442.47 cm^{-1} for water [24]. All these peaks assigned to composite ZrO_2/GO are represented in the following Figure 2.

Diffractograms of our samples show relatively low crystallinity. The diffractogram of the GO sample shows a dominant wide peak at 2θ 26° which is a reflection of graphite planes [24]. Also, there are peaks at 2θ 43° and 2θ 13° as reflections correspond to (001) and (100) planes of GO [27]. We can assume that the oxidation of graphite was incomplete, so we have reflection corresponding to graphite and GO planes. All these peaks assigned to the GO sample are represented in the following Figure 3.
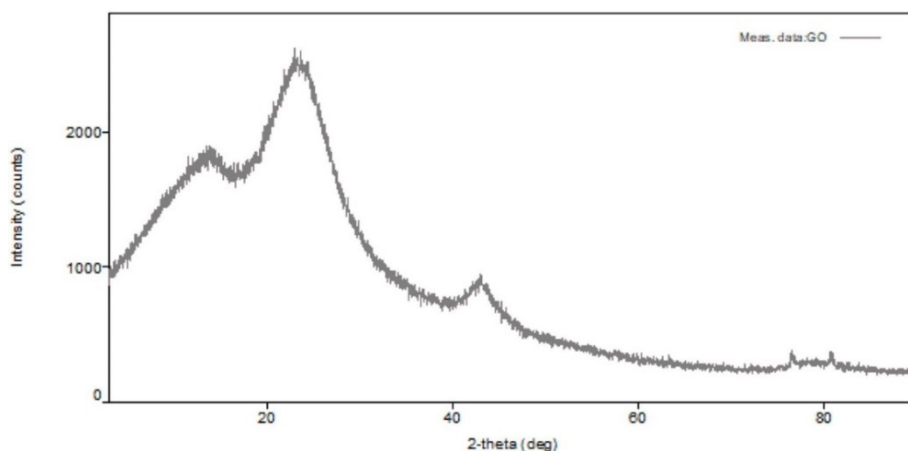
Figure 3. XRD diffractogram of GO sample.

Diffractogram of ZrO_2/GO shows a similar pattern, but the peak at 2θ 13° has been moved to lower angles, near to 2θ 5°. There are no reflections of ZrO_2 which can be explained by the low content of ZrO_2 in the sample and the absence of thermal treatment which is required to create crystalline ZrO_2 phases. All peaks assigned to composite ZrO_2/GO are represented in the following Figure 4.

27
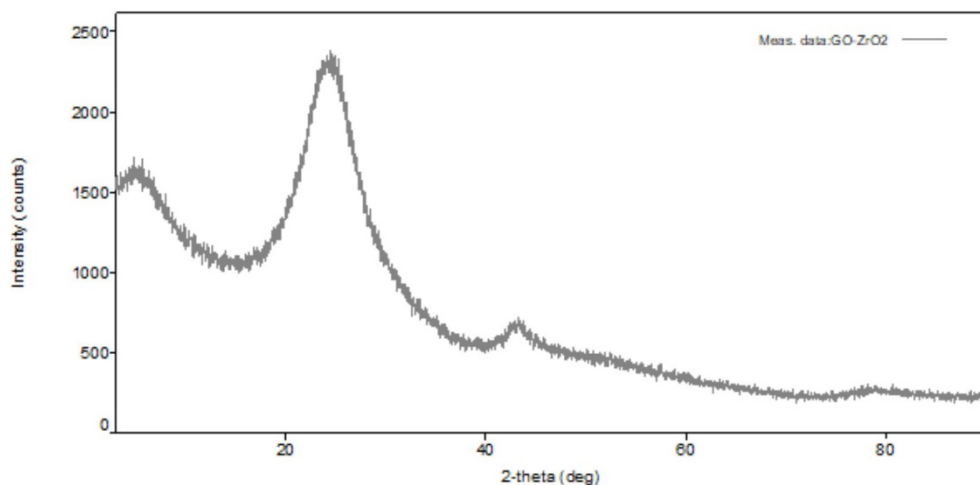
Figure 4. XRD diffractogram of composite ZrO_2/GO.

Textural properties

Textural properties of any material are significant in order to describe important material properties such as strength, chemical reactivity, deformation behavior, and many others. In the following Table 1, textural parameters of N_2 physisorption of both materials GO and ZrO_2/GO are given.

Table 1. Textural parameters of N_2 physisorption of GO and ZrO_2/GO samples

N₂ physisorption at 77 K		GO	ZrO₂/GO
Pore volume (Gurvich) at p/p₀, cm³g⁻¹	0.999	0.136	0.223
	0.98	0.018	0.051
	0.95	0.010	0.042
(B.E.T.) 2 parameters	C	133.0	129.0
	S, m²g⁻¹	6.6	51.3
Mesopores (B.J.H.) Desorption, Standard isotherm: Lecloux for corresponding C value from literature [28]	D_median, nm	18.5	7.6
	D_max, nm	3.6	3.6
	V_meso, cm³g⁻¹	0.012	0.037
Mesopores (Dollim and Heal) Adsorption, Standard isotherm: Lecloux for corresponding C value from literature [28]	D_median, nm	22.7	9.6
	D_max, nm	2.4	2.0
	V_meso, cm³g⁻¹	0.010	0.029

N$_2$ physisorption at 77 K		GO	ZrO$_2$/GO
Micropores (Horvath and Kawazoe), with potential function: Nitrogen on graphite at 77.3 K from literature [29]	D$_{max}$, nm	1.75	0.75
	V$_{meso}$, cm^{3}g^{-1}	0.003	0.021(5)
Micropore volume (Dubinin and Raduskevich)	cm^{3}g^{-1}	0.002(5)	0.180
Surface Area (Kaganer)	m^{2}g^{-1}	7.1	50.4
t-Plot Lecloux 300 > C(Bet) > 100 (Lippens and de Boer) from literature [28]	Total surface area, m^{2}g^{-1}	6.5	48.4
	Micropore volume, cm^{3}g^{-1}	0.002	0.26(5)
	Mesopores surface, m^{2}g^{-1}	3.8	7.9

N$_2$ adsorption onto **GO** and **ZrO$_2$/GO** gives type II isotherms, which means that our samples are nonporous or macroporous materials. These isotherms are represented in the Figure 5.
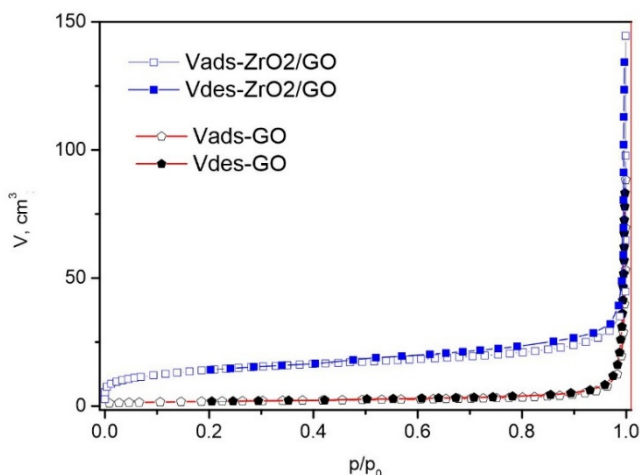
Figure 5. N$_2$ adsorption isotherms of GO and ZrO$_2$/GO samples.

The characteristic shape is the result of nonrestricted monolayer-multilayer adsorption up to high p/p$_0$. Gradual curvature or more precisely less distinctive knee on the curve is an indication of a significant amount of overlap monolayer coverage and the onset of multilayer adsorption. Type H3 hysteresis is observed for both samples which is characteristic of non-rigid aggregates of plate-like particles or systems with macropores that are not completely filed with pore condensate [30].
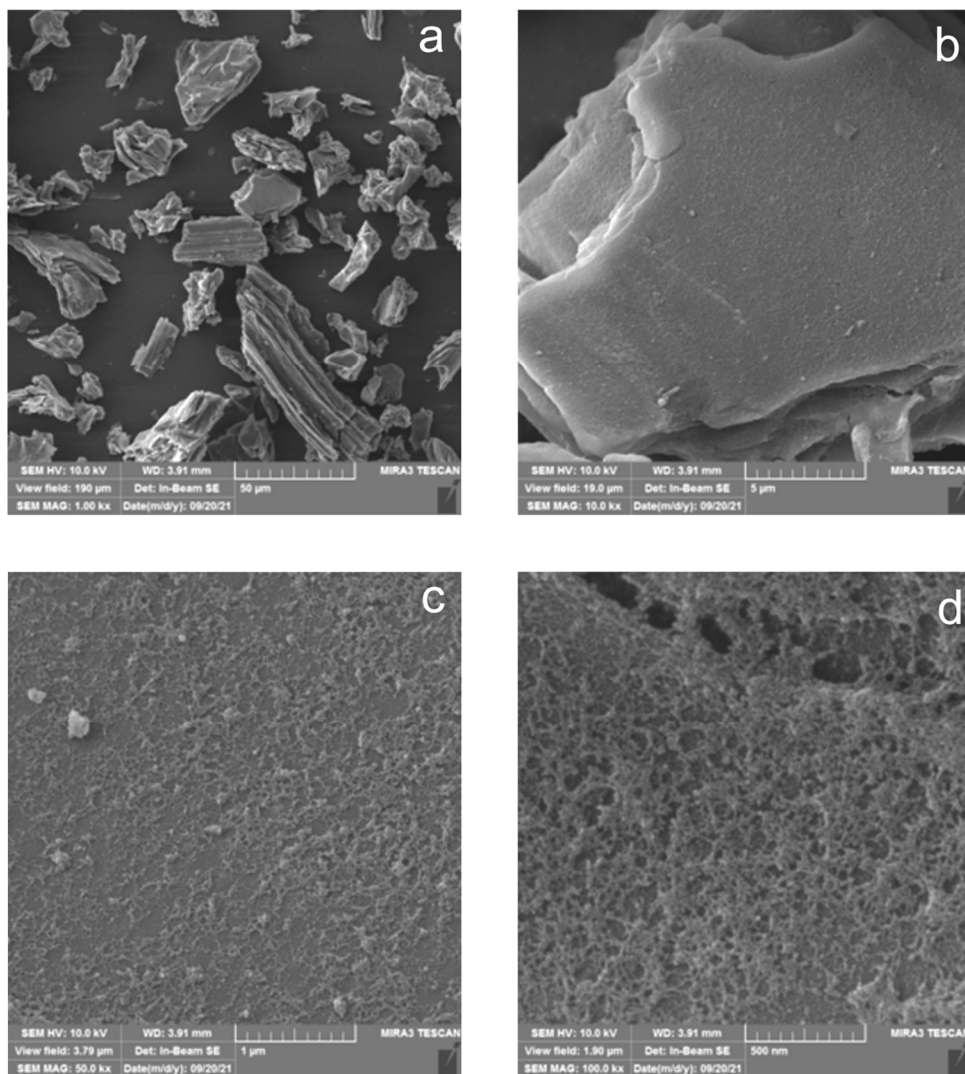
Figure 6. SEM micrograms of pure GO sample (a, b) and ZrO$_2$/GO sample (c, d).

SEM images confirm that the material has a plate-like structure of GO particles with a uniform coating of ZrO$_2$ onto GO particles. GO particles have a layered structure with dimensions around 20 nm. ZrO$_2$ coating has a reticular feature. The coating is uniform with submicrometer dimensions of particles. These SEM pictures are represented in Figure 6.

Sorption

Sorption experiments were conducted in batch mode with 50 cm^3 of dye solution and 50 mg of materials, and stirred on a magnetic stirrer in the dark. Aliquots are taken at specified periods of time and the concentration of dye was determined by a UV-Vis spectrophotometer. For sorption experiments two dyes are chosen, Methylene blue as a cationic dye, and Reactive blue 19 as anionic.

Effect of contact time - The initial concentration of MB was 100 mg dm^{-3} and for RB 19 was 10 mg dm^{-3}. Both materials GO and ZrO$_2$/GO are tested. Results for GO are shown in Table 2, while results for composite ZrO$_2$/GO are shown in Table 3. All results are expressed as the removal of dye as a function of time.

Table 2. Removal of MB and RB 19 dyes by pure GO.

GO	Dye removal, in percentage %	
Time, h	MB	RB 19
0.00	0.00	0.00
0.25	40.65	6.73
0.50	42.87	7.06
0.75	46.49	7.17
1.00	50.28	7.85
2.00	64.77	8.41
3.00	68.01	8.52
4.00	74.23	9.30
6.00	81.31	10.31

Table 3. Removal of MB and RB 19 dyes by composite ZrO$_2$/GO.

ZrO$_2$/GO	Dye removal, in percentage %	
Time, h	MB	RB 19
0.00	0.00	0.00
0.25	11.23	36.55
0.50	13.77	44.83
0.75	14.50	45.05
1.00	14.59	46.26
2.00	19.12	47.48
3.00	21.38	48.25
4.00	22.83	49.69
6.00	28.81	52.12

From the results shown in Tables 2 and 3, we can see that unmodified GO shown better sorption characteristics for cationic dye MB, while modified material ZrO$_2$/GO shown much better removal for anionic dye RB 19.

For all four experiments can be seen that the removal of dyes is more efficient and very fast in the first 30 minutes. After that period of time, free active sites on the material surface become occupied and the removal rate started to slow down and a near-equilibrium state is obtained after 3 hours.

Effect of initial concentration of dyes – These tests were conducted for both dyes. For MB dye initial concentrations were 10, 50, 100, and 200 mg dm^{-3}, and 1, 2.5, 5, and 10 mg dm^{-3} were concentrations of RB 19 dye. 50 cm^3 of dye solution and 50 mg of the composite were stirred in the dark for 2 hours. After 2 hours, solutions were centrifuged to separate composites from suspension. The solution was analyzed on a UV-Vis spectrophotometer to determine the final concentration. Results for GO are shown in Table 4, while results for composite ZrO$_2$/GO are shown in Table 5.

Table 4. Effect of initial concentration of MB and RB 19 dyes on pure GO.

GO					
MB			**RB 19**		
Initial concentration, mg dm^{-3}	Dye removal, %	Sorption capacity, mg g^{-1}	Initial concentration, mg dm^{-3}	Dye removal, %	Sorption capacity, mg g^{-1}
10.0	100.00	9.22	1.0	18.77	0.20
50.0	98.21	48.06	2.5	16.53	0.47
100.0	64.77	65.11	5.0	13.44	0.76
200.0	45.09	86.28	10.0	8.40	0.89

Table 5. Effect of initial concentration of MB and RB 19 dyes on composite ZrO$_2$/GO.

ZrO$_2$/GO					
MB			**RB 19**		
Initial concentration, mg dm^{-3}	Dye removal, %	Sorption capacity, mg g^{-1}	Initial concentration, mg dm^{-3}	Dye removal, %	Sorption capacity, mg g^{-1}
10.0	71.42	5.50	1.0	100.00	0.97
50.0	26.30	4.31	2.5	86.85	2.13
100.0	20.14	9.77	5.0	62.19	3.07
200.0	13.49	11.54	10.0	46.26	4.89

Sorption capacity increased for both materials and both dyes with increasing initial dye concentration. This can be explained by the increase of driving force [31]. Also can be observed that removal of MB dye is more effective with pure GO, while composite ZrO$_2$/GO is more effective in RB 19 dye removal.

Effect of sorbent dose – These tests were also conducted for both materials. Sorbent doses for both GO and ZrO_2/GO materials were 10, 20, 50, and 100 mg. 50 cm^3 of dye solution and an appropriate dose of sorbent were stirred in the dark for 2 hours. After 2 hours, solutions were centrifuged to separate composites from suspension. The solution was analyzed on a UV-Vis spectrophotometer to determine the final concentration. Results for GO are shown in Table 6, while results for composite ZrO_2/GO are shown in Table 7.

Table 6. Effect of sorbent dose of GO on final dye concentration.

GO					
MB			**RB 19**		
Sorbent dose, mg	Dye removal, %	Sorption capacity, mg g^{-1}	Sorbent dose, mg	Dye removal, %	Sorption capacity, mg g^{-1}
10.0	2.96	12.29	10.0	3.43	0.89
20.0	31.04	66.79	20.0	6.18	0.83
50.0	60.57	54.40	50.0	11.47	0.63
100.0	100.00	44.82	100.0	19.08	0.53

Table 7. Effect of sorbent dose of ZrO_2/GO on final dye concentration.

ZrO_2/GO					
MB			**RB 19**		
Sorbent dose, mg	Dye removal, %	Sorption capacity, mg g^{-1}	Sorbent dose, mg	Dye removal, %	Sorption capacity, mg g^{-1}
10.0	20.76	9.30	10.0	14.80	0.73
20.0	33.67	7.62	20.0	54.72	1.37
50.0	71.42	5.50	50.0	100.00	1.03
100.0	100.00	4.64	100.0	30.76	0.16

When the effect of sorption dose is observed, for both materials can be seen that removal increases with the increase of sorbent dose. The exception is the removal of RB 19 with ZrO_2/GO, where 100% removal is achieved with 50 mg of sorbent, and about 30% with 100 mg. Sorption capacity decreases for removal of RB 19 with GO, and MB with ZrO_2/GO, while we have an initial increase and further decrease for removal of MB with GO and RB 19 with ZrO_2/GO. Amount adsorbent per unit mass of the adsorbent decrease due to adsorption sites remaining unsaturated during the adsorption reaction [32,33].

Photocatalysis

The photocatalytic ability of presented materials was studied using the degradation of organic dyes Methylene blue and Reactive blue 19 using the ZrO$_2$/GO composite. Photocatalytic experiments were conducted under UV light with maximum emission at 254 nm. In all experiments irradiation of six lamps, 28 W each were applied. Effect of time, initial dye concentration, and composite mass were investigated.

Effect of irradiation time - Tests were conducted in a UV reactor during the two hour period of irradiation. The experimental setup was that 50 cm^3 of dye solution (initial concentration for RB 19 was 10 mg dm^{-3} and for MB 100 mg dm^{-3}) was stirred on a magnetic stirrer in an opened glass beaker with 50 mg of composite ZrO$_2$/GO (1 g dm^{-3}). Aliquots were taken at the specified time, centrifuged, and concentration (absorbance) was calculated from absorbance determined by UV-Vis spectrophotometer using equations given in experimental part. Results are shown as degradation rate as a function of time and represented in Figure 7 for MB and Figure 8 for RB 19 dye.
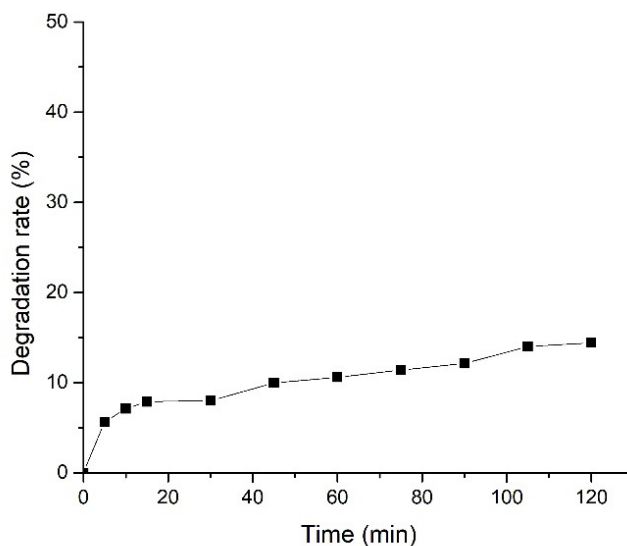

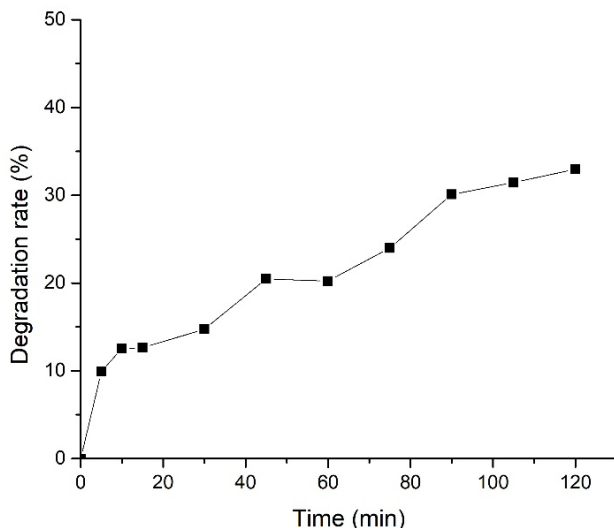**Figure 7.** Effect of irradiation time on degradation of MB dye.

Figure 8. Effect of irradiation time on degradation of RB 19 dye.

From Figures 7 and 8 can be seen that a better degradation rate is achieved for RB 19 dye (about 33%) while the degradation rate of MB is relatively low (only 14%). For both dyes, the increase of degradation rate during the time is slow but constant, so we can suggest that equilibrium is achieved after 90 minutes of irradiation.

Effect of initial concentration of dyes – This effect was conducted for both dyes. For MB dye initial concentrations were 10, 50, 100, and 200 mg dm^{-3}, and 1, 2.5, 5, and 10 mg dm^{-3} were concentrations of RB 19 dye. Tests were conducted in a UV reactor during the two hour period of irradiation. Results are shown as degradation rate as a function of time and represented in Figure 9 for RB 19 and Figure 10 for MB dye.

From Figure 9 can be seen that the degradation rate of RB 19 dye is highly dependent on initial dye concentration. Results show that degradation rate increase from 19% for 5 mg dm^{-3} up to 100% for 1 mg dm^{-3}. Also, as the initial concentration increases degradation process became faster, and for the lowest initial concentration, after 75 min we achieved total degradation. For other concentrations, 90 or more minutes were needed to achieve the maximum degradation rate.
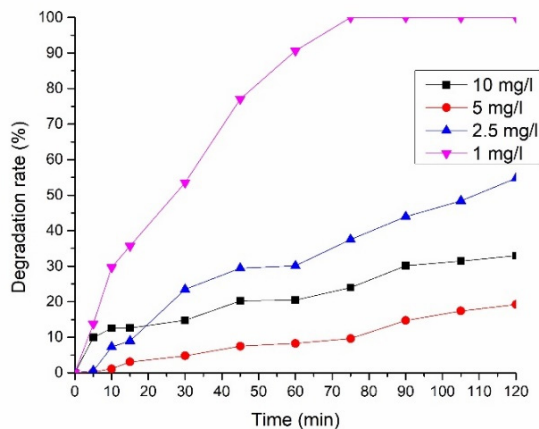
Figure 9. Effect of initial concentration of RB 19 dye on degradation.
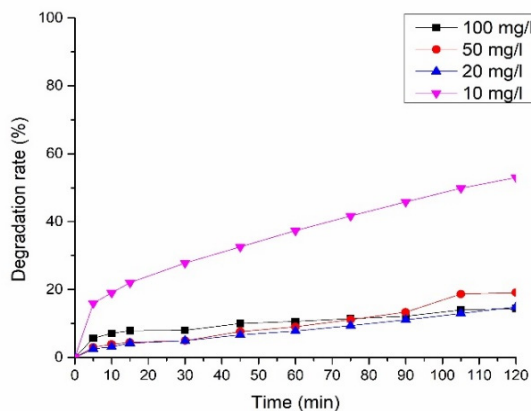
Figure 10. Effect of initial concentration of MB dye on degradation.

Degradation of MB dye is also dependent on the initial dye concentration but is not so obvious as in RB 19 dye case. In the case of MB dye, we have almost the same degradation rate for concentrations between 20 and 100 mg dm^{-3} (14% to 19%). Also, equilibrium is reached after 45 minutes for all samples. The notable increase in degradation rate is achieved for MB concentration 10 mg dm^{-3} without reaching equilibrium.

Effect of amount of composite – Next two figures show the dependence of the degradation rate of dyes as a function of the amount of composite in the system, where we have tested four different amounts (10, 20, 50, and 100 mg). Tests were carried out with an initial concentration of MB 10 mg dm^{-3} and RB 19 1 mg dm^{-3}. 50 cm^3 of dye solution was stirred in a UV reactor in an open glass beaker with the appropriate amount of ZrO$_2$/GO composite. Results are shown as degradation rate as a function of time and represented in Figure 11 for MB and Figure 12 for RB 19 dye.
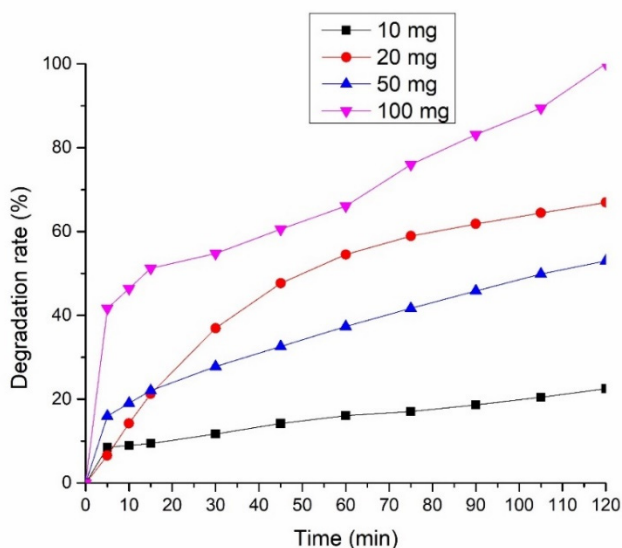
Figure 11. Effect of amount of ZrO$_2$/GO composite on degradation of MB dye.

From Figure 11 can be seen that the degradation rate of MB dye increases as the amount of composite in the system increase. That is quite expected because with increasing amounts of composite, there are more active sites in the system, so more photons can be involved in the photocatalytic process.

An increase in the amount of composite leads to an increase in the degradation rate of RB 19 dye as we can see from Figure 12. As mentioned above, more composite in the system means more active sites, thus the photocatalytic process is more effective. In the case of RB 19 dye, we have total degradation with amounts of composite over 20 mg and with an increase in mass, we have faster total degradation.

37
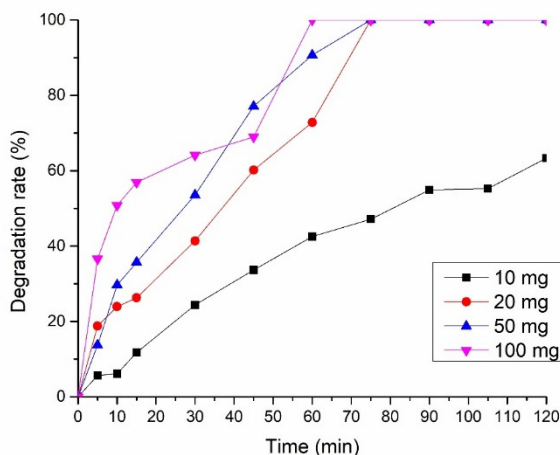
Figure 12. Effect of amount of ZrO_2/GO composite on degradation of RB 19 dye.

CONCLUSIONS

In this paper, we presented the first results of a novel composite and its applications as sorbent and photocatalyst. Results are promising especially for photocatalysis because neither pure zirconia or pure graphene oxide is not photocatalytic active. With this method of synthesis of ZrO_2/GO composite we have obtained possible good photocatalytic material for a wide range of usage. We believe that this paper is only the beginning of new wider research for obtaining more effective and low-cost materials for photocatalytic applications.

EXPERIMENTAL SECTION

Reagents and chemicals

All used chemicals, sodium-nitrate (Centrohem), sulfuric acid (Zorka Pharma), potassium-permanganate (Zdravlje), hydrochloric acid (Zorka Pharma), ethanol (Zorka Pharma), zirconium-isopropoxide (Acros Organics), 2-propanol (Sigma Aldrich), ammonium hydroxide (NRK engineering), Methylene Blue (Merck), Reactive Blue 19 (Merck) were analytical grade and used without further purification. Graphite was commercial grade from Trayal factory with unknown origin. Deionized water was used in all experiments.

Preparation of materials

Graphene oxide preparation - Graphene oxide was synthesized via the modified Hummers-Offeman method [20], where we have the oxidation of graphite with a strong oxidizing agent to exfoliate graphite. The first step was mixing 5.0 g of natural graphite powder of fine grade (150 μm), 2.5 g of sodium nitrate, and 115.0 cm^{-3} of concentrated sulfuric acid in an ice bath, in order to cool the mixture to 0°C. After mixing this suspension for 30 minutes, 15.0 g of potassium permanganate was added in small portions, where the temperature in the reactor needs to be lower than 20°C. After this step, the reactor was heated to 35±3°C and kept at this temperature for the next 30 minutes. As the reaction progressed, the suspension got brownish-grey color and became pasty. In the next step after these additional 30 minutes period, 230.0 cm^{-3} of water was slowly stirred into the paste to prevent violent effervescence, and as a result, the temperature increased to 95-98°C, and this diluted brown suspension was mixed at this temperature for 15 minutes. After 15 minutes, 5.0 cm^{-3} of hydrogen peroxide and additional water (500.0 cm^{-3}) were added to reduce the residual permanganate and manganese dioxide to colorless soluble manganese sulfate and this leads to the bright yellow color of suspension. The last step was filtration of warm suspension and washing of the filter cake with distilled water, 30% hydrochloric acid, and ethanol (amount of each was 150.0 cm^{-3}). The dry product was obtained by centrifugation and was dried at 60°C for 24 hours.

ZrO_2/GO preparation - Zirconia-graphene oxide-based composites were synthesized using the modified sol-gel method, where as a precursor zirconia isopropoxide is used. In the first step of the synthesis, 1.6 cm^{-3} of zirconium isopropoxide was dissolved in 10.0 cm^{-3} of 2-propanol under inert conditions and added 2.0 g of previously synthesized graphene oxide. After that, the second solution (mixture of 20.0 cm^{-3} of water and 20.0 cm^{-3} of 2-propanol) was added drop by drop under vigorous stirring for 1 hour. After one hour of stirring, the pH of the mixture was adjusted to 9.5 by a mixture of NH_3 and H_2O in a volume ratio of 1:3. After that, the mixture was heated with a reflux condensator at 60°C for 3 hours. The last step was filtration of the wet gel and washing of the filter cake with distilled water and 2-propanol (amount of each was 100.0 cm^{-3}). The dry product was dried at 60°C for 24 hours and after that, 3 more hours at 120°C.

Characterization

X-ray diffraction (XRD) analyses were performed using the instrument Rigaku MiniFlex 600 with D/teXUltra 250 high-speed detector and Cu-anode.

Parameters of measurements were angle range 3-90°, step 0.02°, scanning speed 10°/min. The anode voltage was 40 kV and the current 15 mA. Identification was done using PDXL2 Version 2.4.2.0 software and obtained diffractograms were compared to the COD database.

Surface area and pore size distribution were determined by nitrogen adsorption-desorption isotherms. Measurements were done on Sorptomatic 1990 Thermo Finnigan automatic system by physisorption of nitrogen at -196°C. All samples were degassed before measurements at 130°C for 3 h. Specific surface area and pore size distribution were calculated by the BET method using ADO 5.13 Thermo Electron software.

FT-IR analyses were done using MB-100 infrared spectrometer (Bomem Hartman & Braun, Canada).

Morphology of composites was examined by Quanta 200 Scanning Electron Microscope (FEI, Hillsboro, Oregon, USA).

Sorption tests

Sorption tests were conducted in dark to avoid competition and the synergistic effect of sorption and photocatalysis. Cationic dye Methylene blue and anionic Reactive blue 19 dye were used in experiments. All experiments were done in batch mode, 50 cm^3 of dye solution in an Erlenmeyer flask covered with aluminum foil, and an adequate mass of composite was stirred on a magnetic stirrer for a defined period. Samples were collected at the specified time, centrifuged (Hermle Z207 A) for 15 min at 5000 r/min, and tested by UV-Vis spectrophotometer Shimadzu UV-Vis 1650 PC (Shimadzu, Japan). Effects of treatment time, initial dye concentration, and composite mass were investigated. For calculating concentration from absorbance, following equations from calibration curves are used:

$$C = 0.0843 * A + 0.0103 \, ; R^2 = 0.997$$

for RB 19, and:

$$C = 0.1829 * A + 0.0443 \, ; R^2 = 0.998$$

for MB.

Dye removal was calculated using the following equation:

$$R = \frac{C_0 - C_t}{C_0} * 100\%$$

Sorption capacity was calculated using formula:

$$Q = \frac{C_0 - C_t}{m_s} * V$$

In these equations, C is for concentration, R is removal, C_0 for initial concentration, C_t for concentration after time t, A is for absorbance, m_s is for mass of sorbent, and V is volume of solution.

Photocatalytic tests

Photocatalytic tests were performed in a UV reactor with 6 low-pressure Hg lamps (28 W) with maximum emission at 254 nm. Before all photocatalytic tests, the suspension of composite and color solution was stirred in the dark for 24 hours to obtain total adsorption-desorption equilibrium to avoid competition with the photocatalytic degradation process. Cationic dye Methylene blue and anionic Reactive blue 19 dye were used in experiments. Samples were collected at a specified time and centrifuged (Hermle Z207 A) for 15 min at 5000 r/min. The concentrations of dyes were determined by the UV-Vis spectrophotometer Shimadzu UV-Vis 1650 PC (Shimadzu, Japan). For calculating concentration from absorbance, following equations from calibration curves are used:

$$C = 0.0843 * A + 0.0103 \,; R^2 = 0.997$$

for RB 19, and:

$$C = 0.1829 * A + 0.0443 \,; R^2 = 0.998$$

for MB.

Degradation rate was calculated using:

$$D = \frac{C_0 - C_t}{C_0} * 100\%$$

In these equations, C is for concentration, Degradation rate is removal, C_0 for initial concentration, C_t for concentration after time t, A is for absorbance.

ACKNOWLEDGMENTS

REFERENCES

1. B. Lellis; C. Z. Fávaro-Polonio; J. A. Pamphile; J. C. Polonio; *Biotechnol. Res. Innov.,* **2019**, *3,* 275-290.
2. S. Y. Mak; D. H. Chen; *Dyes Pigm.*, **2004**, *61*, 93-98.
3. M. Rafatullah; O. Sulaiman; R. Hashim; A. Ahmad; *J. Hazard. Mater.*, **2010**, *177*, 70-80.
4. D. Ghosh; K. G. Bhattacharyya; *Appl. Clay Sci.*, **2002**, *20*, 295-300.
5. N. K. Nga; N. T. T. Chau; P. H. Viet; *J. Sci.: Adv. Mater. Dev.*, **2020**, *5*, 65-72.
6. A. H. Jawad; A. S. Abdulhameed; N. N. Abd Malek; Z. A. Alothman; *Int. J. Biol. Macromol.*, **2020**, *164*, 4218-4230.
7. S. T. Yang; S. Chen; Y. Chang; A. Cao; Y. Liu; H. Wang; *J. Colloid Interface Sci.*, **2011**, *359*, 24-29.
8. B. Manu; S. Chaudhari; *Bioresour. Technol.*, **2002**, *82*, 225-231.
9. M. Inagaki; T. Imai; T. Yoshikawa; B. Tryba; *Appl. Catal. B: Environ.*, **2004**, *51*, 247-254.
10. Y. Min; K. Zhang; W. Zhao; F. Zheng; Y. Chen; Y. Zhang; *Chem. Eng. J.*, **2012**, *193*, 203-210.
11. N. Zaghbani; A. Hafiane; M. Dhahbi; *Sep. Purif. Technol.*, **2007**, *55*, 117-124.
12. A. Dąbrowski; *Adv. Colloid Interface Sci.*, **2001**, *93*, 135-224.
13. G. Crini; *Bioresour. Technol.*, **2006**, *97*, 1061-1085.
14. K. Krishnamoorthy; R. Mohan; S. J. Kim; *Appl. Phys. Lett.*, **2011**, *98*, 244101.
15. M. N. Chong; B. Jin; C. W. Chow; C. Saint; *Water Res.*, **2010**, *44*, 2997-3027.
16. A. T. Smith; A. M. LaChance; S. Zeng, B. Liu; L. Sun; *Nano Materials Science*, **2019**, *1*, 31-47.
17. C. K. Chua; M. Pumera; *Chem. Soc. Rev.*, **2014**, *43*, 291-312.
18. Z. Wang; J. Liu; W. Wang; H. Chen; Z. Liu; Q. Yu; H. Zeng; L. Sun; *Chem. Commun.*, **2013**, *49*, 10835-10837.
19. X. Y. Wang; A. Narita; K. Müllen; *Nat. Rev. Chem.*, **2017**, *2*, 1-10.
20. W. S. Hummers Jr; R. E. Offeman; *J. Am. Chem. Soc.*, **1958**, *80*, 1339-1339.
21. L. C. Pop; G. Barta; L. C. Cotet; K. Magyari; M. Baia; L. B. Tudoran; R. Ungur; D. Vodnar; L. Baia; V. Danciu; *Stud. Univ. Babes-Bolyai Chem.*, **2022**, *67*, 281-296.
22. L. Wang; J. Ding; Y. Chai; Q. Liu; J. Ren; X. Liu; W. L. Dai; *Dalton Trans.*, **2015**, *44*, 11223-11234.
23. P. S. Chauhan; R. Kant; A. Rai; A. Gupta; S. Bhattacharya; *Mater. Sci. Semicond. Process.*, **2019**, *89*, 6-17.
24. X. Luo; C. Wang; L. Wang; F. Deng; S. Luo; X. Tu; C: Au; *Chem. Eng. J.*, **2013**, *220*, 98-106.
25. H. Di; Z. Yu; Y. Ma; C. Zhang; F. Li; L. Lv; Y. Pan; H. Shi; Y. He; *J. Taiwan Inst. Chem. Eng.*, **2016**, *67*, 511-520.
26. G.I. Titelman; V. Gelman; S. Bron; R.L. Khalfin; Y. Cohen; H. Bianco-Peled; *Carbon*, **2005**, *43*, 641-649.

27. J. Lai; S. Zhou; X. Liu; Y. Yang; J. Lei; Q. Xu; D. Yin; *Catal. Lett.*, **2019**, *149*, 2749-2757.
28. A. Lecloux; J. P. Pirard; *J. Colloid Interface Sci.*, **1979**, *70*, 265-281.
29. G. Horvath; K. Kawazoe; *J. Chem. Eng. Japan*, **1983**, *16*, 470-475.
30. M. Thommes; K. Kaneko; A. V. Neimark; J. P. Olivier; F. Rodriguey-Reinoso; J. Rouquerol; K. S. W. Sing; *Pure Appl. Chem.*, **2015**, *87*, 1051-1069.
31. M. Kostić; S. Najdanović; N. Velinov; M. Radović Vučić; M. Petrović; J. Mitrović; A. Bojić; *Environ. Technol. Innov.*, **2022**, *26*, 102358.
32. Y. Bulut; H. Aydin; *Desalination*, **2006**, *194*, 259-267.
33. C. Raji; T. S. Anirudhan; *Indian J. Chem. Technol.*, **1997**, *4*, 157-162.

REMOVAL OF A BASIC TEXTILE DYE BY RELEASES OF DJEBEL ONK PHOSPHATES

OUISSAM BIBBA[a*], SAMIRA MESKI[a], HAFIT KHIREDDINE[a]

ABSTRACT. The modified natural phosphate of djebel onk was investigated for the removal of cationic textile dye Methylene blue (MB) from aqueous solution. The modified natural phosphate rock powder (MNP) was characterized by means of XRD, IR spectroscopic and thermal analysis. Adsorption studies were carried out under various parameters such as pH, contact time, initial dye concentration and temperature. The equilibrium data were analyzed using Langmuir, Freundlich, Temkin and Dubinin–Radushkevich isotherm models, the results of modeling adsorption of Methylene blue (MB) on modified natural phosphate rock (MNP) show that the Langmuir model present a good coefficient of correlation compared to other models. The kinetics of adsorption were best described by pseudo-second order and the thermodynamic parameters ($\Delta H°$, $\Delta S°$ and $\Delta G°$) of the adsorption were also evaluated. The adsorption process was found not-spontaneous and exothermic.

Keywords: Algerian phosphate, adsorption, methylene blue, isotherme

INTRODUCTION

Great quantities of dyes are produced and applied annually in many industries, including industries textile, cosmetic, of paper, of leather, pharmaceutical and food. It is estimated that over 10,000 various dyes and pigments are used industrially and over $7X10^5$ tons of synthetic dyes are yearly produced globally. About 10-15% of synthetic dyes *are* lost during different processes of textile industry [1].

---

[a] *Bejaia University, Department of Process Engineering, Environmental Engineering Laboratory, 06000 Bejaia, Algeria.*
[*] *Corresponding author: ouissambibba29@gmail.com.*

These effluents are rich in dyes and chemicals, some of which are non-biodegradable and carcinogenic and pose a major risk to health and the environment [2]. Several methods of treatment have been used such as coagulation and flocculation [3], biodegradation [4], membrane filtration [5], chemical oxidation [6], ozonization [7] and adsorption [8]. Adsorption is a simple purification technique that is often applied with inexpensive adsorbents in order to clarify waste waters [9]. Among the adsorbents used in processes of discoloration of water we cite: clays [10], activated carbon [11], phosphate [12], hydroxyapatite [13].

Hydroxyapatite ($Ca_{10}(PO_4)_6(OH)_2$), a calcium phosphate biomaterial, is a very promising candidate for the treatment of the wastewater. Actually, hydroxyapatite (Hap) can be extremely beneficial in the field of environmental management, due in one part to its particular structure and attractive properties, such as its great adsorption capacities, its acid-base adjustability, its ion-exchange capability and its good thermal stability [14-15]. For these reasons, Hap has been widely used for biomedical and environmental applications. Hap can be synthesized chemically or extracted from natural sources. Natural hydroxyapatite is usually extracted from biological sources or wastes such as mammalian bone (e.g. bovine, camel, and horse) [16], marine or aquatic sources (e.g. fish bone and fish scale), shell sources (e.g. cockle, clam, eggshell, and seashell) [17], and plants and algae and also from mineral sources (phosphate rock) [18].

The principal objective of this work is to study the feasibility of using modified phosphate rock as sorbent for removal of methylene blue dye from aqueous solutions. The choice of this material is based on its inexpensive cost and its abundance in the Algerian ores. The influence of different parameters on the adsorption such as: the contact time, the initial concentration of MB the weight of the adsorbent, the pH of the solvent is studied. The kinetics and isotherms of the adsorption process are also investigated.

2. RESULTS AND DISCUSSIONS

2.1. Characterization of the modified natural phosphate rock

The X-ray diffraction (XRD) patterns of the modified natural phosphate rock (MNP) prepared is represented on the Figure 1. We notice that all the peaks registered in the diagram are characteristic to the hydroxyapatite structure.
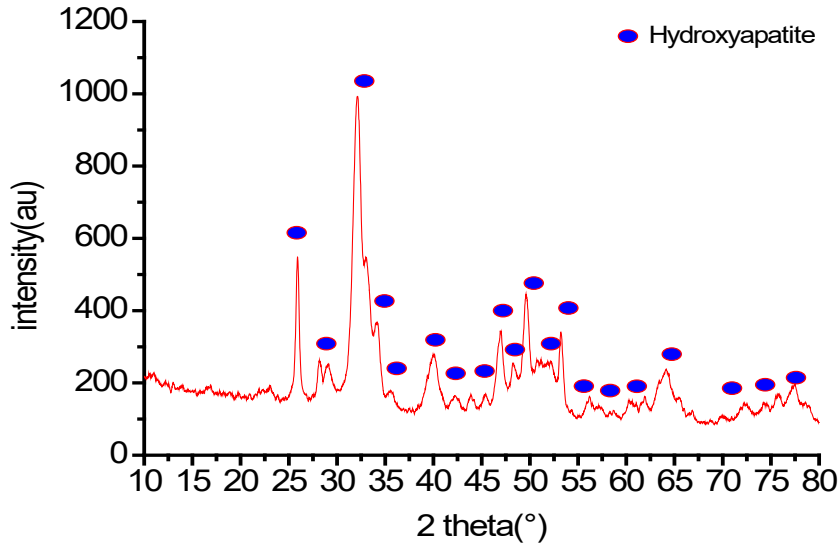
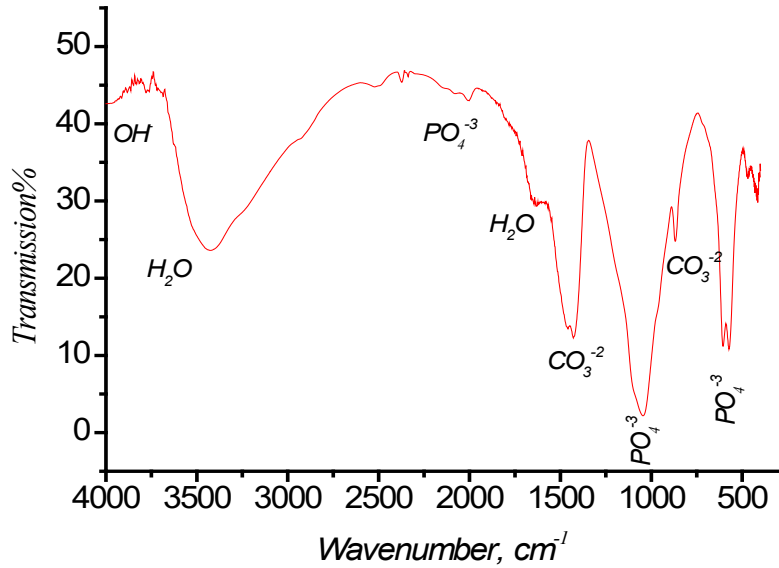**Figure1.** X-ray diffraction of the modified natural phosphate rock.

Figure 2. IR spectra of the modified phosphate rock.

The IR spectra of the apatite prepared from phosphate rock of djebel Onk are illustrated in the Figure 2. The bands between 570 - 606 cm^{-1} and 1090-1042 cm^{-1} correspond to the v_4 and v_3 PO_4 mode. The band of low intensity obtained at 473 cm^{-1} corresponds to the v_2 PO_4 mode of the grouping's apatite phosphates. In addition, the bands at 875 and 1425–1450 cm^{-1} are assigned to carbonate vibrations. The bands at 3430 cm^{-1} and 1630 cm^{-1} corresponding, respectively, to the stretching and bending vibration of water molecule used in hydration of powder prepared. Additional band is observed at 3650 cm^{-1} corresponding to OH vibration characteristic to the apatite structure [19].

The TG curve of the modified natural phosphate rock is shown in the Figure 3. We observe that the powder prepared presents three losses of mass, the first is estimated at 6.44% between 20°C-260°C, which corresponds to the dehydration of MNP (departure of the water contained in the pores). The second loss is 4.21%, obtained between 360-496°C attributed to the loss of chemisorbed water. The third loss is obtained at temperature range 500-1000°C. The weight loss in this region is 4.76 % and is due to the decomposition of carbonates, which are already detected by IR spectroscopy. Calcium carbonate reacts to form the oxide of calcium (CaO) according to the reaction:
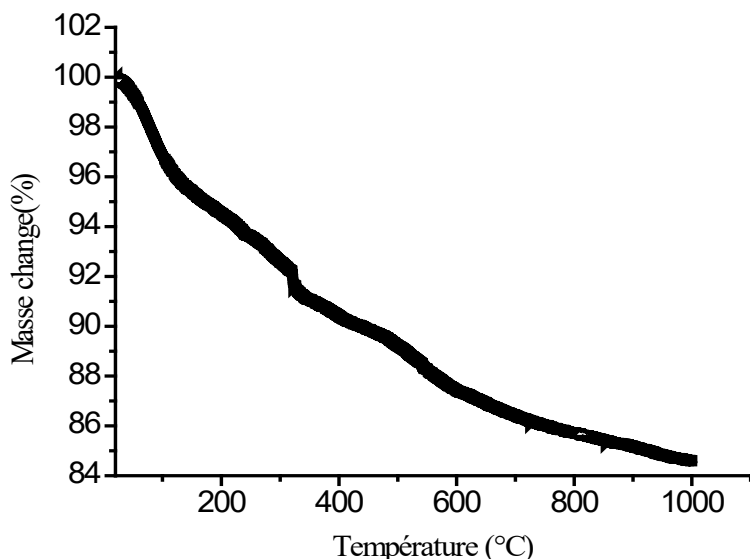
$$CaCO_3 \rightarrow CaO + CO_2 \quad (1)$$
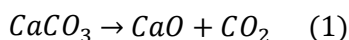
Figure 3. TG analysis of the modified natural phosphate rock.

2.2. Effect of different parameters on MB adsorption

2.2.1. Effect of solution pH

The effect of pH on the removal of methylene blue on the apatite prepared was analyzed in the pH range at 3- 10 at 22 °C, 250 rpm, 1 g of modified natural phosphate rock (MNP) and 250 mL of dye concentration 100 mg/L. The pH was adjusted using 0.1 N NaOH and 0.1 N HCl solutions.

The result in Fig. 4 showed that the removal percentage increase when pH increase from 3 to 9 and decrease for the pH between 9-10. The maximum adsorption of methylene blue was obtained at pH 9.

The low adsorption in acidic medium is due to the repulsion between the positively charged groups of the apatite powder and methylene blue. However, the rapid increase of the removal of MB in the pH range 7-9, can be explained by the attraction force between the positive charge of MB and the negative charge of the powder. These results are similar to those obtained by Khadidja Allam and al (2016) [20] in the adsorption of methylene blue by using hydroxyapatite submitted to microwave irradiation.

According to Liuming Wu and al [21], the reactions responsible for the surface properties of MNP in aqueous solutions are:

$$\equiv POH \rightarrow \equiv PO^- + H^+ \quad (2)$$

$$\equiv CaOH_2^+ \rightarrow \equiv Ca - OH + H^+ \quad (3)$$

Figure 4. Effect of pH on the adsorption of MB dyes on MNP (C_0 = 100 mg. L^{-1}, C_{susp}= 4g.L^{-1}, t=22°C).

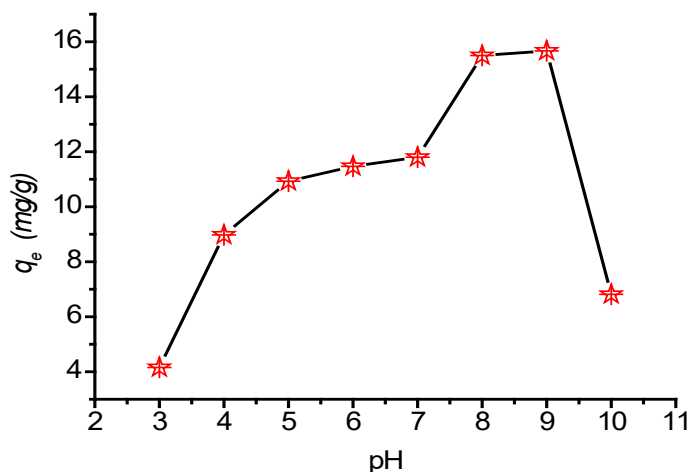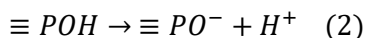For the acidic medium, the positively charged ($CaOH_2^+$) and neutral (P-OH) sites predominate on the MNP surface, giving a positive charge surface for this powder. However, in the basic medium, the neutral (CaOH) and negatively charged (PO^-) species predominated, causing HAP surface to become negatively charged.

The low decrease of the adsorption yield at pH =10 can be associated to the excess of OH^- surrounding the dye by electrostatic attraction, and prevent them from being retained on the anionic sites of the adsorbent.

2.2.2. Effect of initial dye concentration

The evolution of the adsorption percentage of MB in the powder prepared was studied as a function of the initial concentration of MB and contact time. The solution concentration of MB was varied in the range 10- 500 mg/L and the pH solution was adjusted to 9 as it was found to be the optimum pH value from the results of the previous experiment (effect of solution pH).

The curve presented in the figure 5 reveal that the MB adsorption rate is very fast in the first-time contacts with our adsorbent, then reached equilibrium after 60 min. Similar results were obtained by M. Mahmoud and others [22], who studied the adsorption of methylene blue dye onto biopolymer (hydrolyzed oak sawdust (HOSDC)). It was observed that the removal of dye by adsorption on HOSDC was found to be rapid at the initial period of contact time and then to slow down with time. These authors suggest that the phenomenon is due to the forces of attractions between the dye molecule and the adsorbent such as the force of Vander Waals and the electrostatic attractions and as the availability of a large number of sites active on the surface of the adsorbent.

Also, it can be seen from the figure 5 that the adsorption percentage of the MB decrease from 85.76% to 29.87% and 81.5% to 41% at 22 °C and 40°C respectively with the increase in the initial concentration from 10 to 500 mg/L, this can be explained by the competition between the MB molecules for the occupation of actives sites. Generally, an increase in the initial dye concentration in the solution will cause the adsorption sites on the adsorbent surface to become saturated, which eventually leads to a decrease in the removal efficiency.

On the other hand, we observe that for the lower concentrations of MB (10 -200 mg/L), the adsorption percentage values obtained at temperature 22°C is greater than those obtained at 40°C, whereas at high initial MB concentration (500 mg/L) the removal percentage of MB obtained at 40°C is greater than one obtained at 22°C.
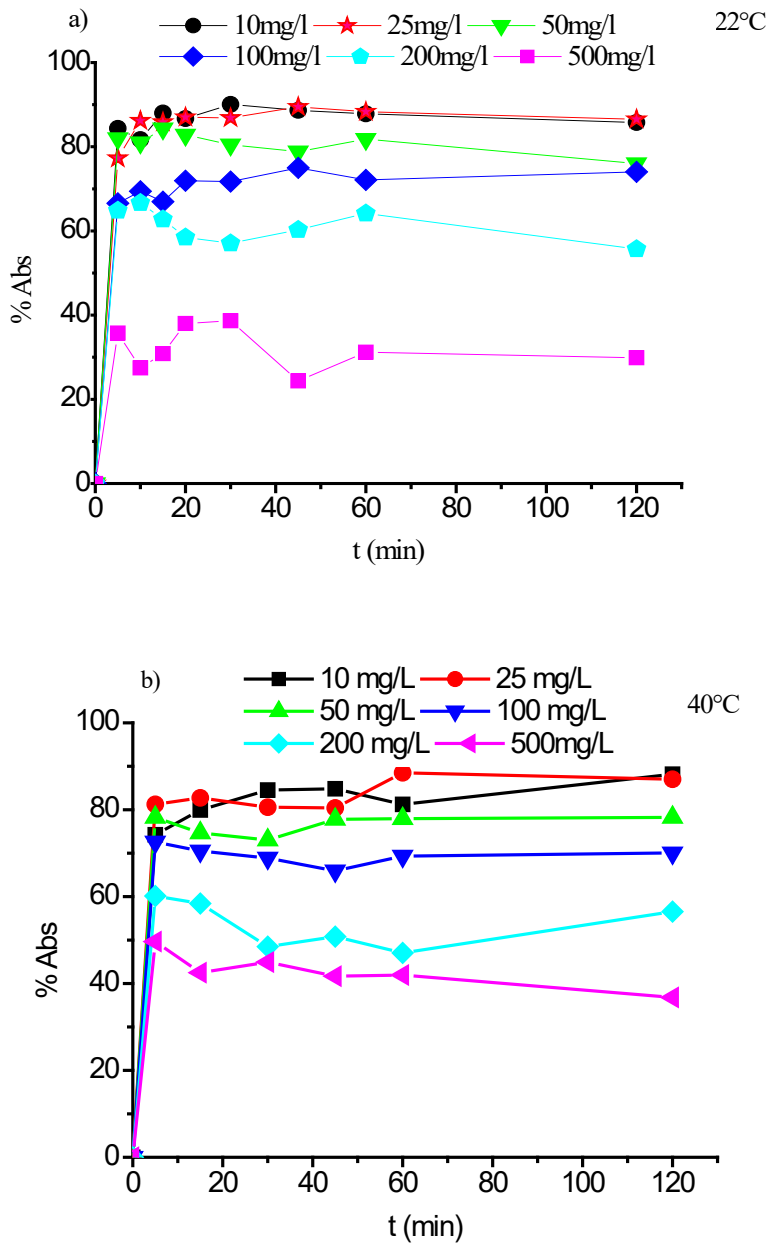
Figure 5. The effect of initial MB dye on percentage dye removal for two temperatures: a, 22°C; b, 40 °C (*pH=9*, C_{susp} = 4 g. L^{-1}).

2.2.3. Effect of mass of MNP

The effect of the mass of adsorbent on the removal percentage of MB was studied at different masses of MNP (0.5, 1, 2, 4 and 6 g/L), at 22°C, 250 rpm, pH 9 and 250 mL of MB solution (100 mg/L).

The results are presented in Figure 6. As the amount of adsorbent increased between 0.5 to 4 g/L, an increase in dye removal was noticed. These results can be explained by the higher number of active sites available as the adsorbent dose increased, facilitating the adsorption process. For the amount of adsorbent higher than 4g/l, the dye removal decreased. This behavior can be explained: As long as the amount of adsorbent added to the dye solution is low, the cations of the dye can easily access the adsorption sites. Adding adsorbent increases, the number of adsorption sites, but the cations of the dye have more difficulty approaching these sites due to congestion, a large amount of adsorbent can create agglomerations of particles, resulting in reduction of the total adsorption surface and consequently a decrease in the removal percentage [23].
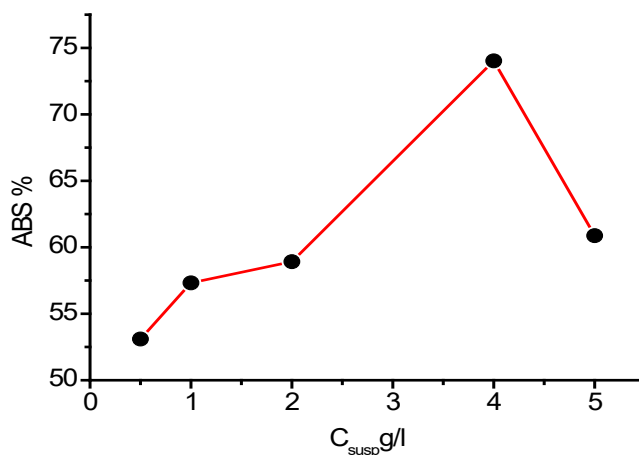
Figure 6. The effect of the concentration of the suspension on percentage dye removal (*pH=9, t* = 22°C).

2.2.4. Effect of temperature

To investigate the influence of temperature on the adsorption process, five different temperatures were studied (22 °C, 40 °C, 50°C and 60 °C), working at a concentration of 100 mg/L, amount of adsorbent of 4g/L and pH 9 of the solution. The obtained results are presented in Figure 7.

The experimental data presented in Figure 7 show that the increase in temperature determined a decrease in adsorption percentage, indicating that the adsorption of cationic dyes (MB) on MNP is an exothermic process.
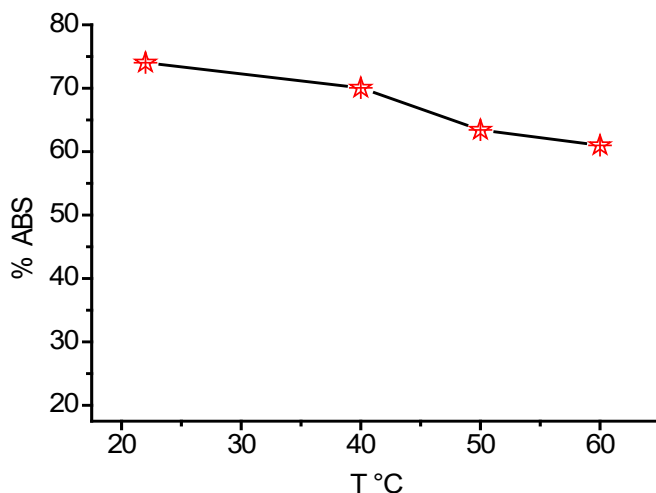
Figure 7. The effect of temperature on percentage dye removal
($pH=9$, C_{susp} = 4 g. L^{-1}, C_0 = 100mg.L^{-1})

2.3. Adsorption isotherms

The isothermal sorption curves of MB on the modified phosphate rock at two temperatures are shown in Fig. 8. According to the shapes of the curves, the isotherms corresponding to MB adsorption onto MNP may be classified as L type of the Giles classification [24]. The L type isotherm suggests a relatively high affinity between MB ions and MNP. This also indicates that no strong competition occurs for the adsorption sites between solvent molecules and adsorbate molecules.

All the sorption parameters of the different models; Langmuir, Freundlich, Temkin and Dubinin-Radushkevich are presented in Table 1. The high correlation coefficients were obtained using the Langmuir (R^2 = 0.998 at 22°C and 0.969 at 40°C) and Freundlich (R^2= 0.946 at 22 °C and 0.989 at 40°C) models with a small X^2. Specifically, the experimental data fitted the Langmuir isotherm model well when the temperature was 22 °C while the Freundlich isotherm model gave higher R^2 coefficient and lower X^2 and RMSE values at 40°C.
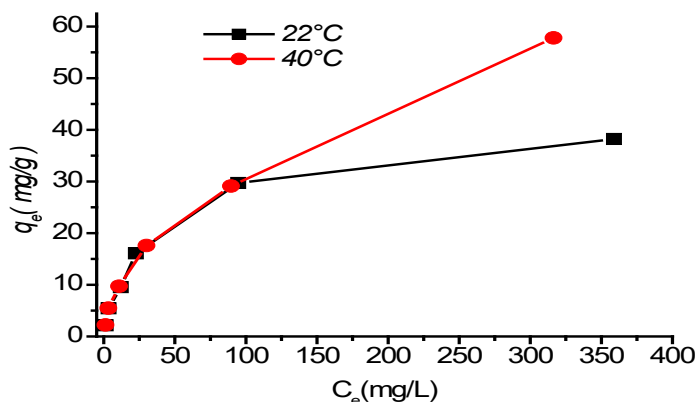
Figure 8. Adsorption isotherms of MB on MNP at different temperatures. 22°C and 40°C (*pH=9*, C_{susp} = 4 g.L^{-1}, *time*= 2h).

Therefore, at 22°C, methylene blue adsorption onto modified phosphate rock followed a Langmuir model, this suggest that the adsorption process takes place on a homogenous surface via monolayer sorption with no contact between sorbed molecules.

The dimensionless constants RL were between 0 and 1, and the values for $1/n$ were less than 1, indicating that adsorption was favored. Moreover, the RL constants increased as the temperature increased, indicating that low temperatures promoted MB adsorption. The parameter 1/n of Freundlich give an indication on the validity of adsorption or of the interactions force of adsorption, if the value of 1/n is equal to 1, adsorption is linear; if it is higher than 1, adsorption is physical; if it is lower than 1, adsorption is a favorable chemical process [23, 25], all the parameter values 1/n found are less than 1 which means that MB dye is favorably adsorbed by the MNP.

The high values of the Temkin model correlation coefficient at 22°C show good linearity, the variation of the Temkin constant relating to the heat of sorption is positive indicating that the adsorption reaction is exothermic [26].

As can be seen in Table 1, the values of Chi- square statistic and RMSE for Dubinin Radushkevich model were 36.739, 11.334 at 22°C and 97.90, 18.83 at 40°C, respectively which are very high in comparison with other models. This reveals that Dubinin Radushkevich model could not describe the experimental isotherm data in the sorption of MB onto MNP.

Table 1. Isotherms parameters by linear method for the sorption of MB by MNP.

	t= 22°C		t=40°C
Langmuir	R^2=0.998 Q_m= 41.442 mg/g K_L=0.031L/mg RMSE=1.293 X^2=1.032		R^2=0.969 Q_m=66.401 mg/g K_L=0.016 L/mg RMSE=4.93 X^2=5.53
Freundlich	R^2= 0.946 K=0.237 L/mg 1/n=0.461 RMSE=5.837 X^2=5.290		R^2= 0.989 K=0.162 L/mg 1/n=0.556 RMSE=1.872 X^2=0.588
Temkin	R^2= 0.962 K_e=0.623 L/g B_t=6.841 b = 358.51 j/mol RMSE=2.400 X^2=4.298		R^2= 0.868 K_e= 0.493 L/g B_t=9.262 b= 280.96 j/mol RMSE=7.112 X^2=9.670
Dubinin-Radushkevich	R^2=0.723 E=0.6031 Kj /mol β = $1.374.10^{-6}$ Q_m=18.378 mg/g RMSE=11.334 X^2=36.739		R^2=0.642 E=0.6868 Kj /mol β =$1.059.10^{-6}$ Q_m=19.915 mg/g RMSE=18.83 X^2=97.903

Table 2. R_L values for different concentration.

Dye concentration(mg/l)	Value of R_L	
	t= 22°C	t= 40°C
10	0.843	0.874
25	0.682	0.736
50	0.5178	0.582
100	0.349	0.411
200	0.211	0.258
500	0.096	0.122

The comparison of the maximum monolayer capacity between Langmuir and Dubinin Radushkevich show that Langmuir reveals a better agreement with experimental data. The value of qm was 41.49 mg/g at 22°C which is more close to experimental capacity (≈ 38mg/g) in comparison with corresponding Dubinin Radushkevich parameter (qm) which is almost half (18.37 mg/g) of the experimental capacity. Consequently, Langmuir model better explained the MB sorption experimental data than Dubinin- Radushkevich model.

2.4. Adsorption kinetics

The values of the correlation coefficient (R^2) and adsorbed amount (q_e) determined by plotting the linear form of the first order kinetics presented in Fig. 9 and Table 3, reveal that this model does not adequately describe the adsorption of the methylene blue on the modified phosphate rock.
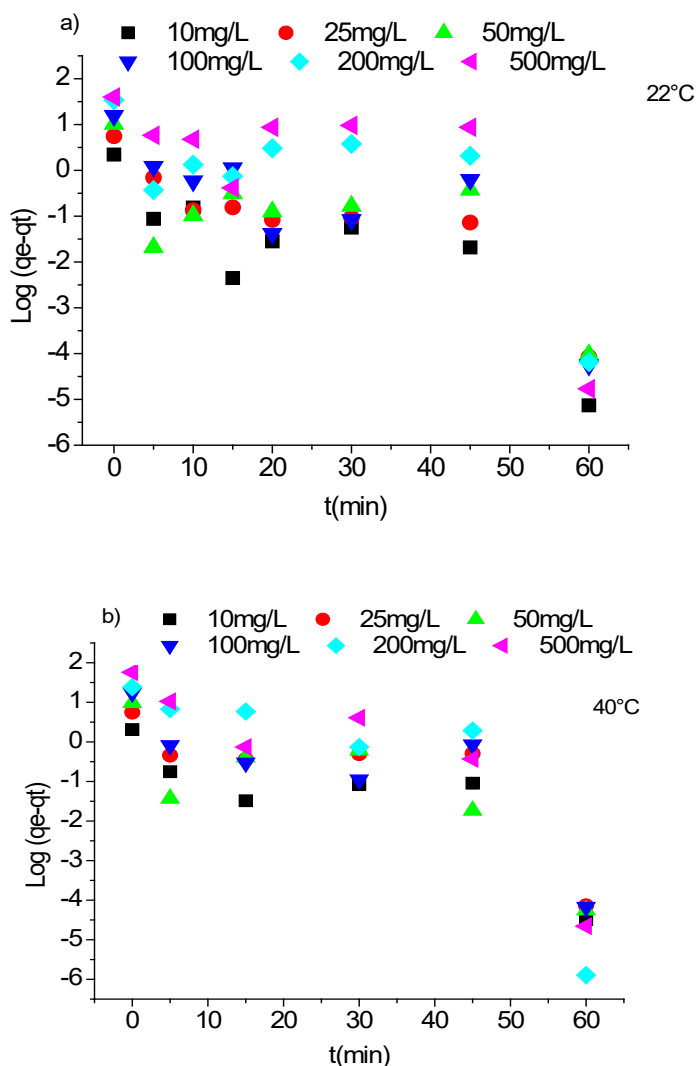

Figure 9. Pseudo- first order model plot for the adsorption of MB onto MNP for two temperatures: a, 22°C; b, 40 °C (*pH*=9, C_{susp}= 4 g. L^{-1}).

Table 3. the pseudo- first order kinetic model parameters of MB dye adsorption onto MNP (t=22°C and t=40°C, time = 60mn).

C_0(mg/l) / t	q_e(mg/g)		K_1 (min^{-1})		q_e(calculated) (mg/g)		R^2		RSME		X^2	
	22°C	40°C	22°C	40°C	22°C	40°C	22°C	40°C	22°C	40°C	22°C	40°C
10	2.212	2.046	0.145	0.128	0.589	1.030	0.668	0.653	**1.808**	1.296	24.180	7.306
25	5.568	5.579	0.135	0.129	1.999	4.540	0.772	0.608	**3.995**	**1.175**	**16.104**	2.200
50	10.264	9.869	0.104	0.142	1.032	2.635	0.433	0.656	**10.161**	**6.582**	86.981	17.095
100	15.667	17.412	0.147	0.143	5.544	7.003	0.659	0.643	**11.339**	**12.799**	16.093	10.312
200	34.232	24.229	0.133	0.214	13.264	87.841	0.401	0.652	**20,620**	**62.132**	14.813	3.248
500	39.894	57.424	0.160	0.191	50.184	69.518	0.496	0.739	**10.344**	34.503	1.513	742.508

The parameters of the second order kinetics are determined from the linear representation of t/q_t as a function of time (Fig. 10). The values of the parameters are grouped in the Table 4, it is noted that the correlation coefficients for the two temperatures studied are very close to 1. Similarly, the values of the adsorption capacities calculated (qe_{cal}) from the pseudo second order model are in same order of magnitude to those of experimental (qe_{exp}).

Higher correlation coefficient values and smaller RMSE and X^2 were obtained for the pseudo-second-order kinetic model compared to those obtained for the pseudo-first-order kinetic model, indicating that MB adsorption on the MNP adsorbent fitted the pseudo-second-order kinetic model at initial fluoride concentrations ranging from 5 to 15 mg/L. Smaller RMSE values indicated smaller differences between the calculated q_t and experimental q_t values.

Table 4. The pseudo-second-order kinetic model parameters of MB dye adsorption onto MNP (t=22°C and t=40°C, time = 60mn).

C_0 (mg/l) / t	q_e(mg/g)		k_2 (g/mg.min)		q_e(calculated) (mg/g)		R^2		RSME		X^2	
	22°C	40°C	22°C	40°C	22°C	40°C	22°C	40°C	22°C	40°C	22°C	40°C
10	2.230	2.08	2.002	4.32	2.22	2.084	0.999	0.996	**0.063**	0.099	0.009	0.180
25	5.593	5.426	0.446	0.248	5.556	5.36	0.999	0.995	**0.141**	**0.282**	**0.011**	0.063
50	10.142	9.68	2.16	0.243	10.131	9.61	0.999	0.998	**0.215**	**0.473**	0.022	0.098
100	16.129	17.398	0.120	1.43	16.480	17.37	0.998	1.000	**0.969**	**0.181**	0.293	0.006
200	33.222	28.40	0.084	0.012	34.235	27.47	0.995	0.980	**2,062**	**5.620**	0.643	7.380
500	36.496	55.26	0.227	0.0143	39.890	54.72	0.970	0.950	**6.170**	13.91	4.257	16.47
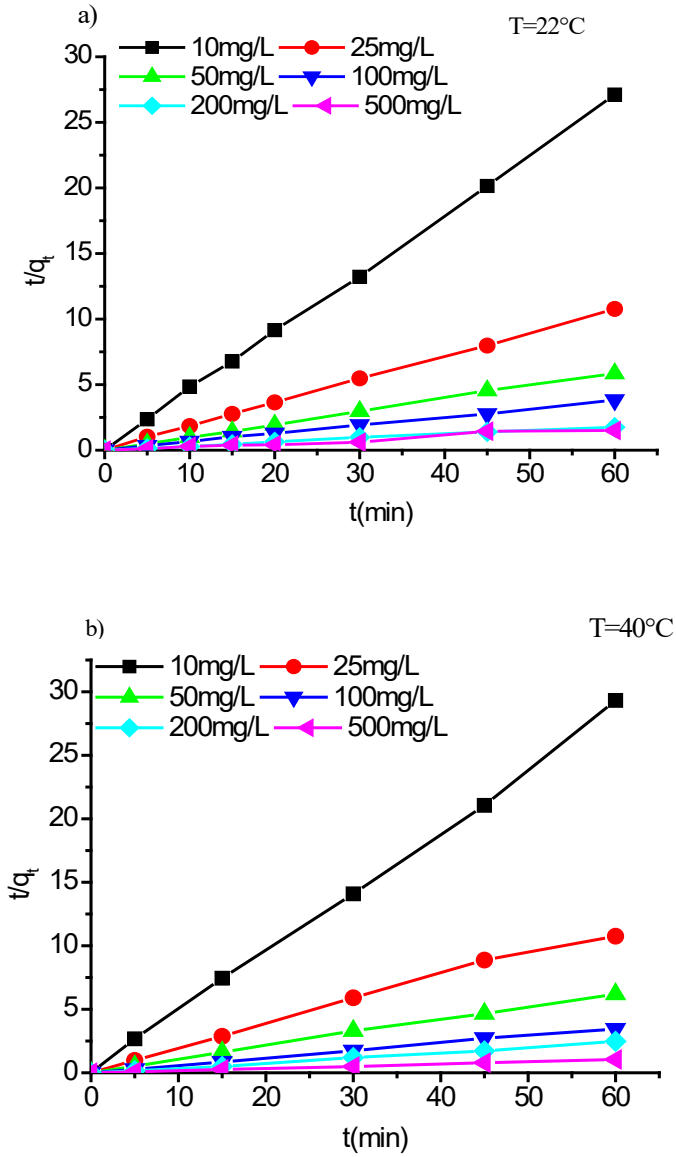
Figure 10. Pseudo-second order model plot for the adsorption of MB onto MNP for two temperatures: a, 22°C; b, 40 °C (*pH*=9, C_{susp}= 4 g. L^{-1}).

2.5. Thermodynamics studies

The thermodynamic study is represented by the plot lnK as a function of 1/T in the Fig 11. The values of the thermodynamic parameters are presented in the Table 5. The negative value of ΔH (- 14.844 KJ/mole) indicates that the adsorption process is exothermic and confirm the experimental results obtained from the influence of temperature study, which indicate that the adsorption yield decreases with increasing temperature. The positive ΔG values revealed that the adsorption process of MB dye onto MNP was not-spontaneous in nature [27]. The negative value of the entropy variation (ΔS°) suggest that the molecules decrease their randomness at the solid-liquid interface during the adsorption [28].
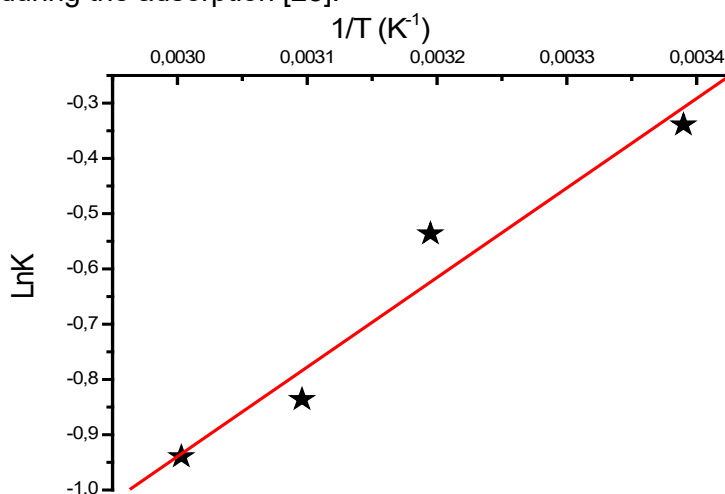
Figure 11. Linear plots of LnK vs. 1/T for methylene blue

Table 5. Thermodynamic parameters for adsorption of MB dye at different temperatures onto MNP.

Temperature (K)	ΔG (KJ/mole)	ΔH° (KJ/mole)	ΔS° (KJ/mole. K)
295	1.085		
313	2.057	-14.844	-0.053
323	2.597		
333	3.137		

Conclusion

The resulting of this study shows the efficiency of methylene blue dye removal in aqueous media by the modified phosphate rock.

The study of the influence of some parameters on the adsorption capacity has shown that the favorable conditions for obtaining a maximum discoloration rate are:

- Concentration of the phosphate suspension C_{susp}=4 g.L^{-1}
- pH of the solution = 9
- agitation speed ω=250 rpm.
- Temperature t=22°C

The adsorption isotherm of MB on MNP for the two-temperature studied (22°C, 40°C) follows the Langmuir and Freundlich models respectively.

The kinetic data is analysed using pseudo first-order and pseudo second-order equations. The experimental data was fitted very well with the pseudo second-order kinetic model.

The negative $\Delta H°$ and $\Delta S°$ values and positive $\Delta G°$ value associated with the adsorption of MB on MNP suggested that the process was exothermic and unspontaneous.

3. MATERIALS AND METHODS

3.1. Adsorbent
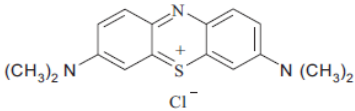
The adsorbent used in this work was the modified phosphate rock of Djbel Onk ores (Kef ESNOUN bir el ater Tebessa) in Algeria. They were repeatedly washed several times with tap water followed by distilled water and then were dried in oven at 100°C for 24 hours. Phosphate rock are crushed and powdered at different fraction. Only the powder of the fraction between 100 and 400 nm grain size, rich in natural phosphate was used in this study.

This powder was totally dissolved in the HNO_3 solution at pH=2 under continuous agitation using a magnetic stirrer for 2 hours at room temperature to obtain calcium and phosphorus precursors. The filtrated solution was then aged for 24 hours after being precipitated with a concentrated ammonium hydroxide solution NH_4OH at room temperature. The precipitate obtained is recovered by a 2nd filtration, washed with distilled water and then dried in an oven at 100°C for 24 hours [18].

3.2. Adsorbate

The adsorbate used is this study is the Methylene blue obtained from Aldrich sigma. The chemical structure and the characteristic of this dye is illustrated in the Table 6.

Table 6. Physicochemical characteristics of the Methylene blue.

Name	Chemical structure	Nature	MW (g.mol^{-1})	λ_{max} (nm)
Methylene blue	$(CH_3)_2 N$ —[structure]— $N (CH_3)_2$; Cl^-	Cationic	319.85	664

3.3. Characterization of the adsorbent

The powder (MNP) obtained was characterized by various methods such as:

• X-ray diffraction (XRD) used the PHILLIPS X pert proof, analytical, system MPD diffractometer with Cu Kα radiation.

• IR using a Shimadzu-8300 interferometer and with adopting the KBr technique 2 mg of the dried sample powder was compacted with 300 mg of potassium bromide using pressure, the measurements were run in the wave number range from 400 to 4000 cm^{-1}.

• The thermal analysis TGA using a thermogravimetric analyzer (LINSEIS STA-PT 1600) heating was performed in a platinum crucible from 25°C to 1000°C at a heating rate of 10°C/min in a stream of nitrogen.

3.4. Adsorption tests

Stock solution of 1g/L of methylene blue (MB) was prepared by dissolving appropriate amount of this dye in distilled water, and the used concentrations were obtained by dilution. Adsorption experiments were carried out in the batch reactors (500 mL Erlenmeyer) containing various amounts of modified natural phosphate as adsorbent and 250 mL of methylene blue solutions having different concentrations (10, 25, 50, 100, 200 and 500 mg/L) and pH (3–10). The pH solution was adjusted with HCl (0.1M) and NAOH (0.1M).

In order to study the effect of the temperature on the adsorption, five adsorption temperatures (22, 40, 50 and 60 °C) were studied. The mixture was well agitated using a shaker 250 rpm until reaching the equilibrium. Preliminary experiments had shown that the equilibrium adsorption was obtained before 2 hours and for agitation speed of 250 rpm. After this time, the samples were filtered by a Millipore membrane filter type 0.45 μm, and the concentrations of the dyes were analyzed using UV–vis spectrophotometer (ICE 3000 SERIE SAA S) by monitoring the absorbance changes at a wavelength of maximum absorbance of methylene blue (664 nm). All experiments were performed in triplicate and experimental errors were found below 5%.

The adsorbed quantity (q_e) and the removal percentage (Y %) were calculated using the following equations:

$$q_e = \frac{(C_0 - C_e).V}{m} \quad (4)$$

$$Y(\%) = \frac{(C_0 - C_t).100}{C_0} \quad (5)$$

Where C_0, C_t and C_e represent, respectively, the dye concentrations (mg/L) in the initial solution, at time t and at the equilibrium, respectively, V is the volume of the dye solution (L) and m is the amount (g) of the sorbent used in the reaction mixture.

3.5. Adsorption isotherm models

Equilibrium adsorption studies were performed to determine the maximum MB adsorption capacities of MNP. Langmuir, Freundlich,Temkin and Dubinin-Radushkevich isotherm models were used to fit the equilibrium adsorption data of MB, onto MNP.

3.5.1. Langmuir model

The Langmuir isotherm is based on monolayer adsorption onto a surface with a finite number of adsorption sites. This model assumes that adsorption energies on the surface are uniform and that there is no adsorbate transmigration in the surface plane [29]. The Langmuir model is represented by the following equation:

$$q_e = \frac{K_L q_m C_e}{1 + K_L C_e} \quad (6)$$

The Langmuir parameters models were given by transforming the equation (6) in its linear form:

$$\frac{C_e}{q_e} = \frac{C_e}{q_m} + \frac{1}{q_m K_L} \quad (7)$$

Where C_e is the equilibrium concentration (mg/L), q_e is the equilibrium adsorption amount (mg/g),q_m is the maximum adsorption capacity (mg/g) and K_L is the Langmuir constant (L/mg).

$$R_L = \frac{1}{1 + k_L c_0} \quad (8)$$

A factor of separation $R_L > 1$ indicates that adsorption is unfavorable, if $R_L = 1$ adsorption is known as linear, adsorption is known as favorable when $0 < R_L < 1$, and a null factor of separation ($R_L = 0$) indicates that adsorption is irreversible [22].

3.5.2. Freundlich model

This model is based on multilayer adsorption. Il this model, the mechanism and the rate of adsorption are functions of the constant n and K_F [26]. The Freundlich isotherm can be expressed as follows:

$$q_e = K_F C_e^{1/n} \qquad (9)$$

The linear form of Freundlich is given by this equation:

$$\mathrm{Ln}\, q_e = \mathrm{Ln} K + \frac{1}{n} \mathrm{Ln} C_e \qquad (10)$$

Where K_F is the constant of Freundlich (L/mg) and n is a constant depicting the adsorption intensity.

3.5.3. Temkin model

The Temkin isotherm account that the heat of adsorption of all molecules in the cover layer decreases linearly with coverage due to the decrease in adsorbent-adsorbate interactions, and adsorption of Temkin isotherm is characterized by a uniform distribution of surface binding energies [11]. The Temkin isotherm is expressed by this equation:

$$q_e = \frac{RT}{b} \ln (K_e . C_e) \qquad (11)$$

The linear form of Temkin isotherm is presented as follows:

$$q_e = B_t \ln K_e + B_t \ln C_e \qquad (12)$$

With B_t= RT/ b (J/mol), the constant of Temkin relating to the heat of sorption and K_e (L/g), the adsorption equilibrium constant corresponding to the maximum binding energy.

3.5.4. Dubinin-Radushkevich model

Dubinin–Radushkevich isotherm is generally applied to express the adsorption mechanism with a Gaussian energy distribution onto a heterogeneous surface [30]. The model is given by the following equation:

$$q_e = q_m \exp(-\beta \varepsilon^2) \qquad (13)$$

The equation (13) can be linearized in form:

$$\ln q_e = \ln q_m - \beta \varepsilon^2 \qquad (14)$$

With q_m, theoretical maximum capacity of adsorbate adsorbed on the surface of the solid and ε potential of Polanyi, corresponding to:

$$\varepsilon = \mathrm{RT ln}\left(1 + \frac{1}{C_e}\right) \quad (15)$$

The constant β represents the adsorption of the molecule on the adsorbent following its transfer since the solution. β and activation energy E (Kj /mol) is used to estimate the adsorption process, are bound by the following relation:

$$E = \sqrt{\frac{1}{2\beta}} \quad (16)$$

- E< 8 kJ/mol : physical adsorption
- 8 < E < 16 kJ/mol: chemical adsorption.

3.5.5. *Error function*

The adsorption process is characterized using different kinetics and isotherm models, where by the linear variant of the models that best fitted with the experimental data is usually determined using the coefficient of determination (R^2). In addition, two error functions: residual root mean-square errors (RMSE) and chi-square statistic X^2 test were used to further reinforce the suitability of these models [ref]

$$X^2 = \sum_{i=1}^{n} \left| \frac{qe_{Exp} - qe_{cal}}{q_{e\,cal}} \right| \quad (17)$$

$$RMSE = \sqrt{\frac{1}{(n-p)} \sum_{i=1}^{n} (qe_{Exp} - qe_{cal})_i^2} \quad (18)$$

The subscripts "exp" and 'calc" show the experimental and calculated values and *N* is the number of observations in the experimental data. If data from the model are similar to the experimental data, X^2 will be a small number; if they are different, X^2 will be a large number. The small the RMSE value, the better the curve fitting.

3.6. Adsorption kinetic models

The kinetic study of the adsorption process reveals the mechanism of adsorption as well as the mode of solute transfer from the liquid to the solid phase. Pseudo-first-order and pseudo-second-order models were used in this study to fit the kinetics data.

3.6.1. Pseudo-first-order kinetic model

The pseudo-first-order model is presented as follows [31]:

$$\log(q_e - q_t) = \log(q_e) - \frac{K_1}{2.303} \cdot t \quad (19)$$

Where:

K_1 (min^{-1}): is the rate constant of pseudo-first order adsorption.

q_e and q_t (mg/g): denote the amount of dyes adsorbed at equilibrium and at time t, respectively.

3.6.2. Pseudo second order kinetic model

The pseudo-second -order model is presented as follows [32] (Zhang, Z and al, 2011):

$$\frac{t}{q_t} = \frac{1}{K_2 \cdot q_e^2} + \frac{1}{q_e} \cdot t \quad (20)$$

Where K_2 (mg/g.min) is the rate constant of pseudo-second order adsorption.

3.7. Thermodynamic study

Thermodynamic parameters, such as standard free energy change (ΔG˚), standard enthalpy charge (ΔH˚), and standard entropy change (ΔS˚) can be calculated using the following equation [33]:

$$K_e = \frac{q_e}{C_e} \quad (21)$$

$$\ln K_e = \frac{\Delta S^\circ}{R} - \frac{\Delta H^\circ}{RT} \quad (22)$$

$$\Delta G^0 = \Delta H^0 - T \Delta S^0 \quad (23)$$

Where:

K_e: is the thermodynamic equilibrium constant (L/g),

T: is the absolute temperature (°K);

R: is the gas constant (8.314 J.mol^{-1}. K^{-1}).

REFERENCES

1. N. Naghmouchi; k. Nahdi; *Adv. Chem.*, **2015**, *11*, 2321-807.
2. M. Dogan; H. Abak; M. Alkan; *J. Hazard. Mater.*, **2009**, *164*, 172–181.
3. I. Khouni; B.Marrot; PH. Moulin; R. B. Amar; *Desalination.*, **2011**, *268*, 27–37.
4. R. Vidhya; A. J. Thatheyus; *Am. J. Microbiol. Res.*, **2013**, *1(1)*, 10-15.
5. G.Ciardelli; L. Corsi; M. Marcucci; *Resour. Conserv. Recycl.*, **2001,** *31*, 189–197.

6. P.K. Malik; S.K. Saha; *Sep. Purif. Technol.*, **2003**, *31*, 241-250.

7. M. Koch; *Chemosphere*, **2002**, *46*, 109-113.

8. B.K. Nandi; A. Goswami; M.K. Purkait; *J. Hazard. Mater.*, **2009**, *161*, 387–395.

9. S. Pandey; J. Ramontja; *Am. J. Chem. App.*, **2016**, *3*, 8-19.

10. A. B. AKarim; B. Mounir; M. Hachkar; M. Bakasse; A. Yaacoubi; *J. Water. Sci.,* **2010**, *23*, 375–388.

11. O. Ferrandon; H. Bouabane; M. Mazet; *J. Water. Sci.,* **1995**, *8*, 183–200.

12. N. Barkaa; A. Assabbane; A. Nounah; L. Laanab; Y. Aîtlchou; *Desalination.*, **2009**, *235*, 264–275.

13. N. Barka ; S. Qourzal ; A. Assabbane ; A. Nounah ; Y. Ait-Ichou ; *J. Saudi Chem. Soc.*, **2011**,*15*, 263–267.

14. A. Corami; S. Mignardi; V. Ferrini; *J. Colloid Interface Sci.*, **2008**, *317*, 402–408.

15. N.Baraka; Q. Samir; A. Ali; N. Abederrahman; A. Yhya; *J. Environ. Sci.*, **2008**, *20*, 1268–1272.

16. S. Meski; H. Khireddine; S. Ziani; S. Rengaraj; M. Silanpaa; *Desalin. Water. Treat.*, **2010**, *16*, 1-11.

17. S. Meski; N. Tazibt; H. Khireddine; S. Ziani; W. Biba; S. Yala; D. Sidane; F. Boudjouan; N. Moussaoui; Water. Sci. Technol., **2019**, *80*, 1226-1237.

18. S. El Asri; A. Laghzizil; A. Saoiabi; A. Alaouib; K., El Abassi; R. M'hamdi; T. Coradin; *Colloids Surf. A Physicochem. Eng. Asp.*, **2009**, *35*, 73–78.

19. A. Chandrasekar; S. Sagadevan; A. Dakshnamoorthy; *Int. J.* Phys. Sci., **2013**, *8*, 1639-1645.

20. K, Allam; A. El Bouari; B. Belhorma; L. Bih; *J Water Resource Prot.*, **2016**, *8*, 358-371.

21. L. Wu; W. Frsling; P. W. Schindler; *J. Colloid Interface Sci. Sci.,* **1991**, *147*, 178-185.

22. M.M, Abd El-Latif; M. Amal Ibrahim, M. F. El-Kady; *Am. J. Sci.*, **2010**, *6*, 267-283.

23. K.M. Kifuani; A.K. Kia Mayeko; PH. N. Vesituluta; B.I. Lopaka; G.E. Bakambo, B.M. Mavinga, J. M. Lunguya, *Int. J. Biol. Chem. Sci.*, **2018**, *12*, 558-575.

24. C.H. Giles; A.P. D'Silva; I.A. Easton; *J. Colloid Interface Sci.*, **1974**, *47*, 766–778.

25. A. B. Karim ; B. Mounir ; M. Hachkar; M. Bakasse; A. Yaacoubi, *Rev. Des Sci. De L'Eau.*, **2010**, *23*, 375–388.

26. O. Hamdaoui; E. Naffrechoux; *J. Hazard. Mater.*, **2007**, *147*, 381–394.

27. S. Farrokhzadeh; H. Razmi; N. Sadeghi; E. M. Khosrowshahi; *HHHM.*, **2020**, *1*, 8-20.

28. B.K. Nandi; A. Goswami; M.K. Purkait; *J. Hazard. Mater.*, **2009**, *161*, 387–395.

29. F. O. Umoh; V. E. Osodeke; I. D. Edem; G. S. Effiong; *OALibj.,* **2014**, *1*, 1-9.

30. M. Horsfall; Jnr; A. I. Spiff; A. A. Abia; *J. Korean Chem. Soc.*, **2004**, *25*, 969-976.

31. N. Fayoud; S.,Alami Younssi; S. Tahiri; A. Albizane; *J. Mater. Environ. Sci.,* **2015**, *6*, 3295-3306.

32. Z. Zhang; L. Moghaddam; Ian. M. O'Hara; O.S. Doherty. William; *Chem. Eng. J.*, **2011**, *178*, 122-128.

33. H. ELBoujaady; M. Mourabet; A. EL Rhilassi; M. Bennani-Ziatni; R. El Hamri, A. Taitai; *J. Mater. Environ. Sci.*, **2016**, *7*, 4049-4063.

STRUCTURE, MAGNETIC PROPERTIES, CORROSION RESISTANCE OF 1.4541 STAINLESS STEEL IN SURFACE SEAWATERS

**OLGA DEMIDENKO[a], ANA-MARIA POPESCU[b]*,
KAZIMIR YANUSHKEVICH[a], ELENA IONELA NEACSU[b],
CRISTINA DONATH[b], VIRGIL CONSTANTIN[b]***

ABSTRACT. We investigated the phase structure, magnetic properties, corrosion resistance, microstructure of 1.4541 (V2A) stainless steel through X-ray diffraction (XRD), magnetic measurement device, gravimetric/electrochemical methods, metallographic microscopy. Corrosion resistance was evaluated in natural seawaters of Mediterranean, Black and Aegean seas. The results show that crystal structure and specific magnetic characteristics are resistant to corrosion action of all seawaters at a temperature of 295 K. The greatest corrosive effect on studied alloy has the Mediterranean Seawater, corrosion penetration is about 0.1290 mm/year. Microscopy confirmed corrosion data.

Keywords: *text, Stainless steel, Sea waters, Corrosion, Micrography, XRD analyses, Magnetization.*

INTRODUCTION

Most metal products are used in corrosive natural environments, so on an industrial scale, there is little alternative to nickel-based steels and alloys that are resistant to corrosion. Stainless steels have a wide industrial application in heavy, energy, mechanical and electronic industries. A very actual problem is the corrosion resistance of such materials in marine media. Therefore, the key to a significant economy is the existence of accurate data on the resistance to marine corrosion, as well as the physical, mechanical, stability properties of stainless steel. Knowledge of processing and operating temperature ranges, as

---

[a] *Scientific Practical Materials Research Centre of NAS Belarus, Laboratory of Physics of Magnetic Materials, 19 P. Brovki Str., Minsk, Belarus.*

[b] *Romanian Academy, "Ilie Murgulescu" Institute of Physical Chemistry, Laboratory of Electro-chemistry and Corrosion, 202 Splaiul Independentei, 060021, Bucharest, Romania.*

* *Corresponding author: popescuamj@yahoo.com, virgilconstantin@yahoo.com.*

well as operating conditions, is also very important information in the widespread use of these steels in corrosive environments. Stainless steel containing 13% chromium and additionally alloyed with nickel, as well as a small amount of silicon and manganese, shows high anti-corrosion properties [1,2]. High chromium content stainless steels have as their main property corrosion resistance, which is very important knowing that corrosion losses can be enormous in some cases. The chromium content in steel over 12% provides high resistance to oxidation and heat resistance [3,4]. It was found that varying the carbon content in the range of 0.08-0.25% affects the quality characteristics and changes the properties. The extension of the study of this issue is generated by the ambiguity of the published results.

The problem of corrosion resistance of stainless steels and alloys based on chromium and nickel, like nickel-based alloy 1.4541(V2A), is still relevant. Therefore, leading research centers carry out comprehensive studies of such materials [5-8]. From the scientific references found we have not been able to get explanation and prediction of the corrosion resistance of the steels that can be used in seawater.

Considering the wide use of 1.4541(V2A) steel in various parts and components that are used in the marine environment, as well as the lack of systematic studies of corrosion of this material in the marine environment, we considered appropriate and interesting the study his corrosion behavior in different seawaters.

In this study, we aim to study structure and magnetic properties of functional nickel-based alloy 1.4541(V2A) along with the corrosive effects of sea waters with different salt content (respectively seawaters from Black Sea, Aegean Sea and Mediterranean Sea). In the same time structure of this stainless steel were studied before and after corrosion process in seawaters. To our knowledge, this study is original, being the first of its kind. Our purpose and objectives are relevant for having a long life in the aggressive marine environment, materials with specific characteristics of the crystalline structure must be used, which leads to the increase of the corrosion resistance in aggressive environments.

RESULTS AND DISCUSSION

X-ray phase analysis of the alloy 1.4541(V2A) (Fig. 1) showed that the alloy contains two phases – γ-phase of iron austenitic $Fm\bar{3}m$ sp. gr. and α'-phase ferrite $Im\bar{3}m$ sp. gr. The unit cell parameter was 0.3595 nm for γ-phase and 0.2877 nm for α'-phase of iron with a phase ratio of 6/1. The average crystallite size is 16.86 nm, and the dislocation density is $3.52 \cdot 10^{-3}$ nm^{-2}.

Figure 2 shows the temperature dependence of the specific magnetization of the 1.4541(V2A) alloy before corrosive action. The inset shows the dependences $\sigma^2=f(T)$, which allow more accurately determining the Curie temperature. At liquid nitrogen temperature, the specific magnetization is 12.4 A·m^2·kg^{-1}. Curie temperature determined from dependence $\sigma^2=f(T)$, equals 890 K. It should be noted that the $\sigma=f(T)$ dependence at cooling is completely different from $\sigma=f(T)$ at heating, that is, the heating of the 1.4541(V2A) alloy to 1060 K is irreversible. The specific magnetization values at nitrogen temperature decrease 5.5 times and amounts to 2.25 A·m^2·kg^{-1}. As X-ray phase analysis showed that two phases are present in the alloy, it can be assumed that a sharp decrease in the magnetization is associated with the restoration of the stable structure of austenite by high-temperature treatment.
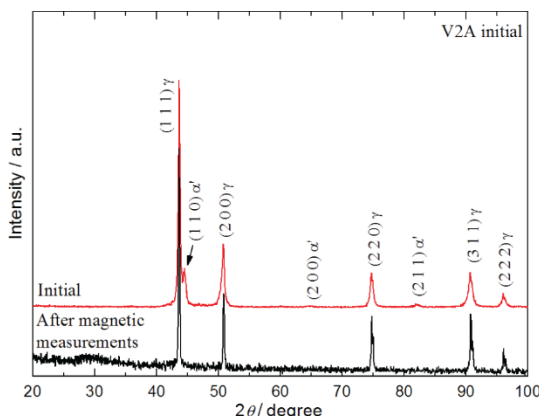

Figure 1. X-ray patterns of 1.4551(V2A) before and after high-temperature annealing
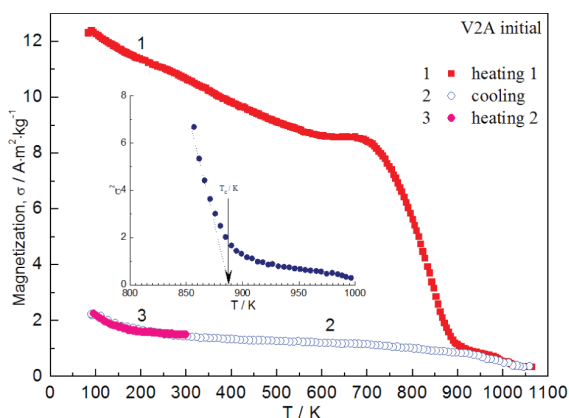

Figure 2. Temperature dependences of the specific magnetization of the 1.4541 (V2A) stainless steel before the corrosive effect of studied sea waters

For understanding this fact, it was carried out an X-ray study of 1.4541 samples after high-temperature annealing during specific magnetization measurements, the results of which are presented as a comparison in Fig. 1. This treatment causes the transformation of α' – γ phase into the austenitic γ phase as shown by the X-ray phase analysis. Slow cooling of the alloy leads to recrystallization of the alloy, the average grain size increases to 41.71 nm, and the dislocation density increases to $5.75 \cdot 10^{-3}$ nm^{-2}. Magnetic hysteresis loops at 77 K and 300 K (Fig. 3) also confirm the presence of only austenitic γ-phase. By heating, to 1100K the alloy becomes completely austenitic by the disappearance of the martensitic phase of the iron.
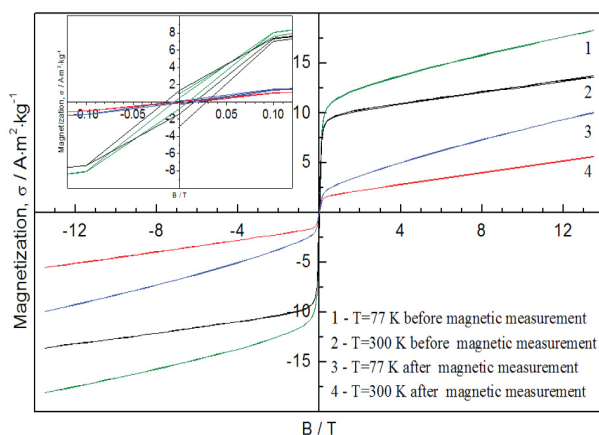

Figure 3. Magnetic hysteresis loops for the 1.4541(V2A) stainless steel before and after high-temperature annealing at 77 K (1 and 2) and 300 K (3 and 4)

The experimental data for mass loss corrosion study of 1.4551(V2A) stainless steel in three seawaters shows a mass loss of 0.0001-0.0004 g at 31 days of immersion in seawaters, followed by a big increase in the mass loss (0.0005-0.0007g) at 65 days of immersion. After that the mass loss (Δm) remains almost constant up to 277 days of immersion. From 308 days of immersion the mass loss has again a lower value and at 365 days the Δm was 0.0004 g in Mediterranean and Aegean sea and 0.0003 g in the Black sea. Finally, the mass loss was in accordance with the salinity of the three seawaters in study.

The calculated corrosion rate (CR=Δm/S×t; Δm, in g, the surface of the sample, S, in cm^2 and the time of immersion, t in h), was the same in the Mediterranean and the Aegean sea, which is normal as the two seawaters have almost the same salinity (38-40 g×L^{-1}). For the Black sea, the corrosion rate is lower as the salinity of that seawater is also lower (17-22 g×L^{-1}). Finally, the corrosion penetration rate (CPR) was calculated for the studied steels corroded in seawaters and the results are presented in Table 1. The CPR, in mm×year^{-1},

represents the depth to which the corrosion has penetrated the mass of the metal for one year and is calculated from the, CR, and the density of the metal, ρ, after the following formula: CPR=(24×365×CR)/(1000×ρ), where: 24 represents the number of hours in a day; 365 is the number of days in a year;1000 is the conversion factor of the units of measurement; ρ is the density of the metal being corroded, $g \times cm^{-3}$. Those data, presented in Table 1, show a very good corrosion resistance as the CPRs determined are much lower than the allowable standard rate, $0.5 \ mm \times year^{-1}$.

Table 1. Calculated corrosion parameters of 1.4541(V2A) stainless steel corrosion in seawater after a total immersion of 365 days.

Corrosion media	Mass loss $\Delta m(g)$	Corrosion rate $(g \cdot cm^{-2} \cdot h)$	CPR $(mm \cdot year^{-1})$
Mediterranean Sea	0.0004	7.1×10^{-9}	7.9×10^{-9}
Aegean Sea	0.0004	7.1×10^{-9}	7.9×10^{-9}
Black Sea	0.0003	5.3×10^{-9}	5.9×10^{-9}

Figure 4 shows the Tafel plots obtained from the polarization curves of the 1.4541(V2A) steel (in the initial state and after the weight loss study) in the tree seawater in the study. The plots corrosion *vs*. time respects a logarithmic law [9]. Corresponding corrosion parameters rates calculated are summarized in Tables 2 and 3.

Table 2. Corrosion parameters for electrochemical corrosion measurements in the water of different seas for 1.4541(V2A) stainless steel in the initial stage.

Corrosion media	E_{OCP} (V)	E_{corr} (V)	i_{corr} (A)	$CR_{init.}$ (mm/year)
Black Sea	-0.325	-0.204	$3.21 \cdot 10^{-6}$	0.0006
Aegean Sea	-0.101	-0.370	$16.24 \cdot 10^{-6}$	0.0122
Mediterranean Sea	-0.172	-0.465	$19.62 \cdot 10^{-6}$	0.1323

Table 3. Corrosion parameters for electrochemical corrosion measurements in the water of different seas for 1.4541(V2A) stainless steel after long-term corrosion.

Corrosion media	E_{OCP} (V)	E_{corr} (V)	i_{corr} (A)	$CR_{corr.}$ (mm/year)
Black Sea	-0.051	-0.465	$3.49 \cdot 10^{-6}$	0.0128
Aegean Sea	-0.125	-0.595	$8.65 \cdot 10^{-6}$	0.0583
Mediterranean Sea	-0.012	-0.983	$17.44 \cdot 10^{-6}$	0.1490

The highest corrosion rate (in both situations: initial and corroded) was obtained in the Mediterranean seawater. In general, the corrosion rate increases with increasing salinity and with decreasing pH. So we measured the pH and TDS for the three seawaters [using a multicomponent Cyber Scan PCD6500-

Eutech Instruments (USA) device] and we present the obtained values in Table 4. The high values of the corrosion rate obtained in Mediterranean seawater are confirmed by the highest value of salinity and a low pH.

Table 4. Some properties of seawaters in the study.

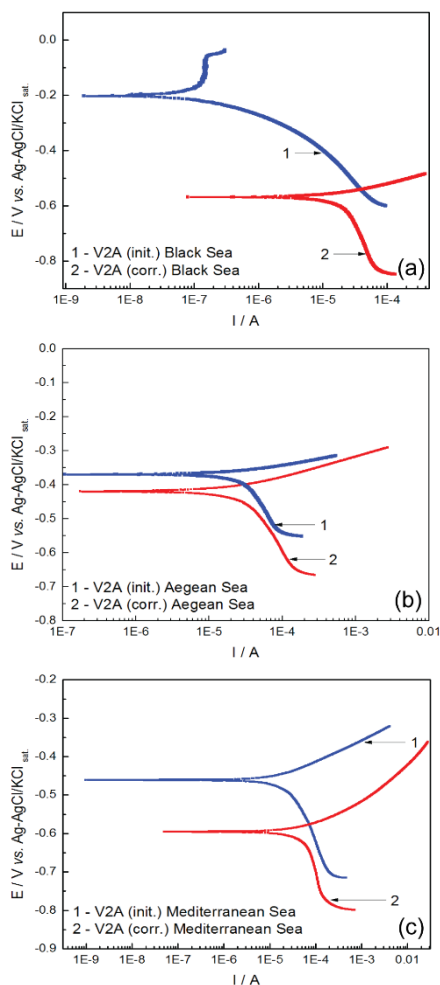| Sample of water	pH	TDS ppt
Black Sea	7.63	13.88
Aegean Sea	7.70	21.70
Mediterranean Sea	7.39	64.93

Figure 4. Tafel plots for 1.4541(V2A) corrosion (initial and after gravimetric long term corrosion) in different natural seawaters.

Figure 5 shows the diffraction patterns of the 1.4551(V2A) stainless steel before the corrosion action of different sea waters and after the corrosion resistance studies by gravimetric and potentiodynamic methods in seawater. The analysis of the diffraction patterns showed that the crystal structure of 1.4551(V2A) in case of longtime exposure in seawater has good corrosion resistance, the structure of the alloy was preserved. Table 5 shows the crystal cell parameters of the α' and γ-phases of 1.4551(V2A) alloy, as well as the average grain size and dislocation density. We did not observe any iron oxides or hydroxides be formed on the surface of the samples.
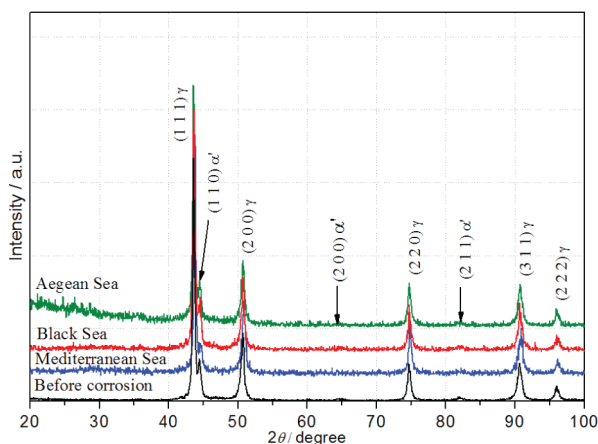
Figure 5. X-ray patterns of 1.4551(V2A) before and after corrosion action of seawaters.

Table 5. Crystal cell parameters of the α 'and γ-phases of the 1.4551(V2A) stainless steel, the average grain size, the density of dislocations.

Corrosion media	γ-phase a (nm)	α'-phase a (nm)	average crystallite size d (nm)	dislocation density δ·10^{-3}(nm^{-2})
Before corrosion	0.3598	0.2879	16.86	3.52
Mediterranean Sea	0.3596	0.2874	16.08	3.86
Black sea	0.3589	0.2870	16.61	3.62
Aegean sea	0.3597	0.2879	16.15	3.83

Figure 6 shows metallographic images of the 1.4551(V2A) stainless steel surface before and after corrosion studies. The analysis of the micrographic images shows that at small magnifications (×100) the effect of the corrosion of the seawater is observed very little. At high magnifications, it is found that Mediterranean and Aegean seawaters have a profoundly visible effect on the surface of 1.4551(V2A) samples. The Mediterranean Sea has the greatest

corrosive effect (one can see in that on the surface of V2A appears many caves). We believe that the corrosion resistance of this stainless steel alloy is given by the content of Cr and Ni. Because we have more austenitic phases than ferrite ones (Fig. 1 and 5) the stainless steel should exhibit good corrosion resistance, as ferrite phases are more susceptible to cracks. From the micrographs, one can see that nickel is mainly extracted during the corrosion process (green areas). The initiation of crevice corrosion may be done in the defect zone of the alloy which helps propagation of corrosion. The metallographic microscopy study supports the corrosion data.
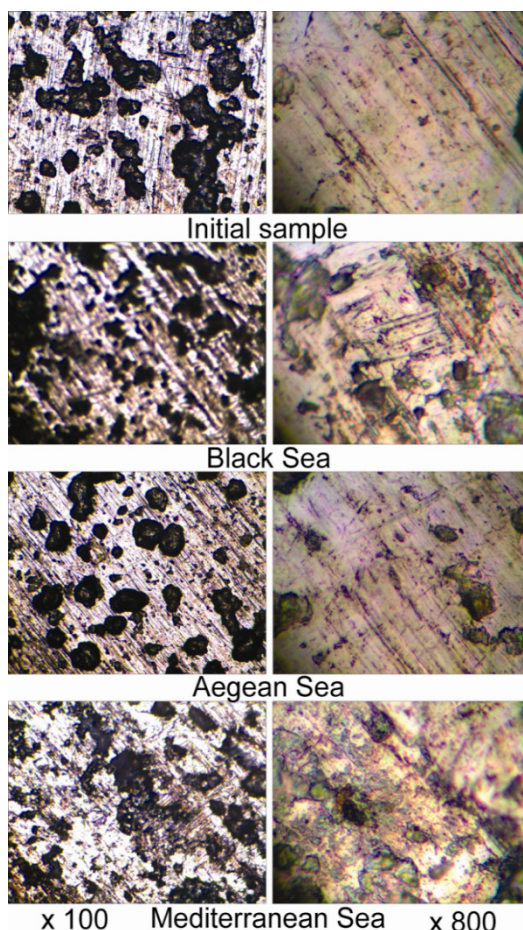

Figure 6. Surface of 1.4541(V2A) alloy samples before and after corrosive action of seawaters: the Mediterranean, Black and Aegean seas (resolution ×100 and ×800)

CONCLUSIONS

It was found that 1.4541(V2A) alloy has two crystalline phases – austenitic γ-phase Fm$\overline{3}$m sp. gr. and ferritic α'-phase Im$\overline{3}$m sp. gr. The cell parameter a before corrosion action is 0.3595 nm for the γ-phase and 0.2877 nm for α'-phase with a phase ratio of 6/1. X-ray patterns analysis after different seawater electrochemical actions showed that in all cases 1.4541(V2A) alloy structure was preserved. Any iron oxides or hydroxides were not observed to be formed on the surface of the samples. The magnitude of the specific magnetization, at nitrogen temperature, decreases 5.5 times and amounts to 2.25 A·m^2·kg^{-1}. X-ray phase analysis showed that two phases are present in the alloy. Thus, it can be assumed that a sharp decrease in magnetization is associated with the restoration of the stable structure of austenite by high-temperature treatment.

Analysis of the corrosion parameters showed that the greatest corrosive effect on studied alloy has the Mediterranean Sea water with a corrosion rate of 0.1323 mm/year, which is confirmed by the results of a study of surface morphology.

EXPERIMENTAL SECTION

Chemical composition of investigated 1.4541(V2A) samples was: 0.08% C, 67.70% Fe, 18% Cr, 11% Ni, 2% Mn, 0.03% S, 0.04% P, 1% Si. 0.15% Ti .

The alloy was used to investigate before and after corrosion by X-ray diffraction of the automated apparatus "DRON-2" in CuKα in angle range 20 ° ≤ 2θ ≤ 100 ° at room temperature. To obtain the XRD pattern, the recording of the reflex intensities takes place automatically with a scan step of 0.03 ° and exposure time of 2-3 s. Using a step of 0.01 ° with exposure at 10 seconds it was determined the parameters of the crystal cell. The FullProf Suite program, which is based on the Rietveld method to clarify the parameters of the crystal cell, was used to process experimental X-ray data. The lattice parameter determination error was ± 0.0003 nm and the average crystallite size is calculated with the Debye-Scherrer formula. The temperature dependences of the specific magnetization were studied in the 77 – 1100 K temperature range by the ponderomotive method in a magnetic field of 0.86 T. The relative error in determining the specific magnetization value is about 4%. Dependences of magnetization on a vibration magnetometer of the universal measuring system "Liquid Helium Free High Field Measurement System" from "Cryogenic Ltd." at 77 and 300 K in fields up to 14 T were studied. Corrosion resistance studies of functional 1.4541(V2A) alloy were carried out at a temperature of 25ºC

by two methods: the weight loss and the potentiodynamic method. The corrosive media used was natural seawater from Black, Aegean and Mediterranean seas. Literature [10-12] presents that the salinity of those sea waters is: 17-18.5 g/L the Black Sea, 38 g/L the Aegean Sea, 37-39 g/L the Mediterranean Sea.

The size of the steel samples used for weight loss (Δm) corrosion, were 50 mm × 25 mm × 5 mm. They were cleaned wet-polished with 2000# grade SiC paper, then cleaned in alcohol and acetone, after which they were dried, weighed, stored in a desiccator until use. The test samples were suspended using glass hooks in 100 mL beakers containing 100 mL various test solutions, studied sea waters, and after each period of immersion, 30 days, the specimens were taken out, washed in running water, to get off the rust formed on the samples, and acetone, dried, and weighed using the electronic digital weighing balance Shimadzu D440400231 which has a sensitivity of 0.01 mg and a standard deviation of ±0.02 mg.

The samples were observed for 367 days and each sample was measured before and after each 30 days immersion time to obtain the Δm; measurements, procedures, precautions are described in [13-15]. After that, the samples were subjected to the potentiodynamic polarization method in a standard three electrodes cell. The polarization tests were conducted using a Princeton Applied Research-PAR, model PARSTAT 2273 potentiostat/galvanostat with "Power Corr" software. The Tafel polarization measurements were performed at $\pm$250mV *vs.*OCP with a scan rate of 0.166 mV/s. The glass working cell is connected to a thermostated bath for temperature control. A specific area (1cm^2) of the alloy sample was used as the working electrode (WE); a platinum sheet and Ag-AgCl/KCl(sat.) were employed as a counter (CE) and respectively reference electrode (RE).

A polarization corrosive study was also done on 1.4541(V2A) samples before being subject to long-term corrosion (initial state). Tafel polarization curves analysis was carried out, and the corresponding electrochemical parameters of corrosion were calculated.

Surface images before and after corrosion exposure with different magnifications (from ×100 to ×800) were performed with an inverted microscope (NY Microscope Comp.) with digital camera acquisition.

ACKNOWLEDGMENTS

REFERENCES

1. S. S. M. Tavares; J. M. Pardal; T. R. B. Martins; M. R. da Silva; *J. Mater. Eng. Perform.*, **2017**, *26*, 2512-2519.
2. B. Liu; X. Wei; W. Wang; J. Lu; J. Ding;, *Sol. Energy Mater. Sol. Cells*, **2017**, *170*, 77-86.
3. L. Taleb; C. Keller; *Int. J. Mech. Sci.*, **2018**, *146-147*, 527-535.
4. Z. Wang; T. A. Palmer; A. M. Beese; *Acta Mater.*, **2016**, *110*, 226-235.
5. S. S. Sawant; B. D. Gajbhiye; S. Tyagi; C. S. Sona; R. Divya; C. S. Mathpati; A. Borgohain; N. K. Maheshwari; *Indian Chem. Eng.*, **2017**, *59*, 242-257.
6. S. Wang; J. Ding; H. Ming; Z. Zhang; J. Wang; *Mater.Charact.*, **2015**, *100*, 50-60.
7. V. V. Zelenskiy; S. V. Nesterenko; L. P. Bannikov; *Coke Chem.*, **2014**, *57*, 167-176.
8. A. A. Lukhvich; V. I. Sharando; A. K. Shukevich; K. I. Yanushkevich; *Russ. J. Nondestruct. Test*, **2015**, *51*, 131-137.
9. J. Kruger; *Passivity*, in: *Uhlig's Corrosion Handbook*, 3-rd ed., R.W. Revie Ed.; NJ: John Wiley & Sons Inc., **2011**, Chapter 12, pp.151-155.
10. https://water.fandom.com/wiki/Black_Sea
11. D. Velaoras; V. Zervakis; A. Theocharis; *The physical characteristics and dynamics of the aegean water masses.* in*: The handbook of environmental chemistry*, D. Barcelo; A. G. Kostianoy Eds.; Springer, Berlin, Heidelberg, Germany, **2021**, Chapter 1, pp.1-29.
12. https://www.esa.int/ESA_Multimedia/Images/2017/05/Mediterranean_Sea_salinity.
13. X. H. Chen; C. S. Chen; H. N. Xiao; F. Q. Cheng; G. Zhang; G. J Yi; *Surf. Coat. Technol.*, **2005**, *191*, 351-356.
14. H. A. Sorkhabi; N. G. Jeddi; F. Hashemzadeh; H. Jahani; *Electrochim. Acta*, **2006**, *51*(18), 3848-3854.
15. B. Jabeera; S. M. A. Shibli; T. S. J. Anirudhan; *Appl. Surf. Sci.*, **2006**, *252*(10) 3520-3524.

WATER SPLITTING STUDIES IN ALKALINE MEDIUM USING GRAPHITE ELECTRODES MODIFIED WITH TRANSITION METAL OXIDES AND COMPOSITIONS CONTAINING THEM

BOGDAN-OVIDIU TARANU[a,*], PAULINA VLAZAN[a], ANDREI RACU[a]

ABSTRACT. Present day scientific research is focused on the identification of renewable and clean alternatives to fossil fuels, with hydrogen being a promising energy source that fulfills both requirements. Given this context, the current work investigates the water splitting electrocatalytic properties of two hydrothermally synthesized transition metal oxides: MnO_2 and Fe_3O_4. Electrodes were obtained by modifying graphite substrates with suspensions in ethanol containing the catalytic materials as such or in compositions, and their activity for the O_2 and H_2 evolution reactions (OER and HER) was studied in alkaline medium. Out of the MnO_2-based electrodes, the one modified with the suspension containing 2 mg MnO_2, 1 mg Carbon Black and 10 μL Nafion solution displayed an OER overpotential (η_{O2}) value, at i = 10 mA/cm^2, of 0.53 V, while the one manufactured using the suspension with 4 mg MnO_2 and 10 μL Nafion solution showed a HER overpotential (η_{H2}) of 0.427 V (at i = -10 mA/cm^2). From the Fe_3O_4-based electrodes, the one modified with the suspension containing 2 mg Fe_3O_4 and 2 mg Carbon Black evidenced the highest catalytic activity for both reactions (η_{O2} = 0.51 V and η_{H2} = 0.43 V).

Keywords: water splitting, oxygen evolution reaction, hydrogen evolution reaction, metal oxide, electrocatalysis

INTRODUCTION

Currently, humanity is witnessing an increase in global energy consumption, global warming and environmental pollution. This situation makes the need to develop sustainable energy sources more important than ever [1]. In the past few years, scientific researchers have been focusing on renewable and clean alternatives to fossil fuels [2], and hydrogen appears to be an ideal fuel, emerging both as a renewable and as a clean energy source [3].

[a] *National Institute for Research and Development in Electrochemistry and Condensed Matter, Dr. A. Paunescu Podeanu street, No. 144, 300569, Timisoara, Romania.*
* *Corresponding author: b.taranu84@gmail.com.*

Hydrogen is abundant in nature due to its presence in water, and current technologies allow its production through renewable, as well as non-renewable sources [4,5]. From the ways in which hydrogen can be generated, water splitting electrolysis stands out as an efficient route with regard to energy conversion and storage, and the necessary power input for this process can be ensured using renewable sources [2,5]. The two half-cell reactions taking place during water splitting are the anodic oxygen evolution reaction (OER) and the cathodic hydrogen evolution reaction (HER), and an important difference between them is that the HER is easier to catalyze, requiring less energy than the OER [6-8]. In the presence of materials that are catalytically active for the two reactions, the amount of energy required for their unfolding decreases [9,10] and, as a result, the potential values at which they occur in practice become closer to the theoretical ones. The search for materials that possess electrocatalytic properties for the OER and HER has led to the identification of efficient catalysts that are also cheaper than the often used noble metal-based ones [10-12]. In fact, the scientific literature includes studies performed using OER, HER, as well as bifunctional catalysts (materials with catalytic activity for both reactions) [13-18].

The present paper describes a study concerning the obtaining of graphite electrodes modified with MnO_2, Fe_3O_4 and with compositions containing these materials together with Carbon Black and/or Nafion solution, and the evaluation of their OER and HER electrocatalytic properties in alkaline medium. The scientific literature shows that the two transition metal oxides are catalytically active for the two half-cell reactions involved in water splitting [19-30]. It is important to point out that, even though there are these previously reported studies, many of the electrodes investigated herein were manufactured using quantitative compositions that have not been previously tested in terms of their HER and OER electrocatalytic performance. For example, in a study reported by Zhao et $al.$ [24] the water splitting properties of defect-engineered ultrathin MnO_2 nanosheets were compared with those of other electrodes, including of a glassy carbon electrode manufactured using a suspension of 5 mg MnO_2 particles and 20 µL Nafion solution dispersed in 980 µL ethanol.

In another investigation, Pokhrel et $al.$ [22] evaluated the OER properties of synthesized manganese oxides utilizing electrodes modified with suspensions containing 5 mg catalyst, 5 mg Carbon Black and 45 µL Nafion solution in 350 µL ethanol. In both examples conductive substrate modification procedures that resemble the ones from the present study were employed. There are however important dissimilarities: in this study a different conductive support was used, modified with compositions based on different quantities of catalytic materials, by themselves or mixed with 10 µL

Nafion solution and/or different quantities of Carbon Black. Such dissimilarities exist between the present investigation and those found in other literature reports that focus on the OER and HER properties of electrodes modified with MnO_2 and Fe_3O_4. Thus, the experimental results and conclusions shown herein serve to complement the current scientific understanding regarding the water splitting catalytic properties of MnO_2- and Fe_3O_4-based electrodes.

RESULTS AND DISCUSSION

A. Electrochemical studies

A.1. OER investigations

In the case of the OER experiments performed on the modified electrodes labeled as shown in **Tables 1** and **2** (introduced in the Experimental section), the polarization curves recorded in 0.1M KOH solution revealed that the most electrocatalytically active Fe_3O_4-based electrode was $G7_{Fe3O4}$, while the highest OER catalytic activity among the MnO_2-based electrodes was observed for $G13_{MnO2}$. As can be seen in **Figure 1a**, at i = 10 mA/cm^2 - a current density value at which the OER overpotential (η_{O2}) value is often determined [12,31,32] - these modified electrodes displayed a higher OER activity than the unmodified graphite sample (G0), and this is true for the higher and lower i values as well. The differences between the three curves are clear and, at the specified current density, the η_{O2} values are 0.66 V for $G7_{Fe3O4}$, 0.57 V for $G13_{MnO2}$ and 0.93 V for G0.

The OER properties of the $G7_{Fe3O4}$ and $G13_{MnO2}$ electrodes were further studied in 1M KOH solution and the recorded LSVs are presented in **Figure 1b**. By comparing the polarization curves obtained in this strong alkaline medium with those traced in 0.1M KOH solution it is observed that the increase in KOH concentration resulted in an increased OER catalytic activity for both electrodes. Thus, at i = 10 mA/cm^2, η_{O2} = 0.51 V for $G7_{Fe3O4}$ and 0.53 V for $G13_{MnO2}$.
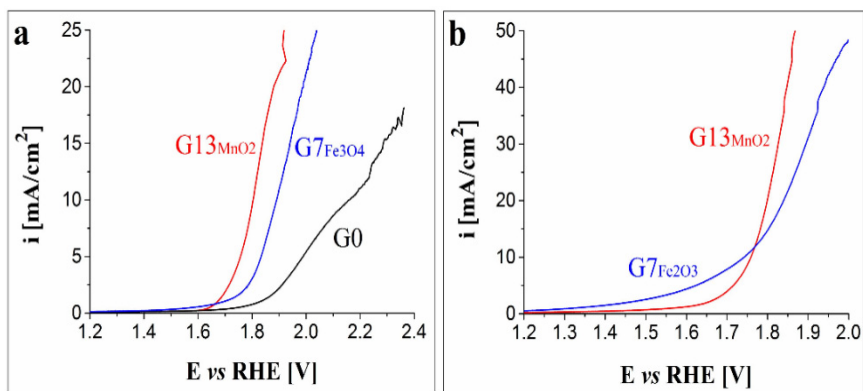
Figure 1. a) LSVs recorded in 0.1M KOH solution on the G0, G7$_{Fe3O4}$ and G13$_{MnO2}$ electrodes. b) LSVs obtained in 1M KOH solution on the G7$_{Fe3O4}$ and G13$_{MnO2}$ electrodes

Because current requirements for materials with OER activity are not limited to the overpotential value, the two modified electrodes were evaluated in terms of other electrochemical characteristics as well. Thus, cyclic voltammetry was employed to estimate their EASA (electroactive surface area) value and the cycles were recorded at different scan rates (v = 100, 150, 200, 250, 300 and 350 mV/s), in 1M KNO$_3$ solution, in the absence and in the presence of 4 mM K$_3$[Fe(CN)$_6$]. Using the acquired data and the Randles-Sevcik equation (presented in the Experimental section), the EASA values were calculated as 0.816 cm^2 for G7$_{Fe3O4}$, 0.45 cm^2 for G13$_{MnO2}$ and 0.388 cm^2 for G0. Since a higher EASA value is indicative of a higher electrocatalytic activity [33], these results point to the improved catalytic properties of the modified electrodes, compared with the unmodified one. **Figures 2a** and **2b** display the plots of the dependence between the peak current densities of the anodic and cathodic peaks of the ferri-/ferrocyanide redox couple and the square root of the scan rate for G7$_{Fe3O4}$ and G13$_{MnO2}$, respectively. The results show that the absolute values of the peak current densities increase with the scan rate, which is characteristic of a diffusion-controlled electron transfer process [34].

The OER kinetics at the interface between the modified electrodes and the electrolyte solution were also investigated. **Figure 2c** introduces the Tafel curves for G7$_{Fe3O4}$ and G13$_{MnO2}$, for which the represented current density values (i$_{EASA}$) were obtained by taking into account the estimated EASA value. The Tafel slopes were calculated using the Tafel equation [35] and were found to be 0.31 and 0.144 V/dec.

The electrochemical stability of the two modified electrodes was evaluated chronoamperometrically by recording i-time curves (**Figures 3a** and **3b**) during six-hour experiments, at the potential values corresponding to i = 10 mA/cm². In the case of the $G7_{Fe3O4}$ electrode the current density did not vary significantly throughout the test. However, the LSVs obtained before and after the investigation (inset in **Figure 3a**) do not overlap entirely. After the test the η_{O2} values corresponding to low i values increased, while the ones correlated with high i values slightly decreased. Thus, at i = 10 mA/cm² η_{O2} became 0.55 V. These differences reflect the stability limitations of the studied electrode.

The current density *vs.* time plot traced during the electrochemical stability test performed on $G13_{MnO2}$ shows that the current density did not vary significantly once it reached 10 mA/cm² (at the 98th minute) and that by the end of the experiment it became 9.55 mA/cm². The inset in **Figure 3b** presents the LSVs from before and after the experiment and they evidence some differences in shape that are more pronounced at high current density values. Following the test, the η_{O2} value at i = 10 mA/cm² slightly changed and became 0.54 V.

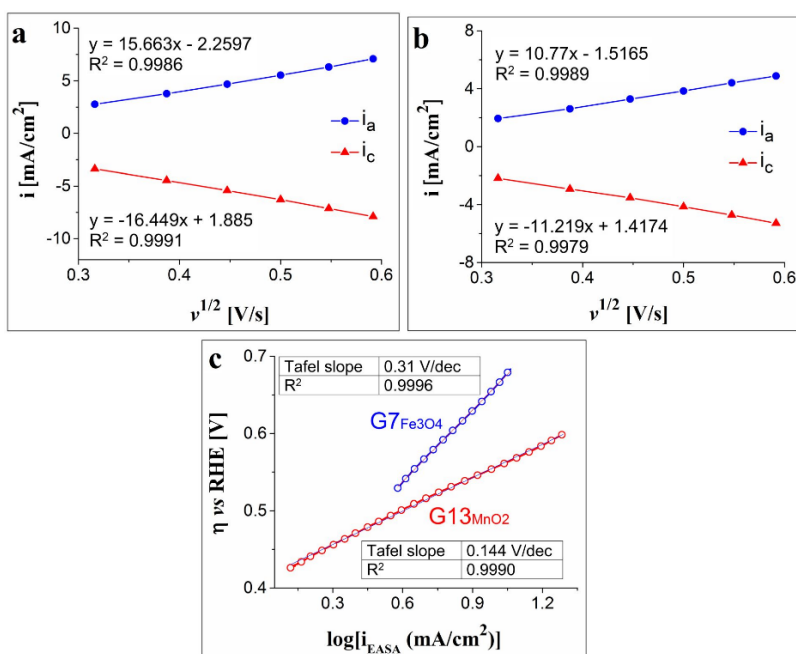**Figure 2.** a) The plots of the anodic and cathodic peak current densities *vs.* the square root of the scan rate (i_a and i_c) for $G7_{Fe3O4}$. b) The plots of the anodic and cathodic peak current densities *vs.* the square root of the scan rate (i_a and i_c) for $G13_{MnO2}$. c) The Tafel plots obtained for $G7_{Fe3O4}$ and $G13_{MnO2}$ in 1M KOH solution
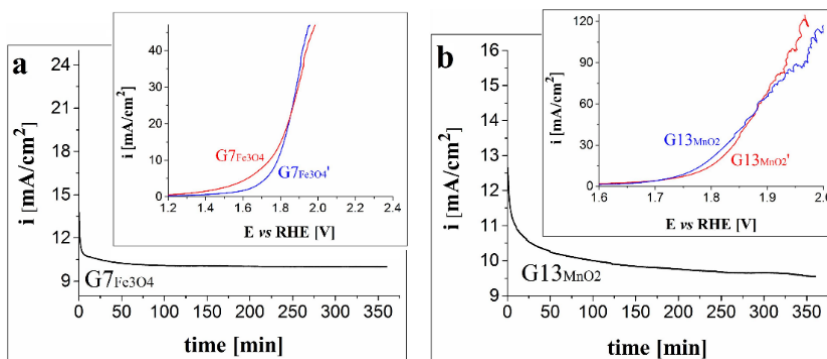
Figure 3. a) The i-time curve obtained on $G7_{Fe3O4}$ in 1M KOH solution and inset with the LSVs from before ($G7_{Fe3O4}$) and after ($G7_{Fe3O4}'$) the stability test. b) The i-time curve recorded on $G13_{MnO2}$ in 1M KOH solution and inset with the LSVs from before ($G13_{MnO2}$) and after ($G13_{MnO2}'$) the stability test

A.2. HER investigations

The LSVs recorded in 0.1M KOH solution during the HER investigations performed on the modified electrodes manufactured using the compositions presented in **Tables 1** and **2** allowed for the identification of the most electrocatalytically active samples (**Figure 4a**). Thus, from the Fe_3O_4-based electrodes $G7_{Fe3O4}$ displayed the lowest η_{H2} value (at i = -10 mA/cm^2) of 0.52 V. In the case of the MnO_2-modified electrodes, the lowest overpotential value was observed for $G11_{MnO2}$ (η_{H2} = 0.62 V). Also, for G0 η_{H2} = 0.74 V.

The two electrodes with the highest HER activity were also investigated in strong alkaline medium and the traced cathodic polarization curves are shown in **Figure 4b**. The increase in KOH concentration led to the decrease of the η_{H2} value ─ at i = -10 mA/cm^2, η_{H2} became 0.43 V for $G7_{Fe3O4}$ and 0.427 V for $G11_{MnO2}$.
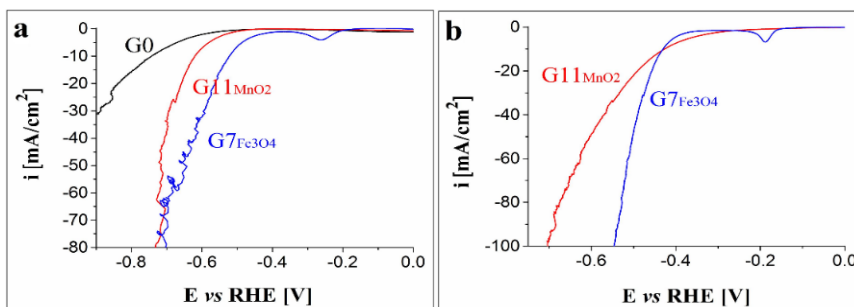
Figure 4. a) LSVs recorded in 0.1M KOH solution on the G0, $G7_{Fe3O4}$ and $G11_{MnO2}$ electrodes. b) LSVs traced in 1M KOH solution on the $G7_{Fe3O4}$ and $G11_{MnO2}$ electrodes

Using the Randles-Sevcik equation and cyclic voltammetry data the EASA value for G11$_{MnO2}$ was estimated as 1.61 cm^2. The graphical representations of the anodic and cathodic peak current densities *vs.* the square root of the scan rate for this modified electrode (**Figure 5a**) indicate a diffusion-controlled electron transfer process. The Tafel plots recorded for G7$_{Fe3O4}$ and G11$_{MnO2}$ in 1M KOH solution are presented in **Figures 5b** and **5c**, and the calculated Tafel slope values are 0.117 and 0.213 V/dec, respectively. Since the former value is in the 0.04 ÷ 0.12 V/dec range, it suggests that the HER taking place on the surface of the G7$_{Fe3O4}$ electrode unfolds according to a Volmer-Heyrovsky mechanism, and the charge transfer rate (the discharge step) is controlled by the desorption step [36,37].

Figure 5. a) The plots of the anodic and cathodic peak current densities *vs.* the square root of the scan rate (i$_a$ and i$_c$) for G11$_{MnO2}$. b) and c) The Tafel plots obtained for G7$_{Fe3O4}$ and G11$_{MnO2}$ in 1M KOH solution. d) The i-time curve recorded on G11$_{MnO2}$ in 1M KOH solution and inset with the LSVs from before (G11$_{MnO2}$) and after (G11$_{MnO2}$') the stability test

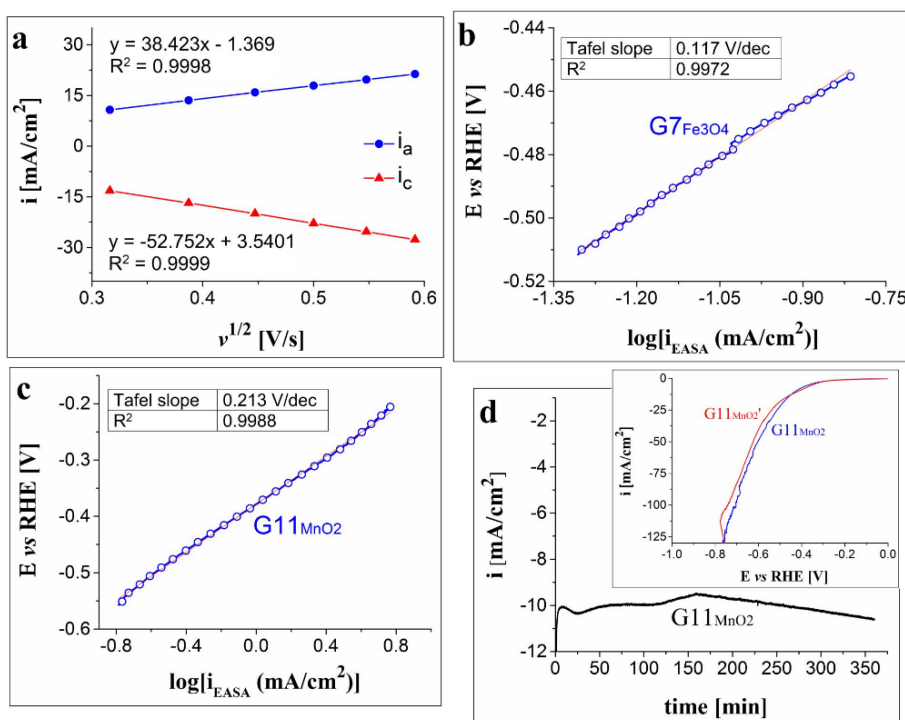The electrochemical stability of the electrodes was also investigated. Regrettably, $G7_{Fe3O4}$ displayed poor stability and because of this it cannot be used efficiently for the HER in alkaline medium. In the case of $G11_{MnO2}$, the chronoamperogram traced during the stability test (**Figure 5d**), by maintaining constant the potential value corresponding to i = -10 mA/cm^2, evidences the relative stability of the electrode. Thus, the current density value varied around -10 mA/cm^2 throughout the experiment. It increased up to -9.5 mA/cm^2 (160th minute) and subsequently decreased down to -10.6 mA/cm^2, at the end of the test. The LSVs obtained before and after the study are inserted in **Figure 5d**. Small differences in shape are observed and the η_{H2} value at -10 mA/cm^2 decreased to 0.414 V – indicating a slight improvement in the catalytic activity of the electrode.

A.3. Further considerations

In general, the OER and HER catalytic activity of a modified electrode is mainly due to structural and transport effects specific to the materials used to modify it [38]. In the case of $G7_{Fe3O4}$, the OER activity was likely the result of the synergistic effect between the materials used to manufacture the electrode – graphite, Fe_3O_4 and Carbon Black - as well as from the quantities of iron oxide and Carbon Black employed to obtain the suspension for substrate modification. The higher the amount of deposited material, the greater the risk that the deposition will organize in the form of thick layers which hinder electrolyte access to the deep pores, leading to a decrease in the electrode's catalytic activity. However, when the deposited amount is too small, the electrode doesn't benefit from enough catalytic material to be efficient. The quantities of 2 mg Fe_3O_4 and 2 mg Carbon Black, utilized to obtain the suspension for the graphite support modification, turned out to be the appropriate amounts amid the ones employed in the present study.

As previously mentioned, the OER catalytic activity of some Fe_3O_4-modified electrodes was investigated by other researchers. For example, Han *et al.* [29] studied the OER on electrodes modified with undoped and Co-doped Fe_3O_4. For the Au electrode modified with undoped Fe_3O_4, the obtained η_{O2} value, at i = 10 mA/cm^2 and in strong alkaline medium (1M NaOH), was ~0.59 V. This value is higher than the one outlined for $G7_{Fe3O4}$, at the same current density and in 1M KOH solution. Another example is the analysis reported by Mirabella *et al.* [30], performed on a glassy carbon electrode modified with undoped and Ni-doped Fe_3O_4 (001). The results obtained on the undoped electrode, in 1M NaOH solution, show that the η_{O2} value is close to 0.6 V even when i = 4 mA/cm^2. Thus, $G7_{Fe3O4}$ is more

catalytically active for the OER than the electrodes manufactured by modifying different conductive substrates with undoped Fe_3O_4. However, this is no longer the case when considering the doped catalytic materials.

Regarding the HER properties of the $G11_{MnO2}$ electrode, while they probably depend to a large extent on structural and transport effects, a couple of observations are worth being mentioned: 1) the high estimated EASA value for this electrode indicates the presence of surface inhomogeneities that generate additional catalytically active sites and can be in the shape of edges or defects [39,40]; 2) the composition used to modify the electrode doesn't contain Carbon Black - the material that increases the electron transfer between the electrode and the electroactive species. The fact that the electrodes modified with compositions containing Carbon Black did not display a HER catalytic activity as good as that observed for $G11_{MnO2}$ could be related to the formation of thick layers during the modification process. Their presence depends on the way in which the materials from the drop-casted suspensions organize at the surface of the conductive substrates. The thick layers prevent the access of the electrolyte solution to the deep pores [41,42], which leads to a decrease in the HER catalytic performance.

Although the water splitting catalytic activity of the $G11_{MnO2}$ electrode is not superior to that of the MnO_2-modified electrodes reported in the scientific literature [24,43], the experimental data contributes to increasing the current understanding concerning the water splitting catalytic properties of MnO_2-based electrodes.

B. Raman analysis

The $G7_{Fe3O4}$, $G11_{MnO2}$ and $G13_{MnO2}$ modified electrodes were characterized by Raman spectroscopy, before and after the chronoamperometric stability test performed during the water splitting experiments. The recorded spectra are presented in **Figures 6** and **7**. In the case of $G7_{Fe3O4}$ (**Figure 6**), it cannot be said that the chemical structure of the materials used to manufacture the electrode changed as a result of the test carried out during the OER investigations. The broad and intense peaks at 1354 and 1597 cm^{-1} probably belong to the conductive carbon present in the combination used to obtain the modified electrode [44], while the peaks at 354, 492, and 700 cm^{-1} can be attributed to the iron oxide [45].

With regard to the $G11_{MnO2}$ and $G13_{MnO2}$ electrodes (**Figures 7a** and **7b**), the spectra recorded after the chronoamperometric experiment are not significantly different from the initial ones, which indicates that the materials used to modify the graphite substrates did not suffer structural changes during the stability testing. In the case of $G11_{MnO2}$, a slight broadening of the

peak at 654 cm^{-1} is observed on the spectrum obtained after the test that can be attributed to sample heating during the Raman analysis. The values at which the peaks identified for the two electrodes appear are similar to those reported in the literature for MnO_2 [46].
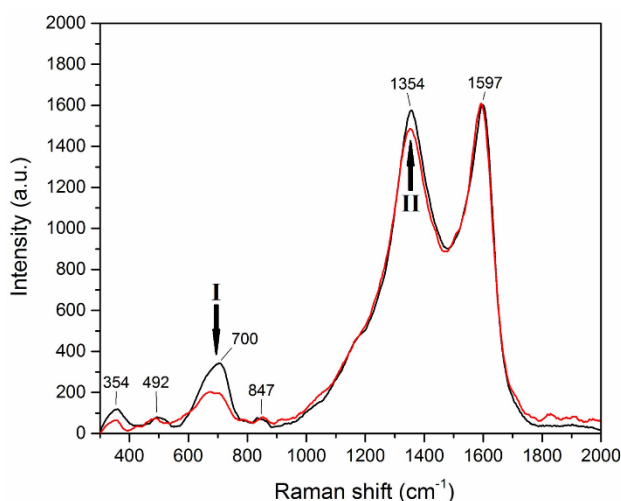

Figure 6. Raman spectra recorded on the G7$_{Fe3O4}$ electrode before the electrochemical stability test (I) and afterwards (II)
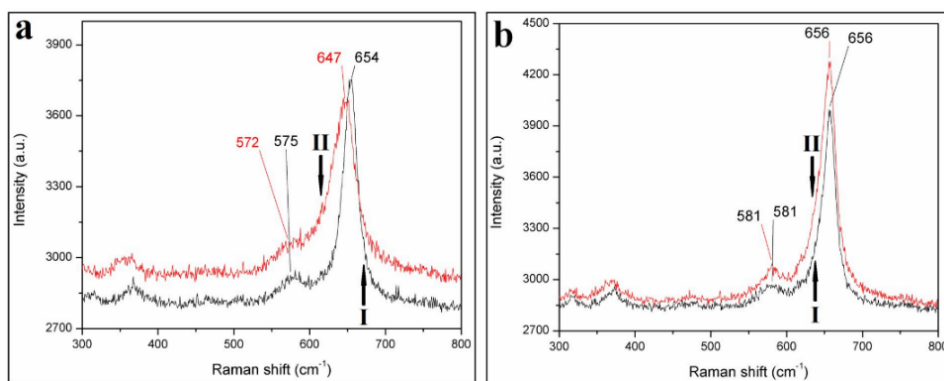

Figure 7. Raman spectra recorded on the G11$_{MnO2}$ (a) and G13$_{MnO2}$ (b) electrodes before the stability test (I) and afterwards (II)

CONCLUSIONS

The water splitting experiments performed in alkaline medium on graphite electrodes modified using suspensions in ethanol containing a transition metal oxide (Fe_3O_4 or MnO_2), as such or in compositions with Carbon Black and/or Nafion solution, have led to the identification of the most catalytically active samples. Out of the iron oxide–based electrodes the most performant was the one labeled $G7_{Fe3O4}$ and it displayed the highest catalytic activity for both O_2 and H_2 evolution reactions. However, the electrochemical stability of this electrode under HER conditions was poor. The main problem with its OER activity is the high Tafel slope value, but its properties can be improved through an optimization process employing a more advanced modification method than drop-casting (such as laser ablation deposition), that will lead to the manufacturing of a more stable sample, having a smaller Tafel slope value.

Regarding the manganese oxide–based electrodes, the best OER activity was observed for $G13_{MnO2}$, while the best HER activity was displayed by $G11_{MnO2}$. In terms of electrochemical stability, the two electrodes were shown to be fairly stable, but an optimization process - focused on deposition method and substrate - is recommended for enhancing their catalytic activity.

EXPERIMENTAL SECTION

Materials and reagents

MnO_2 was synthesized hydrothermally from a mixture of 20 mmol $KMnO_4$, 30 mmol $Mn(NO_3)_2$ and 40 mmol KOH. This mixture was obtained by dissolving each precursor in 20 mL double-distilled water and blending the solutions under continuous stirring, and was transferred into a stainless steel Teflon-lined autoclave. After sealing, the autoclave was placed in an oven at 180 °C. The thermal treatment lasted for 21 hours and was followed by a cooling stage to room temperature. The cooled reaction product was filtered, repeatedly washed with double-distilled water and afterwards with ethanol. The subsequent drying stage lasted for 4 hours at 80 °C.

The synthesis of Fe_3O_4 was also hydrothermal, using 2M NaOH solution and a mixture of $FeCl_3$ x $6H_2O$ and $FeSO_4$ x $7H_2O$ (in 1:2 molar ratio). The precursors were at first dissolved individually in 20 mL volumes of double-distilled water. The mixing took place under continuous stirring and the NaOH solution was added dropwise to the blend, also under stirring. The resulted black suspension was introduced into a stainless steel Teflon-lined

autoclave that was sealed and placed in an oven at 220 ºC, for 5 hours. This stage was followed by cooling at room temperature, after which the reaction product was filtered, washed repeatedly with double-distilled water and then with ethanol, and it was subsequently dried for 4 hours at 80 °C.

The conductive substrate used in the electrode manufacturing process was spectroscopic graphite, type SW.114, from "Kablo Bratislava", National Corporation "Electrocarbon Topolcany" Factory (Slovakia). The MnO_2- and Fe_3O_4-based compositions contained conductive carbon (Carbon Black - Vulcan XC 72 from Fuel Cell Store) and/or Nafion solution (Nafion® 117 solution of 5% concentration from Sigma-Aldrich). Nafion was used as binder to ensure better adhesion between the materials evaluated in terms of their OER and HER catalytic properties and the conductive substrate on which they were deposited. Other reagents used in the study were: KOH, KNO_3, $K_3[Fe(CN)_6]$, 96% C_2H_5OH and $(CH_3)_2CO$, purchased from Sigma-Aldrich, Merck and Chimreactiv. All solutions were obtained using laboratory produced double-distilled water.

Manufacturing of the modified electrodes

Modification of the graphite support with electrocatalytic materials was performed via the drop-casting method. Specifically, by applying droplets from ethanol suspensions prepared by dispersing the MnO_2, Fe_3O_4 and the compositions containing them in 0.5 mL ethanol. After 30 minutes ultrasonication, volumes of 10 µL were prelevated from the suspensions and were applied on the graphite surfaces. This was followed by solvent evaporation at 50 °C and the resulted electrodes were kept at room temperature until their experimental use. Ethanol was employed in the obtaining of the suspensions in part because it is used for this purpose in reported studies investigating the OER and HER properties of MnO_2-based electrodes [22,24,43], but also because it led to an improved dispersion of the Carbon Black particles, considering their hydrophobic nature. **Tables 1** and **2** present the labels used to refer to the modified electrodes, as well as the compositions of the suspensions from which they were obtained.

An electrochemical assembly consisting of a glass cell equipped with three electrodes, connected to a Voltalab PGZ 402 potentiostat (Radiometer Analytical) was employed to perform the electrochemical investigations on the modified electrodes. The counter electrode was a Pt plate ($S_{geom} = 0.8$ cm^2) and the Ag/AgCl electrode (sat. KCl) was used as reference. The unmodified graphite electrode (labeled G0) and the electrodes labeled according to **Tables 1** and **2** were each used as the working electrode ($S_{geom} = 0.28$ cm^2).

Table 1. The labels for the Fe_3O_4-based modified electrodes
and the compositions of the suspensions used to obtain them

Electrode label	Fe_3O_4 powder [mg]	Carbon Black powder [mg]	Nafion solution [μL]
G1$_{Fe3O4}$	2	-	-
G2$_{Fe3O4}$	4	-	-
G3$_{Fe3O4}$	6	-	-
G4$_{Fe3O4}$	2	1	-
G5$_{Fe3O4}$	4	1	-
G6$_{Fe3O4}$	6	1	-
G7$_{Fe3O4}$	2	2	-
G8$_{Fe3O4}$	4	2	-
G9$_{Fe3O4}$	6	2	-
G10$_{Fe3O4}$	2	-	10
G11$_{Fe3O4}$	4	-	10
G12$_{Fe3O4}$	6	-	10
G13$_{Fe3O4}$	2	1	10
G14$_{Fe3O4}$	4	1	10
G15$_{Fe3O4}$	6	1	10
G16$_{Fe3O4}$	2	2	10
G17$_{Fe3O4}$	4	2	10
G18$_{Fe3O4}$	6	2	10

Table 2. The labels for the MnO_2-based modified electrodes
and the compositions of the suspensions used to obtain them

Electrode label	MnO_2 powder [mg]	Carbon Black powder [mg]	Nafion solution [μL]
G1$_{MnO2}$	2	-	-
G2$_{MnO2}$	4	-	-
G3$_{MnO2}$	6	-	-
G4$_{MnO2}$	2	1	-
G5$_{MnO2}$	4	1	-
G6$_{MnO2}$	6	1	-
G7$_{MnO2}$	2	2	-
G8$_{MnO2}$	4	2	-
G9$_{MnO2}$	6	2	-
G10$_{MnO2}$	2	-	10
G11$_{MnO2}$	4	-	10
G12$_{MnO2}$	6	-	10
G13$_{MnO2}$	2	1	10
G14$_{MnO2}$	4	1	10
G15$_{MnO2}$	6	1	10
G16$_{MnO2}$	2	2	10
G17$_{MnO2}$	4	2	10
G18$_{MnO2}$	6	2	10

The graphite supports were in the shape of rods inserted in polyethylene tubes that were sealed to them through heat treatment at 180 °C. One of the ends of each rod was polished with silicon carbide paper (grit sizes: 600, 800

and 1200, respectively) and felt, subsequently washed with water, ethanol and acetone, and dried at room temperature. During the experiments, the polished rod end was immersed into the electrolyte solution, as such or after modification with the catalytic materials, while the other end was connected to the potentiostat.

The values of the electrochemical potential (E) are expressed in terms of the reversible hydrogen electrode (RHE) using Equation (1), the values of the OER overpotential were calculated with Equation (2) [47], and those of the HER overpotential with Equation (3).

$$E_{RHE}\ [V] =\ E_{Ag/AgCl(sat.\ KCl)} + 0.059 \times pH + 0.197 \qquad (1)$$
$$\eta_{O2}\ [V] = E_{RHE} - 1.23 \qquad (2)$$
$$\eta_{H2}\ [V] = |E_{RHE}| \qquad (3)$$

Where: E_{RHE} = the potential of the Reversible Hydrogen Electrode [V], $E_{Ag/AgCl(sat.\ KCl)}$ = the potential of the Ag/AgCl (sat. KCl) electrode [V], η_{O2} and η_{H2} are the OER and HER overpotentials [V].

The current density values (i) referred to in the study are geometric current densities, unless otherwise specified. The OER and HER investigations were performed by recording iR-corrected linear sweep voltammograms (LSVs), at v = 5 mV/s, in 0.1M and 1M KOH electrolyte solutions. For the HER measurements the electrolyte solutions were deaerated with N_2.

The electroactive surface area (EASA) of the most catalytically active electrodes was estimated using Equation (4) - the Randles-Sevcik equation [48,49] - together with cyclic voltammetry data obtained at different scan rates in 1M KNO_3 solution, in the absence and presence of 4 mM $K_3[Fe(CN)_6]$.

$$I_p =\ (2.69\ \times 10^5) \times n^{3/2} \times A \times D^{1/2} \times C \times v^{1/2} \qquad (4)$$

Where: I_p = peak current [A]; n = number of electrons involved in the redox process at T = 298 K; A = working electrode surface [cm^2]; D = diffusion coefficient of the electroactive species [cm^2/s]; C = concentration of the electroactive species [M] and v = scan rate [V/s]. For the ferrocyanide/ferricyanide redox couple n = 1 and the theoretical value of D = 6.7 x 10^{-6} cm^2/s [50].

Raman spectroscopy analysis

The most catalytically performant electrodes identified during the OER and HER studies were analyzed by Raman spectroscopy, using a MultiView-2000 system from Nanonics Imaging Ltd. (Israel), equipped with a

Shamrock 500i spectrograph from ANDOR (UK). The analyses were performed at room temperature, with a 50x objective, using as excitation source a laser radiation with λ = 514.5 nm and an exposure time of 20s.

ACKNOWLEDGMENTS

REFERENCES

1. M. F. Sapountzi; M. J. Gracia; C. J. Weststrate; O. A. H. Fredriksson; J. W. Niemantsverdriet; *Prog. Energy Combust. Sci.*, **2017**, *58*, 1-35.
2. S. Wang; A. Lu; C.-J. Zhong; *Nano Converg.*, **2021**, *8*, 1-23.
3. N. Dubouis; A. Grimaud; *Chem. Sci.*, **2019**, *10*, 9165-9181.
4. L. Li; P. Wang; Q. Shao; X. Huang; *Chem. Soc. Rev.*, **2020**, *49*, 3072–3106.
5. D. Yao; L. Gu; B. Zuo; S. Weng; S. Deng; W. Hao; *Nanoscale*, **2021**, *13*, 10624-1064.
6. Q. Tang; D. Jiang; *ACS Catal.*, **2016**, *6*, 4953−4961.
7. M. I. Jamesh; *J. Power Sources*, **2016**, *333*, 213-236.
8. R. L. Doyle; M. E. G. Lyons; *Phys. Chem. Chem. Phys.*, **2013**, *15*, 5224-5237.
9. S. K. Ghosh; H. Rahaman; Noble metal–manganese oxide hybrid nanocatalysts, in *Noble Metal-Metal Oxide Hybrid Nanoparticles. Fundamentals and Applications. Micro and Nano Technologies*, S. Mohapatra, T. A. Nguyen, P. Nguyen-Tri Eds.; Woodhead Publishing, Sawston, UK, **2019**, Chapter 16, pp. 313-340.
10. I. Concina; Z. H. Ibupoto; A. Vomiero; *Adv. Energy Mater.*, **2017**, *7*, 1-29.
11. M. Chhetri; S. Sultan; C. N. R. Rao; *PNAS*, **2017**, *114*, 8986-8990.
12. P. W. Menezes; C. Panda; S. Loos; F. Bunschei-Bruns; C. Walter; M. Schwarze; X. Deng; H. Dau; M. Driess; *Energy Environ. Sci.*, **2018**, *11*, 1287-1298.
13. W. Li; D. Xiong; X. Gao; L. Liu; *Chem. Commun.*, **2019**, *55*, 8744-8763.
14. T. Priamushko; R. Guillet-Nicolas; F. Kleitz; *Inorganics*, **2019**, *7*, 1-21.
15. P. Xiao; W. Chen; X. Wang; *Adv. Energy Mater.*, **2015**, *5*, 1-13.
16. M. Zeng; Y. Li; *J. Mater. Chem. A*, **2015**, *3*, 14942-14962.
17. J. Li; J. Li; X. Zhou; Z. Xia; W. Gao; Y. Ma; Y. Qu; *ACS Appl. Mater. Interfaces*, **2016**, *8*, 10826–10834.
18. X. Wang; W. Li; D. Xiong; D.Y. Petrovykh; L. Liu; *Adv. Funct. Mater.*, **2016**, *26*, 4067–4077.
19. S. Ghosh; R. N. Basu; *Nanoscale*, **2018**, *10*, 11241-11280.
20. J. Melder; P. Bogdanoff; I. Zaharieva; S. Fiechter; H. Dau; P. Kurz; *Z. fur Phys. Chem.*, **2020**, *234*, 925–978.

21. Y. Meng; W. Song; H. Huang; Z. Ren; S.-Y. Chen; S.L. Suib; *J. Am. Chem. Soc.*, **2014**, *136*, 11452–11464.
22. R. Pokhrel; M. K. Goetz; S. E. Shaner; X. Wu; S. Stahl; *J. Am. Chem. Soc.*, **2015**, *137*, 8384–8387.
23. F. Speck; P. Santori; F. Jaouen; S. Cherevko; *J. Phys. Chem.*, **2019**, *123*, 25267–25277.
24. Y. Zhao; C. Chang; F. Teng; Y. Zhao; G. Chen; R. Shi; G. I. N. Waterhouse; W. Huang; T. Zhang; *Adv. Energy Mater.*, **2017**, *7*, 1-7.
25. M. Mullner; M. Riva; F. Kraushofer; M. Schmid; G. S. Parkinson; S. F. L. Mertens; U. Diebold; *J. Phys. Chem.*, **2019**, *123*, 8304–8311.
26. R. Phul; M. A. M. Khan; M. Sardar; J. Ahmed; T. Ahmad; *Crystals*, **2020**, *10*, 1-14.
27. R. H. Tammam; A. M. Fekry; M. M. Saleh; *Korean J. Chem. Eng.*, **2019**, *36*, 1932-1939.
28. M. B. Askari; A. Beheshti-Marnani; M. Seifi; S. M. Rozatia; P. Salarizadeh; *J. Colloid Interface Sci.*, **2019**, *537*, 186-196.
29. S. Han; S. Liu; S. Yin; L. Chen; Z. He; *Electrochim. Acta*, **2016**, *210*, 942-949.
30. F. Mirabella; M. Müllner; T. Touzalin; M. Riva; Zdenek Jakub; F. Kraushofer; Michael Schmid; M.T.M. Koper; G.S. Parkinson; U. Diebold; *Electrochim. Acta*, **2021**, *389*, 1-11.
31. J. Yang; Q. Shao; B. Huang; M. Sun; X. Huang; i*Science*, **2019**, *11*, 492-504.
32. V. Mani; S. Anantharaj; S. Mishra; N. Kalaiselvi; S. Kundu; *Catal. Sci. Technol.*, **2017**, *7*, 5092–5104.
33. I. Barauskien; E. Valatka; *Mater. Renew. Sustain. Energy*, **2018**, *7*, 1-10.
34. I. Sebarchievici; B.-O. Taranu; M. Birdeanu; S. F. Rus; E. Fagadar-Cosma; *Appl. Surf. Sci.*, **2016**, *39*, 131-140.
35. B.-O. Taranu; M. G. Ivanovici; P. Svera; P. Vlazan; P. Sfirloaga; M. Poienar; *J. Alloys Compd.*, **2020**, *848*, 1-11.
36. Z.-Y. Wu; B.-C. Hu; P. Wu; H.-W. Liang; Z.-L. Yu; Y. Lin; Y.-R. Zheng; Z. Li; S.-H. Yu; *NPG Asia Mater.*, **2016**, *8*, 1-8.
37. X. Wang; YV Kolen'ko; X.-Q. Bao; K. Kovnir; L. Liu; *Angew. Chem. Int. Ed.*, **2015**, *54*, 8188–8192.
38. Z. Liu; H. Tan; D. Liu; X. Liu; J. Xin; J. Xie; M. Zhao; L. Song; L. Dai; H. Liu; *Adv. Sci.*, **2019**, *6*, 1-11.
39. H. Wang; H.-W. Lee; Y. Deng; Z. Lu; P.-C. Hsu; Y. Liu; D. Lin; Y. Cui; *Nat. Comm.*, **2015**, *6*, 1-8.
40. Y. Li; H. Wang; L. Xie; Y. Liang; G. Hong; H. Dai; *J. Am. Chem. Soc.*, **2011**, *133*, 7296–7299.
41. A. Lahiri; G. Li; F. Endres; *J. Solid State Electrochem.*, **2020**, *24*, 2763–2771.
42. I. Boshnakova; E. Lefterova; E. Slavcheva; *Int. J. Hydrog. Energy*, **2018**, *43*, 16897-16904.
43. H. Begum; M. S. Ahmed; S. Jeon; *Electrochim. Acta*, **2019**, *296*, 235-242.
44. R. Hatel; S. E. Majdoub; A. Bakour; M. Khenfouch; M. Baitoul; *IOP Conf. Series: Journal of Physics: Conf. Series*, **2018**, *1081*, 1-7.
45. C. Guo; Y. Hu; H. Qian; J. Ning; S. Xu; *Mater. Charact.*, **2011**, *62*, 148-151.

46. B. Yin; S. Zhang; H. Jiang; F. Qu; X. Wu; *J. Mater. Chem. A*, **2015**, *3*, 5722-5729.
47. Z. Zhao; H. Wu; H. He; X. Xu; Y. Jin; *J. Mater. Chem. A*, **2015**, *3*, 7179-7186.
48. A. Baciu; A. Remes; E. Ilinoiu; F. Manea; S.J. Picken; J. Schoonman; Environm. *Eng. Manag. J.*, **2012**, *11*, 239-246.
49. E.C. Ilinoiu; F. Manea; P.A. Serra; R. Pode; *Sensors*, **2013**, *13*, 7296-7307.
50. M. Yang; Y. Yang; Y. Liu; G. Shen; R. Yu; *Biosens. Bioelectron.*, **2006**, *21*, 1125–1131.

CONTRIBUTIONS TO THE STUDY OF COSMETIC EMULSIONS USING ANALYTICAL – EXPERIMENTAL MATHEMATICAL MODELS

ELENA ADELA MANEA[a], MARIA DELIA PERJU[a], ANDRA TĂMAŞ[a*]

ABSTRACT. The quality of a cosmetic cream is evaluated by classical methods in specific authorized laboratories by periodically measuring the physico-chemical and microbiological quality indicators of the basic emulsions. This paper aims to use systems theory to study cosmetic emulsions by establishing mathematical models that correlate the existing dependencies between different quality indicators. The main parameters that allow the quantification of the stability of the emulsions were monitored in time: the evaporation residue, the pH, the total number of germs, staphylococcus aureus, pseudomonas aeruginosa and the concentration of the active ingredients. Mathematical models were obtained with adequacy indicators that meet the requirements of a good approximation and that can be used as models for control and prediction of stability in the short and medium term, for the types of creams based on the recipes of the emulsions studied.

Keywords: emulsion, quality indicator of cosmetic creams, mathematical model

INTRODUCTION

There is little research in the literature on the use of systems theory and mathematical modeling techniques to characterize cosmetic emulsions. [1,2].

Cosmetic emulsions are heterogeneous dispersed mixtures consisting of two or more immiscible liquids dispersed in each other in the form of droplets, whose diameter is between 0.1 - 100 μm. Emulsions can be simple - U / A (oil in water) or A / U (water in oil), or multiple - U / A / U (U / A emulsion is dispersed in another oily phase) or A / U / A (A / U emulsion is dispersed in another aqueous phase) [3-6].

---

[a] *Politehnica University Timisoara, Faculty of Industrial Chemistry and Environmental Engineering, 6 V. Pârvan Bd., RO-300223, Timisoara, Romania.*
* *Corresponding author: andra.tamas@upt.ro.*

The main property of a cosmetic emulsion that provides a high quality is the stability (chemical, physical and rheological) both in the manufacturing phase and in storage and use. In accordance with the legal rules of national and international law, stability is quantified by the values of specific quality indicators. These are: weight loss (evaporation residue), pH, viscosity, concentration of active ingredients, total number of germs, pseudomonas aeruginosa, staphylococus aureus, yeasts and molds [3-6].

In general, the mathematical model of a system (in this case the cosmetic emulsion) is a set of mathematical relations, equations and inequalities, which characterize and describe the interdependencies between output and input variables, and the limitations imposed for their validity and values [7,8,9].

Figure 1 shows the cosmetic emulsion as a system with input variables, output variables and perturbations [10].
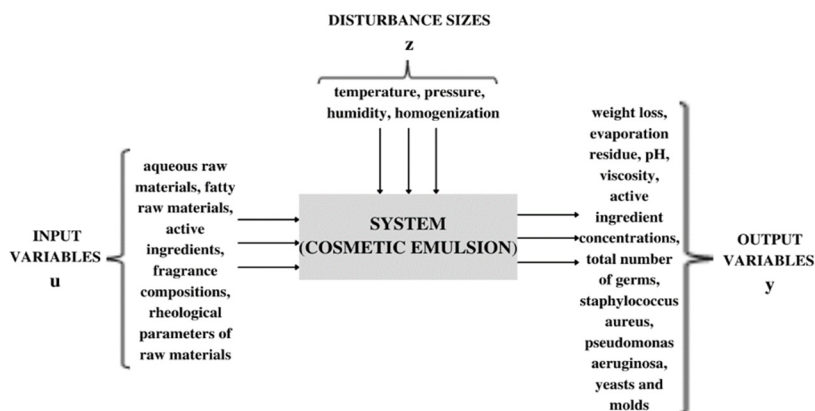

Figure 1. Representation of the cosmetic emulsion as a system

Cosmetic emulsions can present instability phenomena especially during storage, from physico-chemical, mechanical or visual changes of the component substances, to the appearance or presence of microorganisms and bacteria in the finished products. The experimental determinations were performed in a specialized laboratory over four years by analyzing four cosmetic emulsions.

The data obtained were used to generate 3D graphical representations and mathematical equations that are in fact analytical-experimental models. Based on these models, relevant conclusions were drawn on the existing dependencies between different quality indicators that have a major influence on the properties of the studied emulsions. From the point of view of the efficiency of the study, it should be noted its practical importance, which allows specifying the optimal values of physico-chemical parameters required both in manufacturing technology, storage and during use after opening bottles for sale, to ensure the best quality indicators.

The use of determined analytical-experimental mathematical models can replace the classical monitoring of the parameters characteristic of cosmetic emulsions, as well as allow predictions for the optimal values of quality indicators, which will ensure the physico-chemical and microbiological stability of creams.

In this paper, the analytical-experimental mathematical models that define the time dependencies between different physico-chemical and microbiological quality indicators using the database obtained for 4 years for four cosmetic emulsions were determined and verified.

RESULTS AND DISCUSSION

The results of the study performed for the 4 emulsions are presented in the form of sets of graphs in 3D format (figures 2 - 25), of some tables with mathematical expressions that represent the analytical-experimental models (tables 1, 3, 6, 8, 11,13), of some tables in which the values of the adequacy indicators are presented (tables 2, 4, 7, 9, 12, 14) and the tables with the calculated absolute errors (tables 5, 10, 15). The notations used are as follows: evaporation residue - RE (%), total number of germs - NTG (NTG / ml), pH, time - T (months) - T notation according to ISO 80000-1: 2009, error absolute - E (%).

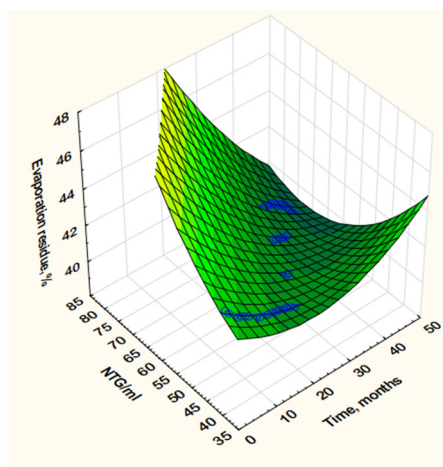### I. a. Dependence of evaporation residue RE of time T and total number of germs NTG

Figure 2 – EMULSION 1   **Figure 3** – EMULSION 2

Figure 4 – EMULSION 3   **Figure 5** – EMULSION 4

Table 1. Equations of mathematical models

Emulsion 1	RE = 44.3772+ 0.1506·T - 0.1773·NTG + 0.0032·T^2 - 0.008·T·NTG + 0.004·NTG^2
Emulsion 2	RE = 37.2398+0.0096·T + 0.068·NTG + 0.0013·T^2- 0.0023·T·NTG +5.2477E $^{-5}$·NTG^2
Emulsion 3	RE = 35.0866 - 0.1323·T - 0.0689·NTG + 0.0041·T^2 - 0.0034·T·NTG + 0.0013·NTG^2
Emulsion 4	RE = 34.7813 - 0.2796·T + 0.013·NTG - 0.0037·T^2 + 0.0055·T·NTG - 0.0015·NTG^2

Table 2. Adequacy indicators

Adequacy indicators	Emulsion 1	Emulsion 2	Emulsion 3	Emulsion 4
Dispersion, σ^2	0.04270	0.00354	0.03110	0.04107
Standard deviation, σ	0.20664	0.05950	0.17635	0.20266
Model accuracy indicator, R^2	0.96191	0.98318	0.99191	0.99419
Correlation coefficient, R	0.98077	0.99155	0.99594	0.99709

I. b. Dependence of residue on evaporation RE of time T and pH
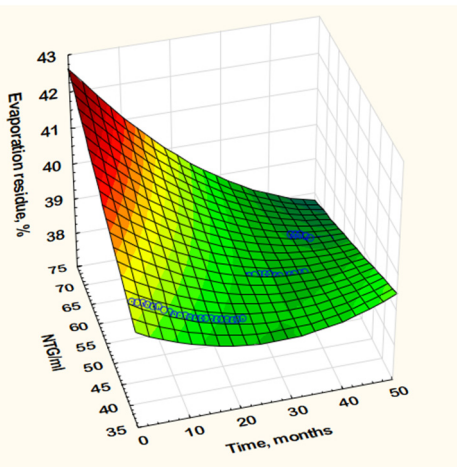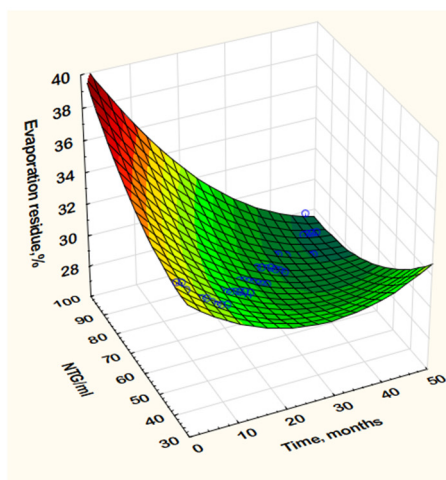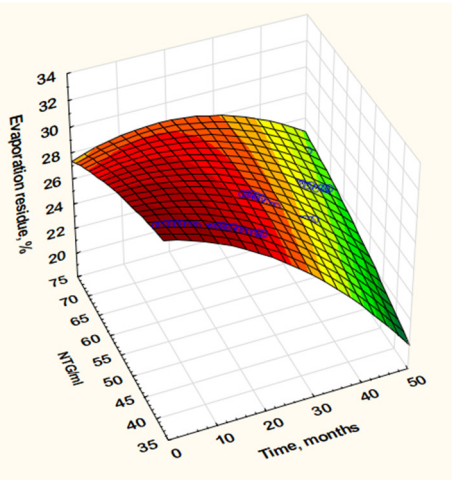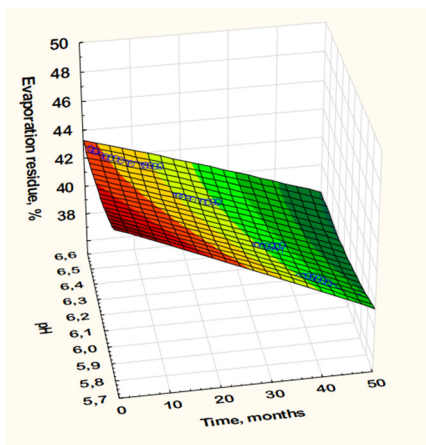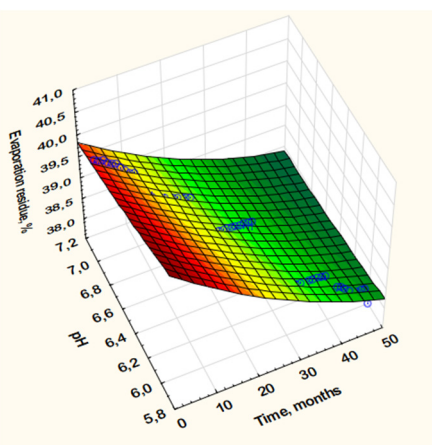

Figure 6 – EMULSION 1
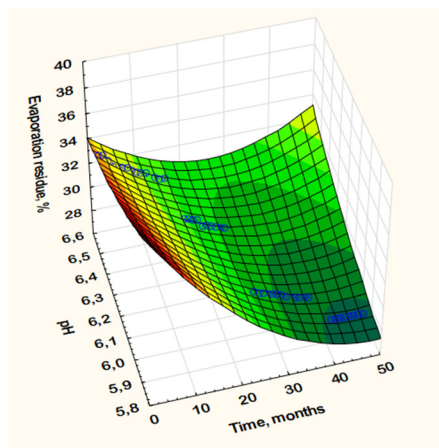

Figure 7 – EMULSION 2

Figure 8 – EMULSION 3
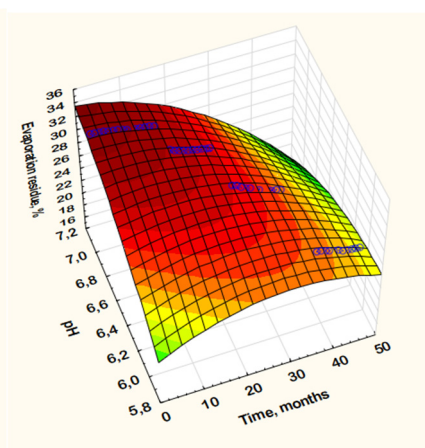
Figure 9 – EMULSION 4

Table 3. Equations of mathematical models

Emulsion 1	RE = 176.1746 - 0.3555·T - 39.2725·pH - 0.0002·T^2 + 0.0391·T·pH + 2.8993· pH^2
Emulsion 2	RE = 48.8903 - 0.1232·T - 1.9672·pH + 0.0005· T^2 + 0.0085·T·pH + 0.0983· pH^2
Emulsion 3	RE = 235.6246 - 2.154·T - 57.3014·pH + 0.0051·T^2 + 0.285·T·pH + 4.0552·pH^2
Emulsion 4	RE = -199.2458 + 2.087·T + 61.4851·pH - 0.0057· T^2 - 0.3003·T·pH - 4.0488· pH^2

Table 4. Adequacy indicators

Adequacy indicators	Emulsion 1	Emulsion 2	Emulsion 3	Emulsion 4
Dispersion, σ^2	0.03909	0.00994	0.02411	0.04825
Standard deviation, σ	0.19771	0.09975	0.15527	0.21966
Model accuracy indicator, R^2	0.96513	0.95275	0.99372	0.99302
Correlation coefficient, R	0.98241	0.97609	0.99685	0.99658

Table 5. Absolute model errors

EMULSIONS	T, [months]	RE measured, [%]	RE calculated according to T and NTG, [%]	Error absolute of the model [%]	RE calculated according to T and pH, [%]	Error absolute of the model [%]
EMULSION 1	1	43.66	43.52	0.32	43.30	0.83
	48	39.18	39.67	1.24	39.29	0.28
EMULSION 2	1	39.92	39.96	0.10	39.87	0.12
	48	37.90	37.98	0.21	38.35	1.17
EMULSION 3	1	34.20	34.41	0.61	34.19	0.03
	48	27.83	27.97	0.50	27.78	0.18
EMULSION 4	1	32.83	32.84	0.03	32.74	0.27
	48	24.98	24.88	0.40	24.46	2.13

Based on the analysis of the 3D graphical representations (figures 2-9) and the equations that constitute the mathematical models obtained (tables 1,3) it is found that in a percentage of 75% the evaporation residue (RE) decreases during the 48 months.

II. a. Dependence of the total number of NTG germs of time T and the evaporation residue RE
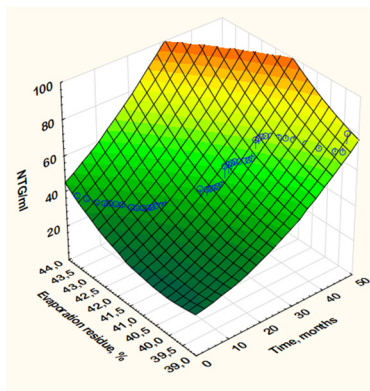
Figure 10 – EMULSION 1   **Figure 11** – EMULSION 2
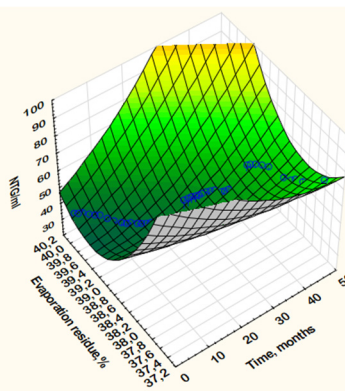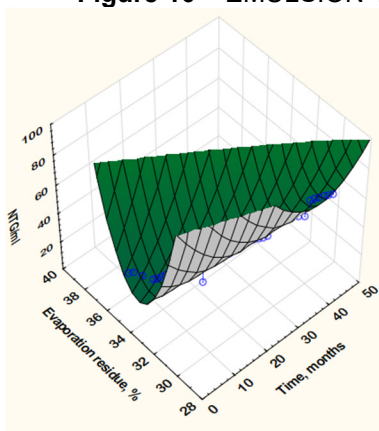
Figure 12 – EMULSION 3   **Figure 13** – EMULSION 4
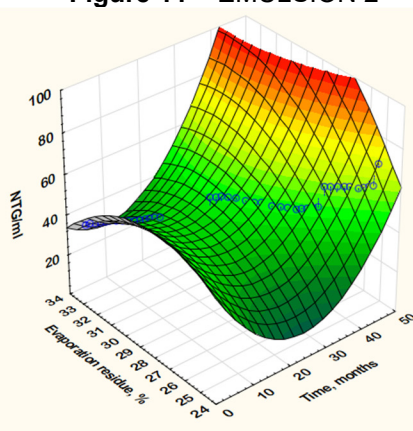
Table 6. Equations of mathematical models

Emulsion 1	NTG = 2621.5113-7.3024·T -129.4987·RE+0.0155·T^2 +0.1949·T ·RE+1.6122·RE^2
Emulsion 2	NTG = 30338.1503-41.89·T -1537.6807·RE+0.0203·T^2 +1.0702·T ·RE+19.5066·RE^2
Emulsion 3	NTG = 7410.9918-53.7877·T -445.2677·RE+0.1036·T^2+1.6602·T ·RE+6.7152·RE^2
Emulsion 4	NTG = -507.7135-7.7856·T +41.0303·RE+0.0696·T^2 +0.1879·T ·RE-0.7384·RE^2

Table 7. Adequacy indicators

Adequacy indicators	Emulsion 1	Emulsion 2	Emulsion 3	Emulsion 4
Dispersion, σ^2	8.62415	6.84058	9.43264	5.06467
Standard deviation, σ	2.93669	2.61545	3.07126	2.25026
Model accuracy indicator, R^2	0.95115	0.90311	0.97126	0.92828
Correlation coefficient, R	0.97580	0.95032	0.98552	0.96347

II.b. Dependence on the total number of NTG germs of time T and pH
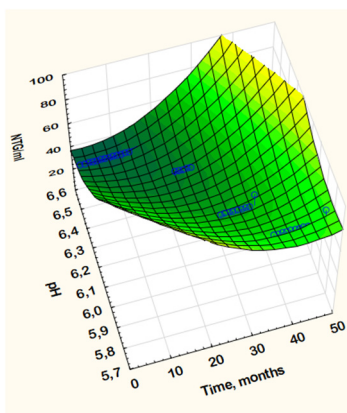
Figure 14 – EMULSION 1   **Figure 15** – EMULSION 2
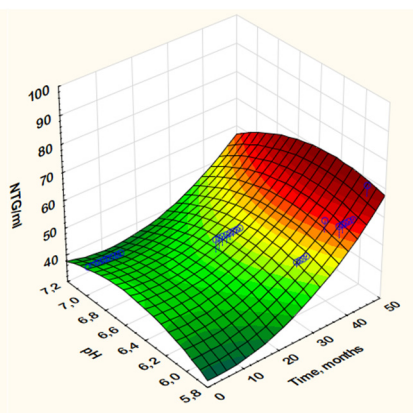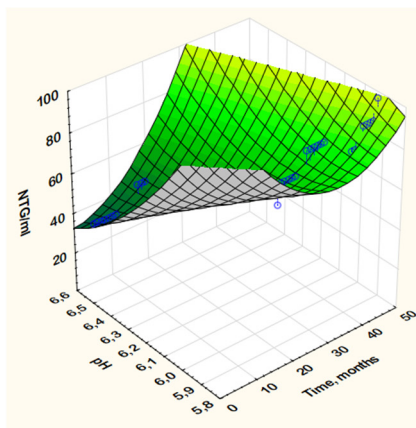
Figure 16 – EMULSION 3   **Figure 17** – EMULSION 4
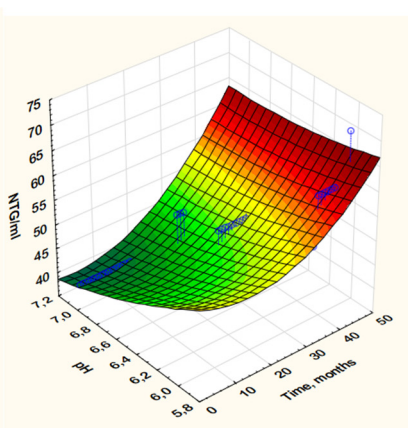
Table 8. Equations of mathematical models

Emulsion 1	NTG = 5570.2525 - 29.9381·T - 1645.7096·pH + 0.0524·T^2 + 4.4981·T·pH +122.3123·pH^2
Emulsion 2	NTG = -613.0804+1.231·T + 198.1065·pH + 0.0153·T^2 - 0.2238·T·pH - 14.9611·pH^2
Emulsion 3	NTG = 4368.8048 - 32.6311·T - 1258.3122·pH + 0.0591 T^2 + 4.9779·T·pH + 91.108 pH^2
Emulsion 4	NTG = 229.291 - 1.2878·T - 46.0972·pH + 0.012·T^2 + 0.1645·T·pH + 2.7219·pH^2

Table 9. Adequacy indicators

Adequacy indicators	Emulsion 1	Emulsion 2	Emulsion 3	Emulsion 4
Dispersion, σ^2	9.43602	6.50852	9.2884	6.63279
Standard deviation, σ	3.07181	2.55118	3.04770	2.57542
Model accuracy indicator, R^2	0.94769	0.90782	0.97170	0.90605
Correlation coefficient, R	0.97349	0.95279	0.98575	0.95187

Table 10. Absolute model errors

EMULSIONS	T, [months]	NTG /ml read	NTG/ml calculated according to T and RE	Error absolute of the model [%]	NTG/ml calculated according to T and pH	Error absolute of the model [%]
EMULSION 1	1	40	41.99	4.74	40.19	0.47
	48	80	74.33	7.63	75.69	5.69
EMULSION 2	1	40	40.63	1.55	40.25	0.62
	48	70	62.49	12.01	65.91	6.21
EMULSION 3	1	40	40.30	0.74	38.87	2.90
	48	100	94.82	5.46	95.85	4.33
EMULSION 4	1	40	41.91	4.56	39.86	0.35
	48	70	68.41	2.32	63.91	9.53

Analyzing 3D graphical representations (figures 10-17) and the equations of the obtained mathematical models (tables 6,8) it is observed that the total number of germs (NTG) increases in proportion of 85% starting from the end of the second year, but remaining in the optimal parameters and during the third.

III.a. pH dependence of time T and evaporation residue RE
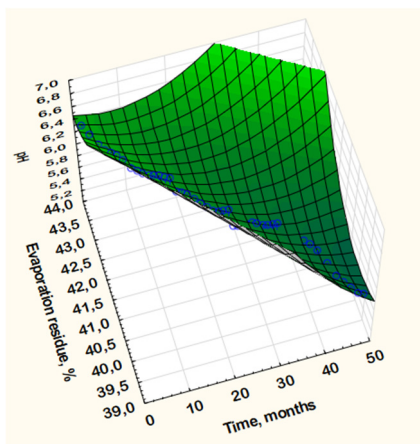
Figure 18 – EMULSION 1   **Figure 19** – EMULSION 2
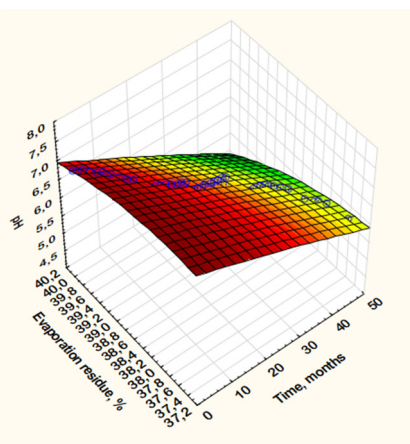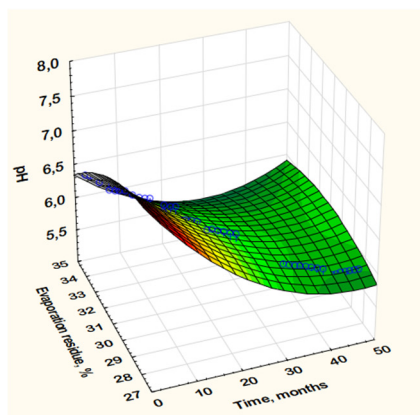
Figure 20– EMULSION 3   **Figure 21** – EMULSION 4
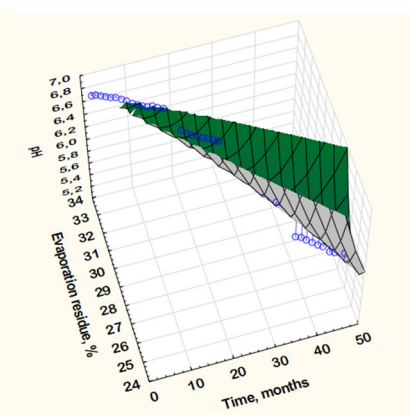
Table 11. Equations of mathematical models

Emulsion 1	pH = 347.7165 - 1.3413·T - 15.4457·RE + 0.0012·T^2 + 0.03·T·RE + 0.1748·RE^2
Emulsion 2	pH = -152.9027 + 0.155·T + 8.5343·RE - 7.9467E-5·T^2 - 0.005·T·RE - 0.1134·RE^2
Emulsion 3	pH = -0.977 - 0.1649·T + 0.6813·RE + 0.0008·T^2 + 0.0033·T·RE - 0.0135·RE^2
Emulsion 4	pH = 318.0388 - 3.043·T - 18.8037·RE + 0.007·T^2 + 0.0918·T·RE + 0.2842·RE^2

Table 12. Adequacy indicators

Adequacy indicators	Emulsion 1	Emulsion 2	Emulsion 3	Emulsion 4
Dispersion, σ^2	0.00304	0.01055	0.00407	0.00904
Standard deviation, σ	0.05520	0.10270	0.06382	0.09506
Model accuracy indicator, R^2	0.96377	0.94496	0.93233	0.93956
Correlation coefficient, R	0.98172	0.97209	0.96557	0.96931

III.b. pH dependence of time T and total number of germs NTG
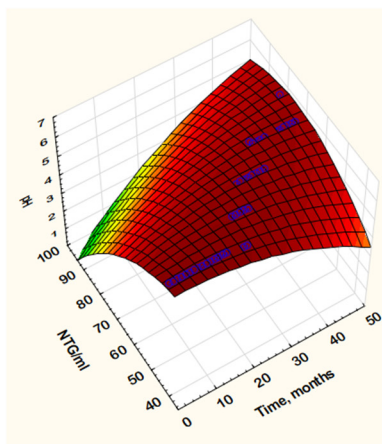
Figure 22 – EMULSION 1
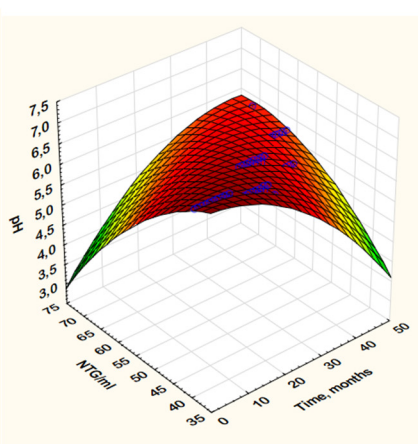
Figure 23 – EMULSION 2
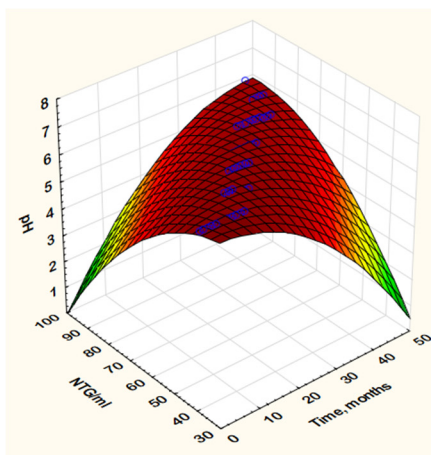
Figure 24 – EMULSION 3
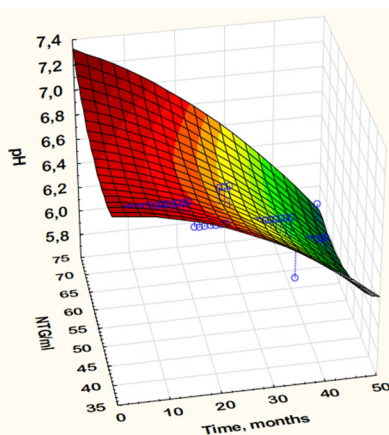
Figure 25 – EMULSION 4

Table 13. Equations of mathematical models

Emulsion 1	pH = 6.2524 - 0.0983·T + 0.0586·NTG - 0.0014·T^2 + 0.0029·T·NTG - 0.0013·NTG^2
Emulsion 2	pH = 6.8415 - 0.1246·T + 0.0687·NTG - 0.0013·T^2 + 0.0033·T·NTG - 0.0016·NTG^2
Emulsion 3	pH = 6.1796 - 0.1109·T + 0.0534·NTG - 0.0024·T^2 + 0.0035·T·NTG - 0.0012·NTG^2
Emulsion 4	pH = 8.1387 + 0.0098·T - 0.0465·NTG - 0.0003·T^2 - 0.0003·T·NTG + 0.0005·NTG^2

Table 14. Adequacy indicators

Adequacy indicators	Emulsion 1	Emulsion 2	Emulsion 3	Emulsion 4
Dispersion, σ^2	0.00354	0.98790	0.00475	0.94983
Standard deviation, σ	0.05953	0.09939	0.06886	0.09745
Model accuracy indicator, R^2	0.95787	0.94844	0.92124	0.93648
Correlation coefficient, R	0.97870	0.97388	0.95981	0.96772

Table 15. Absolute model errors

EMULSIONS	T, [months]	pH read	pH calculated according to T and RE	Error absolute of the model [%]	pH calculated according to T and NTG	Error absolute of the model [%]
EMULSION 1	1	6.50	6.53	0.46	6.53	0.46
	48	5.80	5.69	1.93	5.81	0.17
EMULSION 2	1	7.00	7.03	0.43	7.04	0.57
	48	5.90	5.82	1.37	5.92	0.34
EMULSION 3	1	6.50	6.48	0.31	6.42	1.24
	48	5.90	5.86	0.68	5.47	7.86
EMULSION 4	1	7.00	7.01	0.14	7.08	1.13
	48	6.00	5.80	3.45	6.10	1.64

The 3D graphical representations of pH (figures 18-25) and the equations that constitute the mathematical models obtained (tables 11,13) it is observed a 90% decrease in its values by the end of the study.

Regarding the quality of the mathematical models obtained for the 4 emulsions, it can be seen that they have indicators of adequacy that fall within the requirements of a good approximation (tables 2,4,7,9,12,14). Thus the correlation coefficient R is higher than 0.95, and the absolute errors fall in the range of 0.03% and 12.01% (tables 5,10,15). This situation leads to the conclusion that the mathematical models obtained are true and accurately reflect the behavior of the real model (cosmetic emulsion). Based on the equations of the obtained analytical-experimental mathematical models, presented in tables 1,3,6,8,11 and 13, the variations of the specific quality indicators can be correlated with each other and depending on the time.

This method is comparable to the classical methods of studying cosmetics based on direct experimental determinations with the appropriate equipment. However, these classical methods do not offer the possibility to evaluate qualitatively and quantitatively the structural changes of the emulsions highlighted by the shape of the graphical representations of the determined mathematical models.

The disadvantage of the proposed method is that the determined mathematical models are valid only for well-defined case studies, respectively for concrete limitations of the variations of the parameters taken into account when calculating the quality indicators. In order to ensure a high physico-chemical and microbiological stability of the studied emulsions, ingredients were chosen to ensure a physico-chemical interaction between the components as low as possible, especially after preparation.

CONCLUSIONS

The results obtained in the research show that for the case study presented, the experimental-computational mathematical models describe the physico-chemical processes that take place in cosmetic emulsions, which can lead to changes in the values of some parameters and quality indicators specified by law the EU.

Taking into account the experimental models obtained by the multi-correlation method, it can be seen that preserving emulsions with a well-defined amount of 0.8% methyl paraben improves their quality and stability over time (NTG, RE and pH have changed in the limits imposed by the standards in force, even for emulsions in which the aqueous phase is above 60% found in figures 3,4,5,7,8,9) [11]. The organoleptic properties of the four emulsions were also monitored throughout the 4-year study. It was observed that for almost three years they did not change, so they kept their homogeneous shape, without separation phases, without foreign smell and without color change.

Staphylococcus aureus and Pseudomonas aeruginosa, the other microbiological parameters, remained absent throughout the testing period (as required by legal standards for cosmetics). The final conclusion of the study is that the 4 emulsions cosmetics can have a safe shelf life of up to 3 years, if kept in optimal storage conditions. It is important to note that these cosmetic emulsions (creams) have were packed in polypropylene boxes. Their lids are opened every time they are subjected to quality control analyzes, and when they reach consumers they open daily. As such, in order to maintain a superior quality of cosmetic creams, it is recommended to use airless bottles; the packaging of these vials is airtight and there is no risk of contamination during quality control or during use by consumers.

Given the accelerated development of the use of artificial intelligence, we believe that future technologies for obtaining cosmetic emulsions will be developed very soon only on the basis of computational mathematical models.

EXPERIMENTAL

Preparation of the emulsions

The preparation of the emulsions was carried out in accordance with the specific technology for obtaining them [12,13]. Both the aqueous phase (1) and the oily phase (2) are heated at 80°C and then, the aqueous phase was added over the oily phase and mixed for 8 minutes with a Lab High-shear Homogenizer, at 10000 rpm. After homogenization, the emulsions were cooled to 40°C under continuos stirring (5000 rpm) after which the active ingredients and the perfume were added. The composition of the prepared and analysed emulsions is presented in table 16.

Table 16. The composition of the analysed samples

Ingredients	Composition, wt.%			
	E1	E2	E3	E4
Aqueous phase (1)				
Glycerol	10	5	5	7
Methyl 4-hydroxybenzoate (methylparaben)	0.8	0.8	0.8	0.8
Distilled water	57.29	60.49	63.8	67.39
Sodium lauryl sulfate (anionic emulsifier)	0.5	0.5	0.5	0.5
Oily phase (2)				
Paraffin oil	25	8	6	14
Vaseline	4	20	15	3
Cocoa butter	-	-	0.5	-
Cetaceum	-	-	-	2
Cetostearyl alcohol	2	5	-	2
Cetyl alcohol	-	-	8	-
Stearic acid	-	-	-	2
Active ingredients (3)				
Spirulina	0.1	-	-	-
Honey	-	-	0.2	1
Vitamin E	0.01	0.01	-	0.01
Vitamin A	-	-	-	0.01
Perfume (4)	0.3	0.2	0.2	0.3

After preparation, the emulsions were packed in polypropylene boxes with a lid for sealing. The samples were stored in a room where temperature (15÷25ºC) and air humidity (55÷65%) were monitored.

Determination of pH value and the evaporation residue

The pH value was determined with InoLab pH-meter. The evaporation residue (RE) was determined with thermobalance PCE-MA 50X.

Determination of physico-chemical and microbiological parameters

These parameters were determined using the specific methods of analysis recommended by the current standards [14,15].

Experimental-computational mathematical modeling methodology

As a modeling strategy, the technique of obtaining analytical-experimental models or the so-called computational modeling was chosen. As such, the following steps were taken [7,16-19]:

• Data collection, analysis and interpretation (the database was obtained using experimental determinations performed in the laboratory using physical-chemical and microbiological analysis methods, and the results were presented in tabular form).

• The elaboration of the analytical-experimental mathematical models was performed by processing the database obtained in the laboratory, with the computer program STATISTICA 14.0 (nonlinear regression method), directly obtaining the corresponding graphical representations, the corresponding mathematical equations and the adequacy indicators.

• The testing of the analytical-experimental mathematical models was performed based on the determined adequacy indicators: the adequacy dispersion (σ^2), the standard deviation (σ), the model accuracy indicator (R^2) and the multiple correlation coefficient (R).

• Verification of the authenticity of mathematical models was performed by the classical method of calculating the absolute error according to formula (1):

$$E = 100(y_c - y) / y_c, \% \qquad (1)$$

where:

y_c - the value of the output variable calculated based on the mathematical model,

y - the value of the measured / readable output variable on the graph.

REFERENCES

1. Y. Kashyrina; O. Muratov; G. Sokolskyi; O. Miroshnikov; *Ukr. Food J.*, **2017,** *6(3)*, 524-533
2. S. Bom; L. F. Gouveia; P. Pinto; A. M. Martins; H. M. Ribeiro; J. Marto; *Colloids Surf., B*, **2021,** *205,* 111865
3. K. Sakamoto; R. Y. Lochhead; H. I. Maibach; Y. Yamashita; *Cosmetic Science and Technology; Theoretical Principles and Applications*, Elsevier, **2017**, pp.489-506
4. E. Merică; *Tehnologia produselor cosmetice*, Vol.1, Ed. Corson Iași, **2000,** pp.48-54
5. IFSCC Monograph Number 4; *Introduction to cosmetic emulsions and emulsification*, Micelle Press, Weymouth, Dorset, England, **1997,** pp. 1-23
6. I. Popovici; D. Lupuleasa; *Tehnologie farmaceutică,* Vol.2, Ed. Polirom, București, **2008,** pp.154-258
7. T. Todinca; M. Geantă; *Modelarea și simularea proceselor chimice. Aplicații în Matlab*, Ed. Politehnica, Timișoara, **1999,** pp.7-9, pp. 163-175
8. H.Pîrlea; D. Silaghi-Perju; D.Perju; M.Șuta; *Analytical and experimental mathematical models for nitrogen dioxid dispersion in the atmosphere, basis on monitoring of 3 meteorological parameters in Timișoara, Românîa*, 10th Mediteranean Congress of the Chemical Engineering, Barcelona, Spain, 15-18 November **2005,** Process Engineering, ISBN 84-88233-27-2 pp.549
9. D. Perju; H. Pîrlea; G.A. (Brusturean) Dumitrel; D. Silaghi-Perju, S. Marinescu; *Rev. Chim.*, **2008**, *59(10)*, 1112-1116
10. A.E.Manea; M.D.Perju, A.Tămaș; *J.Eng.Sci.Innovation (JESI),* **2022***, 7(1),* 45-58
11. IFSCC Monograph Number 5; *An introduction to cosmetic microbiology*, Micelle Press, Weymouth, Dorset, England, **1999,** pp. 3-10, 25-27
12. A.E.Manea; A. Tămaș; S.Nițu; D.Perju; *Studia UBB Chemia*, **2021,** *66, 4,* 283-295
13. A.E.Manea; D.Perju; G.A. Brusturean; M. Calisevici; S. Marinescu; *Contributions to the Stabilization Processes of the Cosmetic Creams*, MicroCAD, International Scientific Conference, 2008, Materials Science and Technology, University of Miskolc, Hungary **2008**, pp.65-70
14. *Farmacopeea Română,* ed. a x-a, Ed. Medicală, București, **1993,** pp.981-1019
15. *European Pharmacopeia,* ed.8.0, Vol.I, Council of Europe, Strasbourg, **2014,** pp.188-192
16. A. I. Lucaci; P.Ș. Agachi; *Optimizarea proceselor din industria chimică*, Ed. Tehnică, București, **2002,** pp.17-47
17. J. L. Devore; *Probability Statistic for Engineering and the Sciences,* 8th ed., California Polytehnic State University, San Luis Obispo, **2010**, pp.524-536
18. S. C. Chapra; R.P. Canale; *Numerical methods for Engineers*, 6th ed., McGraw-Hill, New York, **2010**, pp.481-484
19. M. Faier Crivineanu; *Studiul proceselor de emisie a metalelor grele în ape curgătoare utilizând tehnici de modelare matematică* – PhD Thesis, Ed. Politehnica Timișoara, **2012**, pp. 183.

BIOACTIVE COMPOUNDS AND ANTIOXIDANT CHARACTERISTICS OF VARIOUS TOMATO CULTIVARS FROM SERBIA – CHEMOMETRIC APPROACH

JELENA S. NIKOLIC[a*], VIOLETA D. MITIC[a], MARIJA V. DIMITRIJEVIC[b], VESNA P. STANKOV JOVANOVIC[a]

ABSTRACT. Tomato is one of the most consumed foodstuffs around the world and major dietary source of lycopene. The main objectives of this study were evaluation of antioxidant activity, using DPPH, ABTS, FRAP, TRP and CUPRAC assays, as well as total phenolic, total flavonoid, lycopene and β-carotene content in 30 tomato and cherry tomato cultivars commonly consumed in Serbia. Tomato with the highest total phenol and total flavonoid content was tomato Indigo Rose (17.56 mg GAE g^{-1} DW and 30.30 mg RE g^{-1} DW, respectively), which showed excellent antioxidant characteristics. Total lycopene content was lower in yellow tomato species compared to the red ones, and the highest lycopene content was 0.283 mg g^{-1} DW for tomato Red Pearl Big. Cluster analysis yields dendrogram, separating tomato and cherry tomato cultivars into three statistically significant clusters ((D_{link} / D_{max})×100 < 50).

Keywords: Tomato, Antioxidant characteristics, Bioactive compounds, PCA, Cluster analysis

INTRODUCTION

Tomato (*Solanum lycopersicum*) belongs to the family Solanaceae, which includes edible plants such as potatoes, capsicums, and eggplants, but also potentially poisonous plants (jimsonweed and mandrake). All species of this family have toxic alkaloids present in either their leaves or their fruits [1].

Fresh tomatoes are produced worldwide, approximately 180 million tons per year, and it is the third most-produced vegetable. Four times more rice and two times more potatoes are grown around the world [2]. In Serbia,

---

[a] *University of Niš, Faculty of Sciences and Mathematics, Department of Chemistry, Višegradska 33, Niš, Serbia.*
[b] *University of Niš, Faculty of Medicine,Department of Pharmacy, Dr. Zorana Đinđića Boulevard 81, Niš, Serbia.*
[*] *Corresponding author: jelena.cvetkovic@pmf.edu.rs.*

tomatoes are grown on about 20000 ha, with the production of 180000 tons of fruit. Tomato is one of the most valuable products since it's consumed fresh as well as processed products. The importance of this vegetable is indicated by the fact that its consumption is recorded in 164 countries. The average tomato consumption in the world is 20.5 kg per capita, and in our country, it is 16 kg per capita.

Tomato is a source of substances with known health benefits, such as vitamins, minerals, and antioxidants [3]. Tomato consumption decreases the risk of certain types of cancer [4] and cardiovascular diseases [5]. Also, beneficial phytochemicals positively affect immune response, atherosclerosis protection and DNA damage. The health benefit of tomato is attributed mainly to carotenoids present in tomato fruits. The primary carotenoid present in tomato is lycopene [6]. It is naturally occurring carotenoid pigment present in tomato, watermelon, grapefruit, guava, and other fruits, giving fruits red color. It's a primary carotenoid in tomato, accounting for more than 80% of total carotenoids in this fruit [7]. The effects of lycopene on various diseases were studied in the past decades, and a positive impact on chronic diseases like cancer and cardiovascular disease was noticed [8]. Lycopene is also proven antioxidant, but the positive health effect could be achieved through different mechanisms that include modulation of intercellular gap junction communication, hormonal and immune systems, and metabolic pathways [8]. A close link between tomato intake and low cancer risk was also established [9]. Besides lycopene, tomatoes also contain α-, β-, γ-, δ-carotene, zeaxanthin and lutein and also neurosporene, phytoene, and phytofluene [10,11]. Carotene and lycopene content is fortified by cooking. Other compounds present in tomatoes are vitamin C, vitamin E, various phenolics, glycoalkaloids (tomatine) and flavonoids [12]. Micro and macro elements are also present, some in quantities higher compared to other products usually consumed.

Having in mind the lack of comprehensive knowledge about the local vegetable varieties, the present research was aimed to evaluate the total phenolic content (TPC), total flavonoid content (TFC), β-carotene content (TCC), lycopene content (TLC) and antioxidant capacities of 30 tomato and cherry tomato varieties consumed in Serbia. As far as we know, this is the first time that some of the varieties were analyzed. Antioxidant activity of tomatoes was determined by applying DPPH, ABTS, TRP, FRAP, and CUPRAC assays. Multivariate statistical analysis was used to achieve the relationship between analyzed tomato species antioxidant properties and various tests used. Chemometric techniques are used to simplify data set to fewer variables, without losing information. Principal component analysis (PCA) reduces multivariate data preserving most of the variance at the same time while cluster analysis (CA) divides the observations into homogeneous and distinct groups.

RESULTS AND DISCUSSION

Phenolic compounds are a widespread group of plant metabolites. They are vital both for the organoleptic properties of foods and for its positive health effects. The most critical outcomes of phenolic compounds are: antioxidant, antibacterial, and antiviral. Other class of natural products commonly analyzed in plant species are flavonoids. They are classified as low-molecular-weight phenolic compounds that are widely distributed in the plant kingdom [13]. Total phenolic and flavonoid content of 30 tomato and cherry tomato varieties were analyzed in this study, and the results were presented in Figures 1 and 2.
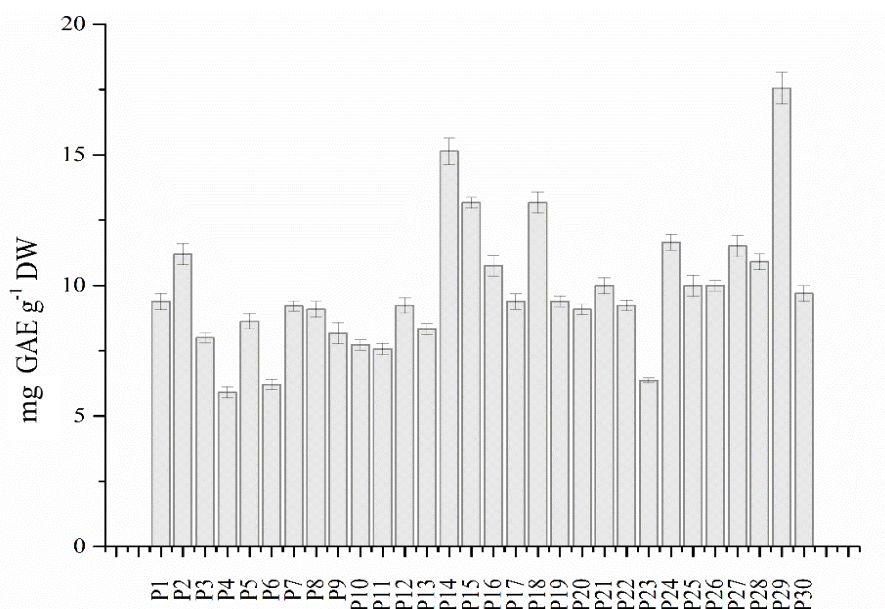
Figure 1. Total phenolic content in analyzed tomato and cherry tomato species

The highest total phenolic content was recorded for sample P29 – Indigo Rose tomato (17.6 mg GAE g^{-1} DW) - tomato cultivar first cultivated the 1960s, crossing tomatoes with wild species from Chile and the Galapagos Islands. Qi [14] analyzed 29 tomato species, and TPC varied significantly from 3.05 to 7.12 mg GAE/g DW. Kahkonen et al. [15] reported that the total phenolic content of tomatoes is up to 2 mg of gallic acid equivalent per 1 g DW, which is slightly lower than our results. The level of phenol compounds in tomatoes can be influenced by various features, including genotype, availability of nitrogen in the root zone, biotic, and abiotic stress-related events [16].

115
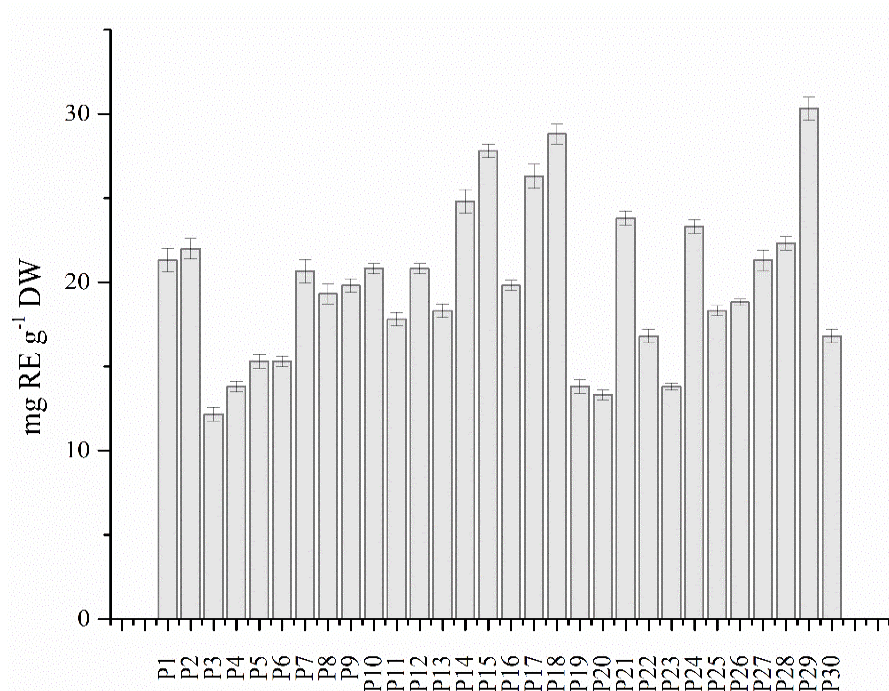
Figure 2. Total flavonoid content in analyzed tomato and cherry tomato species

Barros et al. [17] analyzed phenolic compounds in tomato varieties consumed in Portugal. Cis p-coumaric acid derivative was the most represented compound in yellow and round tomato varieties, while 4-O-caffeoylquinic acid was the most represented in long and heart varieties. The most abundant flavonoid was quercetin pentosylrutinoside in these tomato varieties. According to our study, Indigo Rose tomato also possesses the highest flavonoid content among other analyzed species. The total flavonoid content of Indigo Rose tomato was 30.3 mg RE g^{-1} DW. This tomato is rich in anthocyanins, a class of flavonoids, including delphinidin, petunidin, and malvidin [18].

Tomato contains carotenoids – a group of tetraterpenes fat-soluble pigments. They include β-carotene, β-cryptoxanthin, lutein, and lycopene. Lycopene, one of the most potent antioxidants among dietary carotenoids, is a highly unsaturated hydrocarbon containing 11 conjugated and two unconjugated double bonds, and it is an acyclic isomer of β-carotene. Lycopene and β-carotene content were determined using a spectrophotometer, and the results were presented in Figures 3 and 4.
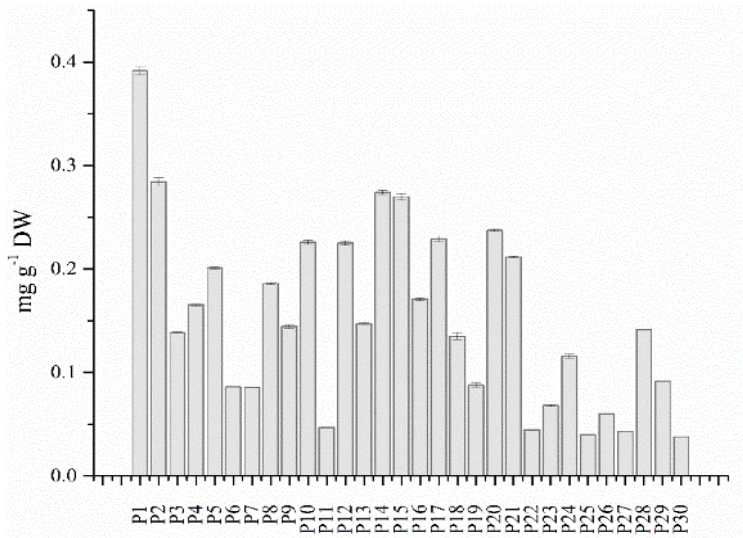
Figure 3. β-carotene content in analyzed tomato and cherry tomato species
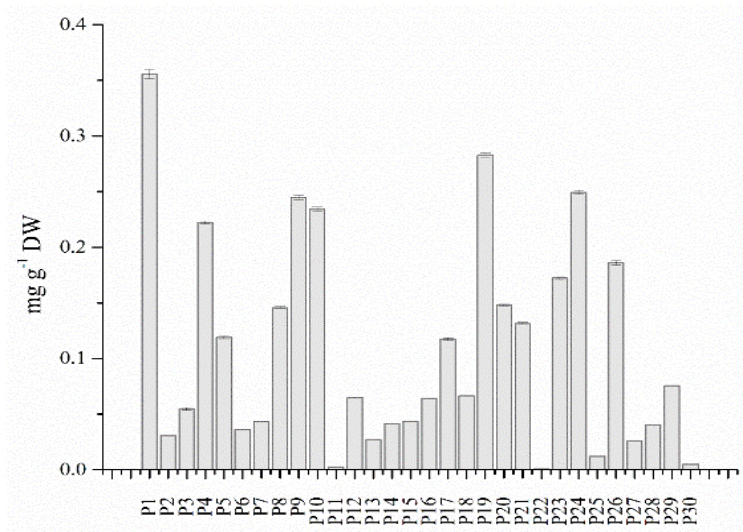
Figure 4. Lycopene content in analyzed tomato and cherry tomato species

Tomato with the highest β-carotene content was P2 - Cherry Datterino Yellow (0.284 mg g^{-1} DW), whereas tomato with the top lycopene content was P19 - Tomato Red Pearl Big (0.283 mg g^{-1} DW). Spectrophotometric assay on β-carotene and lycopene is simple, fast, and inexpensive. Baranska et al. [19]

analyzed β-carotene and lycopene content in tomato using FT-Raman, ATR-IR, and NIR spectroscopy, and results obtained in their study was 2.62−629.00 (lycopene) and 0.23−2.83 mg/100 g (β-carotene). Lycopene content obtained by Baranska et al. [19] was in accordance with results from this study, while β-carotene in our study was slightly higher. Another survey on those pigments in tomatoes was conducted by Burns et al. [20]. Their results recorded that the content of total carotenoids in tomatoes averaged 0.908 mg g^{-1} dry mass, where lycopene represented 0.522 mg g^{-1}. Since carotenoids and lycopene possess antioxidative effects, promote blood flow, and inhibit LDL cholesterol oxidation [18], their analysis is of great importance.

Five different assays were employed to access the antioxidant activity of tomato extracts – DPPH, ABTS, FRAP, TRP, and CUPRAC. Since tests differ in the reaction mechanism, more than one assay should be used to obtain comprehensive information on antioxidant activity. Various standards

Table 1. Antioxidant activity of tomato extracts obtained using
ABTS, DPPH, FRAP, TRP, and CUPRAC assays

| Sample	ABTS (mgTE1g^{-1}DW)	DPPH (mg TE 1 g^{-1} DW)	FRAP (mg Fe 1 g^{-1} DW)	TRP (mg AAE 1 g^{-1} DW)	CUPRAC (mg TE 1 g^{-1} DW)
P1	7.7±0.2	6.5±0.7	3.4±0.3	0.586±0.008	13.5±0.5
P2	7.7±0.1	10.0±0.8	4.3±0.6	0.699±0.007	14.0±0.7
P3	5.6±0.3	6.9±0.6	2.7±0.2	1.83±0.06	8.5±0.5
P4	7.3±0.2	7.8±0.7	2.7±0.3	1.99±0.07	6.2±0.5
P5	7.7±0.4	8.3±0.5	3.7±0.2	1.84±0.07	11.6±0.9
P6	6.6±0.3	7.0±0.6	2.5±0.3	1.2±0.1	8.6±0.6
P7	9.3±0.6	10.5±0.7	4.0±0.1	2.1±0.2	16±1
P8	7.8±0.6	8.8±0.7	4.0±0.3	2.16±0.09	13.2±0.5
P9	7.8±0.3	9.5±0.6	4.0±0.2	1.95±0.07	13.3±0.9
P10	7.8±0.4	10.0±0.9	5.2±0.3	2.2±0.1	17.3±0.9
P11	7.6±0.4	8.7±0.6	3.6±0.2	1.96±0.08	12.6±0.8
P12	7.8±0.3	9.1±0.6	3.8±0.2	2.3±0.2	12.1±0.6
P13	7.0±0.2	7.7±0.6	2.8±0.1	1.70±0.09	9.3±0.5
P14	7.8±0.3	10.3±0.7	4.2±0.3	3.3±0.3	18±1
P15	7.8±0.6	10.7±0.5	5.0±0.3	2.5±0.1	17.6±0.8
P16	7.8±0.3	10.9±0.6	5.1±0.2	2.5±0.1	17.3±0.9
P17	7.8±0.5	11.1±0.9	5.4±0.4	2.9±0.2	17.5±0.7
P18	7.8±0.2	11.1±0.7	5.6±0.3	2.5±0.01	21±2
P19	7.8±0.6	8.9±0.8	3.6±0.2	2.3±0.1	13.8±0.8
P20	7.8±0.3	9.9±0.5	4.2±0.5	2.57±0.09	14.6±0.5
P21	7.8±0.7	10.2±0.9	5.8±0.3	2.6±0.1	16.9±0.9
P22	7.8±0.6	8.3±0.6	3.8±0.2	3.6±0.2	15.9±0.8
P23	3.9±0.1	6.5±0.3	2.9±0.2	1.86±0.06	11.4±0.4
P24	7.2±0.5	9.0±0.8	5.9±0.3	2.5±0.1	17.7±0.8
P25	4.6±0.4	6.5±0.4	2.7±0.2	1.93±0.08	12.5±0.4
P26	5.0±0.4	7.6±0.3	3.4±0.3	2.8±0.1	14.1±0.6
P27	6.8±0.2	6.7±0.2	2.5±0.3	2.3±0.2	12.6±0.8
P28	5.3±0.3	7.4±0.4	2.3±0.1	2.6±0.1	13.2±0.6
P29	7.8±0.5	8.9±0.7	4.3±0.2	2.4±0.2	20±2
P30	7.3±0.4	7.3±0.6	2.8±0.2	2.11±0.09	11.6±0.5

used and results expressed either on fresh or dry weight makes results from the literature hardly comparable. Results obtained using five different assays were shown in Table 1.

DPPH and ABTS assays are based on the radical scavenging of antioxidants from the extracts and determines scavenging capacity stable radical species by antioxidants compounds present in the extracts. DPPH values (mg TE g^{-1} DW) ranged from 6.5 for P1 (Cherry Datterino Green) and P23 (tomato Green Zebra) to 11.1 for P18 (Cherry Russian Red). Cherry Datterino Yellow (10.0 mg TE g^{-1} DW) showed higher antioxidant activity than Cherry Datterino Green (6.5 mg TE g^{-1} DW), indicating that compounds present in yellow tomato significantly affect antioxidant activity. Klunklin and Savage [21] examined the antioxidant characteristics of tomatoes grown under water stress conditions. The mean DPPH values showed a significant difference between the well-watered (0.25 mg TE g^{-1} DW) and water stress treatments (0.40 mg TE g^{-1} DW) for all cultivars. Those values are lower than the values obtained in our study. The same authors also reported antioxidant activity using the ABTS assay [21]. The mean ABTS assay results in their research for the four cultivars was 0.45 mg TE g^{-1} DW for the well-watered fruits, and this was significantly raised to a mean of 0.83 mg TE g^{-1} DW for the drought-stressed tomatoes. In our study, ABTS values were higher (3.9 mg TE g^{-1} DW for P23 to 7.9 mg TE g^{-1} DW for P19), which is in agreement with the results obtained by Kerkhofs et al. [22]. The antioxidant activity of tomato Black Truffle and Cherry Yellow Pear lipophilic and hydrophilic extracts was analyzed by Zanfini et al. [23]. Hydrophilic extract of Cherry Yellow Pear showed higher antioxidant activity than tomato Black Truffle, which is in accordance with our results.

Assays like FRAP, TRP, and CUPRAC are used to evaluate the ability of antioxidants from the sample to donate electrons. Those methods are SET (single electron transfer) based, and change in color (the solution absorbance change) is linked to the antioxidant concentration [24].

FRAP is a fast, reproducible, and non-specific method measuring the reduction of Fe^{3+}-TPTZ to Fe^{2+}-TPTZ by antioxidants at low pH [34]. FRAP values for analyzed tomato species varied from 2.3 mg Fe per 1 g DW for P28 (tomato Black Krim) to 5.9 mg Fe per 1 g DW for P24 (tomato Black Truffle). tomato Omar's Lebenese, Cherry Russian Red, tomato Fantom, tomato San Marzano, and Cherry Brioso showed similar FRAP values like tomato Black Truffle. According to Bernie et al. [25] results from tomato San Marzano showed low FRAP values (0.31 mmol Fe/100 g FW) compared to other tomatoes analyzed in that study, which is opposite to our results, where tomato San Marzano was one of the tomatoes with the highest FRAP values. Tomato Black Truffle showed high amounts of phenolic compounds, flavonoids, and

lycopene. Phenolics are the most abundant antioxidants in the human diet and can donate hydrogen, chelate metal ions, and inhibit enzymatic reactions. However, the main antioxidant in tomatoes might be lycopene, carotenoid class pigment. The presence of phenolic compounds and lycopene makes tomato food of stupendous nutritional characteristics, allowing its consideration as a functional food with positive health effects [26].

In total, reducing power assay (TRP) antioxidants react with potassium ferricyanide to form potassium ferrocyanide, which latter reacts with $FeCl_3$, yielding a blue colored complex, with a maximum absorbance at 700 nm. Searching literature, authors could not find results for this assay regarding all analyzed varieties. Results showed that the antioxidant capacity of analyzed tomatoes ranged from a minimum of 0.586 mg AAE g^{-1} DW in the Cherry Datterino Green variety to a maximum of 3.6 mg AAE g^{-1} DW in the tomato Brandywine Yellow variety. Reducing the power of Brandywine Yellow variety was analyzed by Sidhu et al. [27], and their results for TRP of this tomato were slightly lower (2.0).

As far as we know, CUPRAC assay for determining antioxidant activity has not been used until now on fresh tomato and cherry tomato cultivars. CUPRAC assay is simple and reproducible, and strongly correlated to other assays for antioxidant activity determination [28]. The highest antioxidant capacity using CUPRAC assay was obtained from P18 - Cherry Russian Red (21 mg TE g^{-1} DW). Other cherry tomatoes also showed high antioxidant activity compared to regular tomato fruits Cherry Yellow Pear (18 mg TE g^{-1} DW), Cherry Bell (17.6 mg TE g^{-1} DW), and Cherry Brioso (17.3 mg TE g^{-1} DW). Only tomato Fantom and tomato Indigo Rose (17.5 mg TE g^{-1} DW and 20 mg TE g^{-1} DW, respectively) showed antioxidant activity similar to cherry tomatoes.

Statistical analysis

Statistical analysis was performed to evaluate the relationship between assays used in this study and tomato varieties.

Cooperative effects between antioxidants and plant-food extracts have been previously reported in different chemical systems. The relationship between total phenolic, flavonoid, lycopene, and carotenoid content and antioxidant activity were evaluated using correlation analysis. Correlation coefficients were presented in Table 3. The most significant positive correlations were found between FRAP/DPPH (0.85) and FRAP/CUPRAC (0.81) assays ($p < 0.05$). Interestingly, no correlation was found between lycopene content and any assay used in this study. CUPRAC assay is strongly correlated to total flavonoid (0.77, $p < 0.05$) and total phenolic content (0.72, $p < 0.05$), indicating phenolics and flavonoids are responsible for antioxidant activity of tomato extracts.

Table 2. Correlation matrices of antioxidant activity, total phenolic, flavonoid, lycopene and carotenoid content

	TPC	TFC	TLC	TCC	DPPH	ABTS	FRAP	TRP	CUPRAC
TPC	1.00	**0.78**	-0.23	0.13	**0.37**	0.22	**0.39**	**0.36**	**0.72**
TFC		1.00	-0.13	0.29	**0.54**	0.33	**0.60**	0.25	**0.77**
TLC			1.00	0.34	-0.04	0.05	0.20	-0.20	0.00
TCC				1.00	**0.38**	0.38	0.38	-0.25	0.19
DPPH					1.00	**0.69**	0.85	0.38	**0.72**
ABTS						1.00	**0.55**	0.09	**0.41**
FRAP							1.00	0.34	**0.81**
TRP								1.00	**0.50**
CUPRAC									1.00

Cluster analysis was performed to group tomato varieties based on analyzed characteristics. The dendrogram was constructed by Euclidean distance dissimilarities with Ward's Method of Linkage. The dendrogram of analyzed tomato cultivars was presented in Figure 5.
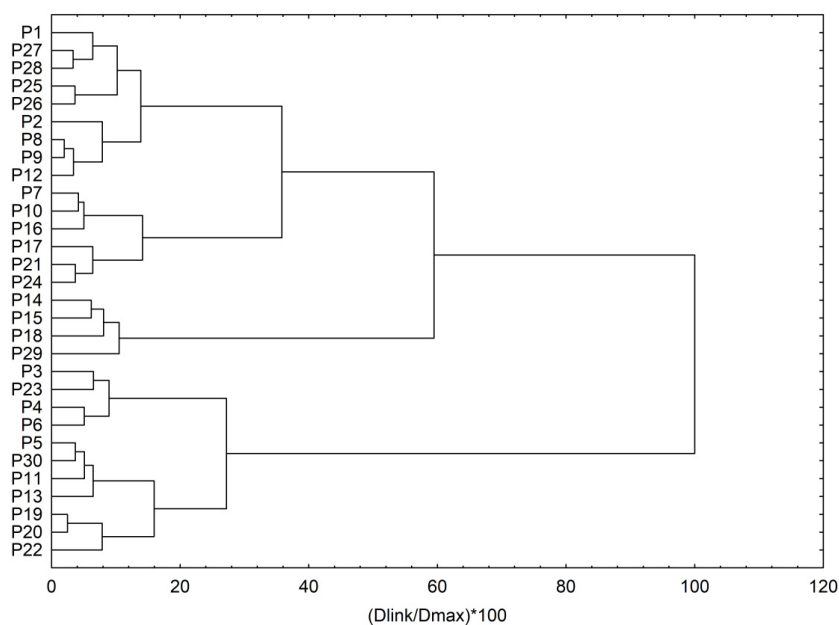
Figure 5. Dendrogram obtained in the cluster analysis of antioxidant activity and total phenolic, total flavonoid, lycopene and carotene content of tomato cultivars

Cluster analysis grouped analyzed tomato cultivars in three statistically significant clusters ($(D_{link} / D_{max}) \times 100 < 50$). These clusters were separated due to differences in antioxidant activity and analyzed phytochemicals among cultivars. The first cluster consists of 15 analyzed tomato cultivars – Cherry Datterino Green, tomato Black Plum, tomato Black Krim, tomato Azoychka, tomato Chreokee Purple, Cherry Datterino Yellow, Cherry Genio, Cherry Anna-Aasa, tomato Couer de Boeuf (in the first subcluster) and Cherry Lipso, Cherry Brioso, tomato San Marzano, tomato Fantom, tomato Omar's Lebanese, tomato Black Truffle (in the second subcluster). These varieties showed higher antioxidant activity, total phenolic, flavonoid, lycopene, and carotene content compared to other analyzed tomatoes. The smallest Euclidean distance was recorded between Cherry Anna-Aasa and Cherry Genio (1.2), indicating those two varieties are the most similar according to analyzed characteristics. Maximum Euclidean distance was found between tomato Indigo Rose and tomato Rio Grande (24.3). Euclidean distance between analyzed tomatoes was small (1.2-24.3), so it can be concluded that 30 tomato varieties analyzed in this study did not differ significantly in terms of analyzed characteristics. Cluster analysis did not separate cherry tomatoes from tomatoes but gave us the ability to quickly interpret an extensive data set.

A principal component analysis (PCA) was performed to obtain an overview of the similarities between samples and investigate the relationship between the assays used for evaluating the antioxidant activity. PCA produced scores and loading plots (Fig. 6a and 6b). Scores plot is a visualization of the differences among analyzed samples, where each tomato was plotted on a graph in which the first two principal components make up x and y axes, while the loading plot explains the contribution of each variable to the total variance. The number of significant principal components was chosen according to criteria set by Kaiser [29], where eigenvalues should be higher than 1. Only PC1 (3.23) and PC2 (1.07) had eigenvalues higher than 1. PC1 explained 64.68% of the total variance, and PC2 explained 19.41%, totalizing 84.09%. Variables grouped together were strongly positively correlated (TPC, TFC, CUPRAC, DPPH, and FRAP). Major contributors to the PC1 were DPPH (-0.93) and FRAP (-0.92). It seems that they are similar to analyzed characteristics, and some observations could be made:

• Cherry Datterino Green and Cherry Datterino Yellow are grouped together, indicating there is no significant difference in analyzed parameters in Green and Yellow Datterino variety;

• Variety with the highest negative contribution to PC1 was Cherry Russian Red (-2.98), variety with the highest antioxidant activity according to DPPH and CUPRAC assays, and high antioxidant activity according to FRAP assay, indicating PCA analysis can be used as a powerful tool in the study of an extensive data set;

• Tomatoes with negative loading on PC2 (tomato Azoychka, tomato Green Zebra, tomato Black Plum, tomato Cherokke Purple, Cherry Yellow Pear, tomato Brandywine Yellow, tomato Black Truffle, tomato Indigo Rose) are tomatoes with no red skin/meat color, and they have similar antioxidant characteristics;

• Tomatoes grouped in the upper and lower right quadrants possess lower values for analyzed characteristics, and they are on the reverse side of the methods used in this study.
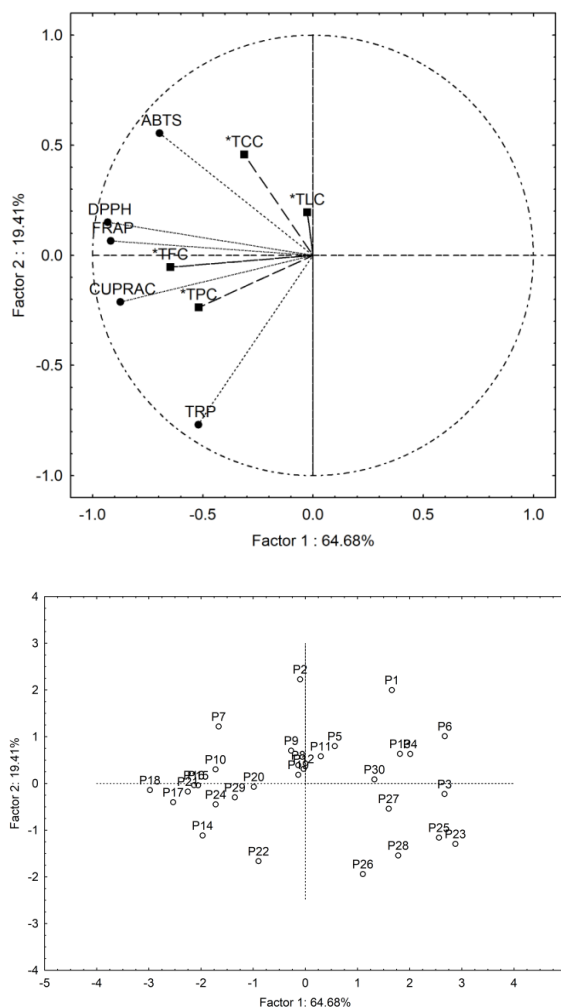
Figure 6. Plots obtained by principal component analysis (PCA); a) loading plot; b) scores plot

EXPERIMENTAL

Plant material and extract preparation

Thirty tomato fruits were obtained from local growers (Nis, Serbia) in July 2018 (Table 3). All samples received similar water and fertilizer treatments and were harvested at the same time. Grounded fresh fruits were lyophilized and kept in the freezer up to analysis. Lyophilized samples were extracted three times (3 x 15 minutes) using methanol in an ultrasonic bath at 25 ºC. Obtained extracts were filtered, evaporated to dryness and dissolved to a final volume of 25mL.

Table 3. List of analysed tomato and cherry tomato

Tomato	Label	Tomato	Label
Cherry Datterino Green	P1	San Marzano	P16
Cherry Datterino Yellow	P2	Fantom	P17
Cherry Tastery	P3	Cherry Russian Red	P18
Rio Grande	P4	Red Pearl Big	P19
Grapola	P5	Teton de Venus	P20
Pink Rock	P6	Omar's Lebenese	P21
Cherry Lipso	P7	Brendywine Yellow	P22
Cherry Genio	P8	Green Zebra	P23
Cherry Anna-Aasa	P9	Black Truffle	P24
Cherry Brioso	P10	Azoychka	P25
Cherry Goldwin	P11	Cherokke Purple	P26
Couer de Bouef	P12	Black Plum	P27
Cherry Koktelpalci	P13	Black Krim	P28
Cherry Yellow Pear	P14	Indigo Rose	P29
Cherry Bell	P15	Ananas	P30

Chemicals and instruments

2, 2'-azino-bis (3-ethylbenzothiazoline-6-sulfonic acid), 2, 2-Diphenyl-1-picrylhydrazyl, Trolox(6-hydroxy-2, 5, 7, 8-tetramethylchroman-2-carboxylic acid), iron(III) chloride hexahydrate, Folin–Ciocalteu reagent, gallic acid, ascorbic acid, and methanol were obtained from Sigma, St. Louis, Missouri, USA. Acetone, Na_2CO_3, HCl, neocuproine, copper(II) chloride dihydrate, 2, 4, 2-tri(2-pyridyl)-s-triazine(TPTZ), phosphate buffer (NaH_2PO_4–Na_2HPO_4), ammonium acetate buffer, $K_3[Fe(CN)_6]$, CCl_3COOH, $K_2S_2O_8$, and $FeSO_4 \times 7H_2O$ were purchased from Merck, Darmstadt, Germany.

Spectrophotometric measurements were performed using a double beam ultraviolet-visible spectrophotometer (Perkin Elmer Lambda 15, Massachusetts, USA).

Total phenolic content (TPC)

The total phenolic content was measured by applying the Folin-Ciocalteu reagent described by Dimitrijevic et al. [30]. A volume of the extract (25 µL) was mixed with 0.5 mL of Folin-Ciocalteu reagent, 2 mL sodium carbonate solution, and 4 mL water. Reaction mixtures were left to stand in the dark for 30 min, and the absorbance was measured at 750 nm. Gallic acid solution was used for calibration curve construction and the results were expressed via mg gallic acid equivalents (GAE) per g of dry weight (mg GAE g^{-1} DW).

Total flavonoid content (TFC)

The total flavonoid content of analyzed samples was determined by a method described by Mitic et al. [31]. Extract aliquot (50 µL) was mixed with 0.15 mL of a $NaNO_2$ solution. After 5 minutes, 0.75 mL of $AlCl_3$ solution was added, and the solution was kept 5 min at room temperature. Then, 1 mL of NaOH solution was added to the mixture, and water was added to a final volume of 5 mL. The absorbance was measured at 510 nm. Rutin solution was used for calibration curve construction and results were expressed as mg rutin equivalents (RE) per g of dry weight (mg RE g^{-1} DW).

β-carotene (TCC) and lycopene (TLC) content

β-carotene and lycopene were determined using the method described by Barros et al. [32]. Lyophilized samples were thawed in the dark and 10 mL of acetone: hexane mixture (4:6, v/v) was added. The solution was filtered, and then the filtrate was read in comparison to a blank (acetone: hexane solution) at different wavelengths (453, 505, and 663 nm). Contents of lycopene and β-carotene contents were calculated according to the equations:

$$Lycopene\ (mg\ 100\ mL^{-1}\ of\ extract) = -0.0458 \times A_{663} + 0.372 \times A_{505} - 0.0806 \times A_{453}\ (1)$$

$$\beta\text{-Carotene}\ (mg\ 100\ mL^{-1}\ of\ extract) = 0.216 \times A_{663} - 0.304 \times A_{505} + 0.452 \times A_{453}\ (2)$$

Antioxidant activity

DPPH radical scavenging capacity: Antioxidant activity on DPPH radicals was performed according to Dimitrijevic et al. [30]. Extract aliquot (25 µL), 1.5 mL of 100 mmol L^{-1} DPPH methanol solution, and methanol to a final volume of 4 mL was shaken, allowed to stand for 60 minutes in the dark and the absorbance was measured at 515 nm. Trolox was used for calibration curve construction. Results were expressed as mg of Trolox equivalents (TE) per g dry weight (mg TE g^{-1}DW).

ABTS radical scavenging capacity: The ABTS radical was produced by the reaction of the stock solution with potassium persulfate [30]. Extract aliquot (25 µL) was mixed with 1.8 mL of ABTS solution and diluted with methanol to a total volume of 4 mL. After 6 minutes at room temperature, absorbance was measured at 734 nm. Trolox was used for calibration curve construction and results were expressed as mg of Trolox equivalents (TE) per g dry weight (mg TE g^{-1} DR).

Total reducing power (TRP) assay: Total reducing power of tomato extracts was determined by the method of Oyaizu [33]. Extract aliquot (10 µL) was mixed with 1 mL $K_3[Fe(CN)_6]$, 1 mL pH 6.6 phosphate buffer, and water. The reaction mixtures were incubated for 30 minutes at 50°C. After that, 1 mL CCl_3COOH and 0.6 mL $FeCl_3$ were added. Ascorbic acid solution was used for calibration curve construction. Absorbance was measured at 700 nm, and results were expressed as mg ascorbic acid equivalents per g of dry extract weight (mg AAE g^{-1}DW).

Ferric-reducing antioxidant power (FRAP) assay: FRAP assay was performed using the method previously described by Benzie and Strain [34]. Extract aliquot (50 µL) was mixed with 1 mL FRAP reagent and diluted with water to a final volume of 4 mL, and after 5 minutes at 37 ºC absorbance was recorded at 595 nm. Ferrous sulfate was used for calibration curve construction. FRAP values of analyzed extracts were expressed as mg of Fe(II) equivalents per g dry weight (mg Fe g^{-1}DW).

Cupric reducing antioxidant capacity (CUPRAC) assay: Cupric ion reducing antioxidant capacity assay was performed using the method of Apak et al. [35]. Extract aliquot (50 µL) was mixed with 1 mL phosphate buffer (pH 7), 1 mL neocuproine, 1 mL $CuCl_2$, and diluted with water to a final volume of 4 mL.

After 30 minutes at room temperature, the absorbance was measured at 450 nm. Trolox was used for calibration curve construction and results were expressed as mg Trolox equivalents per g of dry weight (mg TE g^{-1} DW).

Statistical analysis

Statistical analysis was carried out in Statistica 8.0 software (StatSoft, Tulsa, Oklahoma, USA). A probability level of $p < 0.05$ was considered statistically significant. Correlation between metal content was established using regression analysis at a 95% significance level ($p \leq 0.05$). Cluster analysis was used for sample grouping based on antioxidant activity. In contrast, PCA reckons the correlation structure of the variables creating hypothetical new variables (principal components - PC) that account for as much as possible of the variance (or correlation) in a multidimensional data set [36].

CONCLUSION

Tomato is one of the most consumed foodstuffs both around the world and Serbia. This vegetable is rich in many phytochemicals such as phenolics, flavonoids, vitamins, and minerals. This study aimed to evaluate antioxidant activity, using DPPH, ABTS, FRAP, TRP and CUPRAC assays, as well as total phenolic, total flavonoid, lycopene and β-carotene content in 30 tomato and cherry tomato varieties commonly consumed in Serbia. The most abundant total phenolic and total flavonoid content was recorded for tomato Indigo Rose (17.56 mg GAE g^{-1} DW and 30.30 mg RE g^{-1} DW, respectively). Cherry Russian Red showed the best antioxidant characteristics in two out of five used methods, and excellent results in other methods used. This variety had the highest contribution to the PC1, together with DPPH, FRAP and CUPRAC assays. Cluster analysis permitted separation of analyzed tomato and cherry tomato varieties in three statistically significant clusters. The most significant positive correlations were found between FRAP/DPPH (0.85) and FRAP/CUPRAC (0.81) assays ($p < 0.05$). This indicates that multivariate techniques can be used as a powerful tool to evaluate results obtained by a large number of samples.

ACKNOWLEDGMENTS

REFERENCES

[1] Solanine poisoning *Brit. Med. J.*, **1979**, 2, 1458–14599.
[2] FAO, **2017**, FAOStat http://www.fao.org/faostat/en/?#data Acessed March 20, 2020
[3] L. Frusciante; P. Carli; M.R. Ercolano, R. Pernice; A. Di Matteo; V. Fogliano; N. Pellegrini; *Mol. Nutr. Food Res.,* **2007**, *51(5)*, 609–617.
[4] E. Giovannucci; *J. Natl. Cancer,* **1999**, *91(4)*, 317 – 331.
[5] D. K. Pandey; R. Shekelle; B. J. Selwyn; C. Tangney; J. Stamler; *Am. J. Epidemiol.*, **1995**, *142(12)*, 1269 – 1278.
[6] E. N. Story; R. E. Kopec; S. J. Schwartz; G. K. Harris; *Annu. Rev. Food Sci. Technol.*, **2010**, *1*,189–210.
[7] M. L. Nguyen; S. J. Schwartz; *Food Tech.*, **1999**, *53(2),* 38 – 45.
[8] A. V. Rao; S. Agarwal; *J. Am. Coll. Nutr.*, **2000**, *19(5)*, 563– 569.
[9] A. V. Rao; S. Agarwal; *Nutr. Cancer,* **1998**, *31*, 199–203.
[10] E. Capanoglu; J. Beekwilder; D. Boyacioglu; R. C. H. De Vos; R. D. Hall; *Crit. Rev. Food Sci. Nutr.*, **2010**, *50(10)*, 919-930.
[11] R. C. Ray; A. F. El Sheikha; S. H. Panda; D. Montet; *Int. J. Ferm. Tech.*, **2011**, *1(2)*, 139-148.
[12] R. K. Toor; G. P. Savage; *Food Res. Inter.*, **2005**, *38*, 487–494.
[13] A. N. Panche; A. D. Diwan; S. R. Chandra; *J. Nutr. Sci.*, **2016**, *5*, 1-15.
[14] Y. Qi, Characterization of phytochemicals and antioxidant activities of specialty tomatoes. Master Thesis, The University of Guelph, Canada. **2016**
[15] M. P. Kahkonen; A. I. Hopia; H. J. Vuorela; J. P. Rauha; K. Pihlaja; T.S. Kujala; M. Heinonen; *J. Agric. Food Chem.*, **1999**, *47(10)*, 3954 –3962.
[16] F. Serio; O. Ayala; A. Bonasia; P. Santamaria; Antioxidant Properties and Health Benefits of Tomato In *Progress in Medicinal Plants—Search for Natural Drugs*, J. N. Govil, V. K. Singh, C. Arunchalam Eds.; Studium Press LLC, Houston, TX, USA, **2006**, 159-179.
[17] L. Barros; M. Dueñas; J. Pinela; A. M. Carvalho; C. S. Buelga; I. C. F. R. Ferreira; *Plant Food Hum. Nutr.,* **2012**, *67(3)*, 229–234.
[18] E. Ooe; K. Ogawa; T. Horiuchi; H. Tada; H. Murase; K. Tsuruma; M. Shimazawa; H. Hara; *Biosci. Biotech. Biochem.*, **2015**, *80(2)*, 341–349.
[19] M. Baranska; W. Schütze, H. Schulz; *Anal. Chem.*, **2006**, *78 (24)*, 8456–8461.
[20] J. Burns; P. D. Fraser; P. M. Bramley; *Phytochem.*, **2003**, *62(6),* 939–947.
[21] W. Klunklin; G. Savage, *Foods,* **2017**, *6(8)*, 56.
[22] N. S. Kerkhofs; C. E. Lister; G. P. Savage; *Plant Food Hum. Nutr.*, **2005**, *60(3)*, 117–121.
[23] A. Zanfini; G. G. Franchi; P. Massarelli; G. Corbini; E. Dreassi; *Ital. J. Food Sci.*, **2017**, *29*, 90-99.
[24] R. Apak; S. Gorinstein; V. K. Böhm; M. K. Schaich; *Pure Appl. Chem.*, **2013**, *85(5)*, 957-998.
[25] R. Berni R; M. Romi; L. Parrotta; G. Cai; C. Cantini; *Hortic.*, **2018**, *4*, 51.

[26] A. Pirillo; A. L. Catapano; *G. Ital. Farmacoeconomia Farmacoutilizzazione,* **2014**, *6(4)*, 23–30.
[27] V. Sidhu; D. Nandwani; L. Wang; Y. Wu; *J. Food Qual.*, **2017**, *2017,* 5020742.
[28] V. Mitic; M. Ilic; M. Dimitrijevic; J. Cvetkovic; S. Ciric; V. Stankov Jovanovic; *Fruits,* **2015**, *71(1)*, 57–66.
[29] H. F. Kaiser; *Educ. Psychol. Meas.*, **1960**, *20*, 141 – 151.
[30] M. Dimitrijevic; V. Stankov Jovanovic; J. Cvetkovic; T. Mihajilov-Krstev; G. Stojanovic; V. Mitic; *Anal. Methods,* **2015**, *7(10)*, 4181–4191.
[31] S. S. Mitic; B. T. Stojanovic; M. B. Stojkovic; M. N. Mitic; J. L. Pavlovic; *Bulg. Chem. Commun.*, **2013**, *45*, 326-331.
[32] L. Barros; M. J. Ferreira; B. Queiros; I. C. Ferreira; P. Baptista; *Food Chem.*, **2007**, *103(2)*, 413-419.
[33] M. Oyaizu; *Jpn. J. Nutr.*, **1986**, *44*, 307–315.
[34] I. F. F. Benzie; J. J. Strain; *Anal. Biochem.*, **1996**, *239(1)*, 70–76.
[35] R. Apak; K. Güçlü; M. Özyürek; B. B. Oğlu; M. Bener; *Methods Mol. Biol.*, **2008**, *477*, 163–93.
[36] I. Gergen; M. Harmanescu; *Chem. Cent. J.*, **2012**, *6*, 156.

MODIFICATION OF BENTONITES INOCULATION WITH IRON COMPOUNDS TO AFFORD MAGNETITE CLAYS

BAKYTGUL ASKAPOVA[a]*, KUANYSHBEK MUSABEKOV[a]

ABSTRACT. Bentonites refer to the class of argilliferous folded silicate rocks, which as a whole have such common characteristics, as dispersion (fragmentation), colloidal properties, propensity to wetness, and adsorption properties. The importance of this paper, as it follows from the conclusion, is connected with the study of synthesizing of magnetic clay composites which have high adsorption capacity, as well as with systematization of their properties. Bentonite magnetic composites are among those which can be stabilized using sodium alginate. Magnetic composites synthesized on the basis of bentonite showed the proportion of magnetite corresponding to the proportion of Fe in the composition of the initial clays. Sodium alginate-based stabilization method is an effective one for bentonite magnetic composites.

Keywords: *bentonite, iron impurities, magnetic composite*

INTRODUCTION

All the existing large ore deposits of bentonite clays were formed because of decomposition of volcanic ash and peat water. The total world reserves of bentonite clays make about 5.5 billion tons. China accounts for 2.4 billion tons (about 45%) of the total, the United States accounts for about 15%, and such countries as Turkey, Greece, India and Russia account for 5-7% each of the total reserves. Most of the ore deposits in the world coincide with alkaline earth bentonites, while high-quality bentonites reservoirs are limited due to their concentration in volcanic sedimentary deposits and hydrothermal-metasomatic, geological-industrial areas.

In the world environmentally safe multifunctional hybrid materials get development for using them in biotechnology, medicine, and ecology is solve an urgent problem. Aluminosilicates, montmorillonite and bentonite clays widely occurring in nature those contain at least 70% mineral montmorillonite are

---

[a] *Al-Farabi Kazakh National University, 050040, Al-Farabi Avenue, 71, Almaty, Kazakhstan.*
* *Corresponding author: bakytgul.askapova@bk.ru.*

most promising for production of new composites [1]. They exhibit unique texture and physical-chemical properties, such as a developed specific surface area, a regular distribution of meso- and micropores, thermal stability, and the presence of various active centers of different nature. One method for obtaining composites based on bentonite consists in the modification of aluminosilicate by iron metal particles [2]. The addition of such metal particles promotes destruction of the hierarchical structure formed because of the coalescence of individual crystallites in the layerwise silicate and can cause changing in the texture and physical-chemical properties of the resulting composite. Using iron oxides, as initial magnetite Fe_3O_4 is characterized by a positive magnetic susceptibility. Iron metal particles give control for formation magnetic compounds with in intensification of the solid-liquid separation process.

As for Kazakhstan the reserves of bentonite clays there are rather large [3]. The productive intervals of Kazakhstan's bentonitic montmorillonite deposits are widely developed. They are limited by the folded belt, the Turanian Plate and lowlands, as well as by the basing bordering the Caspian lowland. The deposits of Southern and Eastern Kazakhstan cause the greatest practical interest. In Southern Kazakhstan they are the Darbaza and Kele deposits, whose total reserve makes 58 million tons. Besides, there are the Andreev, Dzerzhinsk and Ildersay deposits, with the total reserve making more than 100 million tons. Eastern Kazakhstan known reservoirs of bentonite clay are those of the Manrak group deposits, whose total reserves make about 50 million tons. The Tagan deposit bentonites (10.6 million tons) and those of the Dinosaur deposit (about 4 million tons) are of high quality [1]. The study of the Tagan deposit has revealed the genesis and distribution pattern of montmorillonitic mudstone varieties, the reserves and nature of bentonites, and the minerals extraction methods.

According to the research results there are three types of bentonite clays including alkaline, alkaline-earth and pharmaceutical one. Due to the special properties of montmorillonites and bentonite clays conditioned by the genesis of the Tagan deposit, the clays can be used in various industrial technologies. Alkaline bentonites are suitable to produce drilling solvents, while the sodium-free montmorillonites are usable in the production of catalysts. The pharmaceutical variety is represented by alkaline montmorillonites of the 12th horizon. The raw material extracted from this horizon is used in production of enterosorbents, capable to withdraw heavy metal ions and radionuclides from the human body [4]. Bentonite clays are usually called fine-dispersed clays, and their main components are montmorillonite ($Al_2O_3*4SiO_2*H_2O$) and beidellite ($Al_2O_3*3SiO_2*nH_2O$). The montmorillonitic group minerals (smectites) have high binding, adsorption and catalytic

abilities. The structure of bentonite rock consists of smectite minerals whose tier-structured crystal lattice is arranged of a single cell frame, each having 3 layers. The upper and lower layers of the $AlSiO_4$ frame are formed from tetrahedras and are called tetrahedral.

Magnetic fluids consist of a dispersed solid magnetic phase, a dispersion medium and stabilization. The fluid components' cumulative characteristics significantly affect the overall properties of the fluid. In the dispersed magnetic phase ferromagnetic and ferrimagnetic metals and metal oxides are often used. For the synthesizing purposes such metals, as Fe, Co, Ni, Gd; nitrides of these metals (for example, Fe_xN); metal oxides (primarily magnetite Fe_3O_4 and maghemite γ-Fe_2O_3); and parts of bimetallic alloys (Ni-Fe, Fe-Pt, Fe-Co, Sn-Co) are used. Ferrites, for example, chemical compounds, are also afforded from iron oxide Fe_2O_3 ore (ferrimagnets) with other metals oxides including special magnetic additives [5-7]. Despite the maximum magnetic saturation of metals, they are very sensitive to oxidation, especially in a highly dispersed state. Therefore, ferrite particles including magnetite, which is often used among ferrites (Fe_3O_4), are used here as the magnetically dispersed phase. The magnetic properties of magnetic liquids are determined by the weight composition of the solid phase, which can reach 25%.

The choice of magneto-containing materials is rather wide, and it can be greatly simplified, if such a question, as good compatibility of surfactants with the particles transporting fluid, as an important factor for stable colloidal suspensions extraction is taken into consideration.

Currently, a wide range of carrier products is used, as follow: water, ethanol, pentanol, glycol, perfluoropolyethylene, synthetic esters, transformer oils, freons, styrene, methylethylketone, kerosene, various synthetic hydrocarbons and organic solvents, vegetable and silicone oils [8-12]. Chemical interaction of the transporting fluid with the magnetic phase and the materials used in the mechanical device is inadmissible and is to be avoided. Stabilizer of magnetic particles in the transportation fluid is an indispensable element for magnetic fluids. The magnetic particles collision triggered off by their intense Brownian motion in the fluid is induced by the magnetic force, thus resulting in coagulation of magnetic particles. Therefore, stabilizing substances are required to prevent the particles collision and oxidation of the surface of the magnetic particles as well [13].

The magnetic particles in the fluid have doubled protective coating each, so that they are prevented from the adhesion effect, and due to the thermal disorder, they are dispersed through the fluid. Therefore, unlike a standard suspension, magnetic fluid particles do not settle to the bottom and remain effective for many years [14]. Stabilizing agents are important in the

synthesizing process of magnetic fluids, as they ensure coagulation stability of the system. The transporting fluid [magnetic particles], i.e., its properties, are critical for the choice of a particular stabilizer. Hence, magnetic fluids based on hydrocarbons (kerosene, marginal hydrocarbons, cold paraffin, vacuum oils) require such stabilizers, as higher alcohols, amines, fatty acids and surfactants (olein, stearin, laurine) [15].

Magnetic fluids and water-based magnetite used as a dispersed phase are practically harmless to the human body. As for water it is a special medium with a number of specific properties. Therefore, water-based magnetic fluids can be used for medical purposes [16]. For instance, a drop of a magnetic fluid is capable to transport the required medicine to the diseased area of a human body [17]. When biocompatible water- and ascorbic acid-based magnetite fluids are introduced into blood vessels as a stabilizer [18], they are capable to remove liposome, which now are controlled magnetically, as the magnetite particles inside them are encapsulated by the introduced drug [19, 20]. Ophthalmology is one more sphere, in which applicability of magnetic fluids is patented.

The aim of this work consisted in obtaining composites based on bentonite and magnetite and in studying their structure, stabilizing and sorption properties.

RESULTS AND DISCUSSION

In Fig. 1 the X-ray phase spectra of magnetite-clay composites are shown. The diffractograms of the composites confirm occurrence of the peaks corresponding to the structure of the mineral type montmorillonite and 8-silicon-oxygen and aluminum–oxygen groups included in the iron oxides γ-Fe_2O_3 (hematite) and $FeO*Fe_2O_3$ (Fe_3O_4-magnetite). An increase in magnetite concentration in the composite gives an increase in the height of iron oxides peaks (30.6° and 37.2°), and the decrease in the height of the Silicon and aluminum oxygen groups of montmorillonite peaks (6.8° and 20.1°).

Penetration of oxides into the clay structure is determined by its iron exchange capacity. The introduction of bentonite into the inter-pack space is provided not only by the physical correspondence of the space between the magnetite particles and the clay layers, but also by chemical interaction, accompanied by significant changes in the structure of bentonite, leading to the formation of new phases. Changes observed on bentonite X-ray diffractograms.
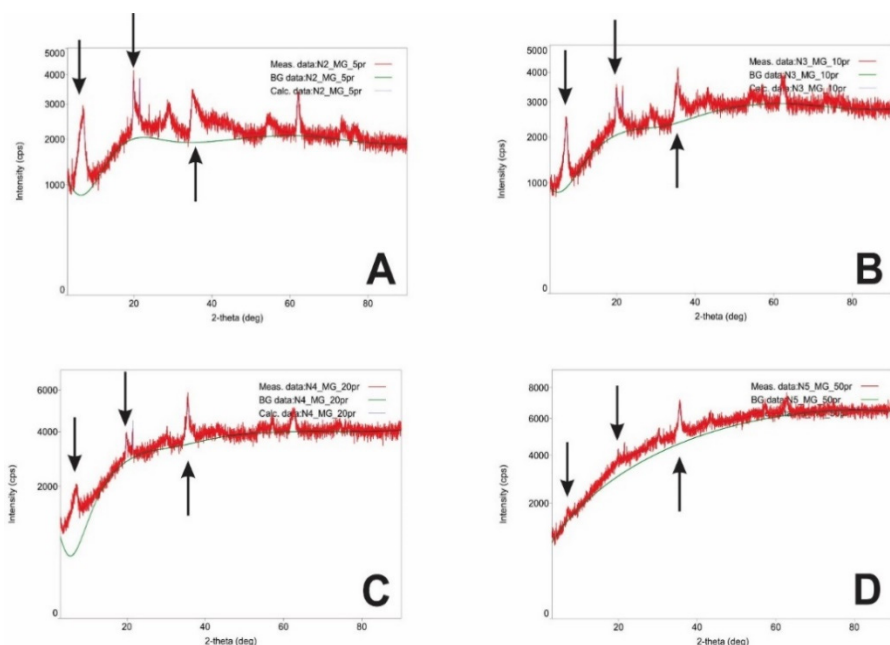
Figure 1. Diffractogram of X-ray phase composites: 5% (A); 10% (B); 20% (C); 50% (D)

Introduction of bentonite into the inter-frame space is adequate to the space between the magnetite particles and the clay layers and the chemical interaction occurring there and causing significant changes in the structure of bentonite leads to formation of new phases.

Ultrasonic dispersion of the afforded clay-magnetite composites, pure bentonite clay and magnetite allowed to obtain water suspensions by crushing the particles to a powdery state. The Figurovsky method of study of the magnetite effect on the hydrosuspensions shrinkage stability and granulometric composition of the Tagan bentonite included investigation of the sedimentation kinetics of the clay particles, which contain various quantities of magnetite (Figure 2). Hydrostatic microbalance captures the change in the mass of composites in size which during the experiment is fixed using a cathetometer through a sieve. The main indicator of the method is the ability to study the sedimentation of dilute suspensions over time. It was found that the increase in the content of magnetic structures increases the size of the particles.
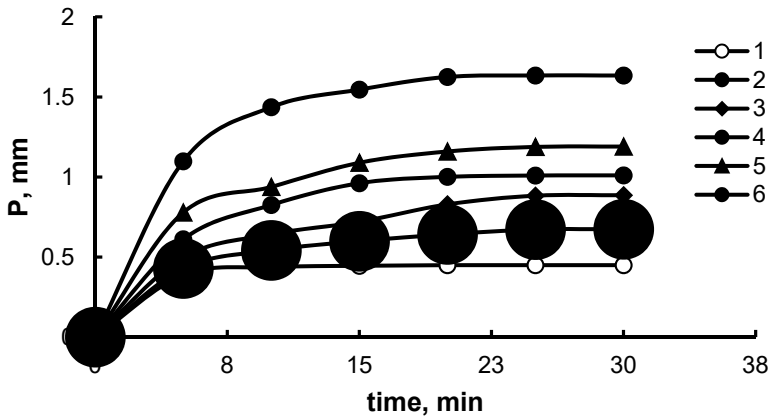
Figure 2. Particles sedimentation curves in hydrosuspension: 1 – bentonite clay, 2 – clay magnetic composite (5 %), 3 – clay magnetic composite (10 %), 4 – clay magnetic composite (20 %), 5 – clay magnetic composite (50 %), 6 – magnetite.
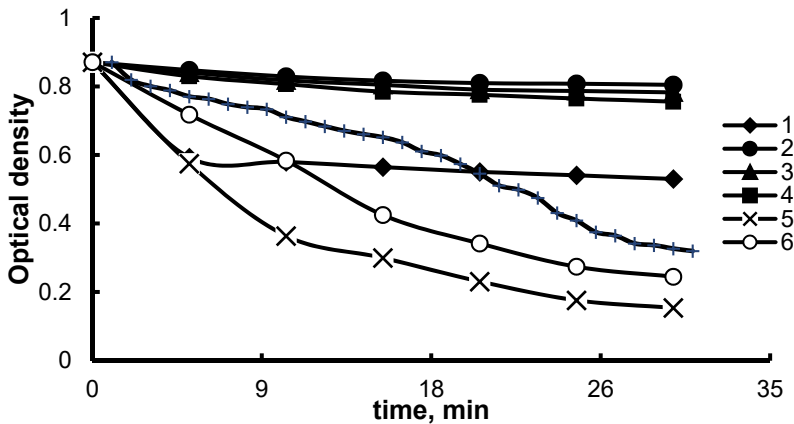
Figure 3. Changes in optical density kinetics of the bentonite hydrosuspension added with sodium alginate and chitosan at different concentrations. 1 – bentonite clay, 2 – 0.25 % Na alginate, 3 – 0.125 % Na alginate, 4 – 0.0625 % Na alginate, 5 – 0.25 % chitosan, 6 – 0.125 % chitosan, 7 – 0.0625 % chitosan

The decrease in the swelling of clay is explained by the water molecules displacement from the inter-frame space, when magnetite is introduced into the structure of bentonite clay. Since the growth of magnetite particles occurs directly in the inter-frame space, and the particle sizes correspond to the inter-frame space dimensions, then almost complete displacement of water molecules takes place there. The effect of stabilizers on the sedimentation

curves was studied in order to afford a stable bentonite hydrosuspension in aqueous medium. The following figure shows the effect on the shrinkage which the bentonite clay particles have in an aqueous medium at different concentrations of chitosan and sodium alginate (Figure 3).

As it follows from the Figure, the effect of sodium alginate on this process is very large, namely: first, a decrease in concentration of sodium alginate by 0.0625% results in a decrease in the deposition rate (Curve 4) and further increase in concentration, i.e. sodium alginate with a concentration of 0.25% leads to a long-term stabilization. When chitosan concentration is equal to 0.25%, the maximum accumulation of sediment is 5 times less than that in pure water. The effect of chitosan on the bentonite particles sedimentation can be explained by the water-soluble polymer's mechanism changes. It is known, in particular, that low concentrated chitosan has a flocculatory effect.

Table 1. Bentonite and its composites' surfaces values

Composite	Content of Fe_3O_4, %	The surface area determined by the thermal desorption method, m^2/g	The surface area determined by the sedimentation method, m^2/g
Bentonite	-	278.5	243.8
MC 1	4.37	305.3	289.7
MC 2	9.62	368.5	355.4
MC 3	24.44	282.7	271.6
MC 4	27.78	189.9	185.6

As it follows from the Table 1, an increase in the amount of magnetite in the composites MC 1 and MC 2 gives the values increase of a certain surface due to the particle sizes decrease. However, the values of the specific surface areas of the MC 3 and MC 4 compositions decrease, despite the small-sized particles of the composites. The reason of this lies in the fact that increased magnetite concentration in this composite gives the pores clogged, since the Fe_3O_4 particles in this composite are located not only on the coating of bentonite clay (like composites MC 1 and MC 2) but in the interplanar space too.

EXPERIMENTAL

The objects of the study were bentonite clay from the Tagan ore deposit (East Kazakhstan oblast) used as clay minerals has the formula, as follows:

$(OH)_4Si_8Al_4O_{20}*n$ (interstratal) H_2O.
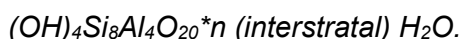
Heaving properties of the Tagan bentonite clays are of great importance, as they indicate the suitability of the clay raw for solvents preparing. Moreover, the raw material does not lose its properties for a long time, even when preserved in a smaller amount in the dispersed phase. For the synthesis of magnetite particles iron salts, as $FeSO_4*7H_2O$ and $FeCl_3*6H_2O$ are used.

Carboxymethyl cellulose (Na-CMC), Na-alginate (Na-ALG), methylcellulose and chitosan are used as stabilizing agents for the magnetite dispersion. Due to the ability of sodium alginate to retain water this substance is used in the manufacture of medicines to improve their dissolving ability. Along with the water-absorbing capacity the agent is good enough to sorb radionuclides from the human body. The substance is resistant to high temperatures, and since the density of Na-CMC is 1590 kg/m^3, this fibrous material has a high stabilizing ability.

Chitosan is a polymer rather coherent to hydrophilic sedimentary shells of hydrophilic adsorptive assemblages. Taking into consideration the anti-allergic properties of chitosan and its ability to deliver biopolymer drugs to diseased areas of human bodies and dose them, the potential of the biopolymer to taken as a polymer matrix is also among the objects of research.

The mineral bentonite extracted at the Tagan deposit was purified from various solid sand impurities and then subjected to heat treatment in a vacuum drying oven at a temperature of 220°C for two hours. In the paper a highly dispersed fraction of the Tagan montmorillonite, with an average radius of 1.4±0.2 mm, measured by the ZetaSizer device (Malvern-NanoZS, England) is described. Montmorillonite was subjected to dispersion in water at pH 7 and fractionation by sedimentation method for 24 hours. The particles that remained unsettled after 24 hours of settling were used then for the research purposes. The turbidimetric method was used to study the suspensions stability. The optical density (A) was measured on a PD-303 spectrophotometer (Japan). The system was subjected to constant slow stirring at a magnetic stirrer, at a wavelength of 540 nm. The kinetics of the optical density changes depending on the electrolyte and flocculant concentration showed the sedimentation rate.

The prepared suspension and stabilizers were stirred in a magnetic stirrer for one minute. The finished system was filled into the cuvette of PD-303 spectrophotometer, and observed for the changes in its optical density with recording them every 40 minutes.

The magnetite particles have been released by the sedimentation method. For this purpose an aqueous solution of ammonium (15%) was added to $FeCl_3*6H_2O$ and $FeSO_4*7H_2O$ solutions, whose pH were 9.5-11.0, in a molar ratio of 2:1, at indoor temperature and normal pressure. The resulting suspension was stirred at ambient temperature for 30 minutes, then filtered, washed with distilled water and dried at 130°C. The simplest and most sensitive device is

Figurovsky's hydrostatic microbalance, the change in the deformation of the rocker during the experiment is recorded using a reference microscope or cathetometer. The sensitivity of the device depends on the length and thickness of the rocker arm. The main advantage of the method is the possibility of studying dilute suspensions with concentrations from 0.2 to 0.001%.

The resulting suspension of magnetite first acquires a black color, but after drying it turns into a dark brown powder. The process reaction equation is, as follows:

$$2FeCl_3 + FeSO_4 + 8NH_4OH \rightarrow Fe_3O_4 + 6NH_4Cl + (NH_4)_2SO_4 + 4H_2O$$

Introduction of magnetite into the clay structure is an effective way to afford magnetic fluids. According to this method the bentonite clay hydrosuspension was added with a solution of divalent iron and settled for 24 hours. Then it was kept in a solution of $FeCl_3$ for about 2 more hours, then settled at the air temperature of 25 °C, using ammonia water with a pH of 9.5-11.0. Finally, there were obtained clay-magnetite composites of brown–black color. This increases the absorption capacity of iron ions on the clay surface and turns them into exchange cations, and displacing water molecules contributes to the expansion of the space between them. Since we knew the theoretical mass of magnetite resulted from the reaction, and assumed that the same amount of it should be formed in the clay structure, appropriate amounts of clay were afforded to produce magnetic clay with a mass of 5, 10, 20 and 50% of magnetite (Table 2).

Table 2. Elemental composition of primary bentonite
and magnetic composite samples

Sample	Composite	Share of Fe, %	Share of Fe$_3$O$_4$, %
Bentonite		−	−
Magnetic composite 5 %	MC 1	0,74	4,37
Magnetic composite 10 %	MC 2	1,84	9,62
Magnetic composite 25 %	MC 3	5,89	24,44
Magnetic composite 50 %	MC 4	6,70	27,78

Synthesizing of magnetite is determined to be according to the reaction, as follows:

$$2FeCl_3 + FeCl_2 + 8NH_4OH \rightarrow Fe3O_4\downarrow + 8NH_4Cl + 4H_2O$$

$$2FeCl_3*6H_2O + FeSO_4*7H_2O + 8NH_4OH \rightarrow Fe_3O_4\downarrow + 6NH_4Cl + (NH_4)_2SO_4 + 23H_2O$$
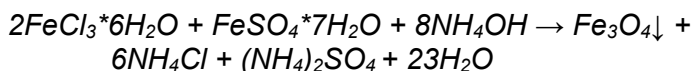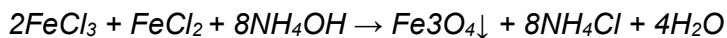
CONCLUSION

For the study purposes of magnetic montmorillonite physicochemical properties in water, the Elmore method [23] was used to afford magnetic montmorillonites with different magnetite (Fe_3O_4) concentrations (5%, 10%, 20% and 50%) from two (Fe^{2+}) and three (Fe^{3+}) valence iron salts in a weak alkaline medium (in an aqueous solution of ammonium hydroxide). The obtained magnetic montmorillonites were studied by the X-ray phase method and proved to contain hematite and magnetite. Natural polymers of sodium alginate and chitosan have been studied for the effect they have on the stability of magnetic montmorillonite hydrosuspension. The maximum stability was observed in the presence of 0.25 % sodium alginate. The flocculation properties of chitosan have been observed at lower concentrations.

REFERENCES

1. O. V. Alekseeva; A. N. Rodionova; N. A. Bagrovskaya; A. V. Agafonov; *Prot.Met. Phys.Chem.Surf.*, **2016**, *52,* 819-824
2. O. V. Alekseeva; A. N. Rodionova; A. V. Noskov; A. V. Agafonov; *Clays Clay Miner.,* **2019**, *67*, 471-480
3. E. M. Sapargaliev; *Geology Subsurface Prot.*, **2008**, *4,* 42-49
4. I. Sharifi; H. Shokrollahi; S. Amiri; *J.Magn.Magn. Mat.,* **2012**, *324,* 903-915
5. J. De Vicente; D. J. Klingenberg; R. Hidalgo-Alvarez; *Soft Matter.,* **2011**, *7,* 3701-3710
6. M. T. López-López; A. Gómez-Ramírez; L. Rodríguez-Arco; J. D. G. Durán; L. Iskakova; A. Zubarev; *Langmuir*, **2012,** *28,* 6232-6245
7. A. Joseph; S. Mathew; *ChemPlusChem*, **2014**, 79, 1382-1420
8. S. Genc; B. Derin; *Curr. Opin. Chem. Eng.*, **2014**, *3*, 118-124
9. P. Ilg; S. Odenbach; *Ferrofluid Structure and Rheology. In: Odenbach S.* (eds) Colloidal Magnetic Fluids. Lecture Notes in Physics, Springer, Berlin, Heidelberg, **2009**
10. Ye. Jien; L. Yating; S. Jiacong; Sh. Jiyan; *Nanomaterials,* **2021***, 11,* 2580
11. A. C. H. Barreto; F. J. N. Maia; V. R. Santiago; V. G. P. Ribeiro; J. C. Denardin; G. Mele; L. Carbone; D. Lomonaco; S. E. Mazzetto; P. B. A. Fechine; *Microfluid Nanofluid,* **2012**, *12,* 677-686
12. E. Annan; E. Nyankson; B. Agyei-Tuffour; S. K. Armah; G. Nkrumah-Buandoh; J. A. M. Hodasi; M. Oteng-Peprah; *Adv. Mat. Sci. Eng.,* **2021,** 6679422
13. F. Canfarotta; S. A. Piletsky; *Adv. Healthc. Mat.,* **2014,** *3,* 160-175
14. K. Iryna; T. Viktoriia; K. Yurii; Z. Nataliia; K. Borys; *Technol. Audit Prod. Reserves,* **2020**, *3 (53),* 12-18
15. L. D. Matteis; L. Custardoy; R. Fernández-Pacheco; C. Magén; J. M. de la Fuente; C. Marquina; M. R. Ibarra; *Chem. Mater.,* **2012**, *24,* 451-456

16. X. Yang; W. Jiang; L. Liu; B. Chen; S. Wu; D. Sun; F. Li; *J. Magn. Magn. Mat.,* **2012,** *324,* 2249-2257
17. S. Rana; J. Philip; B. Raj; *Mat. Chem. Phys.,* **2010,** *124,* 264-269
18. Sh. Barakan; V. Aghazadeh; A. S. Beyragh; S. Mohammadi; *Environ. Dev. Sustain.*, **2020**, *22*, 5273-5295
19. A. Durdureanu-Angheluta; A. Dascalu; A. Fifere; A. Coroaba; L. Pricop; H. Chiriac; V. Tura; B. C. Simionescu; *J. Magn. Magn. Mat.,* **2012,** *6,* 162-166
20. Zh. Lakhbayeva; G. Kurmangazhy; S. Tazhibayeva; D. Artykova; K. Musabekov; *J. Chem. Technol. Metall.,* **2019,** *54,* 603-609
21. J. Chang; J. Ma; Q. Ma; D. Zhang; *J. Appl. Clay Sci.,* **2016,** *119,* 132-140
22. V. Zheltova; A. Vlasova; N. Bobrysheva; I. Abdullin; V. Semenov; M. Osmolowsky; M. Voznesenskiy; O. Osmolovskaya; *Appl. Surf. Sci.*, **2020,** *531,* 147352
23. W. C. Elmore; *Phys. Rev.*, **1938**, *54*, 309-310

RADIOCARBON INVESTIGATION OF TWO LARGE AFRICAN BAOBABS FROM KIZIMKAZI, ZANZIBAR, TANZANIA

ADRIAN PATRUT[a,b]*, ROXANA T. PATRUT[a], LASZLO RAKOSY[c], ILEANA-ANDREEA RATIU[a,b], JENÖ BODIS[a,b], NASSOR MAHMOUD NASSOR[d], KARL F. VON REDEN[e]

ABSTRACT. The article reports the AMS (accelerator mass spectrometry) radiocarbon dating results of Kizimkazi Big tree and Kizimkazi II baobab, two large African baobabs from Zanzibar, Tanzania. Unfortunately, both baobabs toppled and died in 2018 and 2020, during violent storms. The investigation of the two baobabs evinced that the first of them, which was also the biggest tree of Tanzania, consisted of 5 stems, out of which 2 were false ones, and had a closed ring-shaped structure. The second baobab was composed of 4 fused stems and had a cluster structure. Several wood samples were collected from the two baobabs. Seven segments were extracted from the samples and dated by radiocarbon. The oldest segment from Kizimkazi Big tree had a radiocarbon date of 312 ± 18 BP, corresponding to a calibrated age of 380 ± 10 calendar years. According to dating results, the Kizimkazi Big tree died at the age of 400 ± 25 years. The oldest segment from Kizimkazi II baobab had a radiocarbon date of 137 ± 17 BP, corresponding to a calibrated age of 190 ± 10 calendar years. This value indicates that the Kizimkazi II baobab was 250 ± 25 years old when it died.

Keywords: *AMS radiocarbon dating, Adansonia digitata, dendrochronology, age determination, multiple stems, false cavity.*

---

[a] *Babeş-Bolyai University, Faculty of Chemistry and Chemical Engineering, 11 Arany Janos, RO-400028, Cluj-Napoca, Romania.*
[b] *Babeş-Bolyai University, Raluca Ripan Institute for Research in Chemistry, 30 Fantanele, RO-400294 Cluj-Napoca, Romania.*
[c] *Babeş-Bolyai University, Faculty of Biology and Geology, 44 Republicii, RO-400015 Cluj-Napoca, Romania.*
[d] *Private investigator, Kizimkazi Dimbani, Zanzibar, Tanzania.*
[e] *NOSAMS Facility, Dept. of Geology & Geophysics, Woods Hole Oceanographic Institution, Woods Hole, MA 02543, U.S.A.*
* *Corresponding author: apatrut@gmail.com.*

INTRODUCTION

The *Adansonia* genus, which belongs to the Bombacoideae subfamily of Malvaceae, is represented by six species endemic to Madagascar, one species restricted to NW Australia and one or two species distributed throughout the tropics of mainland Africa. The African baobab (*Adansonia digitata* L.) is the best known and widespread of the eight or nine *Adansonia* species. The African baobab is endemic to the arid savanna of mainland Africa between the latitudes 16º N and 26º S. It can also be found on several African islands and outside Africa, in different areas throughout the tropics, where it has been introduced [1-6].

In 2005, we started an extended research project to elucidate several controversial aspects concerning the architecture, growth and age of the African baobab. This research is based on a new approach, which is not limited to fallen specimens, but allows to investigate and date live individuals, as well. Our approach consists of AMS radiocarbon dating of tiny wood samples collected especially from inner cavities, deep incisions/entrances in the stems, fractured stems and from the exterior of large baobabs [7-17]. According to the research results, all large and old baobabs are practically multi-stemmed and exhibit preferentially closed or open ring-shaped structures. The oldest specimens were found to reach ages up to 2,500 years [14].

Since 2013 our investigations include also large and old individuals of the three best-known species of Madagascar, i.e., *Adansonia za* Baill. (Za baobab), *Adansonia rubrostipa* Jum. & H. Perrier (Fony baobab) and *Adansonia grandidieri* Baill. (Grandidier baobab) [18-22].

Zanzibar is an archipelago in the Indian Ocean, 36 km off the east coast of Africa. It is formed by two main islands, Zanzibar (or Unguja) and Pemba, plus over 50 smaller islands.

Over the centuries, Zanzibar has been visited and occupied by traders, explorers and settlers. In 1840, the Sultan of Oman transferred the seat of his Government to Zanzibar. In 1890, the British proclaimed Zanzibar a protectorate. Zanzibar became an independent state in December 1963, but only for a short time. In April 1964, Zanzibar formed an Union with Tanganyika under the name of the United Republic of Tanzania. Today, Zanzibar is still a semi-autonomous region of Tanzania [23].

The climate of Zanzibar is tropical, hot all year around, with two rainy seasons, known as the "long rains" season (March to May) and the "short rains" season (mid-October to December). The annual rainfall can reach 1600 mm in Zanzibar Island and 1900 mm in Pemba.

Zanzibar has a large population of African baobabs, with many big individuals. The baobabs grow especially in Zanzibar Island and Pemba.

According to our estimate, only Zanzibar Island hosts between 1 and 2 million individuals. The baobabs are mainly concentrated in the south-west and south-east, in the central area around Zanzibar Town and in the north-west. Here we present the investigation and AMS radiocarbon dating results of two very large baobabs from Kizimkazi, Zanzibar Island.

RESULTS AND DISCUSSION

The investigated baobabs and their areas. Kizimkazi is located on the south-western coast of Zanzibar Island. It consists of two villages, just down the road from each other. The most important is Kizimkazi Mkunguni (also known as Kizimkazi Mtendeni), a fishing village with a wide beach, new guesthouses and beachfront hotels. The second village, Kizimkazi Dimbani, is located several kilometres to the north and was once a walled city. It is the site of the Shirazi Mosque, the oldest mosque in Zanzibar with inscriptions dating back to 1107 [23]. Kizimkazi hosts many large baobabs, out of which 7 trees have girth values over 15 m. Unfortunately, the two largest trees, which we called Kizimkazi Big baobab and Kizimkazi II baobab, toppled and died recently.

Figure 1. General view of the Kizimkazi Big tree in 2015, taken from the east.

The Kizimkazi Big tree and its area. The impressive baobab was located in Kizimkazi Mkunguni at a distance of only 80 m from the ocean shore. The GPS coordinates are 06º27.209' S, 039º28.298' E and the altitude is 4 m. The mean annual rainfall in the area is 1147 mm, while the mean annual temperature reaches 26.4 °C (Zanzibar Town/Kisauni station). The Big tree had a maximum height of 21.8 m, the circumference at breast height (cbh; at 1.30 m above ground level) was 22.38 m and the overall wood volume was around 310 m^3 (**Figures 1 and 2**). The horizontal dimensions of the canopy were 35.5 (NS) x 46.5 (WE) m. In terms of volume, this baobab of Kizimkazi Mkunguni was the biggest tree not only in Zanzibar, but also in the whole Tanzania. The Kizimkazi Big tree toppled and died during a violent tropical storm in December 15, 2020.

Figure 2. View of the Kizimkazi Big tree taken from the west. The two investigated samples KBT-1 and KBT-2 were collected from the large stem in the centre of the image and from the false stem on the right.

The Big tree consisted of 5 stems, out of which 2 were false stems, which provided a better stability in sandy soils [24]. According to dating results, the baobab exhibited a closed ring-shaped structure [11, 14], with a false cavity

defined by three stems, which was completely closed. This architecture was confirmed in December 2020, when the Big tree split (**Figure 3**) before it collapsed completely (**Figure 4**).

The Kizimkazi II baobab and its area. The second largest baobab of Kizimkazi in terms of girth was located in a private garden of Kizimkazi Dimbani. The GPS coordinates are 06º26.812' S, 039º25.485' E and the altitude is 16 m. The baobab had a maximum height of 22.2 m, the circumference at breast height was 20.45 m and the overall wood volume was around 180 m^3 (**Figures 5**). The horizontal dimensions of the canopy were 25.5 (NS) x 23.3 (WE) m. The baobab had a cluster structure and consisted of 4 perfectly fused stems. The Kizimkazi II baobab also toppled and died due to very strong winds during the monsoon in April 12, 2018.

Figure 3. The Kizimkazi Big tree split during a violent storm in December 2020, revealing the false cavity inside its multi-stemmed trunk.

Figure 4. The Kizimkazi Big tree collapsed totally several days after the violent storm.

Figure 5. General view of the Kizimkazi II baobab. The investigated sample KIIB-1 was collected from the stem on the right of the image.

Wood samples. Two wood samples were collected from the exterior of each baobab with an increment borer.

One sample, labelled KBT-1, with the length of 0.80 m, was collected from the largest stem of the Kizimkazi Big tree, at the height of 1.97 m. A number of four tiny pieces/segments, each 10^{-3} m long (marked from a to d), were extracted from determined positions of sample KBT-1. Another sample, labelled KBT-2, was collected from the deepest end/origin of the biggest false stem, at the height of 2.12 m. One segment (marked x) was extracted from this sample.

Two other samples, labelled KIIB-1 and KIIB-2, with the length of 0.78 m and 0.26 m, were collected from two stems of the Kizimkazi II baobab, at heights of 2.10 and 2.03 m. The second sample KIIB-2 was too short for investigation. Therefore, we investigated only the first sample KIIB-1, from which we extracted two tiny segments (marked a and b) from determined positions.

AMS results and calibrated ages. Radiocarbon dates of the seven sample segments are listed in Table 1. The radiocarbon dates are expressed in ^{14}C yr BP (radiocarbon years before present, i.e., before the reference year 1950). Radiocarbon dates and errors were rounded to the nearest year.

Table 1. AMS Radiocarbon dating results and calibrated ages of samples collected from the Kizimkazi Big tree (KBT) and from the Kizimkazi II baobab (KIIB).

Sample code	Depth[1] [height[2]] (m)	Radiocarbon date [error] (^{14}C yr BP)	Cal CE range 1σ [confidence interval]	Assigned year [error] (cal CE)	Sample age [error] (cal CE)
KBT-1a	0.30 [1.97]	154 [± 20]	1696-1724 [16.0%] **1834-1890 [35.8%]** 1924-... [16.5%]	1862 [± 28]	160 [± 30]
KBT-1b	0.50 [1.97]	212 [± 20]	1671-1684 [12.3%] **1732-1782 [48.5%]** 1796-1804 [7.5%]	1757 [± 15]	265 [± 15]
KBT-1c	0.70 [1.97]	312 [± 18]	1516-1540 [22.5%] **1627-1652 [45.8%]**	1639 [± 12]	380 [± 10]
KBT-1d	0.80 [1.97]	257 [± 19]	**1650-1671 [41.9%]** 1782-1796 [26.4%]	1660 [± 10]	360 [± 10]
KBT-2x	0.50 [2.12]	230 [± 17]	1668-1673 [6.1%] **1739-1798 [62.2%]**	1764 [± 15]	255 [± 15]
KIIB-1a	0.40 [2.10]	95 [± 21]	1821-1830 [10.4%] **1892-1922 [57.9%]**	1907 [± 15]	110 [± 15]
KIIB-1b	0.78 [2.10]	137 [± 17]	1706-1720 [11.0%] **1813-1836 [19.1%]** 1850-1866 [11.7%] 1879-1896 [13.2%] 1904-1926 [13.3%]	1824 [± 10]	190 [± 10]

[1] Depth in the wood from the sampling point. [2] Height above ground level.

Calibrated (cal) ages, expressed in calendar years CE (CE, i.e., common era), are also displayed in Table 1. The 1σ probability distribution (68.3%) was selected to derive calibrated age ranges. For four segments (KBT-1c, KBT-1d, KBT-2x, KIIB-1a), the 1σ distribution is consistent with two ranges of calendar years, for two sample segments (KBT-1a, KBT-1b) it corresponds to three ranges and for one range (KIIB-1b) it corresponds to five ranges. In all these cases, the confidence interval of one range is considerably greater than that of the other(s); therefore, it was selected as the cal CE range of the segment for the purpose of this discussion.

For obtaining single calendar age values of sample segments, we derived a mean calendar age of each sample segment, called assigned year, from the selected range (marked in bold). Sample/segment ages represent the difference between the year 2020 CE (for samples KBT-1 and KBT-2, when the Kizimkazi Big tree died) or the year 2018 CE (for sample KIIB-1, when the Kizimkazi II baobab died) and the assigned year, with the corresponding error. Sample ages and errors were rounded to the nearest 5 yr. This approach for selecting calibrated age ranges and single values for sample ages was used in our previous articles on AMS radiocarbon dating of large and old angiosperm trees.

Dating results of samples. In the case of Kizimkazi Big tree, for the segments extracted from sample KBT-1, which was collected from the exterior, the age values increase from KBT-1a to KBT-1c, after which the age decreases to KBT-1d. This anomalous age sequence is characteristic to baobabs that possess a closed ring-shaped structure with a false cavity inside. In this architecture, for wood samples collected from the exterior of the trunk, as well as for samples collected from the inner cavity walls (if the false cavity has an accessible opening), the age sequence increases from the sampling point up to a point of maximum age, after which it decreases in the opposite direction [11, 14]. For sample KBT-1, segment ages show that the point of maximum age was located between the segments KBT-1c and KBT-1d, i.e., between 0.70 and 0.80 m from the sampling point. Therefore, the maximum age in the direction of sample KBT-1 was around 400 ± 25 calendar yr. The walls of the false cavity, which was defined by 3 fused stems and was completely closed toward the exterior, had a depth of 1.30-1.40 m.

The second sample KBT-2 originated from the largest false stem, namely close to its emergence from the adjacent ordinary stem. The age of segment KBT-2x, i.e., 255 ± 15 years, corresponds to the age of the false stem, which assured a better stability of the huge tree in the sandy soil [24].

For the Kizimkazi II baobab, the investigated sample KIIB-1 was collected from a deep incision (0.30 m) in a stem, at the height of 2.10 m above ground, where the circumference of the four-stemmed trunk was 17.60 m. According to these values, the diametre of the sampled stem at this height

was 2.80 m and its theoretical pith was situated at 1.10 m from the sampling point. Consequently, the distance between the dated segment KIIB-1b, which was 190 ± 10 yr old, and the theoretical pith of the stem was 0.33 m. These values indicate an age of 250 ± 25 yr for the pith of the sampled stem, as well as for the Kizimkazi II baobab.

CONCLUSIONS

The research discloses the AMS radiocarbon investigation results of two very large African baobabs from Kizimkazi, Zanzibar Island, Tanzania, which we called Kizimkazi Big tree and Kizimkazi II baobab. The main aim of our research was to determine the architecture and the age of the two baobabs. Unfortunately, the two baobabs toppled and died in 2020 and 2018, due to violent storms with strong winds. Thus, they are added to the list of monumental baobabs from southern Africa which collapsed and died since 2005.

The Kizimkazi Big tree was composed of 5 stems, out of which 3 were ordinary and 2 were false stems. It exhibited a closed ring-shaped structure, with a false cavity inside which was completely closed. The oldest sample segment had a radiocarbon date of 312 ± 18 BP, which corresponds to a calibrated age of 380 ± 10 calendar yr. According to dating results, the Kizimkazi Big tree started growing 400 ± 25 years ago, while the largest false stem was 255 ± 15 years old.

The Kizimkazi II baobab consisted of 4 perfectly fused stems and had a cluster structure. The oldest sample segment had a radiocarbon date of 137 ± 17 BP, corresponding to a calibrated age of 190 ± 10 calendar yr. According to this value, the Kizimkazi II baobab had an age of 250 ± 25 years when it died.

The obtained dating results demonstrate that, due to the very high amount of precipitation, the baobabs of Zanzibar grow very fast and can reach very large dimensions at a young age.

EXPERIMENTAL SECTION

Sample collection. The wood samples were collected from the two baobabs with a Haglöf CH 800 increment borer (0.80 m long, 0.0054 m inner diameter). A number of seven segments of the length of 10^{-3} m were extracted from predetermined positions along the wood samples. The segments were processed and investigated by AMS radiocarbon dating.

Sample preparation. The standard acid-base-acid pretreatment method was used for removing soluble and mobile organic components [25]. The pretreated samples were combusted to CO_2 by using the closed tube combustion method [26]. Next, CO_2 was reduced to graphite on iron catalyst [27]. Eventually, the resulting graphite samples were investigated by AMS.

AMS measurements. AMS radiocarbon measurements were performed at the NOSAMS Facility of the Woods Hole Oceanographic Institution (Woods Hole, MA, U.S.A.), by using the Pelletron ® Tandem 500 kV AMS system. The obtained fraction modern values, corrected for isotope fractionation with the normalized $\delta^{13}C$ value of -25 $^0/_{00}$, were converted to a radiocarbon date.

Calibration. Radiocarbon dates were calibrated and converted into calendar ages with the OxCal v4.4 for Windows [28], by using the SHCal20 atmospheric data set [29].

ACKNOWLEDGEMENTS

REFERENCES

1. G.E. Wickens, *Kew Bull.*, **1982**, *37(2)*, 172-209.
2. D.A. Baum, *Ann. Mo. Bot. Gard.*, **1995**, *82*, 440-471.
3. G.E. Wickens, P. Lowe, "The Baobabs: Pachycauls of Africa, Madagascar and Australia", Springer, Dordrecht, **2008**, pp. 232-234, 256-257, 295-296.
4. J.D. Pettigrew, L.K. Bell, A. Bhagwandin, E. Grinan, N. Jillani, J. Meyer, E. Wabuyele, C.E. Vickers, *Taxon*, **2013**, *61*, 1240-1250.
5. A. Petignat, L. Jasper, "Baobabs of the world: The upside down trees of Madagascar, Africa and Australia", Struik Nature, Cape Town, **2015**, pp. 16-86.
6 G.V. Cron, N. Karimi, K.L. Glennon, C.A. Udeh, E.T.F. Witkowski, S.M. Venter, A.E. Assobadjo, D.H. Mayne, D.A. Baum, *Taxon*, **2016**, *65*, 1037-1049.
7. A. Patrut, K.F. von Reden, D.A. Lowy, A.H. Alberts, J.W. Pohlman, R. Wittmann, D. Gerlach, L. Xu, C.S. Mitchell, *Tree Physiol.*, **2007**, *27*, 1569-1574.
8. A. Patrut, D.H. Mayne, K.F. von Reden, D.A. Lowy, R. Van Pelt, A.P. McNichol, M.L. Roberts, D. Margineanu, *Radiocarbon*, **2010**, *52(2-3)*, 717-726.
9. A. Patrut, K.F. von Reden, R. Van Pelt, D.H. Mayne, D.A. Lowy, D. Margineanu, *Ann. Forest Sci.*, **2011**, *68*, 93-103.

10. A. Patrut, K.F. von Reden, D.H. Mayne, D.A. Lowy, R.T. Patrut, *Nucl. Instrum. Methods Phys. Res. Sect. B*, **2013**, *294*, 622-626.
11. A. Patrut, S. Woodborne, K.F. von Reden, G. Hall, M. Hofmeyr, D.A. Lowy, R.T. Patrut, *PLOS One*, **2015**, *10(1): e0117193.*
12. A. Patrut, S. Woodborne, K.F. von Reden, G. Hall, R.T. Patrut, L. Rakosy, J-M. Leong Pock Tsy, D.A. Lowy, D. Margineanu, *Radiocarbon*, **2017**, *59(2)*, 435-448.
13. A. Patrut, L. Rakosy, R.T. Patrut, I.A. Ratiu, E. Forizs, D.A. Lowy, D. Margineanu, K.F. von Reden, *Studia UBB Chemia*, **2016**, *LXI, 4,* 7-20.
14. A. Patrut, S. Woodborne, R.T. Patrut, L. Rakosy, D.A. Lowy, G. Hall, K.F. von Reden, *Nat. Plants*, **2018**, *4(7)*, 423-426.
15. A. Patrut, R.T. Patrut, L. Rakosy, D.A. Lowy, D. Margineanu, K.F. von Reden, *Studia UBB Chemia*, **2019**, *LXIV, 2 (II)*, 411-419. doi:10.24193/subbchem.2019.2.35.
16. A. Patrut, S. Woodborne, R.T. Patrut, G. Hall, L. Rakosy, C. Winterbach, K.F. von Reden, *Forests*, **2019**, *10*, 983-993.
17. A. Patrut, A. Garg, S. Woodborne, R.T. Patrut, L. Rakosy, I.A. Ratiu, *PLOS One*, **2020**, *15(1): e0227352.*
18. A. Patrut, K.F. von Reden, P. Danthu, J-M. Leong Pock-Tsy, R.T. Patrut, D.A. Lowy, *PLOS One*, 2015, *10(3): e0121170*. doi:10.1371/journal.pone.0121170.
19. A. Patrut, K.F. von Reden, P. Danthu, J-M. Leong Pock-Tsy, L. Rakosy, R.T. Patrut, D.A. Lowy, D. Margineanu, *Nuclear Instruments and Methods in Physics Research Section B*, 2015, *361*, 591-598.
doi:10.1016/ j.nimb.2015.04.044.
20. A. Patrut, R.T. Patrut, P. Danthu, J-M. Leong Pock-Tsy, L. Rakosy, D.A. Lowy, K.F. von Reden, *PLOS One*, 2016, *11(1): e146977*. doi:10.1371/journal.pone. 0146977.
21. R.T. Patrut, A. Patrut, J-M. Leon Pock Tsy, S. Woodborne, L. Rakosy, P. Danthu, I-A. Ratiu, J. Bodis, K.F. von Reden, *Studia UBB Chemia*, **2019**, *LXIV, 4*, 131-139.
22. A. Patrut, R.T. Patrut, J-M Leong Pock-Tsy, S. Woodborne, L. Rakosy, I-A. Ratiu, J. Bodis, P. Danthu, *Studia UBB Chemia*, **2020**, *LXV, 4*, 151-158.
23. A. Harley, I. Sim, J. Jafferji, "Zanzibar: An essential guide", Gallery Publications, Zanzibar, **2010**, pp. 25-39.
24. A. Patrut, S. Garnaud, O. Ka, R.T. Patrut, T. Diagne, D.A. Lowy, E. Forizs, J. Bodis, K.F. von Reden, *Studia UBB Chemia*, **2017**, *LXII, 1*, 111-120.
25. N.J. Loader, I. Robertson, A.C. Barker, V.R. Switsur, J.S. Waterhouse, *Chem. Geol.*,**1997**, 136(3), 313–317.
26. Z. Sofer, *Anal. Chem.*, **1980**, *52(8)*, 1389-1391.
27. J.S. Vogel, J.R. Southon, D.E. Nelson, T.A. Brown, *Nucl. Instrum. Methods Phys. Res. Sect. B*, **1984**, *5*, 289-293.
28. C. Bronk Ramsey, *Radiocarbon*, **2009**, *51*, 337-360.
29. A.G. Hogg, T.J. Heaton, Q. Hua, J.G. Palmer, C.S.M. Turney, J. Southon, A. Bayliss, P.G. Blackwell, G. Boswijk, C.B. Ramsey, C. Pearson, F. Petchey, P.J. Reimer, R.W. Reimer, L. Wacher, *Radiocarbon*, **2020**, *62(4)*, 759-778.

DESIGN, SYNTHESIS, BIOLOGICAL EVALUATION, AND *IN SILICO* STUDY OF NOVEL UREA DERIVATIVES AS INHIBITORS OF CARBONIC ANHYDRASE AND ACETYLCHOLINE ESTERASE

YUSUF AKBABA[a], RAMAZAN KALIN[a,*]

ABSTRACT. This study aimed to synthesize novel unsymmetrical urea derivatives containing biologically active tryptamine and phenethylamines and investigate their inhibition effects on human carbonic anhydrase (hCA) I and II isozymes as well as acetylcholinesterase (AChE). For this purpose, five different N,N'-dialkyl urea derivatives **18-22** were synthesized from tryptamine and substituted 2-phenethylamine. According to the results of inhibition, all of the synthesized urea derivatives effectively inhibited both hCA (I - II) and AChE enzymes at micromolar concentrations. The IC_{50} values for these molecules were determined to be in the range of 1.214-2.281 µM for hCA-I, 0.888-2.984 µM for hCA-II, and 0.309-0.816 µM for AChE. The most potent inhibitors against hCA-I and hCA-II isozymes are compound 18 (IC_{50}: 1.214 µM; K_i: 0.984 ± 0.277 µM) and compound **19** (IC_{50}: 0.888 µM, K_i: 0.564 ± 0.019 µM), respectively. Furthermore, compound **20** (IC_{50}: 0.309 M and K_i: 0.470 ± 0.039 M) is the most effective AChE inhibitor. Molecular docking studies of compounds with the most effective inhibition were performed. The estimated binding energy values for compounds **18**, **19**, and **20** were calculated to be −7.81, -7.34, and -8.20 kcal/mol, respectively. Finally, the ADME studies were determined these compounds' physicochemical and pharmacokinetic descriptors and drug-like properties.

Keywords: *biological activity, tryptamine, phenethylamine, toxicology, molecular docking, ADME*

INTRODUCTION

N, N'-dialkyl, and N, N'-alkyl aryl ureas are very significant compounds having large application areas due to their physiological and pharmacological activities. For example **1**: (a selective GSK-3β inhibitor) has been evaluated for the treatment of Alzheimer's disease[1][2], **2**: eicosapentaenoic acid

---

[a] *Erzurum Technical University, Faculty of Science, Department of Basic Sciences 25100, Erzurum, Türkiye.*

* *Corresponding author: ramazan.kalin@erzurum.edu.tr.*

derived regulator of cardiomyocyte contraction[3], **3**: (a somatostatin agonist) is used for the treatment of Alzheimer's disease and depression[1,2,4], **4**:1-(1-arylimidazolidine-2-ylidene)-3-(4-chlorobenzyl) urea as antiviral[5], **5**: urotensin-II receptor agonists (ACT-058362)[6], **6**: TRPV1 antagonists (A-425619)[7][8] (Figure 1).
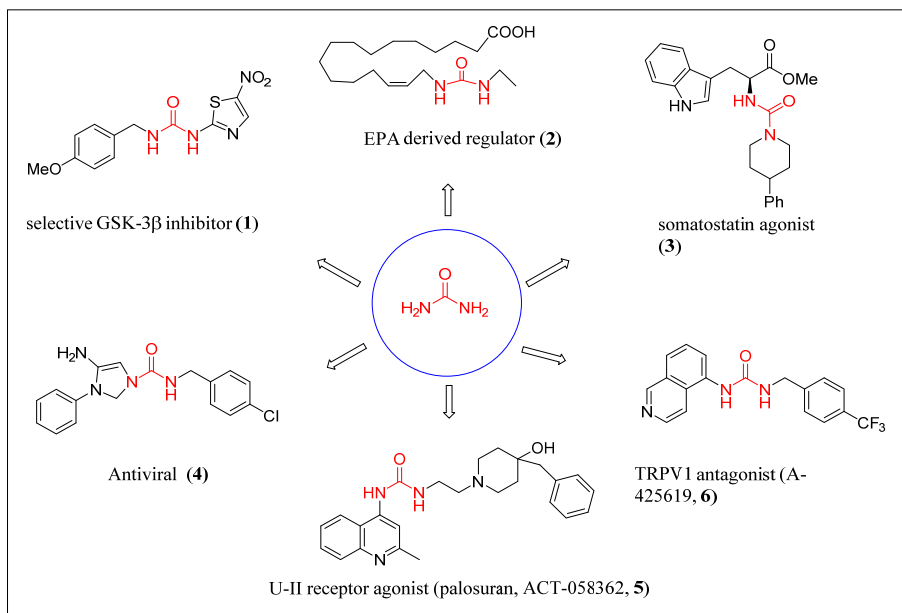

Figure 1. Some biologically active N, N'-dialkyl and N, N'-alkyl aryl urea derivatives **1-6**

On the other hand, in the mammalian brain, tryptamine, an indolamine metabolite of the essential amino acid tryptophan [9], has been demonstrated to activate amine-associated trace receptors and regulate glutamatergic, serotonergic, and dopaminergic system activity[10][11]. Furthermore, 2-phenethylamines are found in a wide range of biologically active compounds and drugs[12].

Carbonic anhydrase (EC 4.2.1.1., CA), a member of the metalloenzyme family, acts as a pH-regulating enzyme in all prokaryotic and eukaryotic life kingdoms[13]. It is known to have 7 different genetic families, namely α, β, γ, δ, ζ, η and θ CAs. α-CAs, which are found in a lot of organisms such as algae, green plants, protozoa, vertebrates, and some bacteria, are the most studied CA family in the world[14]. So far, 16 α-CA isozymes have been identified in terms of catalytic activity, sensitivity to different inhibitor classes, and subcellular localization (cytosolic, membrane-bound, mitochondrial, and saliva secretion).

CAs reversibly hydrate CO_2 (carbon dioxide) to HCO_3 (bicarbonate) and H^+ (proton) through a metal hydroxide nucleophilic mechanism[15]. Also, these isozymes play a crucial role in several metabolic processes such as bone resorption, fluid balance, calcification, edema, osteoporosis, glaucoma, tumor production, pH regulation, cancer, carboxylation reactions, and epilepsy[16].

Acetylcholine (ACh), an important substance for cholinergic neurotransmission in the peripheral and central nervous systems, is a molecule synthesized from choline at pre-synaptic terminals. This molecule is the most basic neurotransmitter that activates the muscles in the peripheral nervous system. Acetylcholinesterase (E.C.3.1.1.7., AChE), which is involved in the hydrolysis mechanism of ACh in living things, is an enzyme that breaks down acetylcholine into choline and acetate in synaptic spaces[17]. Alzheimer's disease (AD) is a dementia disease that occurs as a result of the decrease of neurotransmitters in the brain, such as ACh. AD, a neurodegenerative disorder, is associated with a decrease in the amount of acetylcholine in the brain[18]. In this disease, one of the most complex neuron degradation problems of the 21st century, important functions such as speaking ability, perception and judgment capacity, abstract thinking, and problem-solving are affected. Today, AChE inhibitors such as donepezil and rivastigmine are used to eliminate the symptoms of the disease[19–21].

As discussed above, N-N' dialkyl urea derivatives show significant biological activities. In this study, some new N-N' dialkyl urea derivatives **18-22** derived from tryptamine and phenethylamines were synthesized, and their inhibitory properties against hCA (I-II) and AChE were investigated.

RESULTS AND DISCUSSION

Chemistry

Isocyanates are important precursor intermediates for the synthesis of biologically active compounds. Synthesis of isocyanates occurs very easily with triphosgene in the literature[22]. Therefore, phenethylamines **7-11** were reacted with triphosgene to give isocyanate intermediates **12-16**. Then, the reactions of isocyanates **12-16** with Tryptamine **17** afforded novel unsymmetrical ureas **18-22** in good yields (72%-78%) (Scheme 1). Elemental analysis, IR, ^{1}H-NMR, and ^{13}C-NMR were used to determine the chemical structures of synthesized compounds.
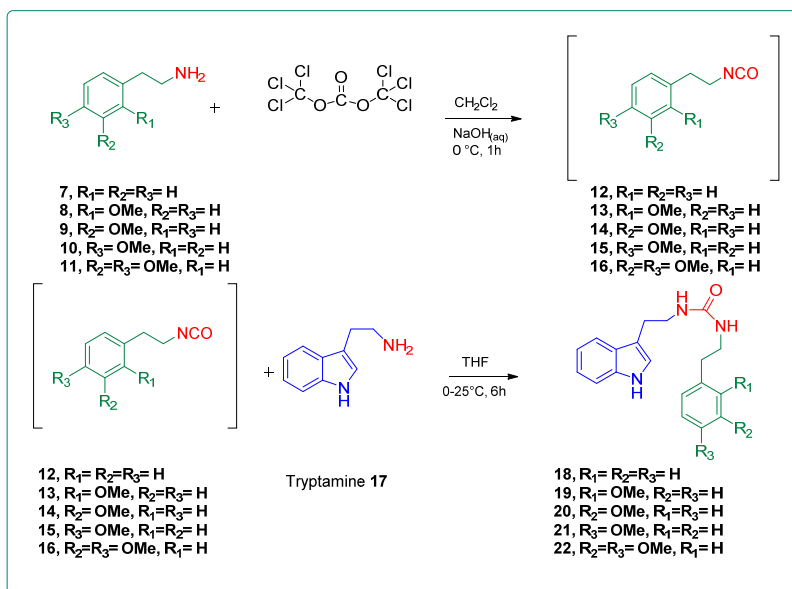
Scheme 1. Synthetic routes to the ureas **18-22**

Biological Studies

Enzymes are generally used as the main target in the development of drugs. By designing suitable inhibitors for enzymes, they can be turned into potential drugs. In the presented study, the in vitro inhibitory effects of the novel synthesized unsymmetrical ureas **18-22** on the hCA-I, hCA-II, and AChE enzyme activities were evaluated.

hCA activity assay

Carbonic anhydrase inhibitors, which have been used clinically for many years, are potential therapeutic drugs for the treatment of many diseases, such as inflammation, neurological disorders, epilepsy, hypoxic tumors, glaucoma, obesity, arthritis, cancer, hemolytic anemia, and dental caries[23]. Dichlorophenamide, acetazolamide, dorzolamide, phentermine, sulpiride, methazolamide, sulthiame, brinzolamide, zonisamide, indisulam, topiramate, and ethoxzolamide molecules are some of the carbonic anhydrase inhibitors are used clinically[13][24]. Acetazolamide (AZA) from these molecules was used as a reference hCA inhibitor in this study. The previous studies have determined that a lot of synthesized molecules such as malononitrile, carbamate, sulfonamide, β-lactam, sulfamide, benzylsulfamide, bromophenol, phenolic, pyridazine, and pyrazoline derivatives were inhibited hCA-I and hCA-II[25-37]. Also, much research have displayed that urea derivatives exhibit effective inhibition, such as other hCAs inhibitor. In this context, novel phthalazine urea,

diphenyl urea, and diaryl urea derivatives were synthesized and determined inhibitory effects against hCA-I and hCA-II. These molecules demonstrated IC_{50} values in the range of 5.28-153.15 µM for hCA-I and 5.51-16.96 µM for hCA-II [38-40]. In another study, Ozgeris et al. synthesized the novel urea derivatives incorporating dopaminergic 2-aminotetralin scaffolds. They discovered that these derivatives effectively inhibited both enzymes, with IC_{50} values ranging from 7.65–9.95 nM for hCA-I and 9.27–74.69 nM for hCA-II[41].

Inhibition parameters (IC_{50}, K_i, and inhibition types) of N-N' dialkyl urea derivatives for cytosolic isoform hCA-I enzyme associated with hemolytic anemia disease were determined. As shown in Table 1, IC_{50} values were found to be 1.214 µM for compound **18**, 1.387 µM for compound **19**, 1.486 µM for compound **20**, 1.249 µM for compound **21**, and 2.281 µM for compound **22**. Inhibition constants (K_i) of the molecules **18-22** were calculated by means of Lineweaver–Burk graphs. These constants were found to be 0.984 ± 0.277 µM for compound **18**, 1.422 ± 0.183 µM for compound **19**, 1.426 ± 0.042 µM for compound **20**, 1.244 ± 0.378 µM for compound **21**, and 4.261 ± 1.287 µM for compound **22**. Although compound **22** noncompetitively inhibited hCA-I, it competitively inhibited all other compounds.

According to the results, it was determined that all urea derivatives effectively inhibited the hCA-I enzyme at a level of µM. Compound **18** is the molecule with the most effective inhibition potential against hCA-I among all these. When the results obtained for hCA-I were compared with the results of the reference inhibitor (AZA), it was found that the inhibitor concentrations were the same (µM) and close to each other. Furthermore, selectivity indexes (SI) of novel urea derivatives **18-22** were displayed in Table 2. Among these compounds, compound **18** (K_is for hCA-I and hCA-II 0.984 ± 0.277 µM and 1.955 ± 0.581 µM, respectively) was determined as the most selective hCA-I inhibitor in these molecules with a SI value (hCA-II/hCA-I) of 1.987.

Table 1. The inhibition results of the novel unsymmetrical ureas on hCA-I and hCA-II enzym

Compound ID	hCA-I			hCA-II		
	IC_{50} (µM)	K_i (µM)	Inhibition Type	IC_{50} (µM)	K_i (µM)	Inhibition Type
18	**1.214**	**0.984 ± 0.277**	**Competitive**	2.975	1.955 ± 0.581	Competitive
19	1.387	1.422 ± 0.183	Competitive	**0.888**	**0.564 ± 0.019**	**Competitive**
20	1.486	1.426 ± 0.042	Competitive	1.130	0.591 ± 0.113	Competitive
21	1.249	1.244 ± 0.378	Competitive	2.984	2.075 ± 0.273	Competitive
22	2.281	4.261 ± 1.287	Noncompetitive	1.935	1.389 ± 0.167	Competitive
AZA[*]	0.743	0.721 ± 0.101	Noncompetitive	0.267	0.239 ± 0.018	Noncompetitive

* Acetazolamide (AZA) was used as a reference inhibitor for hCA-I and hCA-II enzymes.

hCA-II, another cytosolic isozyme, plays a vital role in various diseases such as renal tubular acidosis, edema, osteoporosis, epilepsy, and altitude sickness, especially glaucoma[24]. Inhibition results of synthesized

molecules on hCA-II are summarized in table 1. As can be seen from the table, IC_{50} and K_i values for the hCA-II enzyme are in the range of 0.888 to 2.983 µM, from 0.564 ± 0.019 to 2.075 ± 0.273 µM, respectively. All of the urea derivatives inhibited the hCA-II enzyme at the µM level. Compound **19** showed the strongest inhibition among these compounds with an IC_{50} of 0.887 µM and a K_i of 0.564 ± 0.019 µM. All of the compounds demonstrated competitive inhibition by binding to the active site of hCA-II. The molecules have higher inhibition values than standard inhibitors (AZA). However, inhibitor concentrations are low and at µM level.

According to our results, the novel synthesized N-N' dialkyl urea derivatives inhibited hCA-I and hCA-II enzymes more effectively than all other urea derivatives except novel urea derivatives incorporating dopaminergic 2-aminotetralin scaffolds.

As can be seen in table 2, compound **19** (K_is for hCA-I and hCA-II 1.422 ± 0.183 µM and 0.564 ± 0.019 µM, respectively), with a SI value (hCA-II/hCA-I) of 0.397, was found to be the most selective inhibitor for hCA-II among these compounds.

Table 2. Selectivity index values for K_i constants
of the novel synthesized unsymmetrical ureas

Compound ID	$K_i{}^a$ (TAC^b/AChE)	$K_i{}^a$ (AZA^c/hCA-I)	$K_i{}^a$ (AZA^c/hCA-II)	$K_i{}^a$ (hCA-II/hCA-I)
18	0.149	0.733	0.122	1.987
19	0.091	**0.507**	**0.424**	**0.397**
20	0.155	0.506	0.404	0.415
21	0.054	0.580	0.116	1.668
22	0.106	0.169	0.172	0.609

[a] The K_i rates for the selectivity index; [b] Tacrine; [c] Acetazolamide.

AChE activity assay

Alzheimer's disease is caused by malfunctions in various metabolic pathways. Neurotransmitters in the brain are reduced as a result of this condition. Acetylcholine is the neurotransmitter that has decreased the most[42]. For the treatment or prevention of the disease, the breakdown of acetylcholine should be reduced. This can be achieved by inhibition of AChE, which breaks down acetylcholine. Drugs designed for Alzheimer's disease are used to control the level of acetylcholine, and drug design is carried out accordingly[43].

In recent years, the discovery of novel AChE inhibitors has been the focus of organic chemists and pharmacists in particular. The amino methyl, alkoxy methyl, phloroglucinol, benzimidazole, pyrazoles, bromophenol, imidazole, hydrazine, thiazolidinone, propanolamine, and quinazolinone derivatives were synthesized and investigated the inhibitory effect on AChE [44-55]. Moreover, many studies have examined the inhibitory effects of some urea derivatives on AChE. In this direction, new coumarylthiazole aryl urea, 1,3,4-thiadiazol-2-yl urea, and dopamine analogs incorporating urea were synthesized and investigated their inhibition effects against AChE. The compounds inhibited the AChE enzyme with IC_{50} values in the range of 1.17 µM-4.30 mM. [56-58]. In another study, Kurt et al. synthesized novel benzofuranylthiazole derivatives containing the aryl urea moiety. They determined that these derivatives inhibited AChE enzymes with IC_{50} values in the range of 3.85-78.85 µM[59].

The inhibition effects of novel synthesized urea derivatives **18-22** against AChE were investigated using tacrine, which is a reference compound. In table 3, IC_{50} values, K_i constants, and inhibition types for AChE are demonstrated. IC_{50} values and Ki constants for these new urea derivatives were found to ranging between 0.309 to 0.816 µM and between 0.470 ± 0.039 to 1.349 ± 0.244, respectively. The results showed that all of the synthesized molecules exhibited an inhibitory effect against AChE. The molecule showing the highest inhibition effect was found to be compound **20**, with an IC_{50} value and K_i constant of 0.309 and 0.470 ± 0.039 µM, respectively. The inhibition results were less than that of tacrine (IC_{50}: 0.249 µM) but very close to each other.

According to our results, the novel, synthesized unsymmetrical ureas inhibited the AChE enzyme more effectively than all other urea derivatives.

Table 3. The inhibition results of the novel unsymmetrical ureas on AChE enzyme

Compound ID	AChE		
	IC_{50} (µM)	K_i (µM)	Inhibition Type
18	0.551	0.491 ± 0.029	Competitive
19	0.576	0.809 ± 0.189	Competitive
20	**0.309**	**0.470 ± 0.039**	**Competitive**
21	0.605	1.349 ± 0.244	Noncompetitive
22	0.816	0.688 ± 0.025	Competitive
TAC*	0.249	0.073 ± 0.004	Competitive

* Tacrine (TAC) was used as a reference inhibitor for AChE enzyme.

Molecular docking

Compounds having the most effective inhibition on hCA-I, hCA-II, and AChE according to in vitro studies, were subjected to molecular docking studies to predict the interaction of compounds with receptor proteins. Binding interactions between molecules (compound **18** for hCA-I, compound **19** for hCA-II, and compound **20** for AChE) and enzymes were estimated using AutoDock 4.2.

Table 4. Results of molecular docking of urea derivatives with enzymes

Compound ID	Enzyme	Estimated Free Energy of Binding (kcal/mol)	Estimated Inhibition K_i Constant (µM)
18	hCA-I	-7.81	1.880
19	hCA-II	-7.34	4.150
20	AChE	-8.20	0.984

The estimated binding energy value for the hCA-I receptor was calculated as −7.81 kcal/mol. The best binding poses and 2D ligand-receptor interaction diagrams of compound **18** are shown in Figure 2. In the interaction with hCA-I, compound **18** formed van der Waals interactions with Phe66, Ser65, Gln92, His67, Val62, Pro202, His200, Trp209, and His119 residues. The benzene ring of compound **18** showed a Pi-cation electrostatic interaction with His64 residue and had some hydrophobic interaction such as a pi-pi stacked and pi-pi T-shaped interaction with His94 residue, and pi-alkyl interactions with Ala121, Val143, and Leu198 residues. The urea moiety of compound **18** made a conventional hydrogen bond with Pro201 residue. Besides, the pyrrole ring of compound **18** formed a pi-doner conventional hydrogen bond with Thr199 residue and a pi-alkyl interaction with Leu198 residue.
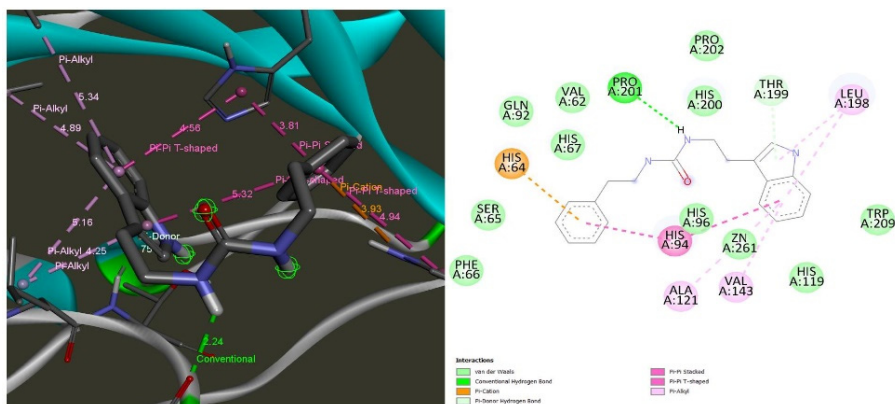

Figure 2. Potential binding modes and 2D ligand-receptor interaction diagrams of compound **18** with hCA-I.

For the interaction of compound **19** with hCA-II receptor, estimated binding energy value was calculated to be -7.34 kcal/mol. Figure 3 demonstrates the optimal binding poses and 2D ligand-receptor interaction diagrams. In the interaction with hCA-II, compound **19** made van der Waals interactions with His4, Phe20, Thr199, His96, His119, Glu106, Trp208, His94, Val206, and Leu140 residues. The benzene ring of compound **19** formed pi-alkyl interactions with Pro201, Val121, and Val142 residues, a pi-sigma interaction with Leu197 residue. The urea moiety of compound **19** made a conventional hydrogen bond with Pro200 residue. The methoxy substituent on the benzene ring of **19** formed a carbon hydrogen bond with Pro200 residue, a pi-alkyl interaction with Trp5 residue, and a conventional hydrogen bond with Trp5 residue. Furthermore, the pyrrole ring of compound **19** formed a pi-cation interaction with Zn261 residue, a pi-alkyl interaction with Leu197 residue, an amide-pi stacked interaction with Thr198 residue, and a conventional hydrogen bond with Thr198 residue.
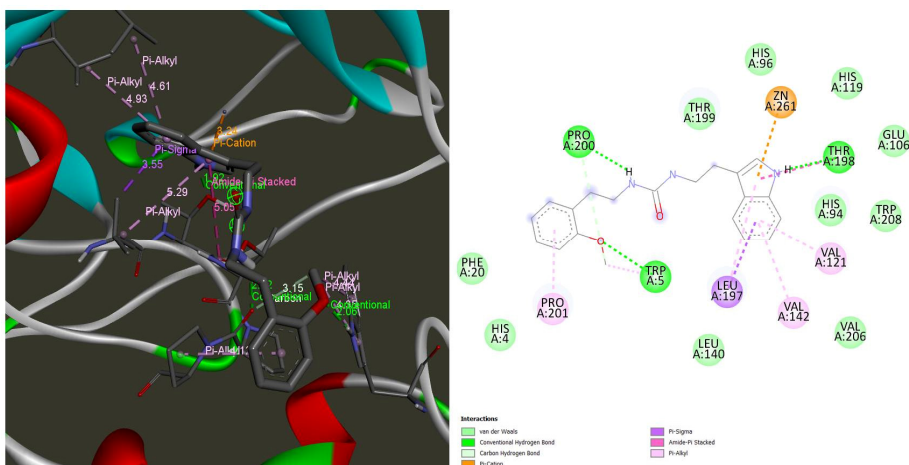

Figure 3. Potential binding modes and 2D ligand-receptor interaction diagrams of compound **19** with hCA-II.

The estimated binding energy of the AChE receptor with compound 20 was determined to be -8.20 kcal/mol. Compound **20**'s best binding poses and 2D ligand-receptor interaction diagrams are demonstrated in Figure 4. In the interaction with AChE, compound **20** formed van der Waals interactions with Ile287, Arg289, Phe288, Tyr334, Tyr70, Gly441, Glu199, Gly118, and Gly119 residues. The benzene ring of compound **20** made a pi-pi stacked interaction with Trp84 residue. The benzylic carbon of compound **20** showed a pi-sigma interaction with Phe330 residue. The urea moiety of compound **20** made a conventional hydrogen bond with Tyr121 residue. The methoxy substituent on the benzene ring of **20** formed conventional hydrogen bond with Ser200, His440

residues, and pi-alkyl interactions with Phe331, Phe290, and His440 residues. The pyrrole ring of compound **20** formed a pi-pi stacked interaction with Trp279 residue and a pi-pi T-shaped interaction with Tyr121 residue. Also, the urea-bound methyl of compound **20** made a carbon hydrogen bond with Asp72 residue. As seen from Table 4, estimated inhibition constants (K_i) for hCA-I, hCA-II, and AChE were predicted to be 1.88 µM, 4.15 µM, and 0.984 µM, respectively.
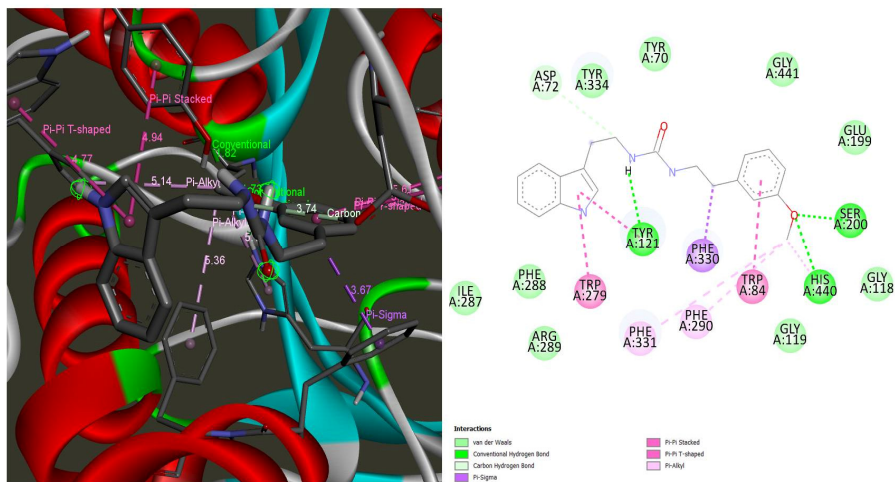

Figure 4. Potential binding modes and 2D ligand-receptor interaction diagrams of compound **20** with AChE.

The ADME analysis for novel synthesized unsymmetrical ureas was carried out. As summarized in Table 5, all urea derivatives showed no deviations from Lipinski's rule of five, including the number of hydrogen bond acceptors, account molecular weight, miLogP (lipophilicity descriptor), number of rotatable bonds, and number of hydrogen bond donors. The molecular weights of all compounds were found to be lower than 500 g/mol. The logP (octanol-water partition coefficient) value calculated for all molecules was determined to be within the range (≤4.15) given according to Lipinski's rule. It has been determined that the total values of the effects of polar structures such as hydrogen, oxygen, and nitrogen on the molecular surface area (Topological Polar Surface Area: TPSA) are lower than 90 Å. So, the SwissADME estimated that these urea derivatives could pass the BBB and be substrates for P-gp efflux. Also, gastrointestinal (GI) absorptions of all molecules are found to be high. Finally, the synthetic accessibility (sa) calculated scores ranged from 2.23 to 2.65, demonstrating that compounds in the present study agree with synthetic observations [60–63].

Table 5. Results of *in silico* ADME analysis for the novel
synthesized unsymmetrical ureas

Properties	Rules	Compounds				
		18	19	20	21	22
Molecular Weight (g/mol)	<500	307.39	337.42	337.42	337.42	367.44
Num. rotatable bonds	<10	8	9	9	9	10
Number of H-bond acceptors	<10	1	2	2	2	3
Number of H-bond donors	<5	3	3	3	3	3
TPSA (Å^2)	20<TPSA<130	56.92	66.15	66.15	66.15	75.38
ABS %		89.4	86.2	86.2	86.2	82.9
miLogP	≤4.15	3.51	3.52	3.54	3.56	3.15
nviolations	≤1	0	0	0	0	0
GI absorption		High	High	High	High	High
BBB permeant		Yes	Yes	Yes	Yes	Yes
P-gp substrate		Yes	Yes	Yes	Yes	Yes
Log K_p (skin permeation) cm/s	(-9.7<log K_p<-3.5)	-6.23	-5.96	-6.43	-6.43	-6.16
Synthetic accessibility (sa)		2.23	2.41	2.43	2.36	2.65

CONCLUSIONS

In this study, we synthesized a set of novel N-N' dialkyl urea derivatives **18-22** by starting from tryptamine, an indolamine metabolite of the essential amino acid tryptophan, and substituted 2-phenethylamines. *In vitro* and *in silico* studies confirmed the potential inhibitory effects of all synthesized urea derivatives on hCA-I and hCA-II isozymes and AChE. These compounds have displayed good inhibition at micromolar concentrations against three metabolic enzymes. The molecules exhibiting the strongest inhibition are compound **18** for hCA-I (IC_{50}: 1.214 μM), compound **19** for hCA-II (IC_{50}: 0.888 μM), and compound **20** for AChE (IC_{50}: 0.309 μM). In addition, physicochemical and pharmacokinetic descriptors and drug-like properties of unsymmetrical urea derivatives were evaluated and showed no deviations from Lipinski's rule of five. Based on our results, the synthesized novel N-N' dialkyl urea derivatives may be useful for the treatment of a lot of diseases such as retinal pathology, glaucoma, epilepsy, and brain edema for CA isozymes and AD for AChE after being supported by in vivo and further toxicity studies.

EXPERIMENTAL SECTION

Materials

All chemicals and analytical reagents used for synthesis, purification, and biological activity were obtained from Sigma-Aldrich and Merck KGaA. The characterization of the organic product was performed using a 400 MHz Bruker NMR instrument. An electrothermal IA9100 capillary melting point device was used to determine the melting point. On a Shimadzu IRTracer-100 spectrophotometer with a single-reflection ATR accessory, FT-IR spectra were acquired. A Leco CHNS-932 device was used for element analysis.

General procedure for the synthesis of Ureas 18-22.

2-Phenethylamine **7-11** (3 mmol) in CH_2Cl_2 (5 ml) was added dropwise to a solution of triphosgene (1 mmol) dissolved in CH_2Cl_2 (15 ml) at 0°C, then a solution of NaOH (3 mmol) prepared in 7 ml of water was added. The mixture was stirred at room temperature for 1 hour after the addition. The water layer was removed. 3X20 mL of water was used to wash the organic phase, which was then dried over magnesium sulfate. The filtrate was evaporated to obtain the isocyanate, which was then used without additional purification. In dry THF (10 ml), the isocyanate **12-16** (1 mmol) was dissolved or suspended and cooled in an ice bath. Tryptamine **17** (1 mmol) was dissolved in dry THF (5 ml) and slowly added to the reaction mixture. At room temperature, stirring was continued for 6 hours. After that, the organic phase evaporated. N, N'-dialkyl ureas **18-22** were obtained by recrystallization from (EtOAc/Hexane [4-1]).

1-(2-(1H-indol-3-yl)ethyl)-3-phenethylurea (18, $C_{19}H_{21}N_3O$)

The product **18** was obtained as a white powder; Yield: 670 mg, (72%); M.p.: 112-114 °C; IR: v_{max} 3289, 3024, 2912, 2369, 1707, 1647, 1502, 1431, 1101, 743 cm^{-1}; ^{1}H NMR (400 MHz, DMSO-d$_6$) δ 10.84 (br.s, 1H, NH), 7.56 (d, J = 7.8 Hz, 1H, ArH), 7.37 (d, J = 8.1 Hz, 1H, ArH), 7.32 – 7.25 (m, 2H, ArH), 7.24 – 7.17 (m, 3H, ArH), 7.14 (d, J = 2.1 Hz, 1H, ArH), 7.13 – 7.04 (m, 1H, ArH), 7.03 – 6.96 (m, 1H, ArH), 6.03 – 5.95 (m, 2H, NH), 3.33 (dd, J = 13.2, 6.9 Hz, 2H, CH$_2$), 3.26 (dd, J = 13.2, 7.0 Hz, 2H, CH$_2$), 2.82 (t, J = 7.2 Hz, 2H, CH$_2$), 2.70 (t, J = 7.2 Hz, 2H). ^{13}C NMR (100 MHz, DMSO-d$_6$): δ = 158.17 (CO), 139.71 (C), 136.24 (C), 128.64 (2CH), 128.26 (2CH),

127.24 (C), 125.94 (CH), 122.59 (CH), 120.88 (CH), 118.34 (C), 118.19 (CH), 111.99 (CH), 111.32 (CH), 40.97 (CH_2), 40.11(CH_2), 36.19 (CH_2), 26.07(CH_2). Anal. Calcd. for $C_{19}H_{21}N_3O$: C, 74.24; H, 6.89; N, 13. 67; found: C, 74,22; H, 6,86; N, 13,70%.

1-(2-(1H-indol-3-yl)ethyl)-3-(2-methoxyphenethyl)urea (19, $C_{20}H_{23}N_3O_2$)

The product **19** was obtained as a white powder; Yield: 780 mg, (76%); M.p.: 96-98 °C; IR: v_{max} 3387, 2964, 2875, 2365, 1709, 1685, 1560, 1492, 1240, 1122, 752, 735 cm^{-1}; ^{1}H NMR (400 MHz, DMSO-d_6): δ = 10.85 (br.s, 1H, NH), 7.53 (d, J = 6.6 Hz, 1H, ArH), 7.33 (d, J = 6.8 Hz, 1H, ArH), 7.25 – 7.02 (overlapped signals, 4H, ArH), 7.00 – 6.81 (overlapped signals, 3H, ArH), 5.94 (br.s, 2H, NH), 3.75 (s, 3H, OCH_3), 3.28 (s, 2H, CH_2), 3.18 (s, 2H, CH_2), 2.77 (s, 2H, CH_2), 2.65 (s, 2H, CH_2). ^{13}C NMR (100 MHz, DMSO-d_6): δ = 158.55 (CO), 157.67 (C), 136.72 (C), 130.49 (C), 127.90 (2CH), 127.73 (C), 123.08 (CH), 121.34 (CH), 120.70 (CH), 118.83 (C), 118.63 (CH), 112.47 (CH), 111.80 (CH), 111.04 (CH), 55.68 (OCH_3), 40.53 (CH_2), 40.5-39 (CH_2, overlapping with DMSO), 31.24 (CH_2), 26.62 (CH_2). Anal. Calcd. for $C_{20}H_{23}N_3O_2$: C, 71.19; H, 6.87; N, 12.45; found: C, 71.30; H, 6.80; N, 12.48%.

1-(2-(1H-indol-3-yl)ethyl)-3-(3-methoxyphenethyl)urea (20, $C_{20}H_{23}N_3O_2$)

The product **20** was obtained as a white powder; Yield: 800 mg, (78%); M.p.: 113-115 °C; IR: vmax 3366, 3292, 2363, 1830, 1654, 1602, 1560, 1460, 1261, 1166, 789, 750 cm^{-1}; ^{1}H NMR (400 MHz, DMSO-d_6): δ = 10.80 (br.s, 1H, NH), 7.52 (d, J = 7.3 Hz, 1H, ArH), 7.32 (d, J = 7.9 Hz, 1H), 7.17 (d, J = 6.2 Hz, 1H, ArH), 7.11 (s, 1H, ArH), 7.08 – 7.00 (overlapped signals, 1H, ArH), 7.00 – 6.91 (overlapped signals, 1H, ArH), 6.75 (s, 3H, ArH), 5.98 – 5.81 (m, 2H, NH), 3.71 (s, 3H, OCH_3), 3.32 – 3.13 (m, 4H, CH_2), 2.79 – 2.71 (m, 2H, CH_2), 2.66 – 2.60 (m, 2H, CH_2). ^{13}C NMR (100 MHz, DMSO-d_6): δ = 159.69(CO), 158.47 (C), 141.82 (C), 136.70 (C), 129.75 (CH), 127.71 (C), 123.06 (CH), 121.35 (2CH), 118.82 (C), 118.63 (CH), 114.68 (CH), 112.45 (CH), 111.92 (CH), 111.78 (CH), 55.31 (OCH_3), 41.28 (CH_2), 40.53 (CH_2), 36.69 (CH_2), 26.61 (CH_2). Anal. Calcd. for $C_{20}H_{23}N_3O_2$: C, 71.19; H, 6.87; N, 12.45; found: C, 71.23; H, 6.84; N, 12.39%.

1-(2-(1H-indol-3-yl)ethyl)-3-(4-methoxyphenethyl)urea (21, $C_{20}H_{23}N_3O_2$)

The product **21** was obtained as a white powder; Yield: 800 mg, (78%); M.p.:118-120°C; IR: vmax 3368, 3292, 2361, 1845, 1707, 1603, 1560, 1459, 1263, 1167, 789, 748 cm^{-1}; ^{1}H NMR (400 MHz, DMSO-*d6*): δ = 10.84 (br.s, 1H, NH), 7.53 (d, J = 8.0 Hz, 1H, ArH), 7.33 (d, J = 8.1 Hz, 1H, ArH), 7.15 – 7.03 (m, 4H, ArH), 6.96 (t, J = 7.4 Hz, 1H, ArH), 6.82 (d, J = 8.3 Hz, 2H, ArH), 5.96 (t, J = 5.3 Hz, 1H, NH), 5.91 (t, J = 5.3 Hz, 1H, NH), 3.69 (s, 3H, OCH$_3$), 3.28 (dd, J = 12.9, 6.6 Hz, 2H, CH$_2$), 3.18 (dd, J = 12.9, 6.5 Hz, 2H, CH$_2$), 2.77 (t, J = 7.0 Hz, 2H, CH$_2$), 2.59 (t, J = 7.1 Hz, 2H, CH$_2$). ^{13}C NMR (100 MHz, DMSO-d_6): δ = 158.55 (CO), 158.04 (C), 136.72 (C), 132.08 (C), 130.07 (2CH), 127.73 (C), 123.08 (CH), 121.34 (CH), 118.83 (C), 118.64 (CH), 114.17 (2CH), 112.47 (CH), 111.80 (CH), 55.40 (OCH$_3$), 41.68 (CH$_2$), 40.53 (CH$_2$), 35.79 (CH$_2$), 26.61 (CH$_2$). Anal. Calcd. for $C_{20}H_{23}N_3O_2$: C, 71.19; H, 6.87; N, 12.45; found: C, 71.26; H, 6.85; N, 12.38%.

1-(2-(1H-indol-3-yl)ethyl)-3-(3,4-dimethoxyphenethyl)urea (22, $C_{21}H_{25}N_3O_3$)

The product **22** was obtained as a white powder; Yield: 840 mg, (75%); M.p.: 110-112 °C; IR: v_{max} 3366, 3294, 2363, 1838, 1654, 1602, 1560, 1460, 1431, 1261, 852, 789, 772 cm^{-1}; ^{1}H NMR (400 MHz, DMSO-d_6): δ = 10.81 (br.s, 1H, NH), 7.53 (d, J = 7.7 Hz, 1H, ArH), 7.33 (d, J = 8.0 Hz, 1H, ArH), 7.11 (s, 1H, ArH), 7.05 (t, J = 7.4 Hz, 1H, ArH), 6.96 (t, J = 7.3 Hz, 1H, ArH), 6.82 (d, J = 8.1 Hz, 1H, ArH), 6.77 (s, 1H, ArH), 6.68 (d, J = 7.9 Hz, 1H, ArH), 5.93 (t, J = 5.2 Hz, 1H, NH), 5.86 (t, J = 5.3 Hz, 1H, NH), 3.71 (s, 3H, OCH$_3$), 3.69 (s, 3H, OCH$_3$), 3.28 (dd, J = 12.9, 6.6 Hz, 2H, CH$_2$), 3.20 (dd, J = 12.7, 6.4 Hz, 2H, CH$_2$), 2.77 (t, J = 7.1 Hz, 2H, CH$_2$), 2.59 (t, J = 7.0 Hz, 2H, CH$_2$). ^{13}C NMR (100 MHz, DMSO-d_6): δ = 158.50 (CO), 149.02 (C), 147.56 (C), 136.71 (C), 132.66 (C), 127.72 (C), 123.06 (CH), 121.35 (CH), 120.89 (CH), 118.82 (C), 118.63 (CH), 112.94 (CH), 112.47 (CH), 112.29 (CH), 111.78 (CH), 55.94 (OCH$_3$), 55.76 (OCH$_3$), 41.54 (CH$_2$), 40.52 (CH$_2$), 36.22 (CH$_2$), 26.62 (CH$_2$). Anal. Calcd. for $C_{21}H_{25}N_3O_3$: C, 68.64; H, 6.86; N, 11.44; found: C, 68,68; H, 6.83; N, 11.46%.

Biological activity

hCA-I and hCA-II isoenzymes were isolated from human erythrocyte cells. As described in previous studies, the purification was performed with an affinity column using sulfanilamide as ligand for CNBr-activated-Sepharose 4B[64]. The AChE enzyme isolated from Electrophorus electricus (Type V\\S,

C2888) was purchased commercially from Sigma-Aldrich Chemie GmbH for inhibition studies. The potential inhibition effects of novel synthesized unsymmetrical ureas on hCA-I, hCA-II, and AChE were examined spectrophotometrically by the activity method introduced by Verpoorte et al. for hCAs (348 nm) and Ellman et al. for AChE (412 nm)[65,66]. In order to obtain the IC_{50} value, activities for hCAs and AChE were measured at 5 different inhibitör (urea derivatives) concentrations. IC_{50} values were determined from the % Activity-Concentration graphics drawn. Then, activity measurements were carried out at 5 different substrates (p-Nitrophenyl acetate (p-NPA) for hCAs, acetylthiocholine iodide for AChE) concentrations, and 3 different fixed inhibitor concentrations in order to determine the inhibition types and K_i values. The inhibition types and K_i values were determined from the plots of 1/V versus 1/[S].

Molecular Docking Studies

AutoDock 4.2 was used to investigate possible docking mechanisms between compounds and enzymes (hCA-I, hCA-II, and AChE)[67]. In docking calculations, the 3D crystallographic structures of hCA-I (PDB code: 3LXE)[68], hCA-II (PDB code: 3HKU)[69], and AChE (PDB code: 1EEA) [70] receptors were utilized. The pdb file formats for enzymes were downloaded from the Protein Data Bank (http: /www.rcsb.org/pdb). ChemDraw software was used to create three-dimensional structures of the derivatives as a sdf file, which was then converted to a pdb file using Avogadro software. Water molecules, metal ions not belonging to the binding pocket, and other superfluous atoms were removed from the protein. Then, the polar H atoms and the Kollman charge were added to the protein, and the missing atoms were repaired. For the calculation of the energetic map, a grid size of 80x80x80 points with a spacing of 0.375 Å was applied. Grid boxes for the active site of protein were centred as x=-13.198, y=36.883, z=37.807 for hCA-I, x=11.497, y=-0.002, z=16.104 for hCA-II, and x=11.244, y=28.066, z=37.217 for AChE. To identify the proper binding locations, orientations, and conformations of ligands, the Lamarckian genetic algorithm was applied. The results docking were analyzed with Discovery Studio Visualizer.

ADME (absorption, excretion, metabolism, and distribution) properties

Physicochemical and pharmacokinetic descriptors, and drug-likeness properties of unsymmetrical urea derivatives were evaluated using the SwissADME web tool. In this context, The parameters such as molecular

weight (MW), percentage absorption (%ABS), the number of hydrogen bonds (n-OHNH donors), logarithm of partition coefficient of the compound between n-octanol and water (miLog P), topological polar surface area (TPSA), the number of hydrogen bond acceptors (n-ON acceptors), and the number of rotatable bonds (n-ROTB) were determined[71,72].

ACKNOWLEDGMENTS

REFERENCES

1. H. Abe; S. Matsunaga; S. Takekawa; M. Watanabe; *Preparation of Indole Amino Acid Derivatives as Somatostatin Agonists or Antagonists.*; **2004**.
2. S. Berg; S. Hellberg; *PCT Int. Appl. WO* **2003**, *2003004478*.
3. J. R. Falck; G. Wallukat; N. Puli; M. Goli; C. Arnold; A. Konkel; M. Rothe; R. Fischer; D. N. Müller; W.-H. Schunck; *J. Med. Chem.* **2011**, *54*, 4109–4118.
4. T. D. Gould; H. Einat; R. Bhat; H. K. Manji; *Int. J. Neuropsychopharmacol.* **2004**, *7*, 387–390.
5. B. Rajtar; E. Szacon; L. Swiatek; M. Rzadkowska; D. Matosiuk; M. Polz-Dacewicz; *J. Pre-Clinical Clin. Res.* **2013**, *7*.
6. P. N. Sidharta; P. L. M. van Giersbergen; J. Dingemanse; *J. Clin. Pharmacol.* **2009**, *49*, 1168–1175.
7. R. El Kouhen; C. S. Surowy; B. R. Bianchi; T. R. Neelands; H. A. McDonald; W. Niforatos; A. Gomtsyan; C.-H. Lee; P. Honore; J. P. Sullivan; *J. Pharmacol. Exp. Ther.* **2005**, *314*, 400–409.
8. P. Honore; C. T. Wismer; J. Mikusa; C. Z. Zhu; C. Zhong; D. M. Gauvin; A. Gomtsyan; R. El Kouhen; C.-H. Lee; K. Marsh; *J. Pharmacol. Exp. Ther.* **2005**, *314*, 410–421.
9. T. A. Jenkins; J. C. D. Nguyen; K. E. Polglaze; P. P. Bertrand; *Nutrients* **2016**; *8*; 56.
10. M. Z. Khan; W. Nawaz; *Biomed. Pharmacother. Biomed. Pharmacother.* **2016**, *83,* 439–449.
11. M. D. Berry; R. R. Gainetdinov; M. C. Hoener; M. Shahid; *Pharmacol. Ther.* **2017**, *180*, 161–180.
12. S. Freeman; J. F. Alder; *Eur. J. Med. Chem.* **2002**, *37*, 527–539.
13. S. Bibi; T. Javed; F. Alam; A. Ali; S. Ali; M. Ullah; H. Bin Asad; M. Hassham; F. Hasan; S. Muhammad; *Pak. J. Pharm. Sci.* **2019**, *32*.
14. A. Karioti; F. Carta; C. T. Supuran; *Molecules* **2016**, *21*, 1649.

15. I. Gulcin; S. Beydemir; *Mini Rev. Med. Chem.* **2013**, *13,* 408–430.
16. A. Kazancı; Y. Gök; R. Kaya; A. Aktaş; P. Taslimi; İ. Gülçin; *Polyhedron* **2021**, *193*, 114866.
17. H. Göçer; A. Akıncıoğlu; N. Öztaşkın; S. Göksu; İ. Gülçin; *Arch. Pharm. (Weinheim).* **2013**, *346*, 783–792.
18. D. G. Wilkinson; P. T. Francis; E. Schwam; J. Payne-Parrish; *Drugs Aging* **2004**, *21*, 453–478.
19. S. Yılmaz; Y. Akbaba; B. Özgeriş; L. P. Köse; S. Göksu; İ. Gülçin; S. H. Alwasel; C. T. Supuran; *J. Enzyme Inhib. Med. Chem.* **2016**, *31*, 1484–1491.
20. A. Akıncıoğlu; M. Topal; İ. Gülçin; S. Göksu; *Arch. Pharm. (Weinheim).* **2014**, *347*, 68–76.
21. S. Hashmi; S. Khan; Z. Shafiq; P. Taslimi; M. Ishaq; N. Sadeghian; H. S. Karaman; N. Akhtar; M. Islam; A. Asari; *Bioorg. Chem.* **2021**, *107*, 104554.
22. T. E. Rose; C. Morisseau; J.-Y. Liu; B. Inceoglu; P. D. Jones; J. R. Sanborn; B. D. Hammock; *J. Med. Chem.* **2010**, *53*, 7067–7075.
23. C. T. Supuran; *Expert Opin. Drug Metab. Toxicol.* **2020,** *16*, 297–307.
24. S. Kumar; S. Rulhania; S. Jaswal; V. Monga; *Eur. J. Med. Chem.* **2020**, 112923.
25. P. Güller; Z. Dağalan; U. Güller; U. Çalışır; B. Nişancı; *J. Mol. Struct.* **2021**, *1239*, 130498.
26. P. Güller; U. Atmaca; U. Güller; U. Çalışır; F. Dursun; *Future Med. Chem.* **2021**.
27. Z. Huyut; Ş. Beydemir; İ. Gülçin; *J. Enzyme Inhib. Med. Chem.* **2016**, *31*, 1234–1240.
28. R. Kocak; E. T. Akın; P. Kalın; O. Talaz; N. Saracoglu; A. Dastan; İ. Gülçin; S. Durdagi; *J. Heterocycl. Chem.* **2016**, *53*, 2049–2056.
29. K. Kucukoglu; F. Oral; T. Aydin; C. Yamali; O. Algul; H. Sakagami; I. Gulcin; C. T. Supuran; H. I. Gul; *J. Enzyme Inhib. Med. Chem.* **2016**, *31*, 20–24.
30. Z. Alım; Z. Köksal; M. Karaman; *Pharmacol. Reports* **2020**, *72*, 1738–1748.
31. Z. Köksal; Z. Alım; S. Bayrak; İ. Gülçin; H. Özdemir; *J. Biochem. Mol. Toxicol.* **2019**, *33*, e22300.
32. H. Genç; R. Kalin; Z. Köksal; N. Sadeghian; U. M. Kocyigit; M. Zengin; İ. Gülçin; H. Özdemir; *Int. J. Mol. Sci.* **2016**, *17*, 1736.
33. Y. Akbaba; E. Bastem; F. Topal; İ. Gülçin; A. Maraş; S. Göksu; *Arch. Pharm. (Weinheim).* **2014**, *347*, 950–957.
34. Y. Akbaba; A. Akıncıoğlu; H. Göçer; S. Göksu; İ. Gülçin; C. T. Supuran; *J. Enzyme Inhib. Med. Chem.* **2014**, *29*, 35–42.
35. S. Göksu; A. Naderi; Y. Akbaba; P. Kalın; A. Akıncıoğlu; İ. Gülçin; S. Durdagi; R. E. Salmas; *Bioorg. Chem.* **2014**, *56*, 75–82.
36. Y. Akbaba; H. T. Balaydın; A. Menzek; S. Göksu; E. Şahin; D. Ekinci; *Arch. Pharm. (Weinheim).* **2013**, *346*, 447–454.
37. A. Akıncıoğlu; Y. Akbaba; H. Göçer; S. Göksu; İ. Gülçin; C. T. Supuran; *Bioorg. Med. Chem.* **2013**, *21*, 1379–1385.
38. N. Berber; M. Arslan; E. Yavuz; C. Bilen; N. Gencer; *J. Chem.* **2013**, *2013*.
39. A. Atahan; N. Gencer; C. Bilen; E. Yavuz; H. Genc; F. Sonmez; M. Zengin; M. Ceylan; M. Kucukislamoglu; *ChemistrySelect* **2018**, *3*, 529–534.

40. F. Celik; M. Arslan; E. Yavuz; D. Demir; N. Gençer; *J. Enzyme Inhib. Med. Chem.* **2014**, *29*, 18–22.

41. B. Özgeriş; S. Göksu; L. P. Köse; I. Gülçin; R. E. Salmas; S. Durdagi; F. Tümer; C. T. Supuran; *Bioorg. Med. Chem.* **2016**, *24*, 2318–2329.

42. M. Topal; H. Gocer; F. Topal; P. Kalin; L. P. Köse; İ. Gülçin; K. C. Cakmak; M. Küçük; L. Durmaz; A. C. Gören; *J. Enzyme Inhib. Med. Chem.* **2016**, *31*, 266–275.

43. M. Heinrich; H. L. Teoh; *J. Ethnopharmacol.* **2004**, *92*, 147–162.

44. İ. Gulcin; M. Abbasova; P. Taslimi; Z. Huyut; L. Safarova; A. Sujayev; V. Farzaliyev; Ş. Beydemir; S. H. Alwasel; C. T. Supuran; *J. Enzyme Inhib. Med. Chem.* **2017**, *32*, 1174–1182.

45. S. Burmaoglu; A. O. Yilmaz; P. Taslimi; O. Algul; D. Kilic; I. Gulcin; *Arch. Pharm. (Weinheim).* **2018**, *351*, 1700314.

46. K. Pedrood; M. Sherafati; M. Mohammadi-Khanaposhtani; M. S. Asgari; S. Hosseini; H. Rastegar; B. Larijani; M. Mahdavi; P. Taslimi; Y. Erden; *Int. J. Biol. Macromol.* **2021**, *170*, 1–12.

47. F. Turkan; A. Cetin; P. Taslimi; İ. Gulçin; *Arch. Pharm. (Weinheim).* **2018**, *351*, 1800200.

48. F. Türker; D. Barut Celepci; A. Aktaş; P. Taslimi; Y. Gök; M. Aygün; İ. Gülçin; *Arch. Pharm. (Weinheim).* **2018**, *351*, 1800029.

49. F. Turkan; A. Çetin; P. Taslimi; M. Karaman; İ. Gulçin; *Bioorg. Chem.* **2019**, *86*, 420–427.

50. D. O. Ozgun; H. I. Gul; C. Yamali; H. Sakagami; I. Gulcin; M. Sukuroglu; C. T. Supuran; *Bioorg. Chem.* **2019**, *84*, 511–517.

51. C. Bayrak; P. Taslimi; H. S. Karaman; I. Gulcin; A. Menzek; *Bioorg. Chem.* **2019**, *85*, 128–139.

52. B. Kuzu; M. Tan; P. Taslimi; İ. Gülçin; M. Taşpınar; N. Menges; *Bioorg. Chem.* **2019**, *86*, 187–196.

53. K. Kucukoglu; H. I. Gul; P. Taslimi; I. Gulcin; C. T. Supuran; *Bioorg. Chem.* **2019**, *86*, 316–321.

54. H. Genç Bilgiçli; P. Taslimi; B. Akyuz; B. Tuzun; I. Gulcin; *Arch. Pharm. (Weinheim).* **2020**, *353,* 1900304.

55. H. G. Bilgicli; D. Ergon; P. Taslimi; B. Tüzün; İ. A. Kuru; M. Zengin; İ. Gülçin; *Bioorg. Chem.* **2020**, *101*, 103969.

56. B. Z. Kurt; I. Gazioglu; F. Sonmez; M. Kucukislamoglu; *Bioorg. Chem.* **2015**, *59*, 80–90.

57. X. Xue; Y. Wang; P. Lu; H. Shang; J. She; L. Xia; H. Qian; W. Huang; *Chem. Pharm. Bull.* **2014**, *62*, 524–527.

58. N. Gök; A. Akıncıoğlu; E. Erümit Binici; H. Akıncıoğlu; N. Kılınç; S. Göksu; *Arch. Pharm. (Weinheim).* **2021,** e2000496.

59. B. Z. Kurt; I. Gazioglu; L. Basile; F. Sonmez; T. Ginex; M. Kucukislamoglu; S. Guccione; *Eur. J. Med. Chem.* **2015,** *102*, 80–92.

60. N. Kumar; S. S. Mishra; C. S. Sharma; H. P. Singh; *Int. J. Appl. Pharm. Biol. Res.* **2016**, *1*, 1–8.

61. K. Palm; P. Stenberg; K. Luthman; P. Artursson; *Pharm. Res.* **1997**, *14*, 568–571.

62. P. Kremers; *Pharmacol. Toxicol.* **2002**, *91*, 209–217.

63. D. J. Begley; M. W. Brightman; *Pept. Transp. Deliv. into Cent. Nerv. Syst.* **2003,** 39–78.
64. S. Adem; E. Akkemik; H. Aksit; P. Guller; A. R. Tüfekci; İ. Demirtas; M. Ciftci; *Med. Chem. Res.* **2019**, *28*, 711–722.
65. J. A. Verpoorte; S. Mehta; J. T. Edsall; *J. Biol. Chem.* **1967**, *242*, 4221–4229.
66. G. L. Ellman; K. D. Courtney; V. Andres Jr; R. M. Featherstone; *Biochem. Pharmacol.* **1961**, *7*, 88–95.
67. G. M. Morris; R. Huey; W. Lindstrom; M. F. Sanner; R. K. Belew; D. S. Goodsell; A. J. Olson; *J. Comput. Chem.* **2009**, *30*, 2785–2791.
68. V. Alterio; S. M. Monti; E. Truppo; C. Pedone; C. T. Supuran; G. De Simone; *Org. Biomol. Chem.* **2010**, *8*, 3528–3533.
69. M. Lopez; B. Paul; A. Hofmann; J. Morizzi; Q. K. Wu; S. A. Charman; A. Innocenti; D. Vullo; C. T. Supuran; S.-A. Poulsen; *J. Med. Chem.* **2009**, *52*, 6421–6432.
70. M. L. Raves; K. Giles; J. D. Schrag; M. F. Schmid; G. N. Phillips; W. Chiu; A. J. Howard; I. Silman; J. L. Sussman; in *Struct. Funct. Cholinesterases Relat. Proteins*; Springer; **1998**, 351–356.
71. A. Daina; O. Michielin; V. Zoete; *Sci. Rep.* **2017**, *7*, 1–13.
72. A. Daina; O. Michielin; V. Zoete; *J. Chem. Inf. Model.* **2014**, *54*, 3284–3301.

CHITOSAN-COATED SILICA NANOPARTICLES DEPOSITED BY ELECTROPHORESIS ON ZINC FOR ANTICORROSIVE PROTECTION

ÁRPÁD FERENC SZŐKE[a], CLAUDINE FILIÂTRE[b], LIANA MARIA MUREȘAN[c*]

ABSTRACT. Silica nanoparticles were covered with a thin layer of chitosan to obtain a positive surface charge. The resulting silica/chitosan nanoparticles were characterized using zeta potential and particle size analysis before being electrophoretically deposited on zinc substrates to obtain an anticorrosive coating. The uniformity of the resulting layers was studied by optical and scanning electron microscopy. The anticorrosive properties were determined using potentiodynamic polarization and electrochemical impedance spectroscopy. Results show non-uniform deposits of nanoparticles. Nevertheless, the electrochemical measurements point to a relatively significant corrosion inhibition efficiency of the coating (*ca.* 60-80%) which increases with the time of deposition.

Keywords: *chitosan, silica nanoparticles, electrophoretic deposition, zinc, corrosion*

INTRODUCTION

Silica nanoparticles are versatile materials [1] with several important advantages such as biocompatibility [2], a simple production process [3], as well as controlled particle size and particle size distribution [4]. Special attention is accorded to porous silica nanoparticles, as in addition to the particle size, the pore size and size distribution can also be tailored for specific applications [5], resulting in the availability of a wide array of nano-, meso- and microporous silica nanoparticles.

[a] *Babeş-Bolyai University, Faculty of Chemistry and Chemical Engineering, Department of Chemistry and Chemical Engineering of the Hungarian Line*
[b] *Institut UTINAM, UMR-CNRS 6213, Université de Bourgogne Franche-Comté, Besançon, France*
[c] *Babeş-Bolyai University, Faculty of Chemistry and Chemical Engineering, Department of Chemical Engineering*
* *Corresponding author: liana.muresan@ubbcluj.ro*

As such, they have been considered for several different applications, such as drug [6] and enzyme [7] carriers, anticorrosive additives [8], adsorption agents, etc. Although these studies mainly focus on porous silica as a possible carrier [9], compact nanoparticles have also been tested as additives in polymeric coatings, usually incorporated into polymeric matrices where they can improve the structural stability of the coatings [8].

Silica surfaces have a negative charge under most pH conditions [10], which is neutralized only by strongly acidic environments. As such, the application of silica nanoparticles on a negatively charged zinc substrate is not possible. To circumvent this problem, silica nanoparticles can be coated with a positively charged polymer, like chitosan. Chitosan (Chit) is composed of randomly distributed β-linked D-glucosamine and N-acetyl-D-glucosamine [11]. As the amine groups can be protonated partially or completely, chitosan becomes soluble in acidic environments. Bridging the positive charges in linear chitosan using covalent or ionic crosslinking agents can significantly affect structural stability, water permeability and solubility [12, 13, 14]. Due to its versatility and ease of structural modification, chitosan is considered a possible eco-friendly alternative for several applications in a wide range of industries such as agriculture [15], medicine [16], anticorrosive protection [17] and water purification [18]. As chitosan possesses antimicrobial properties, it has also been considered to counter microbial corrosion [19]. Previous studies show that thin chitosan layers show good adhesion to zinc surfaces, which can be explained by the presence of trace amounts of oxidized groups on the metal surface [20]. The swelling properties of thin chitosan layers hinder shielding properties. As such, native chitosan cannot form effective anticorrosive coatings [14].

It was assumed that chitosan and silica nanoparticles can form strong electrostatic bonds [21] with a thin chitosan layer surrounding the silica core. This should result in a silica/chitosan nanoparticle with a positive surface charge.

In this context, chitosan-coated silica nanoparticles were produced from commercially available SiO_2 nanoparticles and low molecular weight (lmw) chitosan. These were deposited on zinc substrates to obtain a protective barrier with increased anticorrosive properties. To the best of our knowledge, no previous studies were published regarding films formed by electrophoretic deposition of chitosan-coated silica nanoparticles on zinc substrates.

The nanoparticles were characterized using total organic carbon (TOC) content, particle size and zeta potential analysis. The uniformity of the coatings was studied using optical and scanning electron microscopy. Their anticorrosive properties were determined using potentiodynamic polarization and electrochemical impedance spectroscopy techniques.

RESULTS AND DISCUSSION

Adsorption of chitosan on the silica nanoparticles

TOC analysis shows a decrease in the carbon content in the chitosan solutions when SiO_2 nanoparticles are added to them (Figure 1). This difference was attributed to chitosan adsorption on the surface of the silica cores.
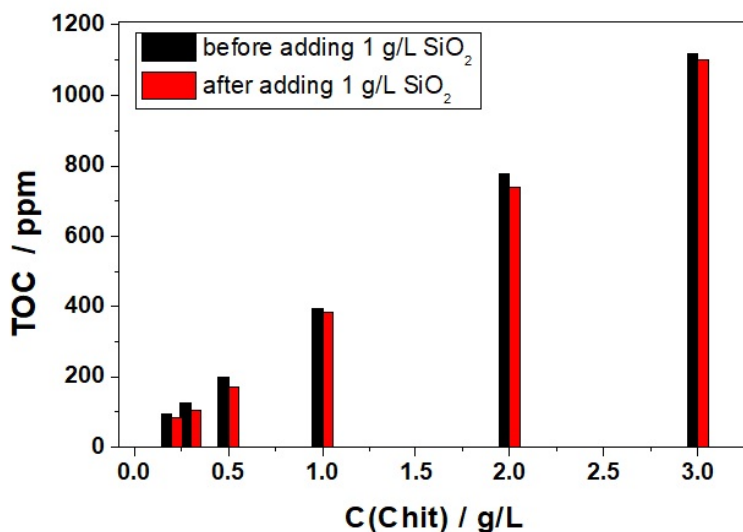

Figure 1. Total organic carbon content analysis of low molecular weight chitosan solutions with varying concentrations before (**black**) and after (**red**) adding 1g/L Si nanoparticles.

The zeta potential of the chitosan-coated silica nanoparticles was determined for different chitosan concentrations. It can be observed, that initially, an increased amount of chitosan resulted in increased zeta potential; which finally reached a plateau at 50-60 mV, when 1 g/L chitosan was added to 1 g/L SiO_2 (Figure 2).

The diameter of the chitosan/SiO_2 nanoparticles was measured in function of chitosan concentration. Composite particle size is equal to about 500 nm for chitosan concentration below 500 mg/g(SiO_2) (Figure 3). Particles are positively charged and the plateau of adsorption is not reached. For higher chitosan concentration, particle size increased. This may be due to polymer adsorption on a few particles.
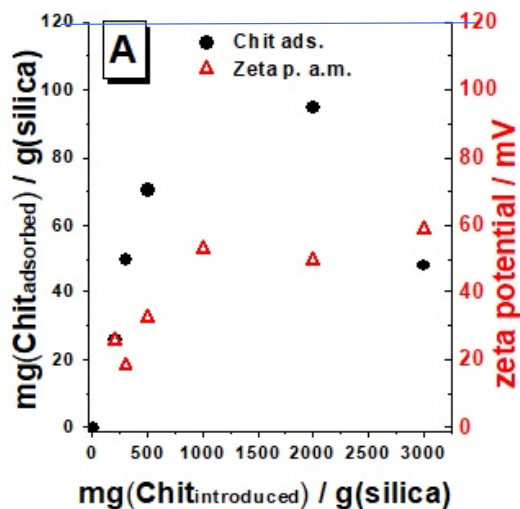
Figure 2. Amount of chitosan adsorbed on SiO_2 (●) and zeta potential determined with auto-mode (**Δ**) as a function of the added amount of chitosan. Experimental conditions: low molecular weight chitosan, 1 g/L silica, 25 °C, pH 4.
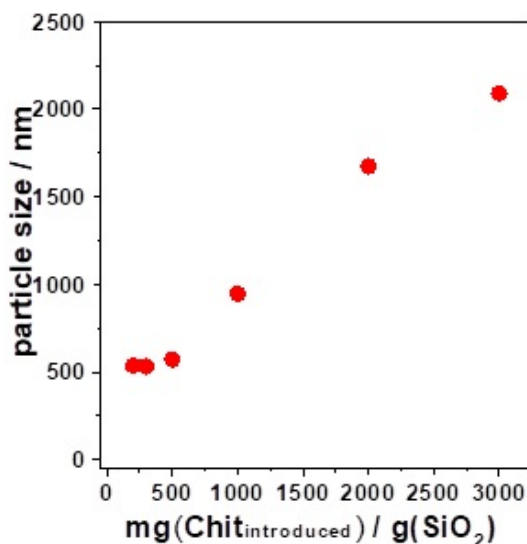

Figure 3. Particle size of chitosan-coated silica nanoparticles as a function of chitosan added to the SiO_2 dispersion. Experimental conditions: low molecular weight chitosan, 1 g/L silica, 25 °C, pH 4
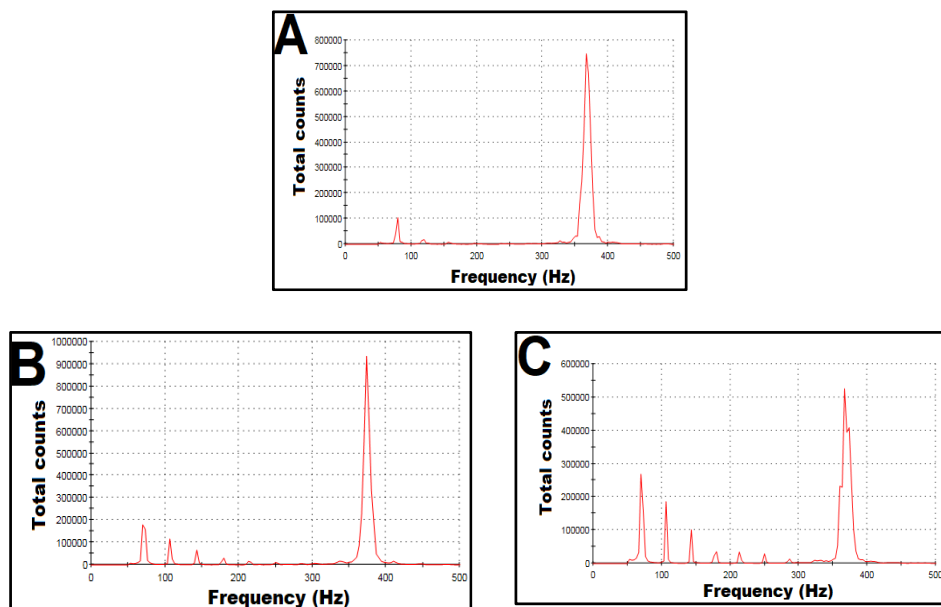
Figure 4. Frequency plots of 500 mg($Chit_{introduced}$)/g(SiO_2) system immediately after agitation (**A**), after 30 minutes of sedimentation (**B**) and after 60 minutes of sedimentation (**C**).

To determine the temporal stability, a chitosan-coated silica nanoparticle dispersion was chosen with minimal particle size (*i.e.* 500 mg chitosan added to 1 g/L silica nanoparticle dispersion). Frequency dependence plots were determined at room temperature at different time intervals after the agitation of the mixtures (Figure 4). These show a relatively monodisperse system initially, which gradually becomes more polydisperse after 30 and 60 minutes of sedimentation, respectively. As such, to obtain a more uniform coating, dispersions should be freshly used.

Optical microscopy of the coated zinc plates

Visual inspection of the coated zinc substrates pointed to a non-uniform surface coverage, which was verified using different optical methods.

Optical microscopy confirmed our initial observation, showing a non-uniform coating of nanoparticles (observable as dark patches on the micrographs). 30 minutes of electrophoretic deposition resulted in only small patches of nanoparticles on the zinc surface (Figure 5 B). An increased time of 90 minutes of electrophoretic deposition increased the amount of deposited particles significantly; however, the uniformity of the coating did not improve significantly (Figure 5 C) [22].
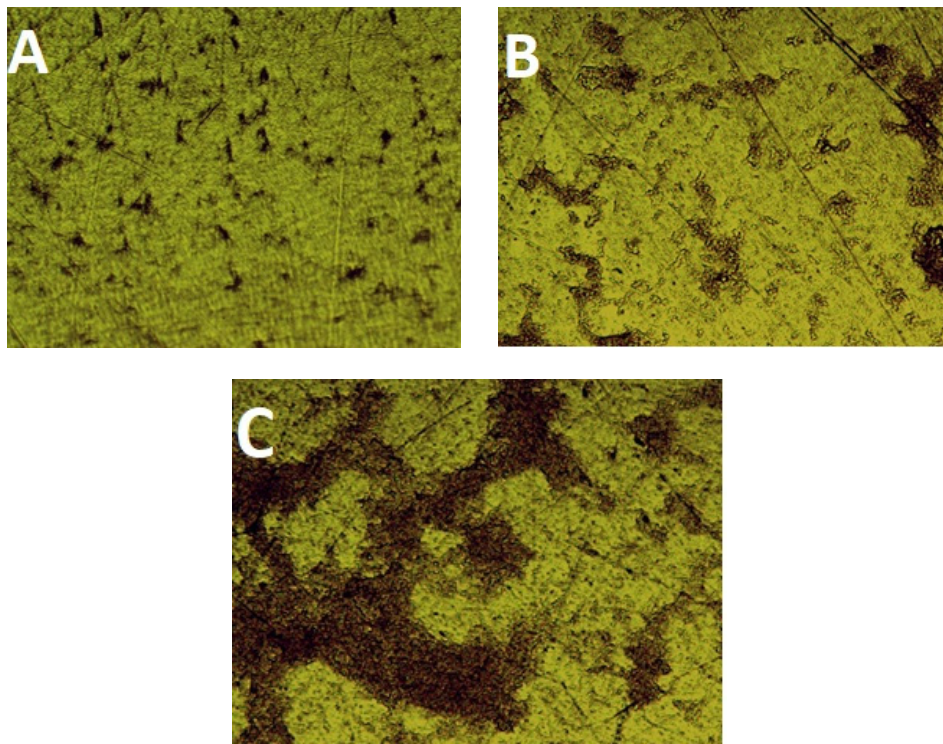
Figure 5. Optical microscopy images of a bare, polished Zn plate (**A**), and zinc substrates coated by electrophoretic deposition for 30 minutes (**B**) and 90 minutes (**C**), respectively. Magnification: **20X**.

Scanning electron microscopy

The scanning electron microscopy study further corroborates the visual and optical microscopy inspection, with a non-uniform coating regardless of ED duration (Figure 6). It should be noted, that the number of nanoparticles and coverage are significantly better when the particles were deposited for 90 minutes.
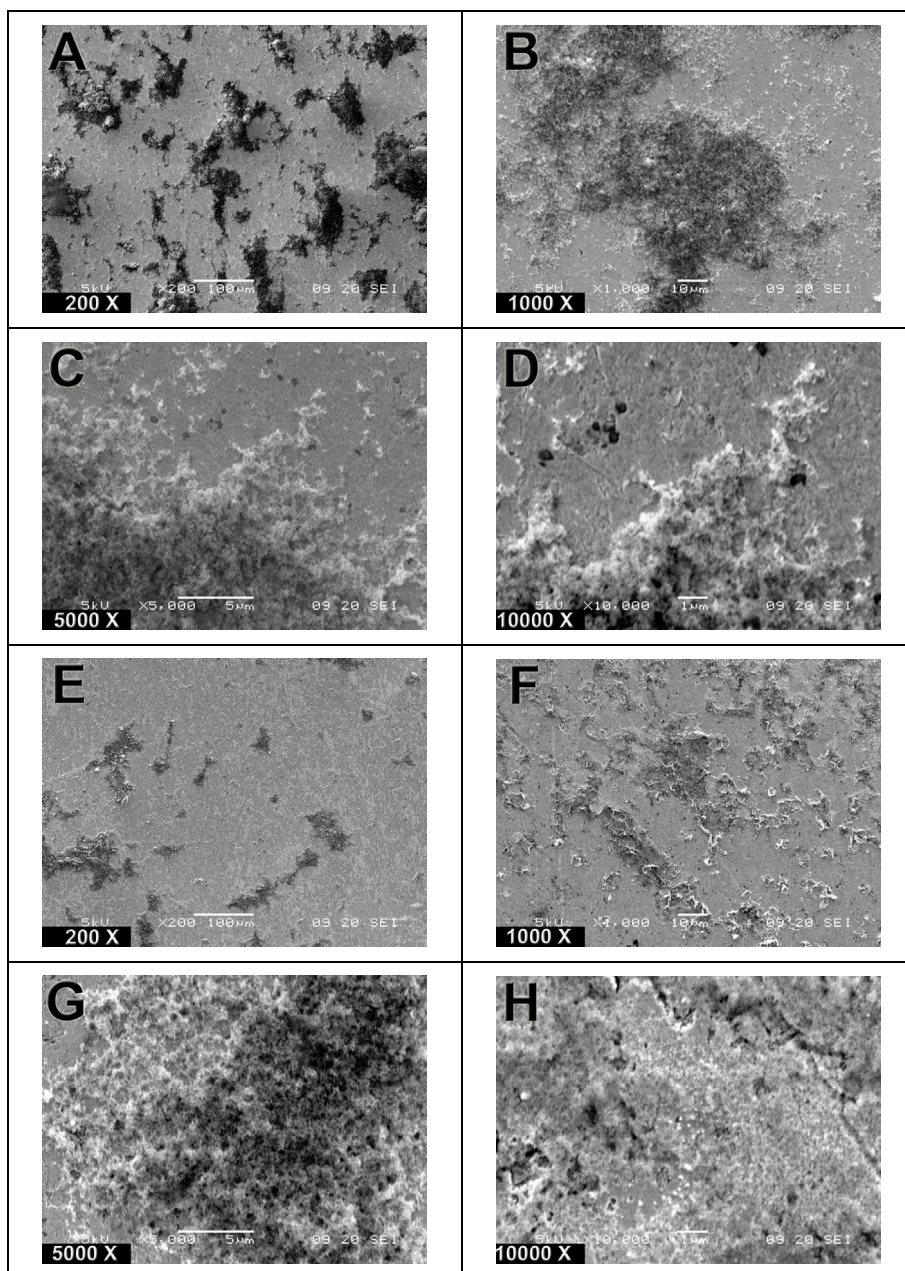
Figure 6. SEM images of coated zinc substrates after 30 minutes (A, B, C, D) and after 90 minutes (E, F, G, H) of ED at increasing magnifications.

Previous studies attributed the good adhesion of dip-coated chitosan layers on zinc to the presence of oxide and hydroxide traces on the metal surface [20]. In our case, it was theorized that the nanoparticles were initially deposited more efficiently at sites where surface defects (irregularity or oxidation) were present. The deposited nanoparticles electrostatically repulsed further nanoparticles, resulting in the uneven coverage [23].

Electrochemical analysis

The polarization resistance of the coated samples was improved compared to bare zinc, as seen from the Nyquist impedance spectra (Figure 7). The fitted equivalent electrical circuit proposed for uncoated Zn was $R(Q_1R_1)$, with R representing the resistance of the Na_2SO_4 electrolyte solution used for electrochemical measurements, R_1 representing the charge transfer resistance and Q_1 is a constant phase element for a non-ideal system, characterizing the double layer capacity through the following equation:

$$C = R^{\frac{1-n}{n}} Q^{\frac{1}{n}}, \text{[24]},$$

where n is a coefficient representing the depressed feature of the capacitive loop.

Similar to our previous studies of chitosan-coated zinc samples, an $R(Q_1R_1(LR_2))$ equivalent circuit showed the best fit for the nanoparticle-coated zinc. In this case, the additional LR_2 pair could be attributed to the resistance of the coating and the swelling properties of chitosan [14]. The similar curves and values of the charge transfer resistance for the reproduced systems (Table 1, *ca.* 3500 Ωcm^2 for 30 minutes and *ca.* 6000 Ωcm^2 for 90 minutes ED) demonstrate a good reproducibility, despite the uneven coating observed by optical studies. It can also be observed that the resistance value attributed to the coating itself greatly increased when 90 minutes of ED was used. This is due to the increased amount of nanoparticles on the zinc surface, as observed in the optical analysis.
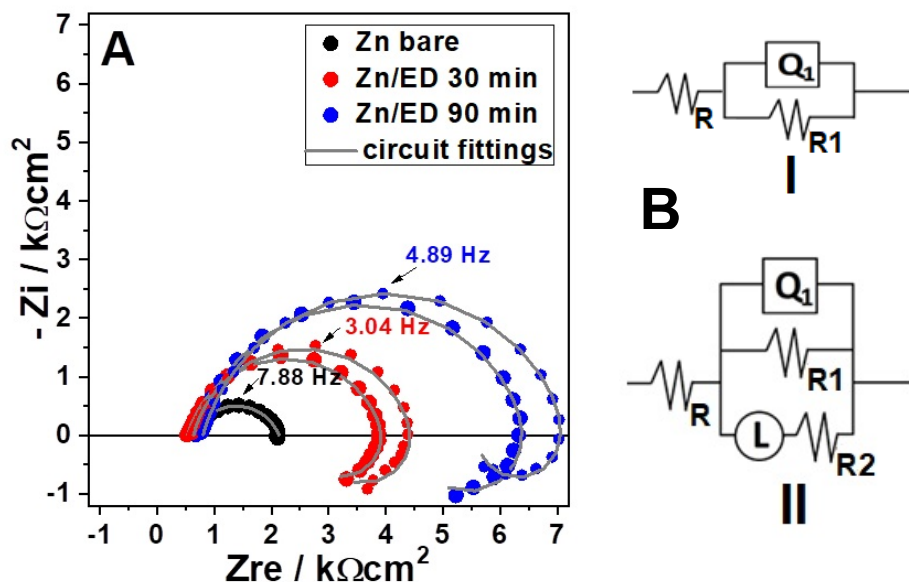
Figure 7. Nyquist impedance spectra of bare Zn and Chit/SiO$_2$ coated Zn (A), and fitted equivalent electric circuits (B) for the bare zinc substrate (B - I) and the nanoparticle-coated zinc substrate (B - II). Experimental conditions: 0.2 g/L Na$_2$SO$_4$ solution (pH 5.0); frequency interval, 10 kHz – 10 mHz; OCP, 60 minutes.

Table 1. Electrochemical parameters obtained from the Nyquist impedance spectra [22].

Samples	R (Ωcm^2)	Q$_1$ (μSs^n)	R$_1$ (Ωcm^2)	L (kH)	R$_2$ (Ωcm^2)	Chi^2
Zn	508	40.0	1460	-	-	0.38 X 10^{-3}
Zn/ED 30 min_1	539	17.8	3419	124	4707	0.72 X 10^{-3}
Zn/ED 30 min_2	638	19.5	3846	109	4983	1.22 X 10^{-3}
Zn/ED 90 min_1	696	15.9	5798	176	10910	0.38 X 10^{-3}
Zn/ED 90 min_2	804	9.50	6428	95	18860	0.22 X 10^{-3}

1 and_2 notations represent the reproduction of the systems in the same conditions

183

Polarization curves (Figure 8) corroborate EIS results with decreased current densities for the coated samples prepared with 30 and 90 minutes of ED [22]. The inhibition efficiency values determined from the polarization curves show an anticorrosive effect of *ca.* 60% for 30 minutes of ED and *ca.* 75% for 90 minutes of ED (Table 2.).
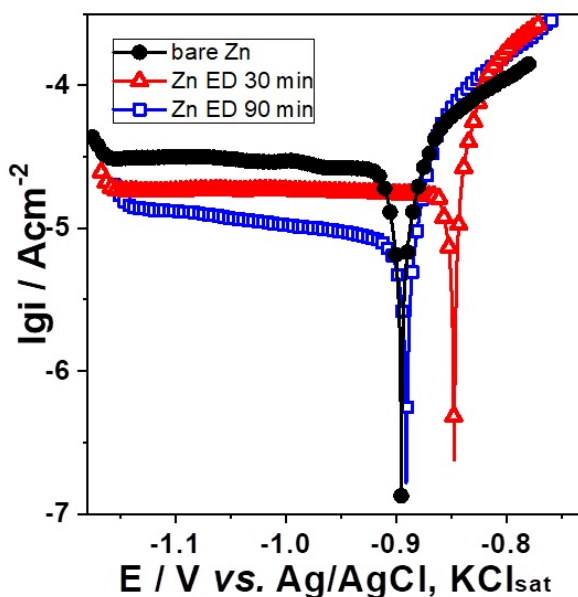

Figure 8. Semi-logarithmic polarization curves (current density *vs.* potential) of bare Zn (●), Zn/ED 30 min (□) and Zn/ED 90 min (▲) systems
Experimental conditions: 0.2 g/L Na_2SO_4 solution, scan rate,
0.166 mV/s, OCP, 60 minutes.

Table 2. Electrochemical parameters of various coated zinc samples determined from the polarization curves [22].

Sample	E_{corr} (V)	b_c (V/dec)	b_a (V/dec)	i_{corr} ($\mu A / cm^2$)	IE (%)
Zn bare	-0.893	-	0.188	41.56	-
Zn/ED 30 min	-0.847	-	0.133	15.00	63.91
Zn/ED 90 min	-0.891	0.949	0.165	9.60	76.90

As a non-destructive method, electrochemical impedance spectroscopy was used to study the short- and long-term effects of exposure to a corrosive environment (Figure 9 and 10, Table 3).

Figure 10. Nyquist impedance spectra of Zn/ED 90 min during short- (A)
and long-term (B) exposure to a corrosive medium.
Experimental conditions: 0.2 g/L aqueous Na_2SO_4 solution (pH = 5),
frequency interval, 10 kHz - 10 mHz, OCP, 60 minutes (day 0),
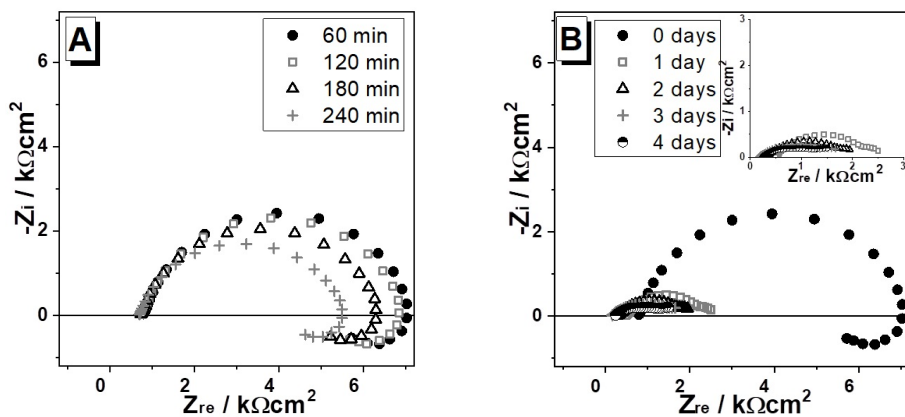10 minutes (days 1-4).

Figure 9. Nyquist impedance spectra of Zn/ED 30 min during short- (A) and long-
term (B) exposure to a corrosive medium. Experimental conditions: 0.2 g/L aqueous
Na_2SO_4 solution (pH = 5), frequency interval, 10 kHz - 10 mHz, OCP, 60 minutes
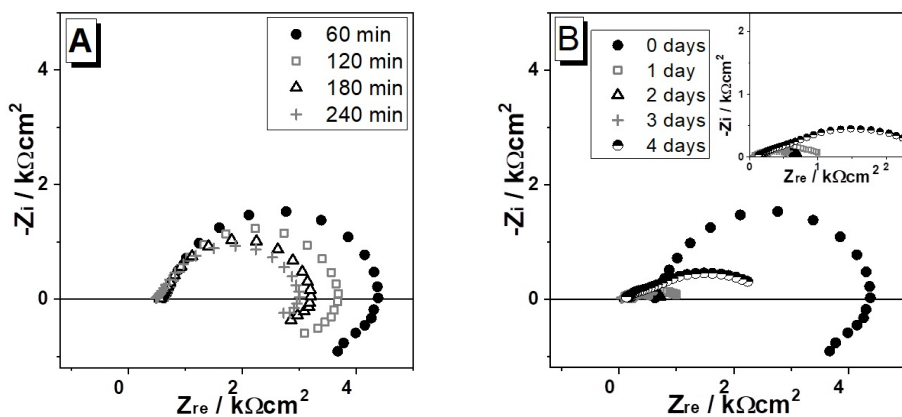(day 0), 10 minutes (days 1-4).

Table 3. Rp value change of studied samples during short- and long-term EIS studies.

Sample	unit	60 min	120 min	180 min	240 min	1 day	2 days	3 days	4 days
Zn/ED 30 min	$k\Omega cm^2$	3.77	3.09	2.66	2.51	0.79	0.60	0.53	2.11
Zn/ED 90 min	$k\Omega cm^2$	6.23	6.07	5.57	4.84	2.01	1.64	1.49	1.25

For both 30 and 90 minutes of ED, the diameter of the Nyquist curves (which represents the polarization resistance) decreased each hour after exposure, pointing to diminishing anticorrosive protection. In the case of samples prepared with 30 minutes of ED, the initial Rp value of 3.77 $k\Omega cm^2$ dropped to 2.51 $k\Omega cm^2$ after 4 hours. For 90 minutes of ED, the initial value of 6.23 $k\Omega cm^2$ dropped to 4.84 $k\Omega cm^2$ in the same time period, underlining that the diminishing effect is less pronounced for substrates coated with 90 minutes of ED. Similarly, the Rp values of corresponding curves were always significantly higher (around twofold) in the case of the longer deposition time.

The study of long-term exposure also shows a gradual polarization resistance decrease, however, in the case of the sample coated with 30 minutes of ED, the polarization resistance actually increased after 4 days (from 0.53 to 2.11 $k\Omega cm^2$) probably due to the deposition of corrosion products on the zinc surface and its partial blocking**.**

CONCLUSIONS

Chitosan-coated silica nanoparticles were successfully prepared by adsorption of the polymer on commercial silica nanoparticles. The so-prepared nanoparticles obtained a significant positive charge in slightly acidic conditions, offering a possibility to be electrophoretically deposited on zinc.

The optical study shows an uneven deposition of nanoparticles on the zinc surface. Electrochemical studies point to significant coverage of the zinc surface, resulting in anticorrosive activity, as proved by both polarization and impedance spectroscopy measurements. This effect is improved when a longer period of deposition is used.

The significant anticorrosive effect of the layers, in contrast with their uniformity probably occurred due to nanoparticle deposition at surface defects.

EXPERIMENTAL SECTION

Materials and methods

37% HCl from VWR was diluted to dissolve the low molecular weight chitosan. The pH was adjusted using NaOH from Riedel-de-Haen. 99.9% Sodium chloride and 99.6% isopropanol were obtained from VWR. Low molecular weight (50000-190000 Da) chitosan (lmw Chit) was purchased from Aldrich, Aerosil 200 silica nanoparticles from Degussa. Distilled water was prepared with a Millipore synergy UV water purifier.

The pH was measured using a pH meter from Mettler Toledo with a combined glass electrode.

The zinc plates were obtained from Bronzker BT and cut into 2x5 cm pieces. The surface of zinc was smoothed by polishing with different types of abrasive paper (2000, 4000, 5000), until mirror-aspect. Any residual powder from the polishing process was removed by 2x5 minutes of ultrasonication in isopropanol. Finally, the zinc plates were rinsed with 0.1 M HCl and distilled water to remove any remaining oxide or hydroxide from the surface [20, 22], and coated immediately.

Adsorption of chitosan on silica, TOC analysis

The adsorption of the chitosan on the silica nanoparticles was determined using TOC analysis on a **T**otal **O**rganic **C**arbon content analyzer from Shimadzu.

A series of lmw Chit (0.02, 0.03, 0.05, 0.1, 0.2, 0.3 w/w%) solutions were prepared by dissolving chitosan in 0.1 M HCl. Following an initial TOC analysis to be used as a reference, the pH of the solutions was set to 4 (favoring adsorption) and silica nanoparticles were added to reach a concentration of 1 g/L. To adequately cover the silica nanoparticles with chitosan, it is preferred that the two materials have an opposite surface charge. Chitosan molecules get protonated in acidic conditions and their surface charge becomes more positive with a lower pH. In contrast, silica surfaces have a negative surface charge, which becomes neutral only in strongly acidic environments. As such, a pH level of 4 was chosen, where chitosan dissolves effectively through protonation, while the silica nanoparticles should still have a negative surface charge.

The agglomerates in the silica nanoparticles were dispersed by 5 minutes of ultrasound treatment. The mixture was then left overnight under agitation, so the chitosan was adsorbed on the nanoparticles. The suspensions were then centrifuged at a speed of 10000 rpm, for 10 minutes; parameters were determined with equation (1) [22].

$$v = \frac{2\,(\rho_p - \rho_L)\,Gg\,a_p^2}{9\,\eta} \tag{1}$$

Where:

v - sedimentation speed (m/s)

ρ_P - density of the particles (kg/m^3)

ρ_L - density of the liquid (kg/m^3)

g - gravitational constant (m/s^2)

η - viscosity (Pa*s)

a_P – particle radius (m)

G – number that multiplies g because of the rotation speed

$$G = \frac{R\omega^2}{g}$$

The resulting chitosan solution was studied by TOC analysis. The results were compared to the reference solutions before some of the dissolved chitosan was adsorbed on the silica nanoparticles.

Zeta potential and particle size analysis

The study was conducted on a Zetasizer from Malvern Panalytical. The same series of solutions were used to determine the zeta potential and particle size of the Chitosan/SiO$_2$ nanoparticles.

Electrophoretic deposition

Based on previous experience and results obtained for adsorption and zeta potential, an optimized recipe was used consisting of 200 mL solution containing 0.04025 w/w% Chit (or 402,5 mg Chit$_{introduced}$/gSi), 1 g/L silica nanoparticles, 0.365 M HCl (to dissolve the chitosan), NaOH (to set the pH levels to the desired value of 4) and 0.3 M NaCl. A minimum amount of 30 minutes (under constant stirring) was given for the adsorption to take place [22].

An undivided three-electrode cell was put together with a platinum-plate as the counter electrode, a Ag/AgCl reference electrode and the polished Zn plate as the working electrode.

The electrophoretic deposition (ED) was conducted at an applied potential of -1.5 V under constant, slow magnetic stirring. If we observed a large amount of bubble formation, the voltage was decreased to -1.4 V. After 30 minutes, or 90 minutes, respectively, the suspension was replaced with distilled water and, for a few minutes, a potential of -5 V was applied to stabilize the coated system [25].

Optical microscopy and SEM analysis

Following ED, the samples were dried. To verify the dispersion of the nanoparticles and the effectiveness of the coating, optical microscopy (with a Moticam microscope camera, 5 MP and an Olympus IC 20 microscope objective) and scanning electron microscopy (JEOL 5510LV) were conducted on the coated samples.

Electrochemical study

Electrochemical measurements were performed using a PARSTAT-2273 computer-controlled potentiostat (Princeton Applied Research, United Kingdom). An undivided electrochemical cell containing the coated zinc sample (1 cm^2 surface area) as the working electrode, a platinum wire as the counter (Type P131 Radiometer, France) and a Ag/AgCl,KCl$_{sat}$ reference electrode (Radiometer, France) were connected to the potentiostat. All experiments were carried out at room temperature (25 °C) [22].

Electrochemical impedance spectroscopy (EIS) measurements were conducted in a 0.2 g/L aqueous Na_2SO_4 (pH = 5) solution as the electrolyte. It should be noted that this pH value differs from the ideal pH for the coated nanoparticle formation (which is pH 4). The reason for this is that previous studies point to chitosan being relatively stable at these conditions [14], as well as the fact that naturally occurring corrosive environments often have similar pH values.

The open circuit potential (OCP) was measured for 60 minutes before the initial EIS measurements. In the case of subsequent EIS measurements (after exposures to the corrosive medium between 1 hour and 4 days), the open circuit potential was stable after 10 minutes.

The frequency interval of the measurements was 10^4 Hz - 10^{-2} Hz at open circuit potential (OCP). The experimental spectra were fitted with different electrical equivalent circuits by using the ZSimpWin 3.21 software.

Potentiodynamic polarization curves were recorded with a scan rate of 10 mV/min, in a potential range of OCP ± 200 mV vs. Ag/AgCl, KCl$_{sat}$. The inhibition efficiency was calculated using the formula (2):

$$IE(\%)= 100 \cdot \frac{i^0_{corr}-i_{corr}}{i^0_{corr}} \tag{2}$$

ACKNOWLEDGEMENTS

REFERENCES

1. P. G. Jeelani; P. Mulay; R. Venkat; C. Ramalingam; *Silicon-Neth.*, **2020**, *12*, 1337–1354

2. O. Esim; S. Kurbanoglu; A. Savaser; S. A. Ozkan; Y. Ozkan, Nanomaterials for Drug Delivery Systems. In *New Developments in Nanosensors for Pharmaceutical Analysis*, S. A. Ozkan, A. Shah Eds.; Academic Press, **2019**, Chapter 9, pp. 273-301

3. L. P. Singh; S. K. Bhattacharyya; R. Kumar; G. Mishra; U. Sharma; G. Singh; S. Ahalawat; *Adv. Colloid Interfac.*, **2014**, *214*, 17-37

4. S. Nagappan; A. Mohan; A. M. Thomas; J.-M. Yoo; N. Eid; I. Chung; B. Ameduri; C.-S. Ha; *RSC Adv.*, **2021**, *11*, 2194-2201

5. E. Albert; N. Cotolan; N. Nagy; Gy. Sáfrán; G. Szabó; L.-M. Mureşan; Z. Hórvölgyi; *Microp. Mesopor. Mat.*, **2015**, *206*, 102-113

6. N.-T. Nguyen-Thi; L. P. P. Tran; N. T. T. Le; M.-T. Cao; T.-N. Tran; N. T. Nguyen; C. H. Nguyen; D.-H. Nguyen; V. T. Than; Q. T. Le; N. Q. Trun; *Processes*, **2019**, *7(11)*, 805

7. B. Szokol; G. Hornyánszki; J. Nagy; *Stud. U. Babes-Bol. Che.,* **2019**, *LXIV 2 Tom I*, 69-78

8. L. V. Mora; S. Naik; S. Paul; R. Dawson; A. Neville; R. Barker; *Surf. Coat. Tech.*, **2017**, *324*, 368-375

9. M. Yeganeh; M. Omidi; S. H. H. Mortazavi; A. Etemad; M. H. Nazari; S. M. Marashi; Application of mesoporous silica as the nanocontainer of corrosion inhibitor. In *Micro and Nano Technologies, Corrosion Protection at the Nanoscale*, S. Rajendran, T. A. N. H. Nguyen, S. Kakooei, M. Yeganeh, Y. Li, Eds.; Elsevier, **2020**, Chapter 15, pp. 275-294

10. S. H. Behrens; D. G. Grier; *J. Chem. Phys.,* **2001**, *115*, 6716-6721

11. R. C. Cheung; T. B. Ng; J. H. Wong; W. Y. Chan; *Mar. drugs*, **2015**, *13(8)*, 5156–5186

12. J. Berger; M. Reist; J. M. Mayer; O. Felt; N. A. Peppas; R. Gurny; *Eur. J. Pharm. Biopharm.,* **2004***, 57,* 19–34

13. L. Y. Pozzo; T. F. Conceição; A. Spinelli; N. Scharnagl; A.T.N. Pires; *Carbohyd. Polym.*, **2018**, *181,* 71–77

14. Á. F. Szőke; G. S. Szabó; Z. Hórvölgyi; E. Albert; L. Gaina; L. M. Muresan; *Carbohyd. Polym.*, **2019**, *215*, 63-72

15. S. Bandara; H. Du; L. Carson; D. Bradford; R. Kommalapati; *Nanomaterials-Basel,* **2020**, *10(10)*, 1903

16. D. Zhao; S. Yu; B. Sun; S. Gao; S. Guo; K. Zhao; *Polymers-Basel*, **2018**, *10(4)*, 462

17. Á. F. Szőke; G. Szabó; Z. Simó; Z. Hórvölgyi; E. Albert; A. G. Végh; L. Zimányi; L. M. Muresan; *Eur. Polym. J.,* **2019***, 118*, 205-212

18. A. J. Al-Manhel; A. R. S. Al-Hilphy; A. K. Niamah; *J. Saudi Soc. Agric. Sci.,* **2018**, *17(2),* 186-190

19. P. A. Rasheed; R. P. Pandey; K. A. Jabbar; A. Samara; A. M. Abdullah, A. M.; K. A. Mahmoud; *Materials,* **2020***, 13(11),* 2484

20. Á. F. Szőke; G. S. Szabó; Z. Hórvölgyi; E. Albert; A. G. Végh; L. Zimányi; L. M. Muresan; *Int. J. Biol. Macromol*., **2020**, *142*, 423-431

21. M. Dabóczi; E. Albert; E. Agócs; M. Kabai-Faix; Z. Hórvölgyi; *Carbohyd. Polym.*, **2015**, *136*, 137–145

22. Á. F. Szőke; Polymer-modified surfaces for electroanalytical applications and anticorrosive protection, PhD Thesis, **2019**

23. C. Dange-Delbaere; C. C. Buron; M. Euvrard; C. Filiatre; *Colloid. Surface. A*, **2016**, *493*, 1-8

24. M. N. Kakaei; J. Neshati; A. R. Rezaierod; *Prot. Met. Phys. Chem. Surf.,* **2018**, *54*, 548–556

25. C. Pignolet; C. Filiatre ; A. Foissy; *Langmuir,* **2008**, *24(18),* 10181-10186.

HALOGEN-BONDED SUPRAMOLECULAR ARCHITECTURES INVOLVING 2,7-DIPYRIDYLFLUORENE AND 1,3,5-TRIFLUORO-2,4,6-TRIIODOBENZENE TECTONS – A SPECTACULAR EVOLUTION FROM CATEMERS TO 2D HALOGEN BOND ORGANIC FRAMEWORKS (XBOF)

LIDIA CĂTA[a], IOANA GEORGETA GROSU[b], MARIA MICLĂUŞ[b], NICULINA DANIELA HĂDADE[a], ION GROSU[a] and ANAMARIA TEREC[a,*]

ABSTRACT. A spectacular 2D Halogen Bond Organic Framework (XBOF) was prepared by the mechanochemical solvent-drop grinding method (SCD) starting from 2,7-dipyridylfluorene and 1,3,5-trifluoro-2,4,6-triiodobenzene tectons. The formation of the supramolecular assembly was proved by powder X-ray diffraction measurements and the structural details were collected from the single crystal X-ray diffraction investigations.

Keywords: N···I and I···F halogen bonds, XBOFs, dipyridylfluorene, 1,3,5-trifluoro-2,4,6-triiodobenzene, single crystal X-ray diffraction structure

INTRODUCTION

The literature data reveal exciting supramolecular host-guest complexes involving macrocycles, [1] cryptands, [1a, 1b, 2] cages [1a, 1b, 3] or mechanically interlocked systems (e.g. rotaxanes or catenanes).[4] The fascinating world of supramolecular architectures was enriched by spectacular self-assembly processes of single molecules [5] or by self-sorting and directed assembly of complementary molecules having as driving forces hydrogen [6] or halogen bonds, [7] hydrophobic contacts, [8] charge transfer complexes [9] and cation- [1a, 1b, 10] or anion-organic [1b, 11] interactions.

[a] *Babes-Bolyai University, Faculty of Chemistry and Chemical Engineering, Department of Chemistry and SOOMCC, Cluj-Napoca, 11 Arany Janos, 400028, Cluj-Napoca, Romania*
[b] *National Institute for Research and Development of Isotopic and Molecular Technologies, 67-103 Donath str., RO-400293, Cluj-Napoca, Romania*
* *Corresponding author: anamaria.terec@ubbcluj.ro*

Halogen bonds [12] proved to be versatile tools in supramolecular chemistry. The obtaining of pure organic supramolecular structures by the cocrystallisation (supramolecular synthesis) of polydentate halogen donors and halogen acceptors lead to outstanding XBOFs [Halogen(X) Bond Organic Frameworks; 1D, [7c, 13] 2D [14] or 3D [7d, 15] polymeric structures].

In a previous work we investigated the N⋯I halogen bond-based formation of catemers using 2,7-dipyridylfluorene (2,7-DPF) **1** as halogen acceptor and *ortho*-, *meta*- and *para*-diiodo-tetrafluorobenzene (DITFB) isomers (**2**–**4**; Figure 1) as halogen donors. [7c] The single crystal X-ray diffraction structures of these 1D polymers (catemers I-III) revealed a significant correlation between the structures of the polymers and the geometries of the halogen donors (Figure 2).

In this context we considered of interest to develop N⋯I halogen bond-based 2D networks (XBOFs) using 2,7-DPF (**1**) as ditopic halogen acceptor and 1,3,5-trifluoro-2,4,6-triiodobenzene (**5**, TFTIB) as tritopic halogen donor (Figure 3).
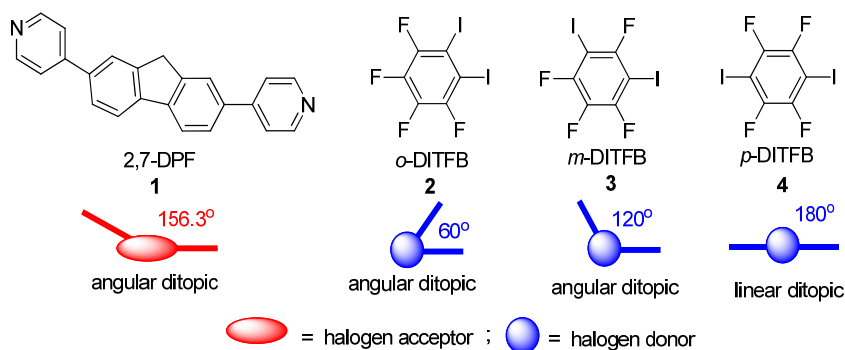

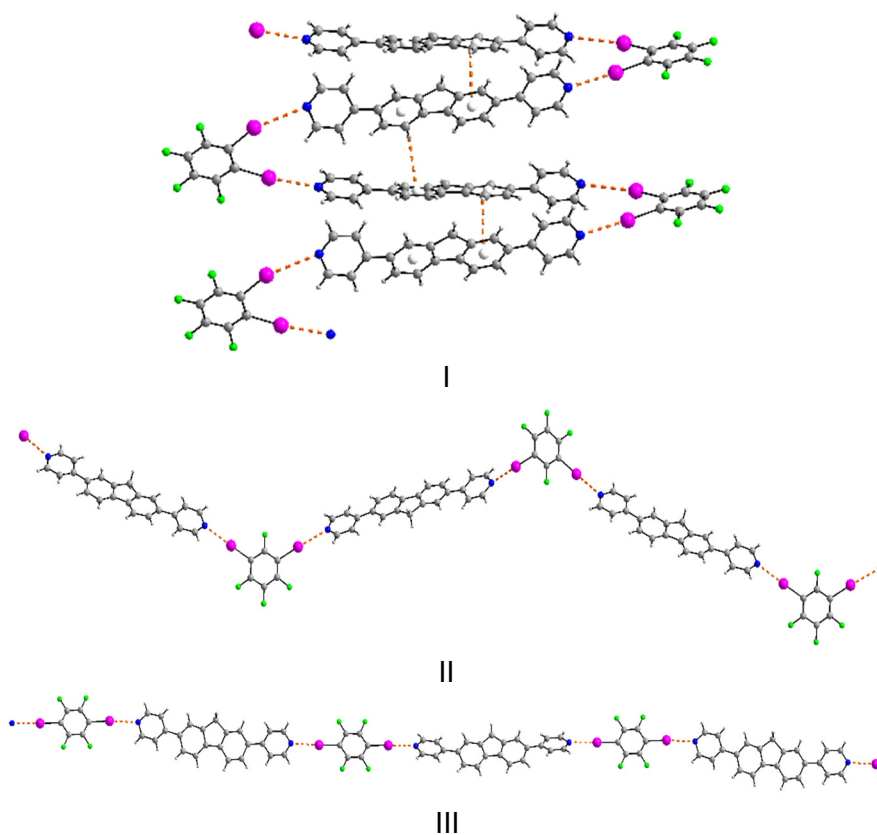**Figure 1.** Halogen donors and acceptors used for the access to 1D polymers by N⋯I contacts

I

II

III

Figure 2. N···I halogen bond catemers with angular (I and II)
and linear (III) geometries

2,7-DPF
1

156.3°

ditopic angular

TFTIB
5

120°
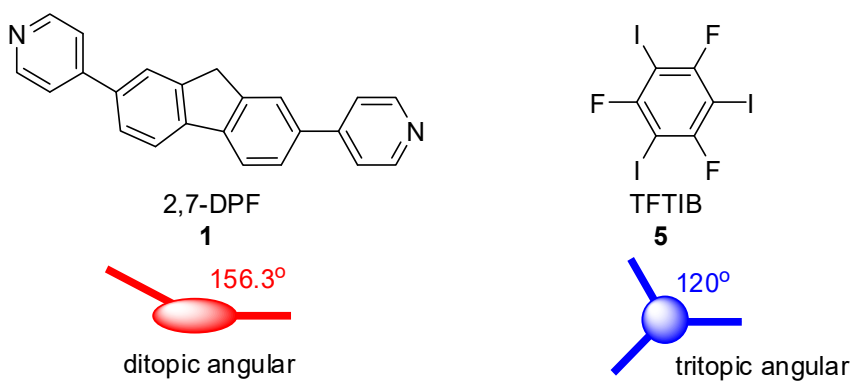
tritopic angular

Figure 3. Proposed halogen acceptor (**1**) and halogen donor (**5**) for the access to
2D Halogen Bond Organic Frameworks (XBOFs)

RESULTS AND DISCUSSIONS

The halogen bond-based supramolecular architecture **(2,7-DPF)(TFTIB)** was obtained by the mechanochemical solvent-drop grinding method (SDG) [16] using a Retsch MM400 mixer mill (120 min at 30 Hz) with stainless steel grinding jars (1.5 mL). 2,7-Dipyridylfluorene (**1**; 0.06 mmol) and 1,3,5-trifluoro-2,4,6-triiodobenzene (**5**; 0.04 mmol) were used in stoichiometric amounts (Scheme 1). Small amount (50 µL) of chloroform was added as solvent.
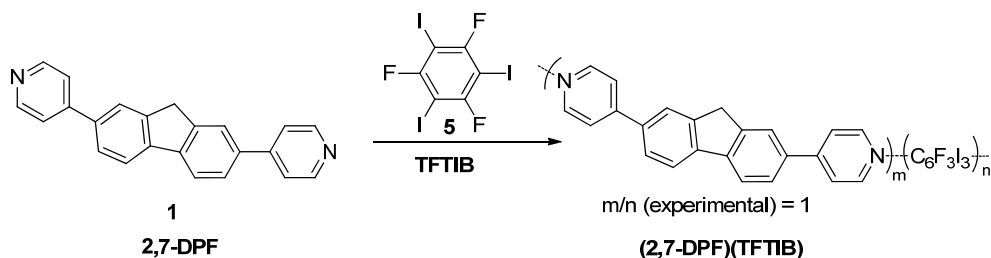
Scheme 1

The formation of the self-assembled entities was monitored by powder X-ray diffractometry (Figure 4). Single crystals suitable for the molecular structure determination were obtained by slow evaporation of the solvent from a CHCl₃ solution of **(2,7-DPF)(TFTIB)**. Surprisingly, in the crystal, an experimental ratio of 2,7-DPF / TFTIB = 1 was observed instead of the expected 2,7-DPF / TFTIB = 3 / 2 ratio. The equimolecular ratio of halogen
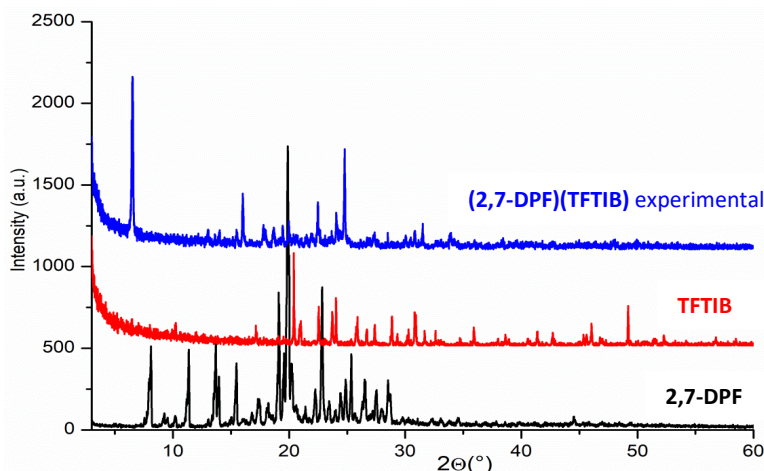

Figure 4. Powder X-ray diffraction spectra of compound 2,7-DPF (bottom)**,** TFTIB (middle) and **(2,7-DPF)(TFTIB)** (top)

donors and acceptors was confirmed using powder X-ray diffractometry for the bulk powder, too. The experimental spectrum (of the raw product) and the theoretical one (calculated from the single crystal X-ray diffraction measurements) (Figure 5) were similar and proved the presence of the same structures in the bulk powder product and in the measured crystal.
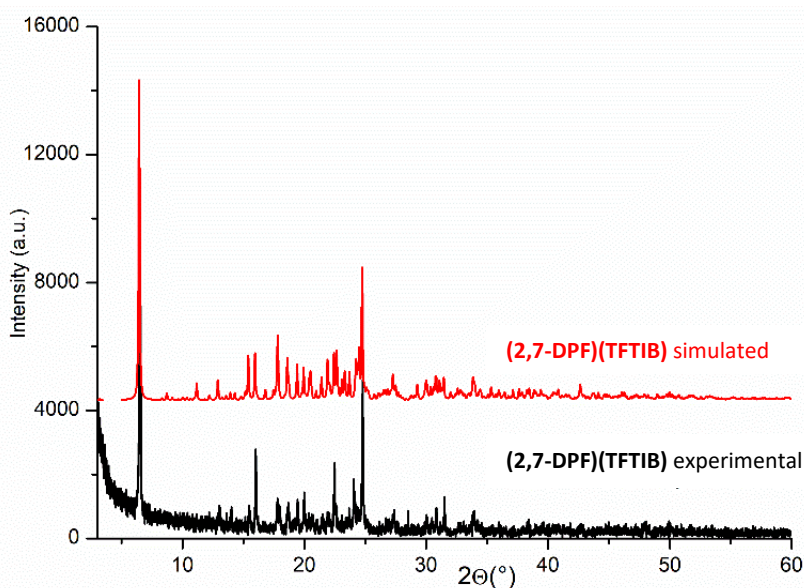

Figure 5. Experimental (bottom) and simulated (top) powder X-ray diffraction spectra of cocrystal **(2,7-DPF)(TFTIB)**

The repetitive unit in the single crystal X-ray diffraction structure of **(2,7-DPF)(TFTIB)** shows two geometries for the 2,7-DPF units connected to the TFTIB moieties, unit A and unit B (Figure 6a). The fluorene units are slightly curved, with a dihedral angle between the benzene rings of 7.1° (unit A) and 5.8° (unit B), respectively. Interestingly, the pyridine moieties exhibit quite different torsion angles with the adjacent benzene rings in the two units: 13.45° and 32.36° in unit B, and very close values for the torsion angles in unit A, 26.82° and 31.15°, respectively, bringing the pyridyl units almost coplanar to each other in the latter case, with consequences in their different association pattern as mentioned further.
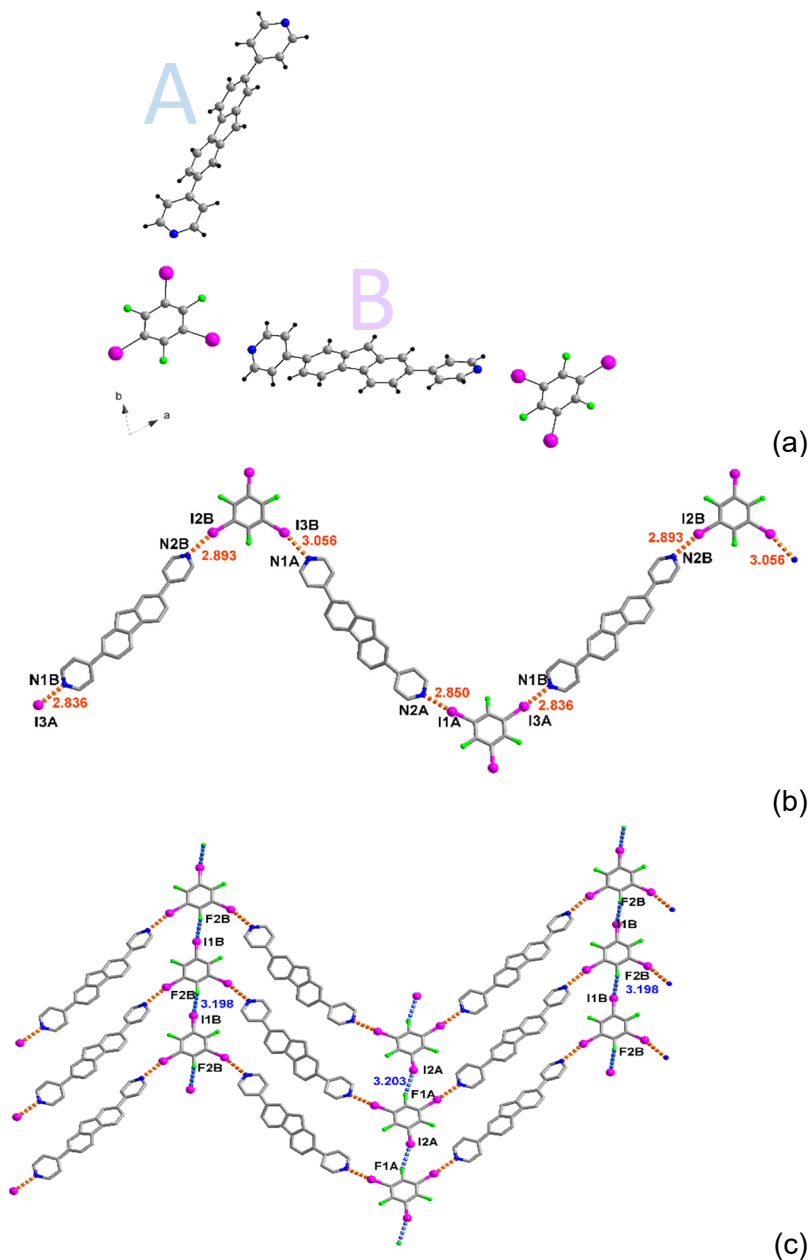
Figure 6. Halogen bonding motifs in the single crystal X-ray structure of
(2,7-DPF)(TFTIB) cocrystal: repetitive unit (A and B units) (a); I···N (orange)
generated catemer (b); 2D sheet *via* additional I···F contacts (blue) (c).

The thus determined structure of the cocrystal was found to contain halogen-bonded 2,7-DPF and TFTIB molecules. The 2,7-DPF is participating in halogen bonding with the nitrogen acceptor atoms, while TFTIB acts as a ditopic halogen donor in this arrangement as only two of its iodine atoms are involved in I···N halogen bonding, most probably due to steric impediments, resulting into zig-zag infinite supramolecular chains (Figure 6b). The TFTIB moiety is involved further *via* its third iodine atom in I···F contacts that lead to the formation of a quasi-coplanar 2D sheet, parallel to the crystallographic *a* axis (Figure 6c). In order to assess the strength of the formed halogen bonds, the relative shortenings of the I···Acceptor bonds were calculated and are included in Table 1 alongside the values for the halogen bond length and C–I···Acceptor angles.

Table 1. Halogen bond length (*d*), Angle, Relative Shortening (*R.S.)* of I···Acceptor distances in **(2,7-DPF)(TFTIB)** cocrystal

I···Acceptor	*d*(I···Acceptor)/Å	*R.S.*[‡]/%	Angle (C–I···Acceptor)/°
I1A···N2A	2.85	19.26	172.19
I3A···N1B	2.836	19.66	176.07
I2B···N2B	2.893	18.05	167.77
I3B···N1A	3.056	13.43	164.44
I2A···F1A	3.203	7.16	160.95
I1B···F2B	3.198	7.3	163.44

[‡] *R.S.* was calculated as $R.S. = \{1 - d(\text{I}\cdots\text{Acceptor})/[r_{vdW}(\text{I}) + r_{vdW}(\text{Acceptor})]\}*100$

As observed in Table 1, the nitrogen atoms form quite strong halogen bonds, 18-19.66% shorter than the sum of the van der Waals radii in most cases and the bond angles are acceptable. The I···F bonds are less shortened, but in good agreement with other similar assemblies [14d] and contribute to the overall stability of the structure.

The 2D sheets stack further into layers *via* reciprocal C-H···aromatic contacts between H atoms pertaining to the pyridine rings in one sheet and the phenyl ring of the fluorene in the next sheet ($d_{C(23B)-H\cdots\text{centroid Ph}}$ = 3.153 Å) and moreover interconnected by C-H···F hydrogen-bonding contacts ($d_{C(3B)-H\cdots F1B}$ = 3.207 Å) with a shifted TFTIB unit underneath into a complex 3D architecture (Figure 7). It is interesting to mention that only unit B of 2,7-DPF is involved in such short contacts, while for unit A only significantly larger contact values were observed.
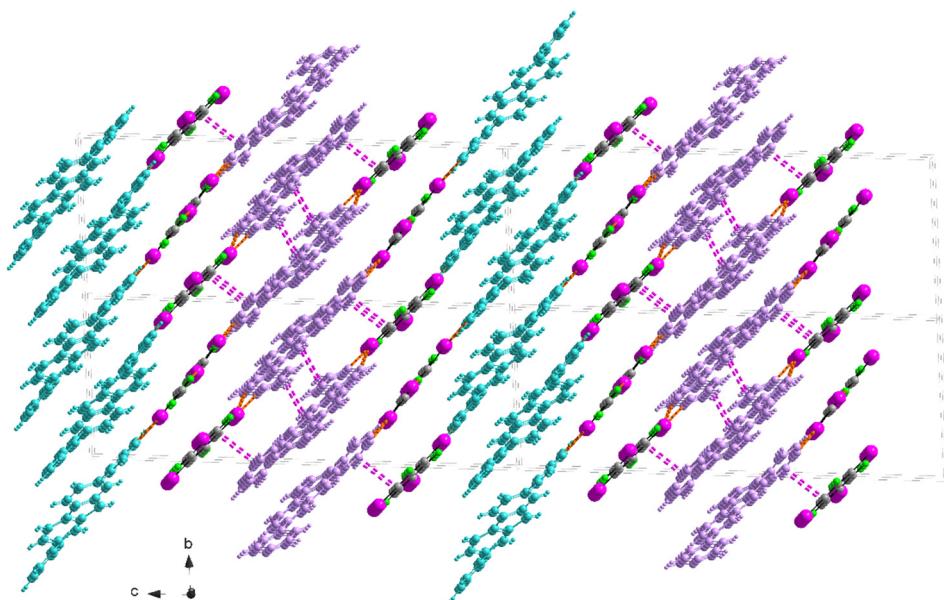
LIDIA CĂTA, IOANA GEORGETA GROSU, MARIA MICLĂUŞ,
NICULINA DANIELA HĂDADE, ION GROSU, ANAMARIA TEREC

Figure 7. Double layers interconnected by C–H···aromatic and C–H···F contacts
(violet) in **(2,7-DPF)(TFTIB)** – A units are represented in aqua, B units in pink

CONCLUSIONS

Ditopic halogen acceptor 2,7-DPF and tritopic halogen donor TFTIB
form a 2D halogen bond organic framework (XBOF) by N···I and I···F
contacts. The sheets are connected in a 3D structure by C–H···aromatic and
C–H···F interactions. The TFTIB molecules form catemers by I···F contacts
and thus, only two iodine atoms of the donor molecules are involved in N···I
contacts. The competition between I···N and I···F halogen bonds determines
the peculiar supramolecular structure of **(2,7-DPF)(TFTIB)** co-crystal and the
unexpected 2,7-DPF / TFTIB equimolecular ratio in the crystals.

EXPERIMENTAL PART

General data for X-ray diffraction measurements for **(2,7-DPF)(TFTIB)**

X-ray Powder Diffraction (XRPD)

X-ray patterns were collected at room temperature with a Rigaku Smart
Lab multipurpose diffractometer, using Cu Kα1 radiation (λ= 1.54056 Å),
equipped with a 9 kW rotating anode. For the acquisition of the experimental

data Smart Lab Guidance software were used. The samples were ground to a fine homogeneous powder using an agate pestle and mortar and mounted in a sample holder. The measurements were performed in the 3–60° range in steps of 0.01°.

Single-crystal X-ray diffraction measurement

Single-crystal diffraction data were collected, at room temperature, on an Oxford Diffraction SuperNova dual wavelength diffractometer with operating mirror monochromated MoKα radiation mode (λ = 0.71073 Å). X-ray data collection was monitored and all the data were corrected for Lorentzian, polarization and absorption effects using CrysAlisPro program [Agilent Technologies, CrysAlis PRO, Yarnton Oxfordshire, England: Agilent Technologies, 2010] Olex2 program was used for the crystal structures solution and refinement, [17] SHELXT was used for structures solutions and for full matrix least-squares refinement on F2 (Table 2). [18]

Table 2. Crystallographic data for **(2,7-DPF)(TFTIB)**

Identification code		(2,7-DPF)(TFTIB)	
Empirical formula	$C_{58}H_{30}F_6I_6N_4$	$\gamma/°$	72.835(4)
Formula weight	1658.30	Volume	2695.4(2) Å^3
Wavelenght	1.54184	Z	2
Temperature	293(2) K	Density (calculated)	2.043 g/cm^3
Crystal system	triclinic	Absorption coefficient mm^{-1}	27.685
Space group	P-1	F(000)	1556.0
a/Å	9.2485(3)	Reflections collected	17255
b/Å	11.1194(6)	Data/restraints/parameters	9965 /2/667
c/Å	27.5846(9)	Goodness-of-fit on F^2	1.104
$\alpha/°$	84.698(3)	Final R indexes [I>=2σ (I)]	R_1 = 0.1048, wR_2 = 0.2715
$\beta/°$	85.714(3)	Final R indexes [all data]	R_1 = 0.1333, wR_2 = 0.3333
		Largest diff. peak/hole / e Å^{-3}	2.82/-1.72

The structural data were deposited at Cambridge Crystallographic Data Center (number CCDC 2180363).

LIDIA CĂTA, IOANA GEORGETA GROSU, MARIA MICLĂUŞ,
NICULINA DANIELA HĂDADE, ION GROSU, ANAMARIA TEREC

REFERENCES

[1] a) J.-M. Lehn, *Supramolecular chemistry: concepts and perspectives*; VCH, Weinheim, **1995**; b) J. W. Steed, J. L. Atwood, *Supramolecular Chemistry*, Wiley, New York, **2009**; c) Lehn, J.-M., *Angew. Chem. Int. Ed.* **2015**, *54*, 3276 – 3289; d) D. Qiao, H. Joshi, H. Zhu, F. Wang, Y. Xu, J. Gao, F. Huang, A. Aksimentiev, J. Feng, *J. Am. Chem. Soc*. **2021**, *143*, 15975−15983; e) J. Wang, Y.-Y. Ju, K.-H. Low, Y.-Z. Tan, J. Liu, *Angew. Chem. Int. Ed.* **2021**, *60*, 11814 – 11818; f) M. Balog, I. Grosu, G. Plé, Y.Ramondenc, E. Condamine, R. Varga, *J. Org. Chem.* **2004***, 69,* 1337-1345.

[2] a) S. Sarkar, P. Sarkar, P. Ghosh, *J. Org. Chem.* **2021**, *86*, 6648−6664; b) C. V. Crişan, A. Soran, A. Bende, N. D. Hădade, A. Terec, I. Grosu, *Molecules,* **2020**, *25*, nr. 3789; c) C.V. Crişan, A. Terec, N. D. Hădade, I. Grosu, *Tetrahedron*, **2015**, *71*, 6888-6893.

[3] a) W. Wang, Y.-X. Wang, H.-B. Yang, *Chem. Soc. Rev.* **2016**, *45,* 2656–2693; b) G. Liu, M. Zeller, K. Su, J. Pang, Z. Ju, D. Yuan, M. Hong, *Chem. Eur. J.* **2016**, *22*, 17345 – 17350; c) S. Wang, T. Sawada, K. Ohara, K. Yamaguchi, M. Fujita, *Angew. Chem. Int. Ed.* **2016**, *55*, 2063 –2066.

[4] a) J. E. M. Lewis, M. Galli, S. M. Goldup, *Chem. Commun.* **2017**, *53*, 298—312; b) N. Pearce, M. Tarnowska, N. J. Andersen, A. Wahrhaftig-Lewis, B. S. Pilgrim, N. R. Champness, *Chem. Sci.*, **2022**, *13*, 3915–3941; c) C.-Y. Chen, H.-C. Xu, T.-H. Ho, C.-J. Hsu, C.-C. Lai, Y.-H. Liu, S.-M. Peng, S.-H. Chiu, *J. Org. Chem.* **2021**, *86*, 13491−13502.

[5] a) I. Hisaki, *J. Incl. Phenom. Macrocycl. Chem*. **2020**, *96*, 215–231; b) P. Li, P. Li, M. R. Ryder, Z. Liu, C. L. Stern, O. K. Farha, J. F. Stoddart *Angew. Chem. Int. Ed*. **2019**, *58*, 1664 – 1669; c) R.-B. Lin, Y. He, P. Li, H. Wang, W. Zhou, B. Chen, *Chem. Soc. Rev*. **2019**, *48*, 1362-1389; d) T. Adachi, M.D. Ward, *Acc. Chem. Res*. **2016**, *49*, 2669 – 2679; e) Y.-L. Li, E. V. Alexandrov, Q. Yin, L. Li, Z.-B. Fang, W. Yuan, D. M. Proserpio, T.-F. Liu, *J. Am. Chem. Soc*. **2020**, *142*, 7218−7224; f) M. Circu, V. Pascanu, A. Soran, B. Braun, A. Terec, C. Socaci, I. Grosu, *CrystEngComm,* **2012,** *14,* 632-639.

[6] a) Y. Feng, D. Philp, *J. Am. Chem. Soc*. **2021**, *143*, 17029−17039; b) Y. Liu, J. Dai, Z. Zhang, Y. Yang, Q. Yang, Q. Ren, Z. Bao, *Chem Asian J*. **2021**, *16*, 3978–3984; c) I. Hisaki, C. Xin, K. Takahashi, T. Nakamura, *Angew. Chem. Int. Ed*. **2019**, *58*, 11160 – 11170; d) S. A. Boer, M. Morshedi, A. Tarzia, C. J. Doonan, N. G. White, *Chem. Eur. J.* **2019**, *25*, 10006 – 10012; e) L. Pop, N. D. Hădade, A. van der Lee, M. Bărboiu, I. Grosu, Y.-M. Legrand, *Cryst. Growth Des.*, **2016**, *16*, 3271–3278.

[7] a) L. Sun, W. Zhu, X. Zhang, L. Li, H. Dong, W. Hu, *J. Am. Chem. Soc.* **2021**, *143*, 19243−19256; b) G. Gong, S. Lv, J. Han, F. Xie, Q. Li, N. Xia, W. Zeng, Y. Chen, L. Wang, J. Wang, S. Chen, *Angew. Chem. Int. Ed.* **2021**, *60*, 14831 –14835; c) I. G. Grosu, L. Pop, M. Miclăuş, N. D. Hădade, A. Terec, A. Bende, C. Socaci, M. Bărboiu, I. Grosu, *Cryst. Growth Des.,* **2020***, 20*, 3429-3441; d) L. Pop, I. G. Grosu, M. Miclăuş, N. D. Hădade, A. Pop, A. Bende, A. Terec, M. Barboiu, I. Grosu, *Cryst. Growth Des.,* **2021***, 21*, 1045-1054; e) M. Miclăuș, X. Filip, C. Filip, F. Martin, I. G. Grosu, *J. Pharm. Biomed. Anal.* **2016**, *124,* 274-280.

202

[8] a) F. Biedermann, W. M. Nau, H.-J. Schneider, *Angew. Chem., Int. Ed*. **2014**, *53*, 11158−11171; b) J. H. Jordan, B. C. Gibb, *Chem. Soc. Rev*. **2015**, *44*, 547−585; c) L. Pop, F. Dumitru, N. D. Hădade, Y.-M. Legrand, A. van der Lee, M. Bărboiu, I. Grosu, *Org. Lett.* **2015**, *17*, 3494−3497.

[9] a) H. Su, S. A. H. Jansen, T. Schnitzer, E. Weyandt, A. T. Rösch, J. Liu, G. Vantomme, E. W. Meijer, *J. Am. Chem. Soc*. **2021**, *143*, 17128−17135; b) J. Hwang, P. Li, K. D. Shimizu, *Org. Biomol. Chem*. **2017**, *15*, 1554−1564; c) A. Das, S. Ghosh, *Angew. Chem., Int. Ed*. **2014**, *53*, 2038−2054.

[10] a) S. Yang, A. Miyachi, T. Matsuno, H. Muto, H. Sasakawa, K. Ikemoto, H. Isobe *J. Am. Chem. Soc*. **2021**, *143*, 15017−15021; b) D. Preston, *Angew. Chem. Int. Ed*. **2021**, *60*, 20027 – 20035; c) J. Shi, M. Wang, *Chem Asian J*. **2021**, *16*, 4037–4048.

[11] a) I. G. Grosu, M. I. Rednic, M. Miclăuş, I. Grosu, A. Bende, *Phys. Chem. Chem. Phys*. **2017**, *19*, 20691-20698; b) M. I. Rednic, R. A. Varga, A. Bende, I. G. Grosu, M. Miclăuş, N. D. Hădade, A. Terec, E. Bogdan, I. Grosu, *Chem. Commun.*, **2016**, *52*, 12322-12325.

[12] a) D. M. P. Mingos, Series Editor for *Structure and Bonding*, Metrangolo, P; Resnati, G; editors for volume 126: *Halogen Bonding – Fundamentals and Applications*, Springer, Berlin, **2008**, volume 126; b) P. Metrangolo, G. Resnati, editors, *Halogen Bonding II, Impact on the Materials Chemistry and Life Sciences*, *Topics in Current Chemistry*, Springer, Berlin, **2015**, volume 359; c) P. M. J. Szell, S. Zablotny, D. L. Bryce, *Nat. Commun*. **2019**, Article number: 916; d) G. Cavallo, P. Metrangolo, R. Milani, T. Pilati, A. Priimagi, G. Resnati, G. Terraneo, *Chem. Rev*. **2016**, *116*, 2478 – 2601.

[13] a) M. C. Pfrunder, A. S. Micallef, L. Rintoul, D. P. Arnold, K. J. P. Davy, J. McMurtrie, *Cryst. Growth Des*. **2014**, *14*, 6041−6047; b) V. I. Nikolayenko, D. C. Castell, D. P. van Heerden, L. J. Barbour, *Angew. Chem., Int. Ed*. **2018**, *57*, 12086−12091; c) D. Bulfield, E. Engelage, L. Mancheski, J. Stoesser, S. M. Huber, *Chem. Eur. J*. **2020**, *26*, 1567−1575.

[14] a) N. Biot, D. Bonifazi, *Chem. Eur. J.* **2020**, *26*, 2904−2913; b) M. Su, X. Yan, X. Guo, Q. Li, Y. Zhang, C. Li, *Chem. Eur. J.* **2020**, *26*, 4505−4509; c) M.-P. Zhuo, Y.-C. Tao, X.-D. Wang, Y. Wu, S. Chen, L.-S. Liao, L. Jiang, *Angew. Chem. Int. Ed.* **2018**, *57*, 11300−11304; d) N. Baus Topić, N. Bedeković, K. Lisac, V. Stilinović, D. Cinčić, *Cryst. Growth Des.* **2022**, *22*, 3981-3989.

[15] a) S. Shankar, O. Chovnik, L. Shimon, M. Lahav, M. E. van der Boom, *Cryst. Growth Des*. **2018,** *18*, 1967−1977; b) N. Chongboriboon, K. Samakun, T. Inprasit, F. Kielar, W. Dungkaew, L. W.-Y. Wong, H. H.-Y. Sung, D. B. Ninkovic, S. D. Zaric, K. Chainok, *CrystEngComm* **2020**, *22*, 24−34; c) K. Raatikainen, K. Rissanen, *CrystEngComm* **2011**, *13*, 6972−6977.

[16] a) J. L. Howard, Q. Cao, D. L. Browne, *Chem. Sci.* **2018**, *9*, 3080−3094; b) M. Leonardi, M. Villacampa, J. C. Menéndez, *Chem. Sci*. **2018**, *9*, 2042−2064; c) M. Obst, B. Konig, *Eur. J. Org. Chem*. **2018**, 4213−4232.

[17] O. V. Dolomanov, L. J. Bourhis, R. J. Gildea, J. A. K. Howard, H. Puschmann, *J. Appl. Cryst*. **2009**, *42*, 339-341.

[18] G. M. Sheldrick, *Acta Cryst. A* **2015**, *71*, 3-8.